RIKAGAKU KENKYUSHO
the Institute of Physical and Chemical Research
Wako-shi, Saitama Pref., JAPAN

’74

IPCR cyclotron
Progress Report 1974

Vol. 8

IPCR Cyclotron Progress Report

Vol. 8

The Institute of Physical and Chemical Research
"RIKAGAKU KENKYUSHO" Wako-shi, Saitama, 351 JAPAN
December, 1974

Editors

F. Ambe	M. Imamura
M. Odera	H. Sakairi
A. Hashizume	

This volume contains recent information of the IPCR Cyclotron, informal reports and abstracts of papers which will be published at scientific meetings or in publications by staff members, guests, and visitors.

CONTENTS

8. RADIOCHEMISTRY AND NUCLEAR CHEMISTRY

9. RADIATION CHEMISTRY AND RADIATION BIOLOGY

10. PREPARATION OF RADIOISOTOPES AND LABELED COMPOUNDS

11. RADIATION MONITORING

12. A NEW MACHINE

1. INTRODUCTION

The cyclotron has been operated for eight years with prudent care to and constant improvements by the technical staffs and operation crew. Total work time of the machine reached as much as 38,000 h until the end of 1974.

As in the previous years, the heavy ion acceleration was the main mode of operation in this year. The acceleration of boron ions was tested and proved successful.

Experimental and theoretical studies on nuclear reactions and level structures were continued. Researches related to radiation chemistry and radiation biology were carried out mainly using heavy ions. On-line optical and ESR spectroscopy was applied to study the difference in LET effects by heavy and light projectiles. Charged-particle activation analysis, production of radio-isotopes and preparation of labeled compounds for medical use were carried out. The analysis on the states of atomic electrons by the methods such as inner shell excitation by heavy ions and measurements of angular correlation of annihilation gamma-rays were made.

The development of the polarized ion source has been completed. It is scheduled to be installed in the cyclotron of the Institute for Nuclear Study, University of Tokyo, in 1975 and will be used by people of the both institutes, IPCR and INS.

The heavy-ion linac project was approved by the Government this year. The progress of its construction and related researches will be described in this and the following issues.

It is our great regret to announce the sudden death of Dr. H. Tahara, Chief of the Organic Synthesis Laboratory, on January 2, 1975. His work on the preparation of ^{18}F-labeled compounds greatly contributed to the field of medical diagnosis.

H. Hagihara

Hitosi Hagihara, Chairman
The Cyclotron Board

2. MACHINE OPERATION

H. Nakajima, K. Ogiwara, S. Fujita, K. Ikegami,
T. Kageyama, S. Kohara, and H. Takebe

During the period from Oct. 1973 to Oct. 1974 the cyclotron was operated on the 24 h a day basis. Statistics of machine operation is shown in Table 1. The working time meter on beam which indicated 4373 h is decreased by about 13 % compared with last year. However, total days of the machine time was decreased only by 2.5 %. This difference comes from the fact that 19 days were occupied for adaptation of the machine time and the cooling period for residual radiation in the scheduled machine time.

Requirements of heavy ion beams continued to increase and the cyclotron was operated 113 days with the heavy ion source, which was 45 % of the total days of the scheduled machine time, that is, was increased more than 21.5 % compared with last year. Table 2 shows machine time allotments to various activities in this period.

A major part of slight troubles were: Some printed circuit cards were lost by touching with sockets, cooling pipes were choked-up with fur, and fatigued materials with cracks were found at joints between a bellows and cooling pipes for the movable liners in the accelerating chamber.

A transition to the higher mode oscillation of the RF-system sometimes brought about great difficulty to realize higher accelerating voltage, especially for heavy ions. Cooling system of the movable short was changed and capability of anti-transition was improved.

Table 1. Machine operation time and day.

Date	Oscillator	Ion source	Beam
Oct. 23, 1973	32976 (h)	35693 (h)	6652 (h)
Oct. 22, 1974	37715 (h)	40591 (h)	11025 (h)
365 days	4739 (h)	4908 (h)	4373 (h)
Percent of 365 days	54.1 %	56 %	50 %

Schedule in this period:

Machine time	249 (days)
Overhaul and installation work	49 (days)
Periodical inspection and repair	27 (days)
Vacation and holidays	40 (days)

Table 2. Scheduled machine time and subjects of activity in the period, IX

	Subject	Heavy ion	Light particles	Total
Nucl. phys.	Direct reaction	1561 (h)	1670 (h)	3231 (h)
	In-beam spectroscopy	549	142	691
	RI production	0	84	84
Fields other than nucl. phys.	Nuclear chemistry	0	433	433
	Radiation chemistry	172	13	185
	Radiation biology	131	80	211
	Solid state physics	0	222	222
	Inner atomic shell excitation study	24	0	24
Outside users	Nuclear medicine	0	192	192
	Nuclear fuel study	0	121	121
	RI Production	24	17	41
	Development of instruments	45	46	91
Total		2506 (h)	3020 (h)	5526 (h)
Percent in total		45.3 %	54.7 %	100 %

Maintenance operation and engineering

Exchange of ion source	58 (h)
Reserved for machine time adjustment and cooling of radiation	456 (h)
Machine inspection and repair	624 (h)
Total	1138 (h)

3. MACHINE DEVELOPMENT AND ACCELERATOR PHYSICS

3-1. Acceleration of Boron Ions in the Cyclotron

A. Shimamura and I. Kohno

It was planned to accelerate B ions in the cyclotron. For this purpose, the production of multiply-charged ions of B using the IPCR ion source was studied at a test bench, and sufficient quantities of $^{10}B^{3+}$ and $^{11}B^{3+}$ ions were obtained. These B ions were successfully accelerated in the cyclotron employing the following procedure.

(1) Gas flow system

Figure 1 shows the gas flow system of BCl_3, which was used as the sample gas. Since

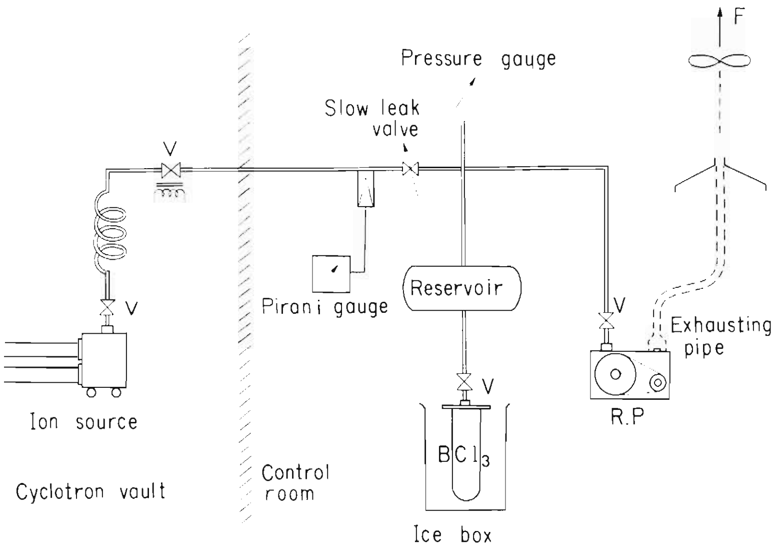

Fig. 1. Gas flow system.

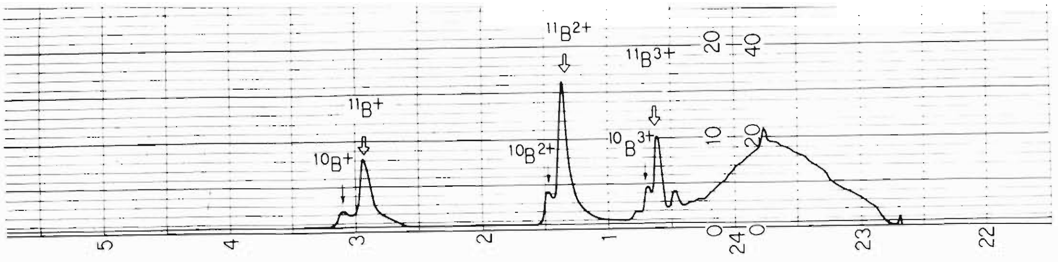

Gas : BCl_3

Arc power = 700V , 2.3 A

p = 2.5×10^{-5} Torr.

Magnetic field = 0.6 Wb/m^2

Fig. 2. A m/q spectrum of the ion beam measured at the test bench when BCl_3 gas was fed. Arc power: 700V, 2.3A, Vac. = 2.5×10^{-5} Torr. Magnetic field = 0.6 Wb/m^2.

BCl_3 is a liquid whose vapor pressure at 0°C is about 400 Torr, the reservoir of BCl_3 was dipped in ice-water. This gas was introduced into the ion source through a slow leak valve. The gas flow system was evacuated by an auxiliary rotary pump. Since BCl_3 reacts with H_2O in the air, the exhausted gas was discharged to outdoors using a blower so as not to make any trouble. The gas flow rate was measured with a Pirani gauge.

(2) Production of multiply-charged ions of B

Figure 2 shows the m/q spectrum of ^{10}B and ^{11}B ions measured in the test bench.$^{1)}$ In the spectrum peaks corresponding to $^{11}B^{+}$, $^{10}B^{+}$, $^{11}B^{2+}$, $^{10}B^{2+}$, $^{11}B^{3+}$ and $^{10}B^{3+}$ ions were found. As the yields were measured in a unit of electric current, the particle yield of B^{3+} ions was one-third times that of B^{+} ions at the same current reading.

(3) Acceleration of B ions

$^{10}B^{3+}$ and $^{11}B^{3+}$ ions were accelerated in the cyclotron. Fig. 3 shows a m/q spectrum of ions accelerated in the cyclotron when BCl_3 gas was introduced into the ion source.

The spectrum was measured by varying the strength of the magnetic field at a radius of 69cm. These $^{11}B^{3+}$ and $^{10}B^{3+}$ ions were extracted from the cyclotron at intensities of 4 μA and 1 μA respectively. The energy ranges of $^{11}B^{3+}$ and $^{10}B^{3+}$ ions obtained in the IPCR cyclotron were 50 to 72 MeV for the former and 45 to 70 MeV for the latter.

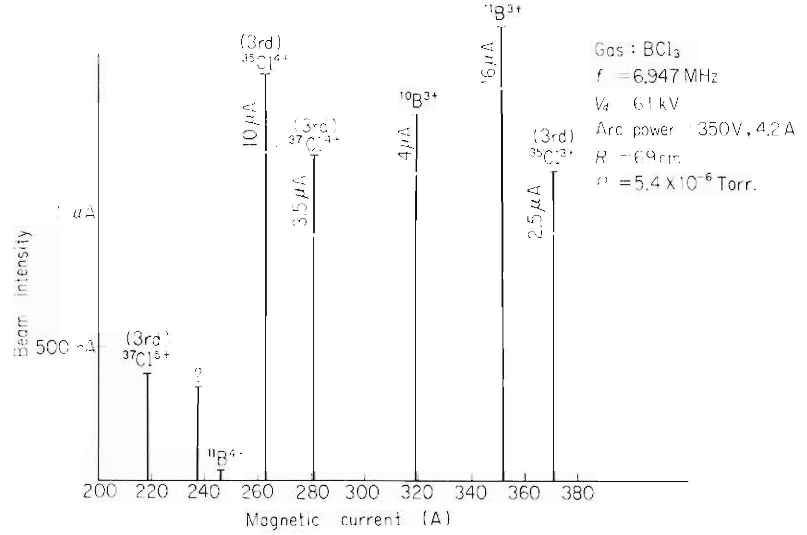

Fig. 3. A m/q spectrum of the ion beam in the cyclotron when BCl_3 gas was fed to the source.

Reference

1) I. Kohno et al.: IPCR Cyclotron Progr. Report, 1, 13 (1967).

4. NUCLEAR PHYSICS

Scattering and Reactions

4-1. Incident Energy Dependence of Optimum Q-Values in Multinucleon Transfer Reactions Induced by Heavy Ions

T. Mikumo, I. Kohno, K. Katori, T. Motobayashi,
S. Nakajima, M. Yoshie, and H. Kamitsubo

We report here on the systematics of positions of the maximum in the distribution of excitation energy $E_x^m(B)$ and the corresponding Q-Values $Q^m(B)$ of a residual nucleus B, deduced from the continuous spectra ("bumps") of b of the reactions of type A(a, b) B, and on their dependence on E_a. Using ^{14}N and ^{12}C beams and targets of f-p shell nuclei (^{50}Ti, ^{52}Cr, ^{53}Cr and ^{54}Fe), we studied nuclear reactions at energies about twice to three times higher than the Coulomb barrier ($E_L = 60 \sim 95$ MeV). The reactions studied are listed in Table 1, together with useful experimental conditions and experimental results. Typical spectra for $^{52}Cr + ^{14}N$ reactions at 80 MeV at $\Theta_L = 22°$ are shown in Fig. 1.

Table 1. Multi-nucleon transfer reactions. A (a, b) B.

A=a	E_L (MeV)	E_i (MeV)	E_i/B_C (r_0=1.4fm)	E_i-B_C (r_0=1.4fm)	b measured	Θ_L (b) (deg)
$^{52}Cr + ^{14}N$	95	74.9	2.89	49.0	^{13}C, ^{12}C, ^{12}B, ^{11}B, ^{10}B, ^{10}Be ^{9}Be, ^{7}Be, ^{7}Li, ^{6}Li, ^{4}He	16, 20, 25
	90	70.9	2.73	44.6	"	16, 25, 18, 22, 27
	80	63.0	2.43	37.1	"	18, 22, 27
	70	55.2	2.16	29.3	"	22, 27
	64	50.4	1.95	24.5	"	20, 27
$^{53}Cr + ^{14}N$	90	71.2	2.74	45.0	^{16}O, ^{15}O, ^{15}N, ^{13}C, ^{12}C, ^{11}B, ^{10}B, ^{10}Be, ^{9}Be, ^{7}Be, ^{7}Li, ^{6}Li, ^{4}He	10, 12, 15, 18 24, 27, 30, 33
$^{50}Ti + ^{14}N$	70	54.7	2.41	32.0	^{13}C, ^{12}C, ^{11}B, ^{16}B	25
$^{54}Fe + ^{14}N$	70	55.6	1.94	26.9	"	26
$^{52}Cr + ^{12}C$	90	73.1	2.97	48.5	^{10}B, ^{10}Be, ^{9}Be, ^{7}Be	18
	70	56.9	2.31	32.3	^{10}B, ^{10}Be, ^{9}Be	18, 22
	60	48.8	1.98	24.2	"	17, 19, 22, 25, 27
$^{50}Ti + ^{12}C$	60	48.4	2.13	25.7	"	25
$^{54}Fe + ^{12}C$	60	49.1	1.86	22.7	"	25

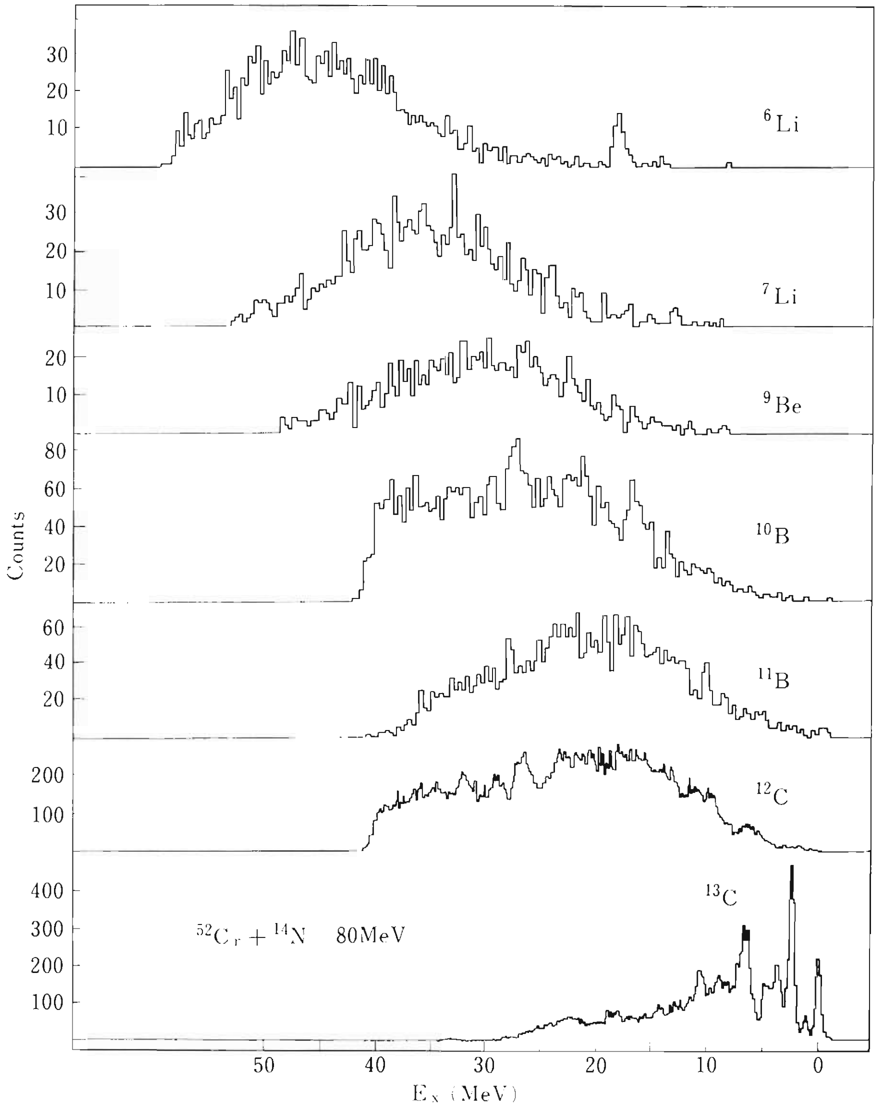

Fig. 1. Energy spectra of ^{13}C, ^{12}C, ^{11}B, ^{10}B, ^{9}Be, ^{7}Li and ^{6}Li particles emitted in the ^{52}Cr + ^{14}N reaction at an energy of 80 MeV and a laboratory angle of 22 degrees.

Note first the following characteristic features about the Q^m (B) of reactions, in particular, ^{52}Cr + ^{14}N (E_L = 95, 90, 80, 70 and 64 MeV) and ^{53}Cr + ^{14}N (E_L = 90 MeV) which were most widely studied.

(1) For incident c.m. energies E_i considerably higher than the Coulomb barrier B_c for the a+A system, the spectrum shape of b is mainly characterized by a continuous bell-shaped form (bump). The shapes of bumps are very asymmetric for smaller n, the number of transferred nucleons, while they approach symmetric forms for the larger n. Further insight of the energy spectra of ^{53}Cr + ^{14}N at 90 MeV at various angles reveals the existence of two components in the bump (with b = ^{13}C, ^{12}C, ^{11}B, ^{10}B): a higher energy part (hard component) and a lower energy part (soft component), the peaks of which are separated by $\gtrsim$ 10 MeV. They correspond, presumably, to "quasi-elastic" and "deep-inelastic" processes,[1] respectively. In the angular range

investigated ($\Theta_L = 10 - 33^\circ$). the relative intensity of the hard component is higher at forward angles, while that of the soft component higher at larger angles. We discuss separately about the characteristic features of their angular distributions and the absolute yields. Following discussions are concerned with the systematics of peak positions of overall bumps.

(2) The spectrum shape does not reflect the structure of target nuclei sensitively. For instance, the spectra of ^{52}Cr + ^{14}N → ^{54}Mn + ^{12}C and ^{53}Cr + ^{14}N → ^{55}Mn + ^{12}C are quite similar in shape at the same bombarding energy.

(3) In general, $|Q^m(B)|$ increases with an increase in n for a given incident channel (Fig. 2) as reported elsewhere.$^{2)}$ The accuracy of the values of Q^m is, in most cases, within about ± 2 MeV.

(4) $Q^m(B)$ varies very slowly with Θ_L, angle of emission of b, and often remains almost constant throughout a wide range of Θ_L investigated, especially in ^{53}Cr + ^{14}N → ^{55}Mn + ^{12}C

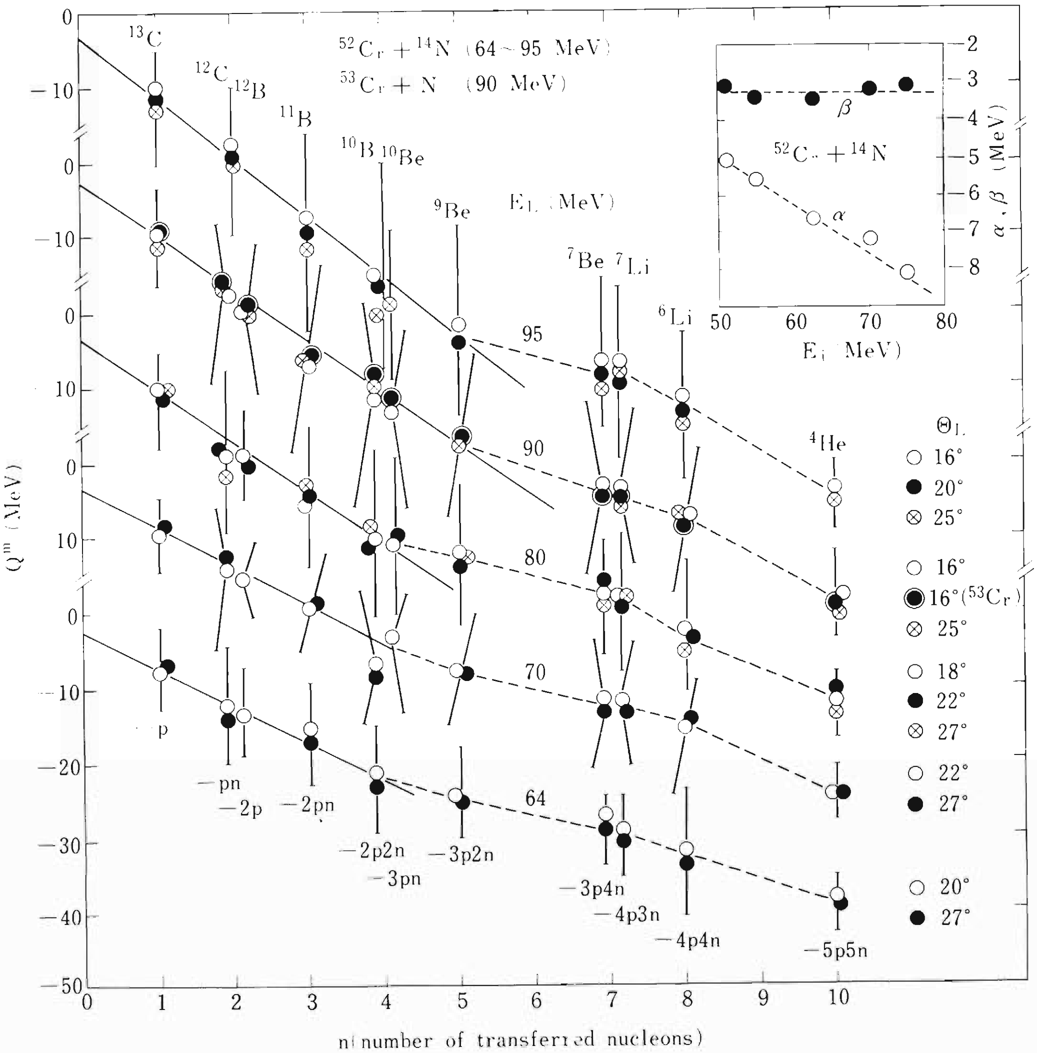

Fig. 2. Q^m vs. n (number of transferred nucleons) curves for ^{13}C, ^{12}C, ^{12}B, ^{11}B, ^{10}B, ^{10}Be, ^{9}Be, ^{7}Be, ^{7}Li, ^{6}Li and ^{4}He particles emitted from the ^{52}Cr + ^{14}N reactions at energies of 64, 70, 80 and 95 MeV, and the ^{53}Cr + ^{14}N reaction at an energy of 90 MeV.

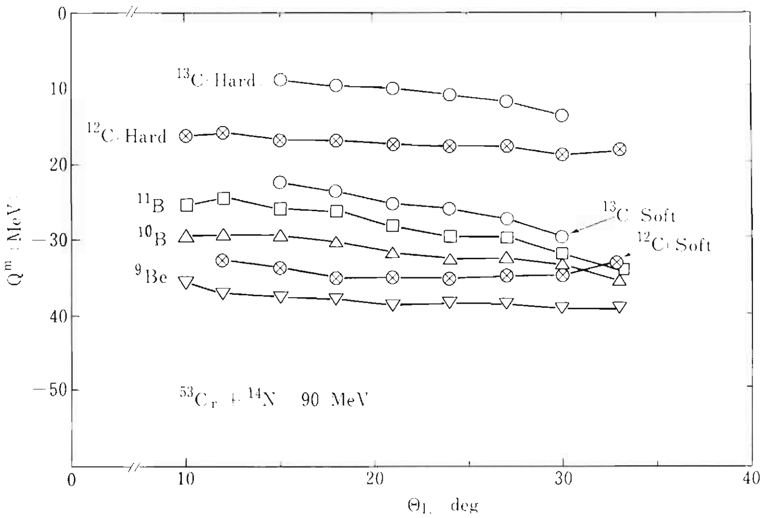

Fig. 3. Q^m vs. Θ_L (detected laboratory angle) curves for ^{13}C, ^{12}C, ^{11}B, ^{10}B and ^{9}Be particles emitted from the $^{53}Cr + {}^{14}N$ reaction at an energy of 90 MeV. For ^{11}B, ^{10}B and ^{9}Be hard and soft components are not separated.

with a very high Q_{gg} value (+ 5.28 MeV), Q_{gg} being the Q-value of the reaction leaving the both final products in the ground states. This situation is shown in Fig. 3 in contrast with the cases for sub-Coulomb or near-Coulomb reactions, where $E_x{}^m(B)$ is strongly dependent on Θ_L.[3)]

(5) Absolute yield of the peak of the bump is strongly dependent on Q_{gg} values among the isotopes studied.

We now discuss the systematics of peak positions of bumps. If we plot Q^m values as a function of n, we obtain an almost linear reaction,

$$Q^m = \alpha n + \beta$$

until n reaches a certain number of transferred nucleons n_0, as shown in Fig. 2. For $^{52}Cr + {}^{14}N$ and $^{53}Cr + {}^{14}N$ (E_L = 64 ~ 95 MeV), n_0 = 5 is at higher energies, while n_0 = 4 at lower energies. The vlues of α's are found to be almost proportional to E_i in $^{52}Cr + {}^{14}N$ reactions, giving a relation:

$$\alpha = \gamma E_i + \delta.$$

In these cases α = −(5 ~ 8) MeV/nucleon and β varies with a, but is nearly independent of E_i. These relations hold in either of the proton and neutron transfers; in other words, for the same a, adjacent A and a given E_i, Q^m's are almost the same for a given n (between isobars of products b), e.g., in ^{12}C and ^{12}B, ^{10}B, and ^{10}Be, ^{7}Be and ^{7}Li (despite large differences in $E_x{}^m(B)$ between isobars of the residuals B).

These characteristics are interpreted as follows: Q^m is rewritten as

$$Q^m = Q_{gg} - E_x^m = E_f - E_i = -\overline{\Delta E},$$

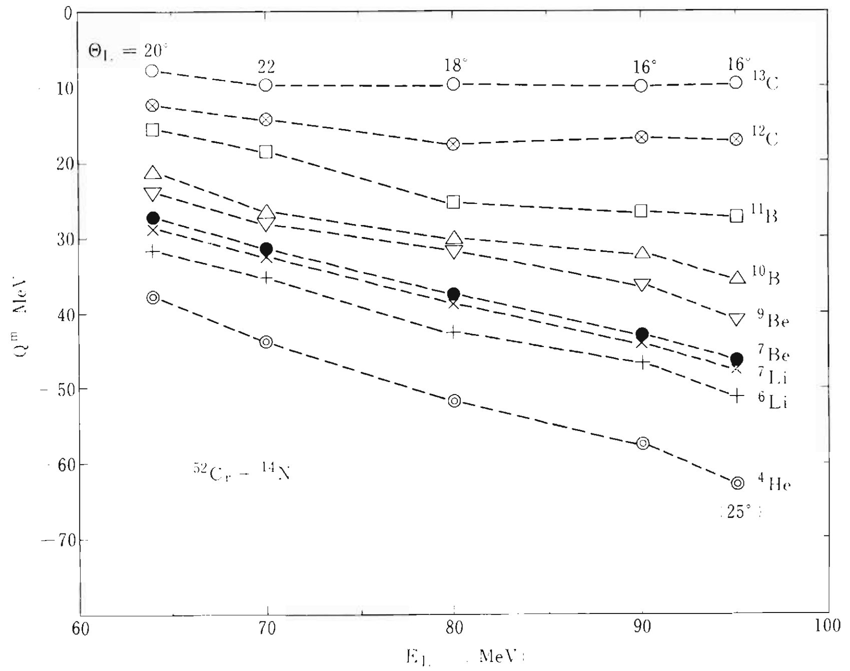

Fig. 4. Q^m vs. E_i (incident energy of projectiles) curves for ^{13}C, ^{12}C, ^{11}B, ^{10}B, ^{9}Be, ^{7}Be, ^{7}Li, ^{6}Li and ^{4}He particles emitted in the $^{52}Cr + ^{14}N$ reaction.

where $\bar{E}_f$ is the mean c.m. energy in the outgoing channel and $\Delta\bar{E}$ is the total energy loss. The linear relations like $Q^m = \alpha n + \beta$ and $\alpha = \gamma E_i + \delta$ reflect the fact that a constant amount of energy is lost per nucleon transfer as long as n is not too large, and this constant rate of energy loss is proportional to the incident energy. If $E_i - B_c$ is large enough, say $\gtrsim$ 30 MeV, the energy loss per nucleon is almost constant until $n = n_0 \approx 5$. For the transfer of nucleon number n beyond n_0, the residual energy of the penetrating particle becomes no more enough to continue to transfer the same amount of energy, or some other reaction mechanism becomes more important. Hence the linear relation is broken down and Q^m is saturated against n. Such a saturation begins at smaller n_0 for smaller $E_i - B_c$ values. The segment of linear line, β looks to reflect the energy loss of the incident particle a in the nuclear matter A due to inelastic processes.

Turning the eyes to the transitions for larger n, say $n \gtrsim 7$, we should remark the following points:

1) Q^m vs. n deviates largely from the linear relation.

2) Q^m vs. E_i has a steeper gradient. The largest gradient is seen with ^4He, where the peak energy value of the outgoing particle b is almost independent of incident energy.

3) The shape of the bump approaches a symmetric form.

4) The peak cross section σ^m increases with increase of n, attaining a very large value for ^4He.

These facts suggest the presence and the importance of reaction mechanism other than those discussed above.

The studies on the systematic features about Q^m, together with the absolute cross sections and angular distributions, may throw light on the elucidation of the mechanism of multinucleon transfer reactions.

References

1) D. H. E. Gross and H. Kalinowski: Phys. Lett., 48B, 302 (1974); A. G. Artukh, G. F. Gridnev, V. L. Mikheec, V. V. Volkov, and J. Wilczynski: JINR E7-6970, Dubna (1973); J. Wilczynski: Phys. Lett., 47B, 484 (1973).

2) T. Mikumo, I. Kohno, K. Katori, T. Motobayashi, S. Nakajima, M. Yoshie, and H. Kamitsubo: Proc. Int. Conf. Reactions between complex Nuclei, Nashville, 1, 64 (1974).

3) N. Anantaraman, K. Katori, and J. P. Schiffer: Proc. of "Symp. on Heavy Ion Transfer Reactions", Argonne National Laboratory, PHY-1973B, 413 (1973); W. von Oertzen: ibid., p. 675 (1973).

4-2. Multi-nucleon Transfer Reactions on Mo-Isotopes by ^{14}N at $E_L = 97$ MeV

M. Yoshie, H. Kamitsubo, K. Katori, I. Kohno,
T. Motobayashi, S. Nakajima, and T. Mikumo

Multi-nucleon transfer reactions between heavy nuclei sufficiently high above the Coulomb barrier have attracted much attention in connection with the reaction mechanism. Systematic data presented by the DUBNA group$^{1)}$ show quite interesting behavior in the cross sections, which depend on the reaction Q-values (Q_{gg}) regularly. Discussions on this regularities and their interpretations are found in the literature.$^{1)}$ Also, Q-values which give maximum cross sections in the energy spectra were interpreted considering the reaction kinematics.$^{2)}$

Particle production cross sections of He, Li, Be, B, C, and O isotopes in the bombardment of all the stable Mo-isotopes by ^{14}N projectiles supplied by the Cyclotron were measured at $E_L = 97$ MeV at two angles $\theta = 25°$ and $30°$. Conventional counter telescope systems were used to identify the particles. Self supporting targets had the thicknesses from 0.45 to 1.0 mg/cm^2. The overall energy resolution was 1 MeV in the worst case. Particle yields were normalized to the forward angle elastic scattering yields measured with the same counter to give the absolute values of production cross sections.

By varying the targets from ^{100}Mo to ^{92}Mo, Q_{gg} changes its value appreciably for a certain reaction, which makes it possible to study the dependence of the cross sections and the spectrum shape on Q_{gg}. On the other hand, it is expected that the angular distributions of

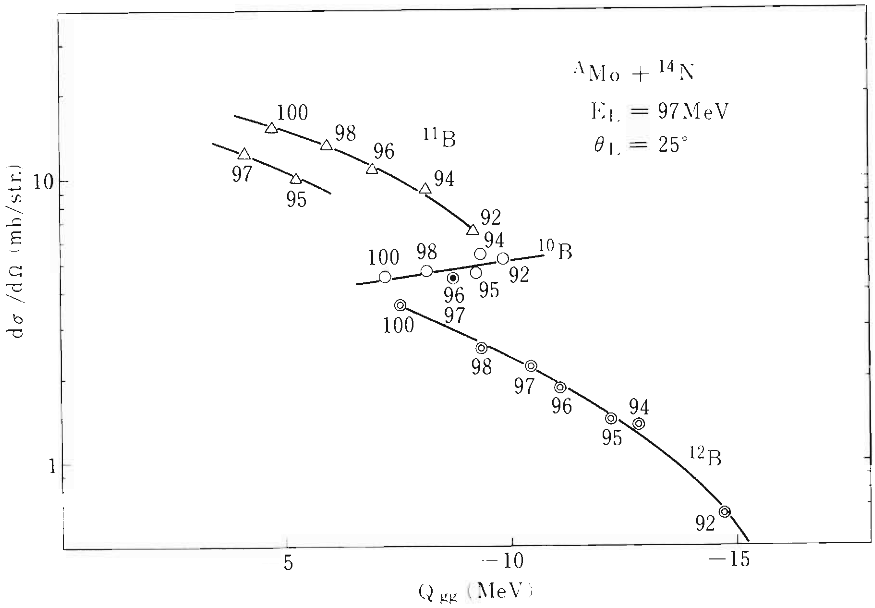

Fig. 1. Production cross sections of B-isotopes in bombardment of Mo-isotopes by ^{14}N at $E_L = 97$ MeV. The numbers in the figure are the mass numbers of the targets.

products do not suffer much changes from the classical estimates. So, the cross sections measured at certain fixed angle are good measures of total cross sections if one type of ejectile is considered. As an example, production cross sections of B-isotopes are plotted against Q_{gg} in Fig. 1. The yields of ^{10}B and ^{12}B are each on one line, whereas the cross sections of ^{11}B from the odd mass targets are slightly smaller than those from the even mass targets. Note that in the former case the neutron numbers of the target residues are even for even mass targets and odd for odd mass targets, whereas the situation is opposite in the latter case. This fact may be due to the effect of the pairing energy.

To characterize the bell-shaped energy spectrum, three Q-values were defined as follows: one is the Q-value which gives the maximum cross sections (Q^m), and the remainning two are those for which each cross section is a half of that at Q^m. These three Q-values are shown also for the B-isotopes in Fig. 2. As the target becomes lighter, the spectrum becomes nallower. Despite the large changes in Q_{gg}, the Q^m remains rather constant, which indicates the importance of reaction kinematics.

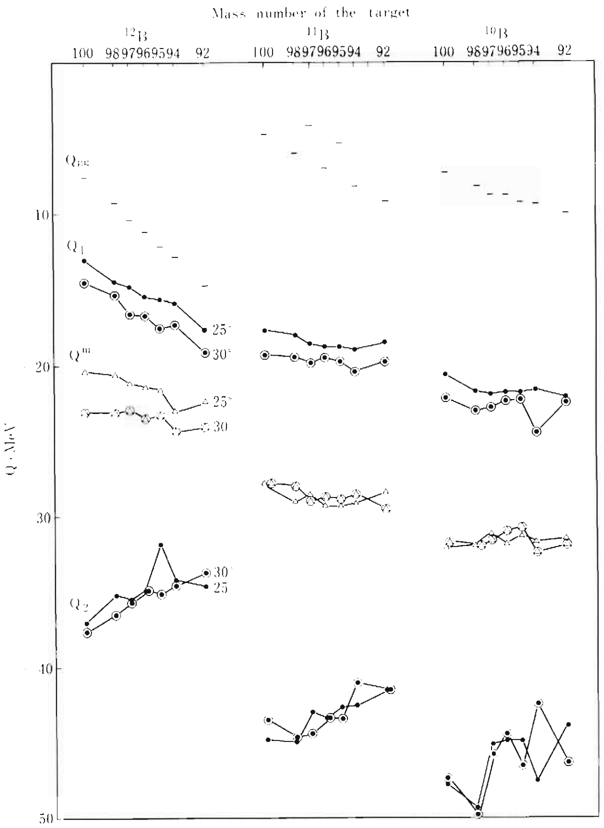

Fig. 2. Three Q-values which characterize the energy spectra of B-isotopes with Q_{gg} are plotted against the mass numbers of the targets. Energy spectra have maxima at Q^m and $\Gamma = Q_1 - Q_2$ gives the FWHM.

References

1) A. G. Altukh, G. H. Gridnev, V. L. Mikheev, V. V. Volkov, and J. Wilczyński: Nucl. Phys., A211, 299 (1973) and the references therein.

2) P. J. Siemens, J. P. Bondorf, D. H. E. Gross, and F. Dickmann: Phys. Lett., 36B, 24 (1971).

4-3. Single-nucleon Transfer Reactions on ^{92}Mo Induced by ^{14}N and ^{12}C

M. Yoshie, K. Katori, I. Kohno, T. Mikumo,
T. Motobayashi, S. Nakajima, and H. Kamitsubo

In order to elucidate the validity of the semi-classical and DWBA theories, single nucleon transfer reactions on ^{92}Mo by ^{14}N and ^{12}C were studied.[1] Beam energies were 97 and 75 MeV for ^{14}N, and 90 and 60 MeV for ^{12}C ions. Conventional counter telescopes were used to detect the emitted particles and the data were recorded on a magnetic tape event by event for later analyses. A self-supporting target of 450 μg/cm^2 was used and the typical energy resolution was 400 keV.

Angular distributions for four transfer channels were measured in the ^{14}N induced reactions, and only the proton transfer was studied in the ^{12}C induced reactions. The angular distributions of elastic scatterings were also measured, and these data were analyzed with the optical model using a search code.[2] Representative parameter sets are listed in the Table 1.

Table 1. Optical potential.

System	E_L (MeV)	V (MeV)	W (MeV)	r_0 (fm)	a (fm)	r_c (fm)
^{92}Mo + ^{14}N	97 (75)	94 (117)	25	1.15	0.5	1.2
^{92}Mo + ^{12}C	90 (60)	120 (127)	25	1.13	0.5	1.2
^{92}Mo + ^{11}B	70	100	25	1.15	0.5	1.2

Optical potential parameters which are found under the constraints $r_R = r_I = r_0$, $a_R = a_I = a$.
Energy dependence is explained by varying the depth V.

Single particle levels studied by the light-ion transfer reactions[3] have also been observed in the present study. Two different projectiles made it possible to study the effects of kinematical matching conditions, that is, the ^{12}C induced reactions have large negative Q-values compared with those of ^{14}N induced reactions, and only the high spin levels are favored in the former case. As an example, energy spectra of neutron stripping reactions are given in Fig. 1. In the (^{12}C, ^{11}C) reaction, $d_{5/2}$ and $s_{1/2}$ states are suppressed. The semi-classical theory developed by Brink[4] reproduces the data well at least qualitatively.

The angular distributions are shown in Fig. 2, together with the theoretical cross sections calculated using the exact finite range DWBA code developed by Tamura and Low.[5] Since the first excited states ($p_{1/2}$) were not resolved from the ground states ($g_{9/2}$) in the proton transfer reactions, the DWBA fits were made using the following formula :

$$\left.\frac{d\sigma}{d\Omega}\right|_{\text{exp.}} = N \sum_{\text{states}} C^2S(1)\, C^2S(2) \left.\frac{d\sigma}{d\Omega}\right|_{\text{DW}} ,$$

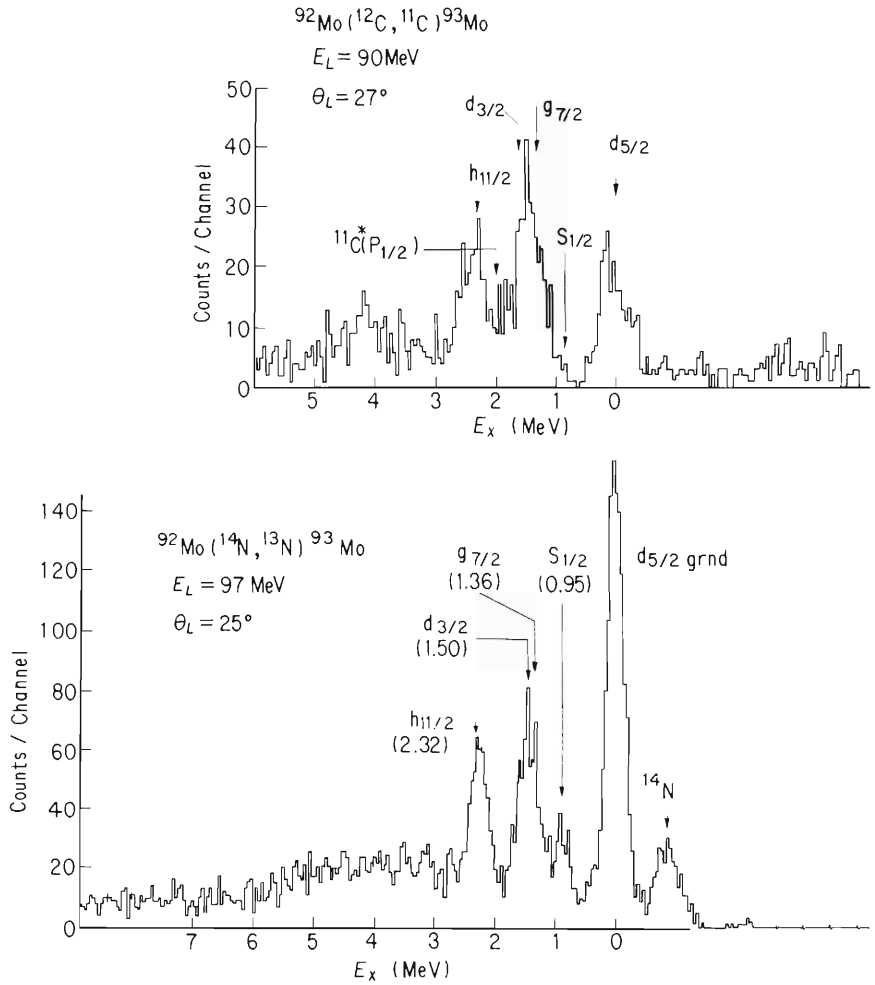

Fig. 1. Energy spectra of neutron stripping reactions on ^{92}Mo by ^{14}N and ^{12}C. The same states in ^{93}Mo are populated in both reactions, but the peak strengths are different from each other (see text).

where $C^2S(1)$ and $C^2S(2)$ are the S'-factors of the heavy system found in the references[3], and those of the light system calculated by Cohen and Kurath.[6] N is a normalization factor.
The transferred nucleon was assumed to be bound in a potential well of Woods-Saxon form with a radius of $R = 1.2A^{1/3}$ and the diffuseness $a = 0.65$ fm, where A is the mass number of the core nucleus. The well depth V was searched around 60 MeV to give the actual binding energy, and V_{LS} was 7 MeV. The N-factor defined above varied from 0.5 to 0.8 case by case in the calculations on the angular distributions to ground state groups of the residual nuclei induced by ^{14}N. Incident energy dependence of the magnitudes of the cross sections was well accounted for. The (^{12}C, ^{11}B) and (^{12}C, ^{13}N) reactions shown in Fig. 2 had N-factors of about 1.7 and 0.9 respectively, which are slightly larger than those in the case with ^{14}N. In the proton transfer reactions, positions of the angular distribution maximum differ by a few degrees between stripping and pick-up, whereas in the neutron transfer reactions it does not. The DWBA theory explains these differences reasonably well.

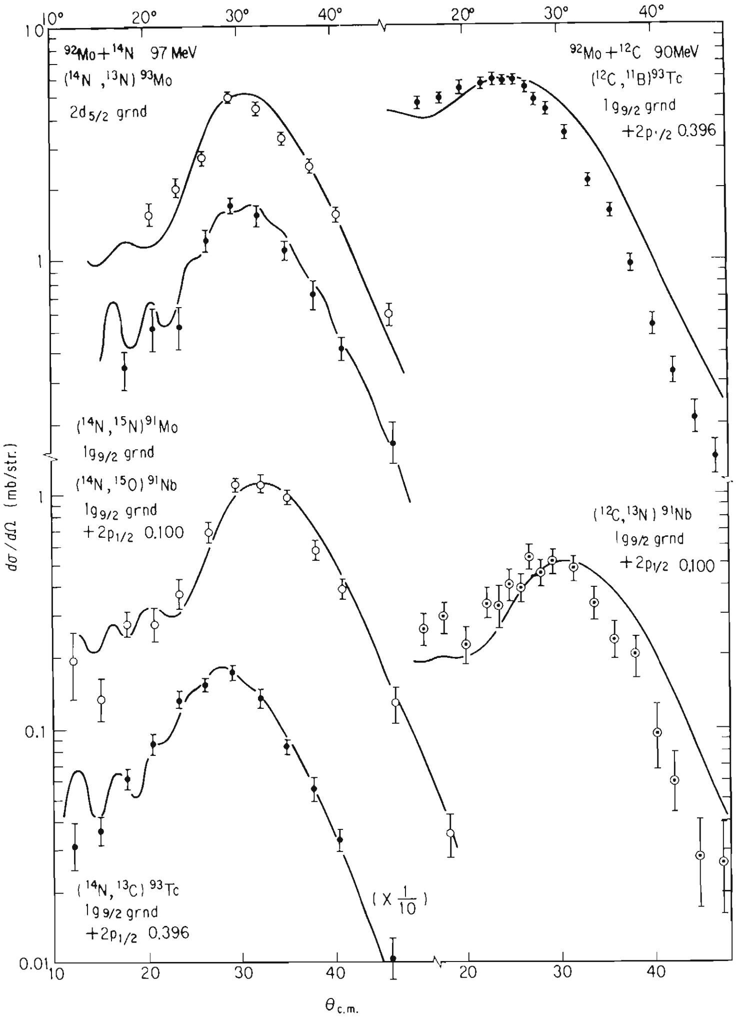

Fig. 2. Angular distributions of single nucleon transfer reactions on ^{92}Mo by ^{14}N and ^{12}C obtained by the DWBA calculation (solid lines). Incident channel optical parameters given in Table 1 are also used for the exit channel.

In the (^{12}C, ^{11}B) and (^{12}C, ^{13}N) reactions, the calculated angular distributions take always backward positions compared with the experimental ones. For the (^{12}C, ^{11}B) reaction, the use of the exit channel parameters which reproduce the elastic scattering of ^{11}B on ^{92}Mo does not remove this discrepancy.

References

1) M. Yoshie, K. Katori, I. Kohno, T. Mikumo, T. Motobayashi, S. Nakajima, and H. Kamitsubo: Proc. Intern. Conf. on Reactions between Complex Nuclei, Nashville, North-Holland, Amsterdam (1974).

2) T. Wada: IPCR Cyclotron Progr. Rep., 2, 87 (1968).

3) R. L. Kozub and D. H. Youngblood: Phys. Rev., C4, 535 (1971); J. B. Moorhead and R. A. Moyer: ibid., 184, 1205 (1969); R. L. Kozub and D. H. Youngblood: ibid., C7, 404 (1973); R. Chapman, J. E. Kitching, and W. Mclatchie: Nucl. Phys., A196, 347 (1972).

4) D. M. Brink: Phys. Lett., 40B, 37 (1972); N. Anyas-Weiss, J. Becker, T. A. Belote, J. C. Cornell, P. S. Fisher; P. N. Hudson, A. Menchaca-Rocha, A. D. Panagiotou, and D. K. Scott: ibid., 45B, 231 (1973).

5) T. Tamura and K. S. Low: Comp. Phys. Commun., (in press).

6) S. Cohen and D. Kurath: Nucl. Phys., A101, 1 (1967).

4-4. Transfer Reactions Induced by ^{14}N on ^{12}C at 79 MeV

T. Motobayashi, I. Kohno, S. Nakajima, M. Yoshie,
K. Katori, T. Mikumo, and H. Kamitsubo

Transfer reactions induced by ^{14}N and ^{12}C on (f-p) shell nuclei$^{1)}$ and heavy nuclei$^{2)}$ have been reported previously. In these cases multi-nucleon transfer reactions showed only a "bump" in the energy spectrum. Because of large level densities together with the rather poor energy resolution (400 – 600 keV) we could not see any transition to a certain level of the residual

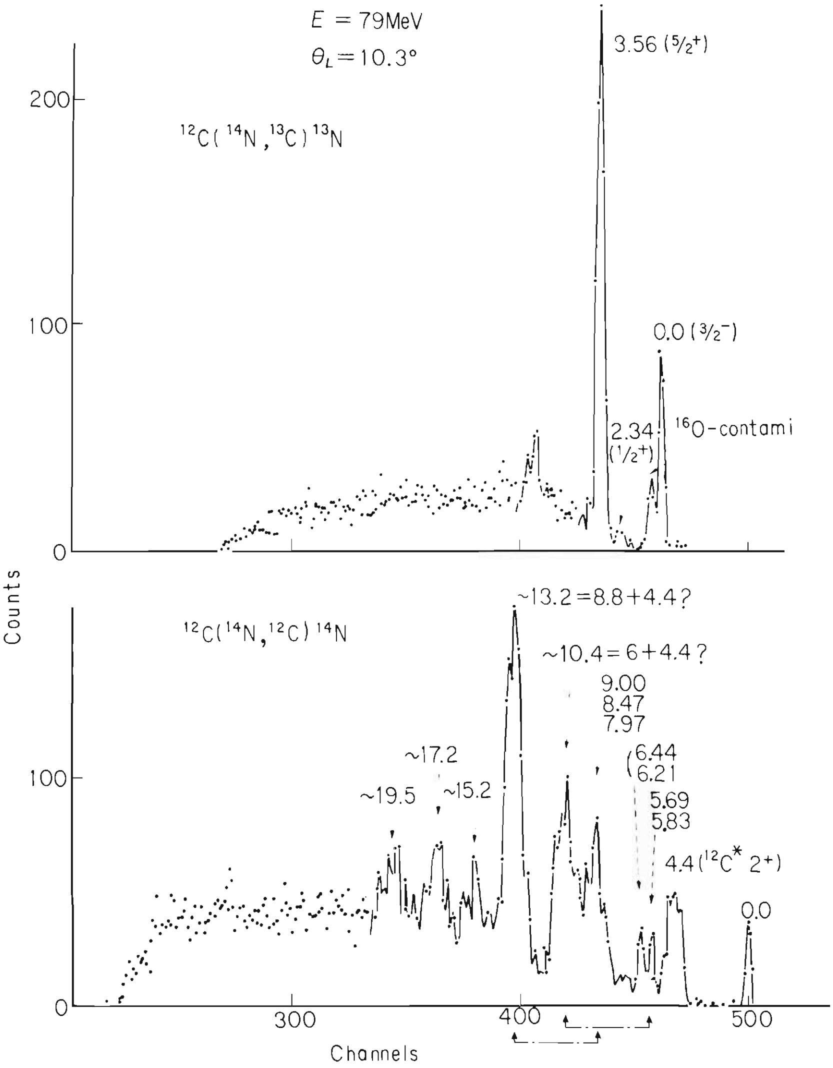

Fig. 1. Energy spectrum of reactions ^{12}C (^{14}N, ^{13}C) ^{13}N and ^{12}C (^{14}N, ^{12}C) ^{14}N. 10.4 MeV and 13.2 MeV peaks in the reaction ^{12}C (^{14}N, ^{12}C) ^{14}N are expected to be populated due to the excitation of both ^{14}N and ^{12}C(4.43 MeV 2^+).

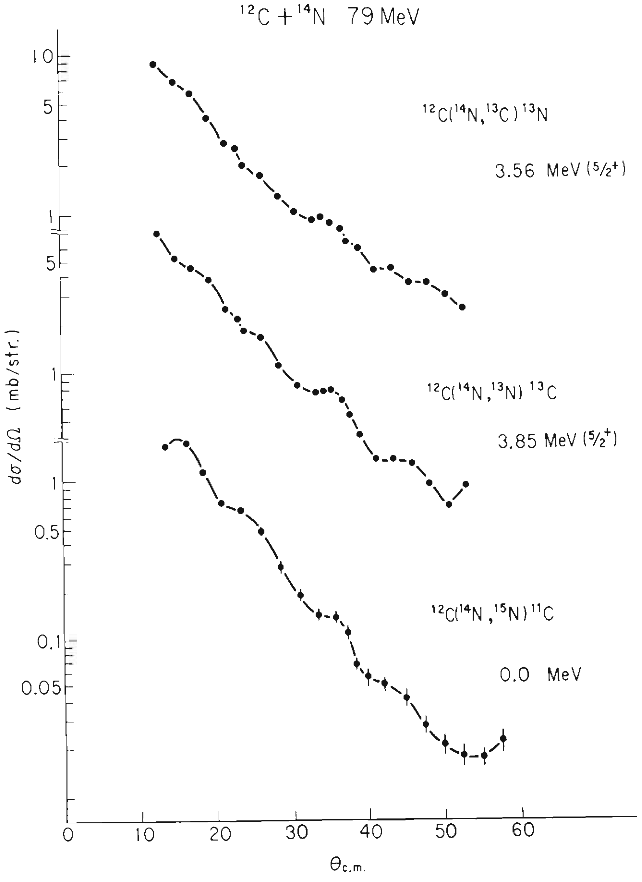

Fig. 2. Angular distributions of one-nucleon stripping reactions $^{12}C(^{14}N, ^{13}C)^{13}N$ and $^{12}C(^{14}N, ^{13}N)^{13}C$ and pick-up reaction $^{12}C(^{14}N, ^{15}N)^{11}C$.

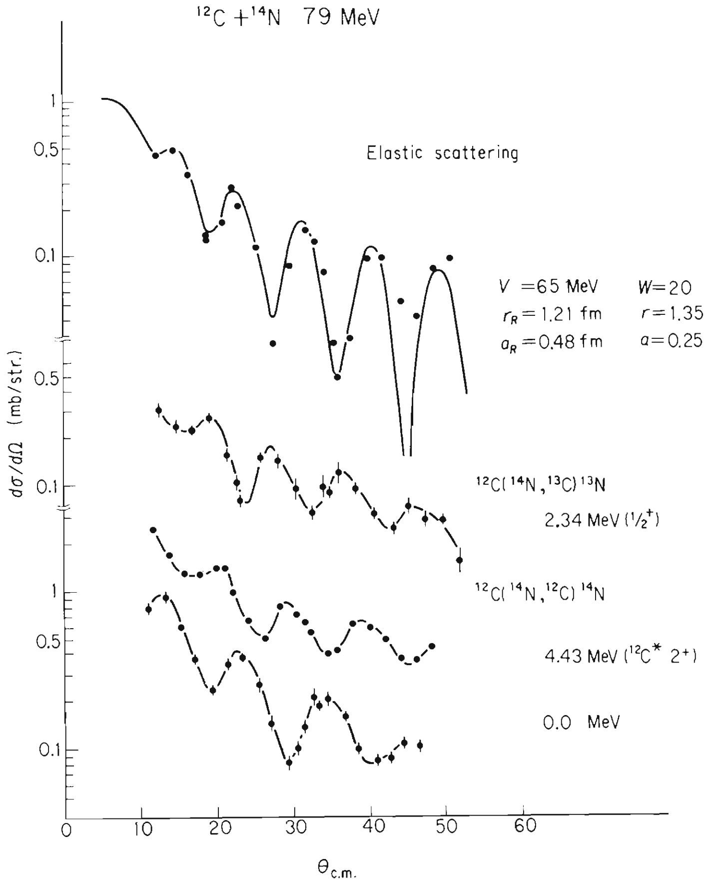

Fig. 3. Angular distributions of elastic scattering, one-nucleon transfer reaction $^{12}C(^{14}N, ^{13}C)^{13}N(s_{1/2})$, and two-nucleon transfer reaction $^{12}C(^{14}N, ^{12}C)^{14}N$. For elastic scattering, solid line is calculated using the optical potential of Ref. 7 .

nucleus. We have done an experiment on transfer reactions induced by 79 MeV ^{14}N on ^{12}C, for light nuclei having relatively low level densities. In the experiment ^{14}N^{4+} beams provided by the IPCR cyclotron were used. A ΔE–E counter telescope was used to identify emitted particles. Signals from the ΔE and E counters were processed by parallel analog-to-digital converters (A.D.C.s). Signals from A.D.C.s were stored event by event on a magnetic tape using a DDP-124 computer. After the experiment, the data were analyzed by means of Goulding-type mass identification formula. The target was of ^{12}C self-supported foil about 70 μg/cm^2 thick. The energy resolution was 350 – 500 keV.

(1) One-nucleon transfer reactions

The spectrum of the ^{12}C(^{14}N, ^{13}C)^{13}N reaction is shown in Fig. 1. Like transfer reactions on heavier nuclei, the peaks corresponding to low lying states of ^{13}N are prominent. Angular distributions of some one-nucleon transfer reactions are shown in Figs. 2 and 3. For the angular distribution for the 2.34 MeV(1/2$^+$) state in ^{13}N excited by ^{12}C(^{14}N, ^{13}C)^{13}N, its diffraction pattern is out of phase to that of elastic scattering shown also in Fig. 3. The diffraction model[3] indicates that this phasing is due to the even-L transfer, whereas the transfer reaction by ^{14}N is expected to populate the $s_{1/2}$ state with L = 1, because the transferred proton is in the $p_{1/2}$ orbit of ^{14}N. This discrepancy has been also found by the Berkeley group[4] for the ^{12}C(^{14}N, ^{13}N)^{13}C reaction through which the 3.09 MeV ($s_{1/2}$) state in ^{13}C (the analogue state of the 2.34 MeV state in ^{13}N) were excited.

(2) ^{12}C(^{14}N, ^{12}C)^{14}N

The spectrum for the two-nucleon (d) transfer reaction is shown in Fig. 1. We can see some selectively excited peaks even at higher excitation energies. This is very different from the case of heavier targets. It is also remarkable that the 4.4 MeV state in ^{12}C is strongly excited. This means that d+^{12}C (4.43 MeV) is more likely than d+^{12}C (0.0 MeV) as the structure of ^{14}N or the coupled channel effect of the excitation of ^{12}C (0.0 MeV) to ^{12}C (4.43 MeV) is important.

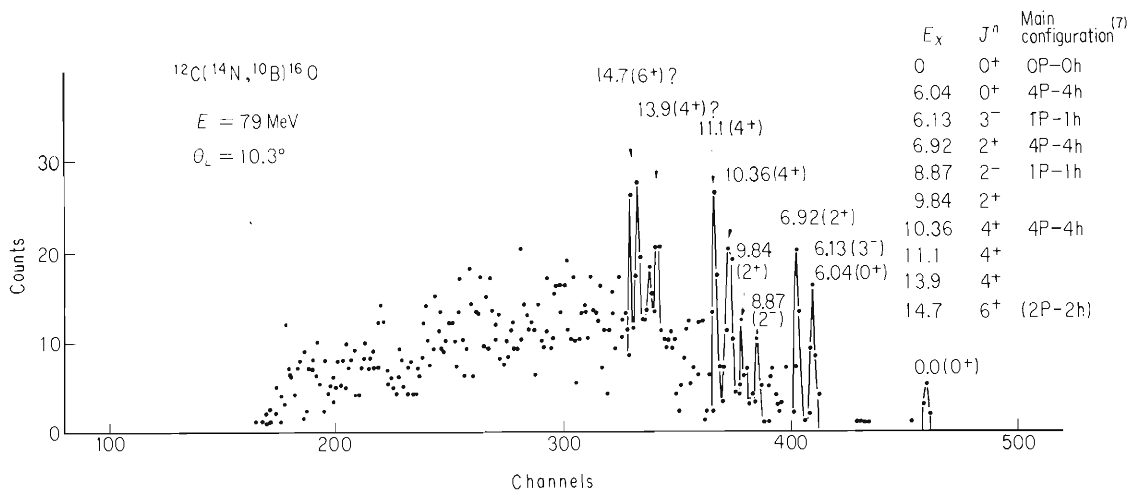

Fig. 4. Energy spectrum of the ^{12}C(^{14}N, ^{10}B)^{16}O reaction. Excitation energies, J$^\pi$, and a possible configulation[8] of ^{16}O are indicated.

(3) $^{12}C(^{14}N, ^{10}B)^{16}O$

The spectrum of the $^{12}C(^{14}N, ^{10}B)^{16}O$ reaction is shown in Fig. 4. Many states in ^{16}O were identified. Compared with other data on α-transfer reactions,$^{5),6)}$ the excitation of (4p − 4h) states is rather weaker. This indicates that the (^{14}N, ^{10}B) reaction is not so dominated by the α-cluster transfer process as in case of (^{6}Li, d) or (^{12}C, ^{8}Be). Angular distributions for 6.05 MeV (0^+) + 6.13 MeV (3^-) and 6.92 MeV (2^+) +7.11 MeV (3^-) (mainly 6.92 MeV) are shown in Fig. 5.

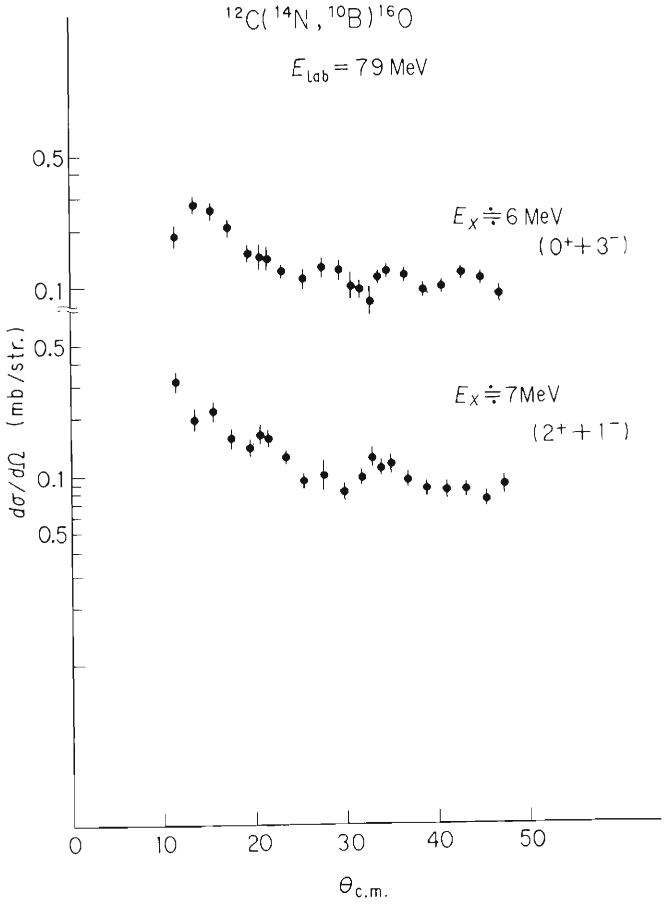

Fig. 5. Angular distributions of the $^{12}C(^{14}N, ^{10}B)^{16}O$ reaction.

References

1) I. Kohno, S. Nakajima, I. Yamane, M. Yoshie, M. Odera, and H. Kamitsubo: IPCR Cyclotron Progr. Rep., 6, 23 (1972).

2) T. Motobayashi, I. Kohno, S. Nakajima, M. Yoshie, K. Katori, T. Mikumo, and H. Kamitsubo: ibid., 7, 32 (1973).

3) K. R. Greider: "Nuclear Reactions Induced by Heavy Ions", North-Holland, Amsterdam, p. 217 (1970).

4) R. M. de Vries, M. S. Zisman, J. G. Gramer, K.–L. Liu, F. D. Becchetti, B. G. Harvey, H. Homeyer, D. G. Kovar, J. Mahoney, and W. von Oertzen: Phys. Rev. Lett., 32, 680 (1974).

5) K. Meier-Ewert, K. L. Bethge, and K.–O. Pfeiffer: Nucl. Phys., A110, 142 (1968).

6) G. J. Wozniak, H. L. Harney, K. H. Wilcox, and Joseph Cerny: Phys. Rev. Lett., 28, 1278 (1972).

7) I. Kohno: Sci. Papers I.P.C.R., 68, 38 (1974).

8) G. E. Brown and A. M. Green: Nucl. Phys., 75, 401 (1966).

4-5. Analysis of Elastic Scattering of ^{16}O by ^{19}F

T. Motobayashi and B. Imanishi

When there is a large probability for a nucleus B to be represented as a composite of two nuclei a and c, an exchange of the nucleus a is expected to be very important in the interaction between B and a.[1] We analyzed elastic scattering of ^{16}O by ^{19}F by the coupled channel method[2] considering the exchange process of ^{16}O-core. In this analysis the FACOM 230-75 computer of I.P.C.R. was used.

If we consider only the direct and transfer channel, and also neglect the spin-dependent force, the total wave function of anguler momentum L is written as

$$\Psi^{(L)}=\frac{u(r)}{r}\phi(\hat{\mathbf{r}},\mathbf{R})+(-1)^{N}\frac{u(r')}{r'}\phi(\hat{\mathbf{r}}',\mathbf{R}'),$$

where r and **R** represent the co-ordinate vectors between B and a, and between b and c, respectively (Fig. 3), and $\hat{\mathbf{r}}=\frac{\mathbf{r}}{|\mathbf{r}|}$. N is the number of constituent nucleons of core a or b, and a $(-1)^{N}$-factor appears through the exchange of the nucleus a and b. Substituting this wave function into the equation,

$$<\phi(\hat{\mathbf{r}},\mathbf{R})|(E-H)|\Psi^{(L)}>_{\hat{\mathbf{r}},\mathbf{R}}=0$$

we obtain the equation for u(r),

$$\begin{aligned}&\left\{E-\left(-\frac{\hbar^2}{2\mu}\frac{d^2}{dr^2}+\frac{\hbar^2}{2\mu}\frac{L(L+1)}{r^2}+U(r)\right)\right\}u(r)\\&+\left\{E-\left(-\frac{\hbar^2}{2\mu}\frac{d^2}{dr^2}+\frac{\hbar^2}{2\mu}\frac{L(L+1)}{r^2}+U(r)\right)\right\}\int dr'K^{(1)}(r,r')u(r')\\&+\int dr'\left\{K^{(2)}(r,r')-U(r)K^{(1)}(r,r')\right\}u(r')=0,\end{aligned}\tag{1}$$

where

$$K^{(1)}(r,r')=(-1)^{N}Jrr'\int d\hat{\mathbf{r}}\,d\hat{\mathbf{r}}'\;\phi(\hat{\mathbf{r}},\mathbf{R})\phi(\mathbf{r}',\mathbf{R}')$$

$$K^{(2)}(r,r')=(-1)^{N}Jrr'\int d\hat{\mathbf{r}}\,d\hat{\mathbf{r}}'\;\phi(\mathbf{r},\mathbf{R})\left\{V_{ab}(x)+V_{ac}(\mathbf{R}')\right\}\phi(\hat{\mathbf{r}}',\mathbf{R})\phi(\hat{\mathbf{r}},\mathbf{r}')$$

and J is the Jacbian for co-ordinate transformation ($\hat{\mathbf{r}}$, **R**) to ($\hat{\mathbf{r}}$, $\mathbf{r}'$), and U(r) is the optical potential between B and a. $K^{(2)}$-$UK^{(1)}$ is the exact DWBA form factor in the post-form, and $K^{(1)}$ is called non-orthogonal kernel. As $K^{(1)}$ and $K^{(2)}$ in Eqn. (1) are both non-local operators, it is time-consuming to solve it for computer calculation. We have first made the calculation of heavy ion approximation (H.I.A.) which is not so time-consuming. In order to consider the effect of $K^{(1)}$ to some extent, we solve the equation for v(r) obtained by the transformation $v=\sqrt{1+K^{(1)}}u$. If the terms of the order $(K^{(1)})^2$ or higher are neglected, the equation of

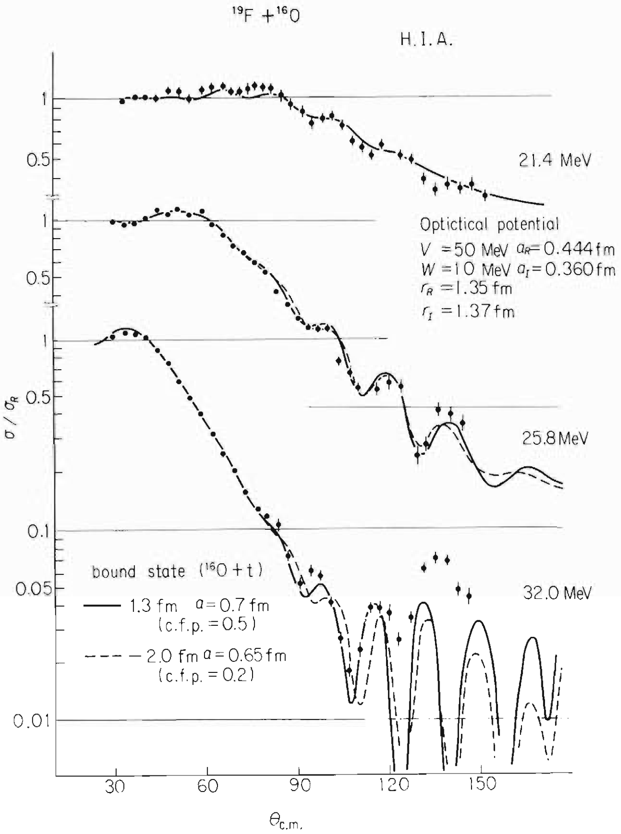

Fig. 1. Angular distributions at E = 21.4, 25.8, and 32.0 MeV. The parameters of the optical potential are decided so as to fit to the data of forward angle scatterings where the transfer process is negligible.

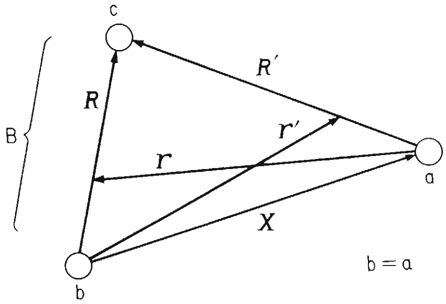

Fig. 3. Co-ordinate vectors of the system. In our case, c is triton, a and b are both ^{16}O, and B = (c+b) = (c+a) is ^{19}F.

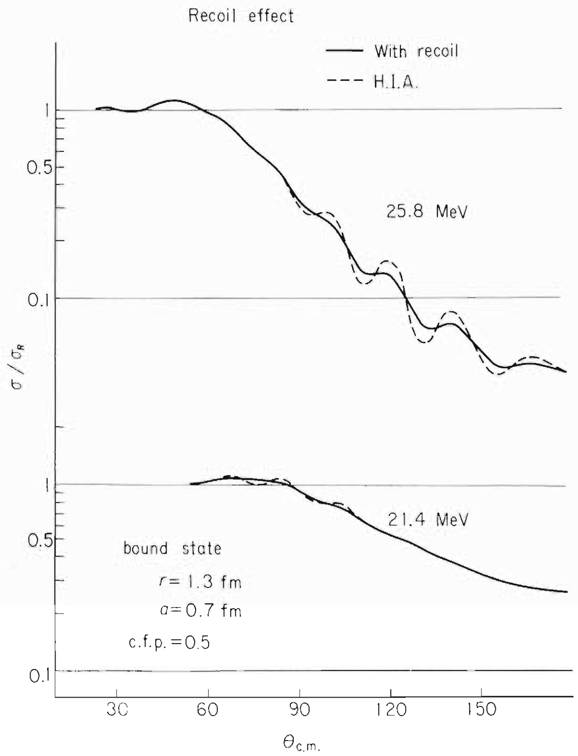

Fig. 2. Full recoil calculation (solid lines) is compared with H.I.A. calculation (dashed lines). For each case the same value of coefficient of fractional parentage is used.

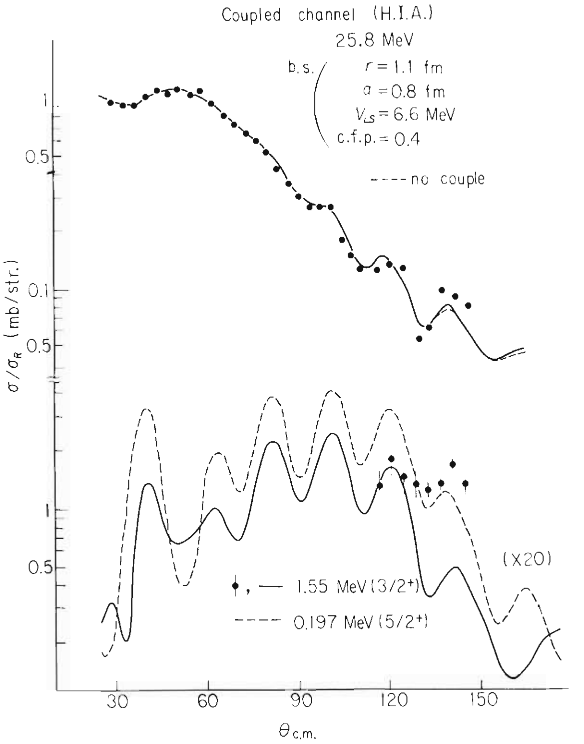

Fig. 4. Angular distributions of elastic and inelastic scatterings obtained by the coupled channel calculation. The calculated values of the inelastic scatterings are multiplied by 20.

H.I.A. is

$$\left[E-\left\{-\frac{h^2}{2\mu}\frac{d^2}{dr^2}+\frac{h^2}{2\mu}\frac{L(L+1)}{r^2}+U(r)\right.\right.$$
$$\left.\left.+\frac{1}{\sqrt{1+K^{(1)}}}\left(\frac{K(\text{post})+K(\text{prior})}{2}\right)\frac{}{\sqrt{1+K^{(1)}}}\right\}\right]V(r)=0,$$

where K(post) and K(prior) are exact no-recoil DWBA form factors in the post- and prior-form respectively.

The cross sections of H.I.A. calculated are compared with the data in Fig. 1. Data at 32 MeV were obtained by Kyoto University group,$^{3)}$ and data at 21.4 and 25.8 MeV were obtained using the tandem Van de Graaff accelerator at the University of Tokyo. In this calculation ^{19}F is considered to be ^{16}O+t, and the potential of Woods–Saxon type was used for the interaction between ^{16}O and t. Two kinds of parameter-sets (which were chosen to reproduce the binding energy of ^{19}F) were used for this potential, and both sets gave good fits to the data. This indicates the importance of ^{16}O-core-exchange process and the insensitivity of the nuclear interior. Coefficients of fractional parentage (c.f.p.) for ^{19}F = ^{16}O+t obtained are in good agreement with the results of the LCONO method obtained by the Hiderberg group.$^{4)}$

However, a full recoil calculation for solving exactly the Eqn. (1) gives a conclusion different from the result of H.I.A. In Fig. 2 the results of full recoil calculation are compared with that of H.I.A. This indicates that the calculation of H.I.A. overestimates the transfer amplitude. This strong recoil effect is due to the fact that the transferred particle (triton) is rather heavy compared with the case in which the transferred particle is a nucleon.$^{5)}$

We also have calculated the cross sections for the inelastic scatterings by the coupled channel method (H.I.A.). We took into account the couplings between the ground state ($1/2^+$), the 0.2 MeV-state ($5/2^+$), and 1.5 MeV-state ($3/2^+$) of ^{19}F. These states are assumed to have the (^{16}O+t)-structure, and two kinds of the reaction process were considered. One is the inelastic process arising from the excitation of ^{19}F by the interaction between triton in ^{19}F and projectile ^{16}O. The other is the transfer process in which triton is transferred to projectile ^{16}O to form the excited state of ^{19}F. The results are shown in Fig. 4. Though the diffraction phase is the same as that of the experimental results, the absolute value cannot be reproduced by the calculation above (the calculated value is about 20 times smaller than the experimental value).

References

1) G. M. Temmer: Phys. Lett., 1, 10 (1962); W. von Oertzen: Nucl. Phys., A148, 529 (1970).
2) B. Imanishi: Proc. of Symp. on Heavy-Ion Scattering at Argonne, ANL-7837, 295 (1971).
3) K. Fujii et al.: Private communication.
4) A. Gamp, H. G. Bohlen, M. Feil, N. Marquardt, W. von Oertzen, and R. L. Walter: Proc. of Symp. on Heavy-Ion Transfer Reactions at Argonne, Argonne Physics Devision Informal Report, PHY-1973B, 503 (1973).
5) B. Imanishi, H. Ohnishi, and O. Tanimura: Proc. of Conf. on Reactions between Complex Nuclei, 1, 25 (1974).

4-6. DWBA Analyses of One-nucleon Transfer Reactions Induced by Heavy Ions on the N = 28 Target Nuclei

S. Nakajima, I. Kohno, and M. Yoshie

The (^{14}N, ^{13}C) reaction has been studied on a ^{52}Cr target at incident energy 70 MeV. Angular distributions of the cross section for several transitions were analyzed by the exact finite range DWBA code SATURNMARSI.[1]

Optical model parameters listed in Table 1 were obtained from fitting to the ^{52}Cr + ^{14}N elastic scattering data. Though the set III did not give a good fit to our data, it is currently used to explain the (^{16}O, ^{15}N) reactions on the f-p shell nuclei.[2] The same parameters were employed for both the entrance and exit channels except the set IV, where those for the exit channel were taken to fit the elastic scattering of ^{52}Cr + ^{12}C at an incident energy of 60 MeV.

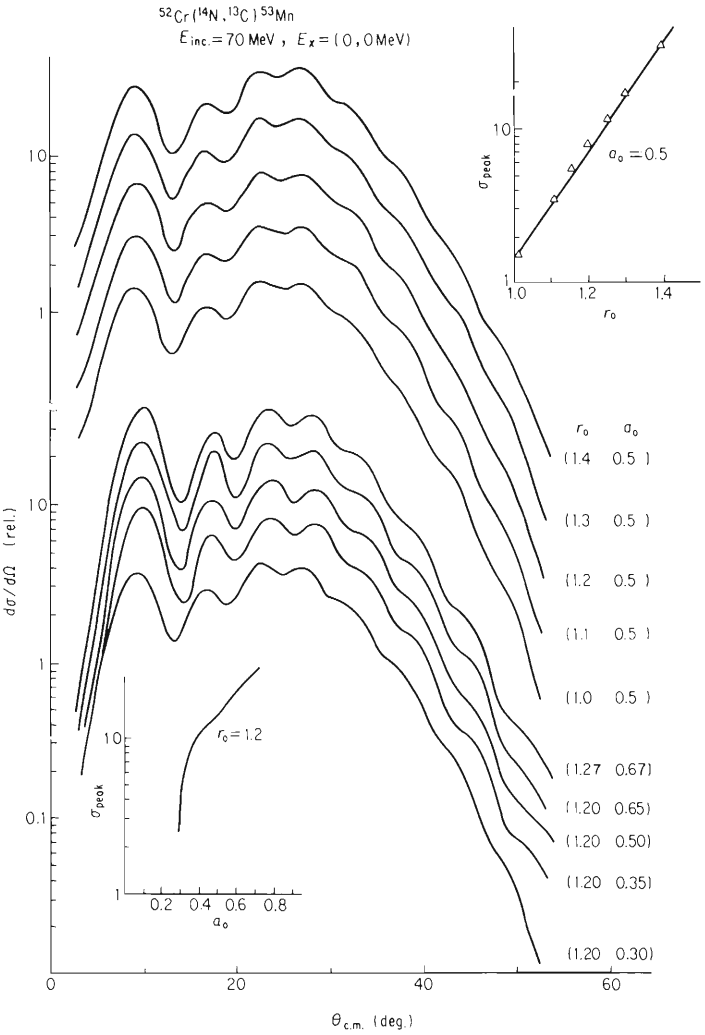

Fig. 1. Influence of the optical parameter set on the angular distribution. The bound state parameters are r_0 = 1.25 fm and a_0 = 0.67 fm.

Table 1. Optical model parameter sets used in calculation.

		V (MeV)	W (MeV)	r_R (fm)	r_I (fm)	a_R (fm)	a_I (fm)
Set I		60.0	8.0	1.02	1.18	0.70	0.52
Set III		100.0	40.0	1.22	1.22	0.49	0.49
Set IV	entrance	60.0	11.1	1.02	1.18	0.70	0.52
	exit	60.0	18.25	1.04	1.18	0.78	0.56
Set V		100.3	40.1	1.12	1.09	0.52	0.56

The results of DWBA calculations using these parameters are shown in Fig. 1. The proton bound state wave function was obtained from a Woods-Saxon potential with r_0 = 1.25 fm and a_0 = 0.67 fm. The results of DWBA calculations were highly sensitive to the choice of these parameters. The set IV reproduced satisfactorily the experimental angular distribution in shape but its magnitudes were more than 5 times as large as the experimental values. As is shown in Fig. 2, it is possible to reduce the absolute strength by using smaller bound state parameters.

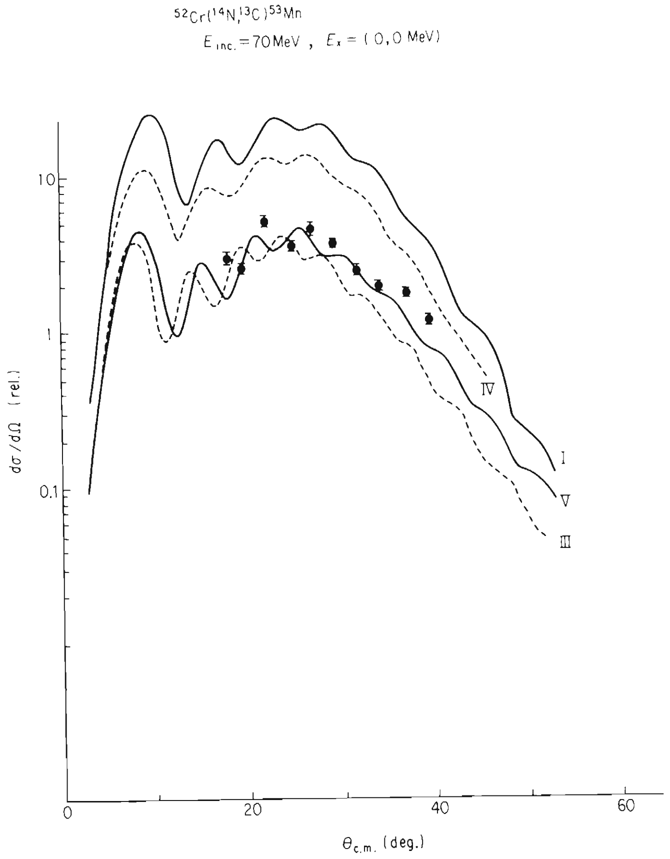

Fig. 2. Influence of changing the bound state parameters on the angular distribution. The optical potential parameter set IV was adopted in calculation.

On the other hand, the set III reproduced proper magnitudes with the standard bound state parameters (r_0 = 1.25 fm, a_0 = 0.67 fm). Contributions of the interior of nucleus to the results of calculation seems of different degree for the set III and IV.

Experimental results have been obtained also with the targets of ^{50}Ti and ^{54}Fe. Analysis of these data is going on.

References

1) T. Tamura and K. S. Low: Private communication.
2) H. J. Korner, G.C.Morrison, L. R. Greenwood, and R. H. Siemssen: Phys. Rev., C7, 107 (1973).

4-7. Long-Range α-Particle Decays and Level Structure of ^{216}Ra

T. Nomura, K. Hiruta, M. Yoshie, H. Ikezoe,
T. Fukuda, and O. Hashimoto*

We have studied the level structure of ^{216}Ra by means of in-beam spectroscopy for long-range α-particle decays and γ-rays following the ^{208}Pb(^{12}C, 4n) and ^{207}Pb(^{12}C, 3n) reactions and established the level sequence up to 11^- (possibly 14^+), including a 7 nsec isomer with spin 8^+. Short-lived α-particle decays were observed from 4^+, 6^+, 8^+, and 10^+ states; their reduced widths were estimated from the branching ratios of α- to γ-transitions.

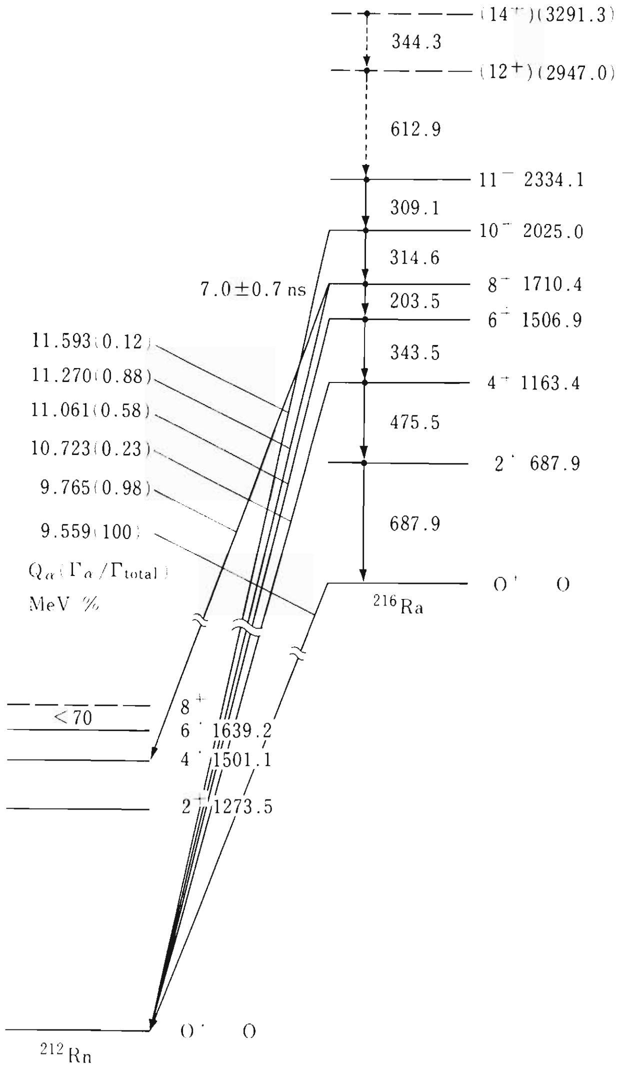

Fig. 1. A decay scheme of ^{216}Ra established in this work. The level sequence of ^{212}Rn is taken from Ref. 1.

---

* Institute for Nuclear Study, Tokyo University

A decay scheme of ^{216}Ra constructed in this work is shown in Fig. 1. Decay properties of long-range α-particle transitions observed are summarized in Table 1.

Table 1. Transition properties of long-range α-particle decays from ^{216}Ra.

E_α (MeV)	Q_α (MeV)	$J_i \rightarrow J_f$	$t_{1/2}(J_i^\pi)$ (ns)	r_α/r_{total} (%)	$t_{1/2,\alpha}$(exp) (ns)	$t_{1/2,\alpha}$(cal)[a] (ns)	HF	HF(L)[b]	Reduced HF
9.349	9.559	$0^+ \rightarrow 0^+$	182±10[c]	100	182±10	182	[1]	11	[1]
9.551	9.765	$(8^+ \rightarrow 4^+)$	7.0±0.7	0.98	714±91	63.0	11	4.8	2.3
10.491	10.723	$4^+ \rightarrow 0^+$	0.10[d]	0.23	48	0.929	50	4.2	12
10.823	11.061	$6^+ \rightarrow 0^+$	0.51[d]	0.58	88	0.275	314	19	17
11.028	11.270	$8^+ \rightarrow 0^+$	7.0±0.7	0.88	795±84	0.120	6630	135	49
11.345	11.593	$10^+ \rightarrow 0^+$	0.79[d]	0.12	658	0.042	15700	1270	12

a) Calculated from the barrier penetrability for S-wave α-particles and normalized on the groundstate α-decay.

b) Hindrance factors due to the centrifugal barrier are calculated from the formula given in Ref. 2.

c) Taken from Ref. 3.

d) Calculated values.

References

1) K. H. Maier, J. R. Leigh, F. Pühlhofer, and R. M. Diamond: J. de Physique, C6, 221 (1971).

2) J. O. Rasmussen: Nucl. Phys., 44, 93 (1963); J. O. Rasmussen: "Alpha-, Beta- and Gamma-ray Spectroscopy", Ed. K. Siegbahn, North-Holland, Amsterdam, p. 701 (1968).

3) T. Nomura, K. Hiruta, T. Inamura, and M. Odera : Nucl. Phys., A217, 253 (1973).

4-8. Angular Distributions of Long-Range α-Particles Emitted from High Spin States in ^{216}Ra and Statistical Tensors

T. Fukuda, T. Nomura, W. Kutschera, and K. Hiruta

In a preceeding paper[1], we have shown that high-spin states in ^{216}Ra decay with α-particle transition in competition with γ-ray emission. Angular distributions of these α-particles must be governed by the high rank of statistical tensors like ρ_6 and ρ_8, and therefore are expected to give more complete information on the nuclear alignment produced by nuclear reactions, which can hardly be obtained by γ-ray angular distribution measurements.

Angular distributions of α-particles from J^+ ($J = 4, 6, 8$: ^{216}Ra) → 0^+ (^{212}Rn) transitions were measured from 6° to 90° in the ^{207}Pb(^{12}C, 3n) reaction at $E_{c12} = 72$ MeV. Figure 1 shows the angular distributions normalized to the yield of the ground-to-ground decay whose angular distribution must be isotropic. The angular distribution of the $8^+ \rightarrow 0^+$ α-particle transition can be written in the following way:

$$W(\theta) \propto \sum_k \rho_k(J=8)\ b_k(L=8)\ F_k(O\,L\,L)\ P_k(\cos\theta)$$

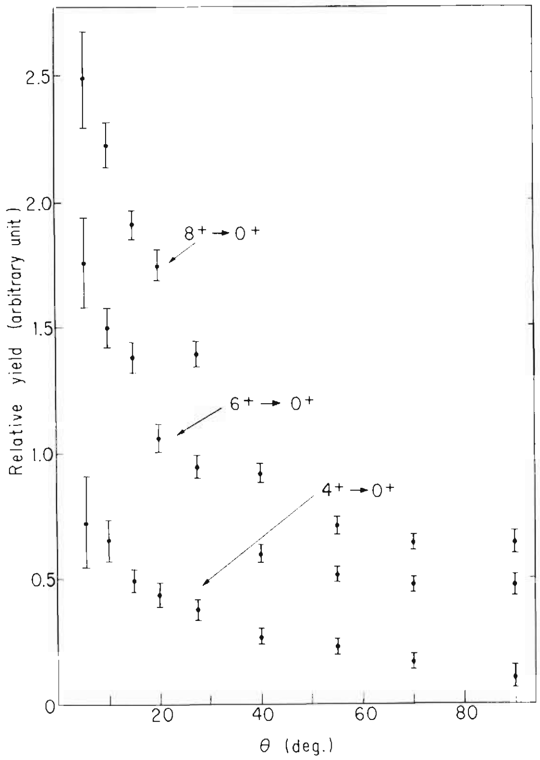

Fig. 1. Angular distributions of α-particles from the 4^+, 6^+, and 8^+ states in ^{216}Ra.

where the notation is conventional (b_k is the particle parameter for α-transition with angular momentum L = 8). It should be noted that the angular distributions for $4^+ \rightarrow 0^+$ and $6^+ \rightarrow 0^+$ can be expressed using the same statistical tensors because they are populated by the E2 γ-transitions following the γ-decay of the 8^+ state.[1]

The statistical tensors for the 8^+ state yielded from a preliminary analysis of $W(\theta: 8^+ \rightarrow 0^+)$ is given in Table 1. A more accurate analysis is now in progress.

Table 1. Statistical tensors for the 8^+ state.

ρ_2	ρ_4	ρ_6	ρ_8	ρ_{10}
-0.762 ± 0.025	0.562 ± 0.035	-0.234 ± 0.045	0.065 ± 0.054	-0.012 ± 0.053

Reference

1) T. Nomura, K. Hiruta, M. Yoshie, H. Ikezoe, T. Fukuda, and O. Hasimoto : IPCR Cyclotron Progress Report, 8, 30 (1974)

4-9. The (^{3}He, ^{3}He), (^{3}He, ^{3}He′), and (^{3}He, α) Reactions on ^{13}C

T. Fujisawa, H. Kamitsubo, T. Wada, M. Koike
Y. Tagishi,* and T. Kanai

Differential cross sections of (^{3}He, ^{3}He), (^{3}He, ^{3}He′), and (^{3}He, α) reactions on ^{13}C have

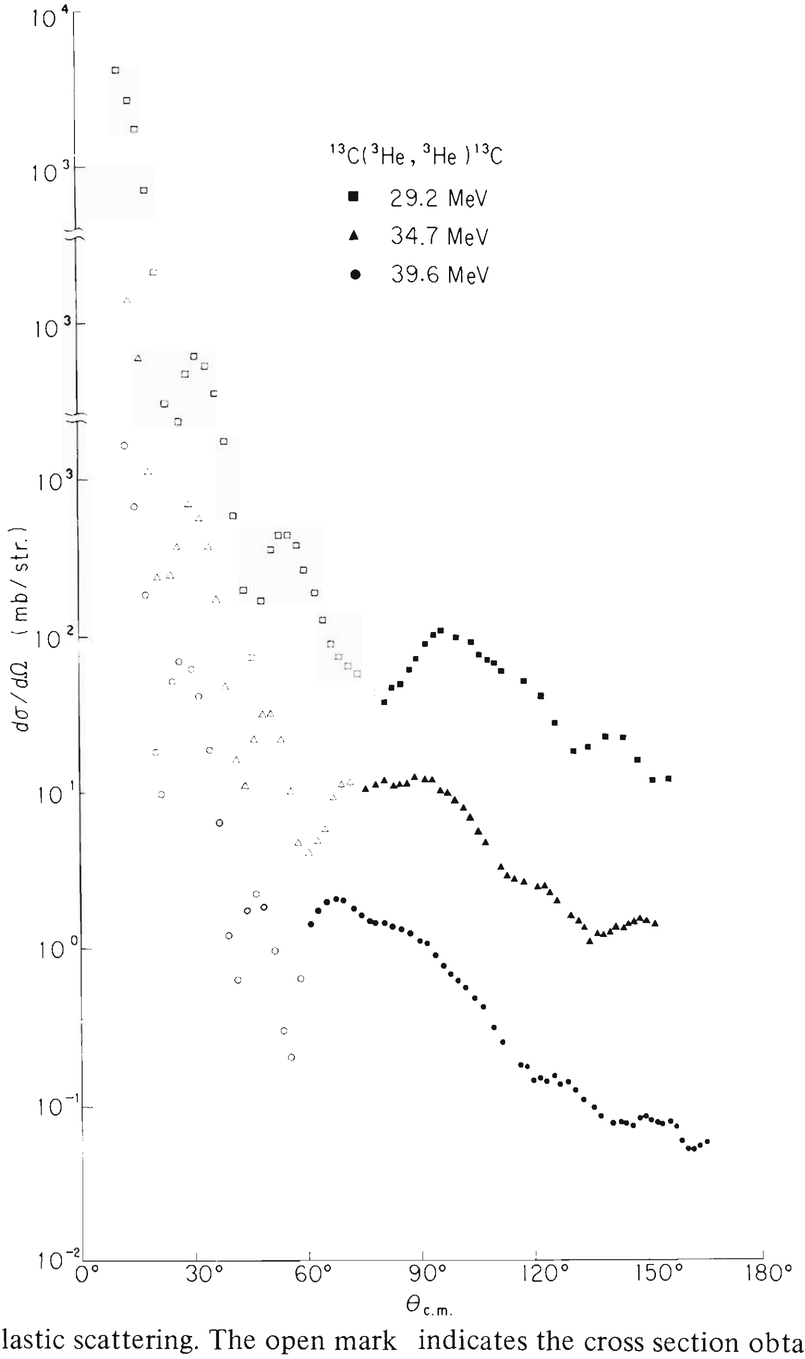

Fig. 1. a) Elastic scattering. The open mark indicates the cross section obtained from subtracting the estimated yield of the elastic scattering on ^{12}C from the overlaped yields of the elastic scatterings on ^{12}C and ^{13}C.

---

* Tokyo Univ. of Education

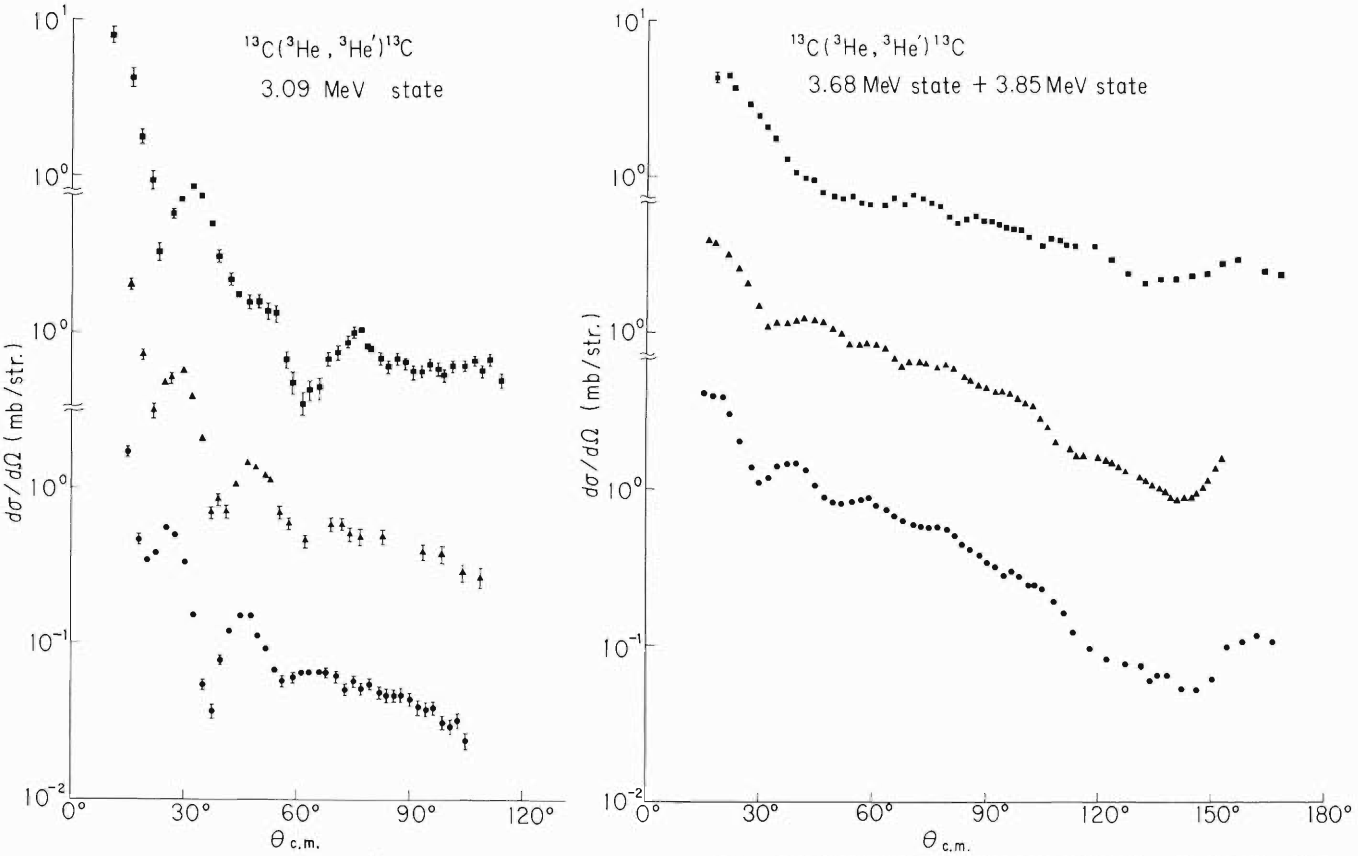

b) The 3.09 MeV ($1/2^+$) state of ^{13}C.

c) Sum of the 3.68 MeV ($1/2^-$) and 3.85 MeV ($5/2^+$) states of ^{13}C.

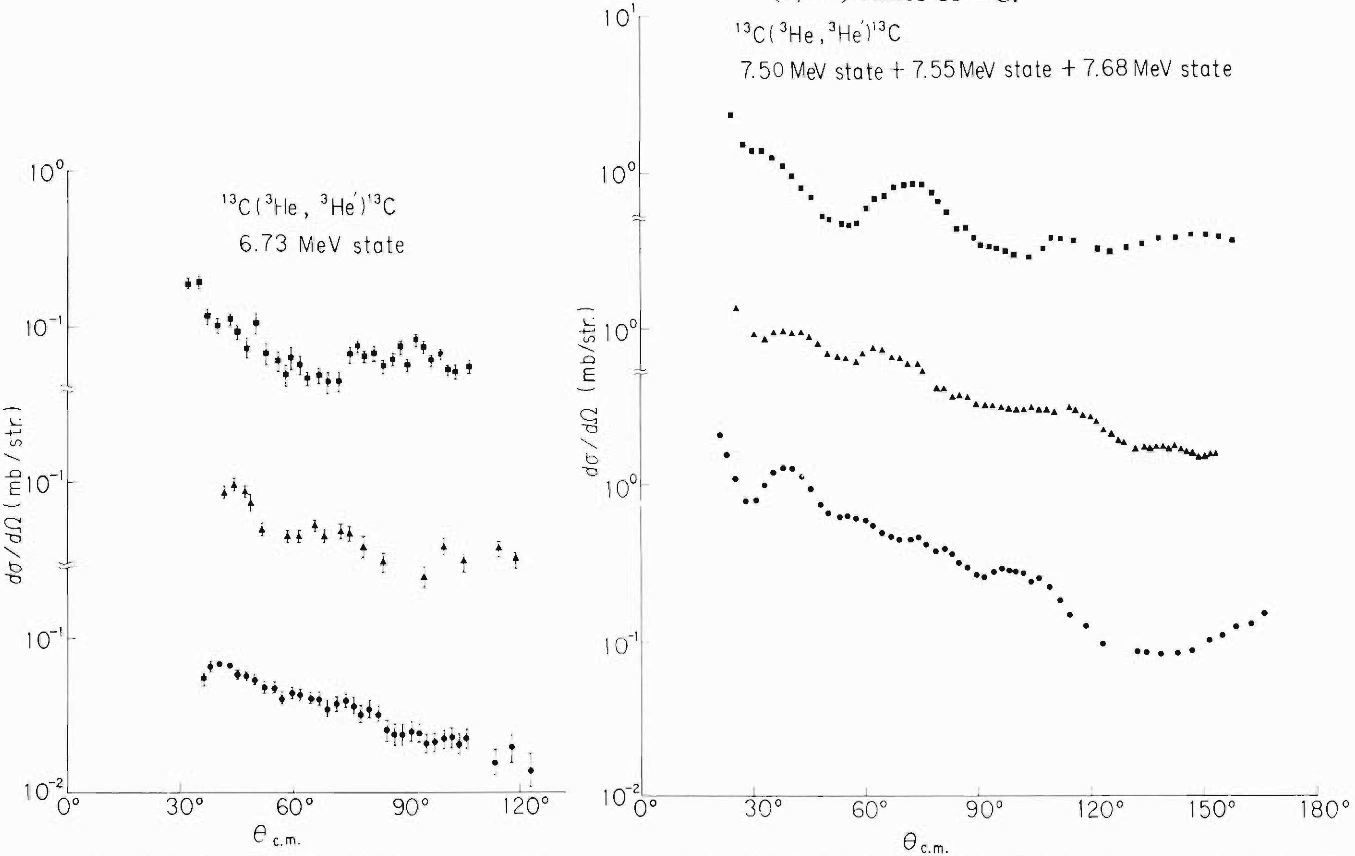

d) The 6.87 MeV ($5/2^+$) state of ^{13}C.

e) Sum of the 7.50 MeV, 7.55 MeV and 7.68 MeV ($3/2^+$) states of ^{13}C.

Fig. 1. Angular distributions of the differential cross sections of the $^{13}C(^3He, ^3He)^{13}C$ and $^{13}C(^3He, ^3He')^{13}C$ reactions.

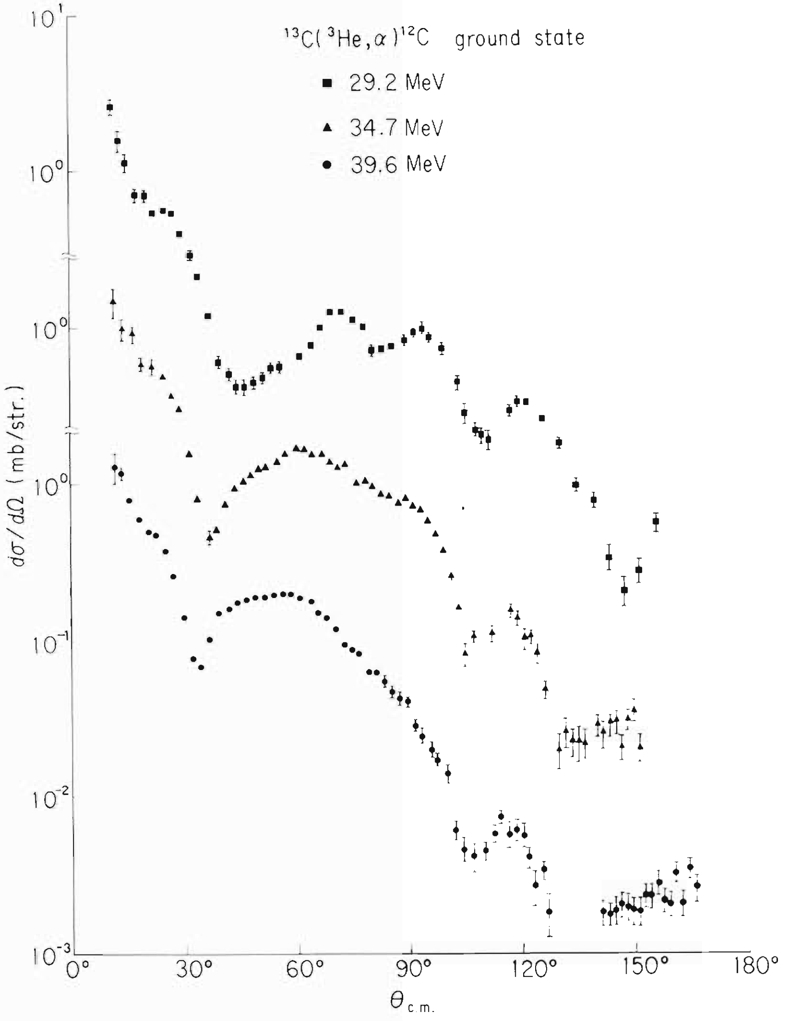

Fig. 2. a) The ground (0^+) state of ^{12}C.

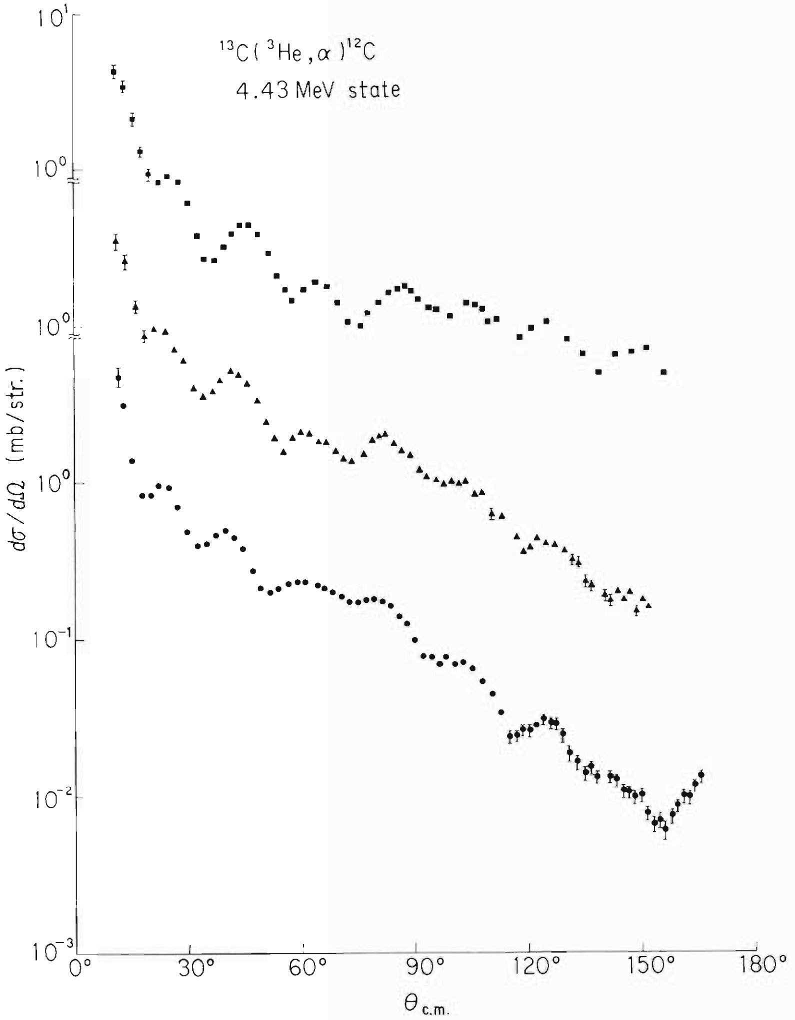

Fig. 2. b) The 4.43 MeV (2^+) state of ^{12}C.

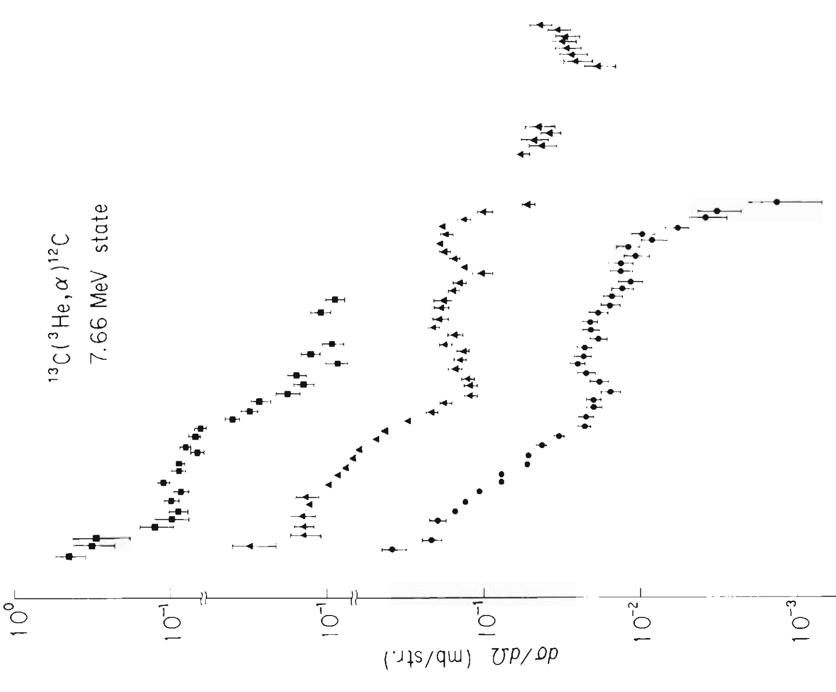

Fig. 2. c) The 7.66 MeV (0^+) state of ^{12}C.

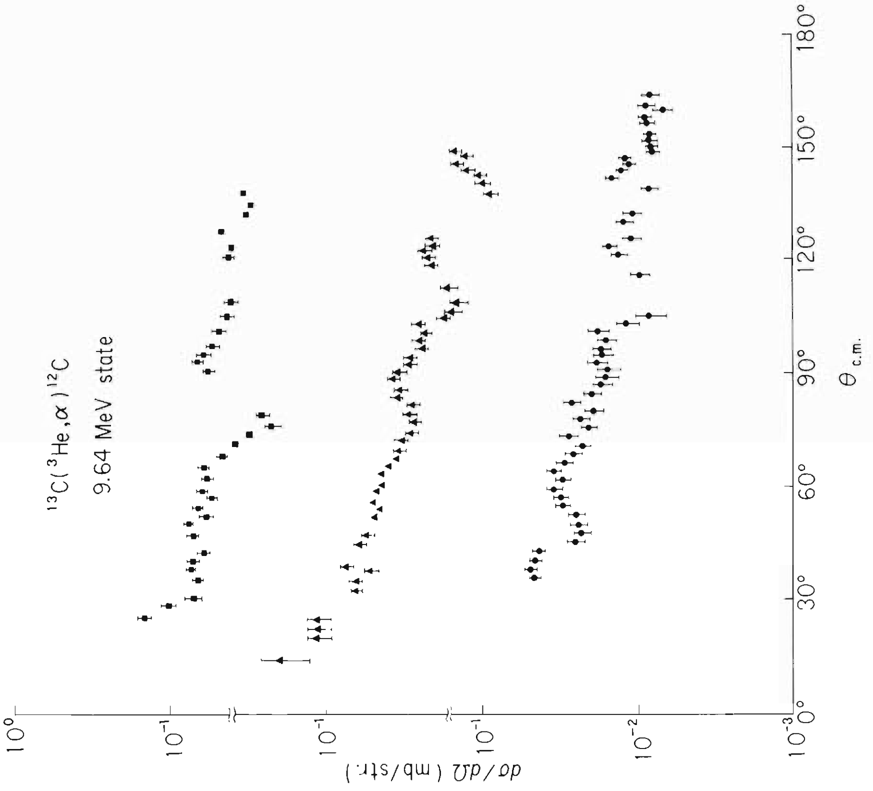

Fig. 2. d) The 9.64 MeV (3^-) state of ^{12}C.

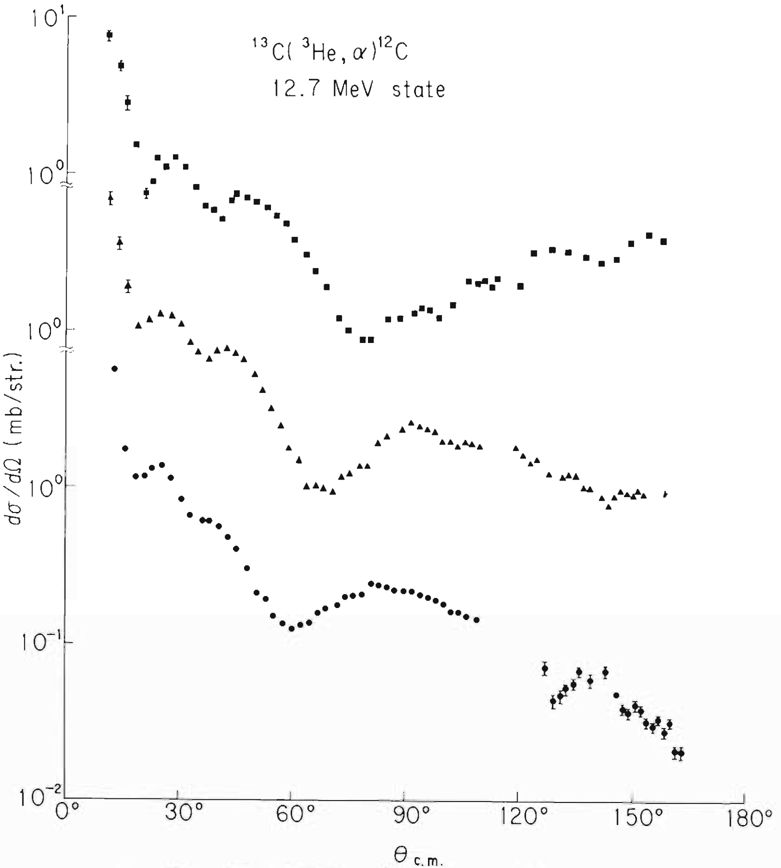

e) The 12.7 MeV (1^+) state of ^{12}C

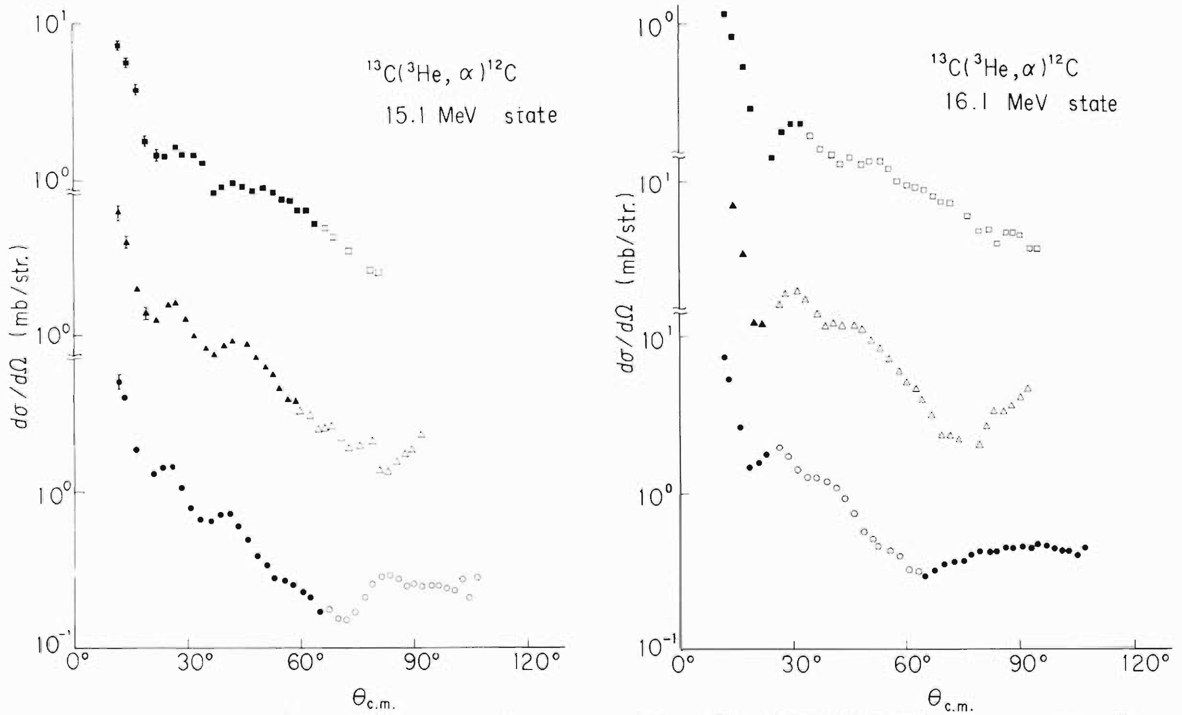

f) The 15.1 MeV (1^+) state of ^{12}C. The open mark shows the cross section obtained from subtracting the estimated yield of the ground state of ^{11}C from the overlaped yields of the 15.1 MeV state of ^{12}C and the ground state of ^{11}C.

g) The 16.1 MeV (2^+) state of ^{12}C. The open mark indicates the cross section obtained from subtracting the estimated yield of the 2.0 MeV state of ^{11}C from the overlaped yields of the 16.1 MeV state of ^{12}C and the 2.0 MeV state of ^{11}C.

Fig. 2. Angular distributions of the differential cross sections of the ^{13}C(^{3}He, α)^{12}C.

been measured at incident energies of 29.2, 34.7, and 39.6 MeV in order to study the mechanism of these reactions. The angular distributions of the differential cross sections are shown in Figs. 1 and 2. The experimental procedure of the study was reported previously.$^{1)}$

Reference

1) T. Fujisawa, H. Kamitsubo, T. Wada, M. Koike, Y. Tagishi, and T. Kanai: IPCR Cyclotron Progr. Rep., 7, 46 (1973).

4-10. A Study of Resonance States Induced by $^{16}O(^{3}He, d)^{17}F$ and $^{28}Si(^{3}He, d)^{29}P$ Reactions

K. Koyama, N. Nakanishi, H. Yokomizo,
S. Yamada, and H. Ohnuma

Recently the study of stripping reactions leading to unbound states have been improved very much, particularly on the theoretical treatment in the framework of the DWBA. An interesting object of this study is the possibility of comparing the unbound form factors with those extracted from the resonance reactions, which may be a cross check to the mechanisms of these two different types of reactions.

Differential cross sections were measured on the reaction $^{28}Si(^{3}He, d)^{29}P$ at an incident energy of 29.3 MeV and the reaction $^{16}O(^{3}He, d)^{17}F$ at 41.5 MeV. The ^{28}Si target was a self-supporting foil of natural silicon with thickness of 1.98 mg/cm^2 which was prepared by vacuum evaporation. The ^{16}O target was of gas type. Two gas chambers were prepared; one had 5 μm nickel foil windows, the other had 3 μm Havar foil and 0.5 mg/cm^2 Mylar foil windows, and gas pressures were 365 Torr. and 260 Torr. respectively.

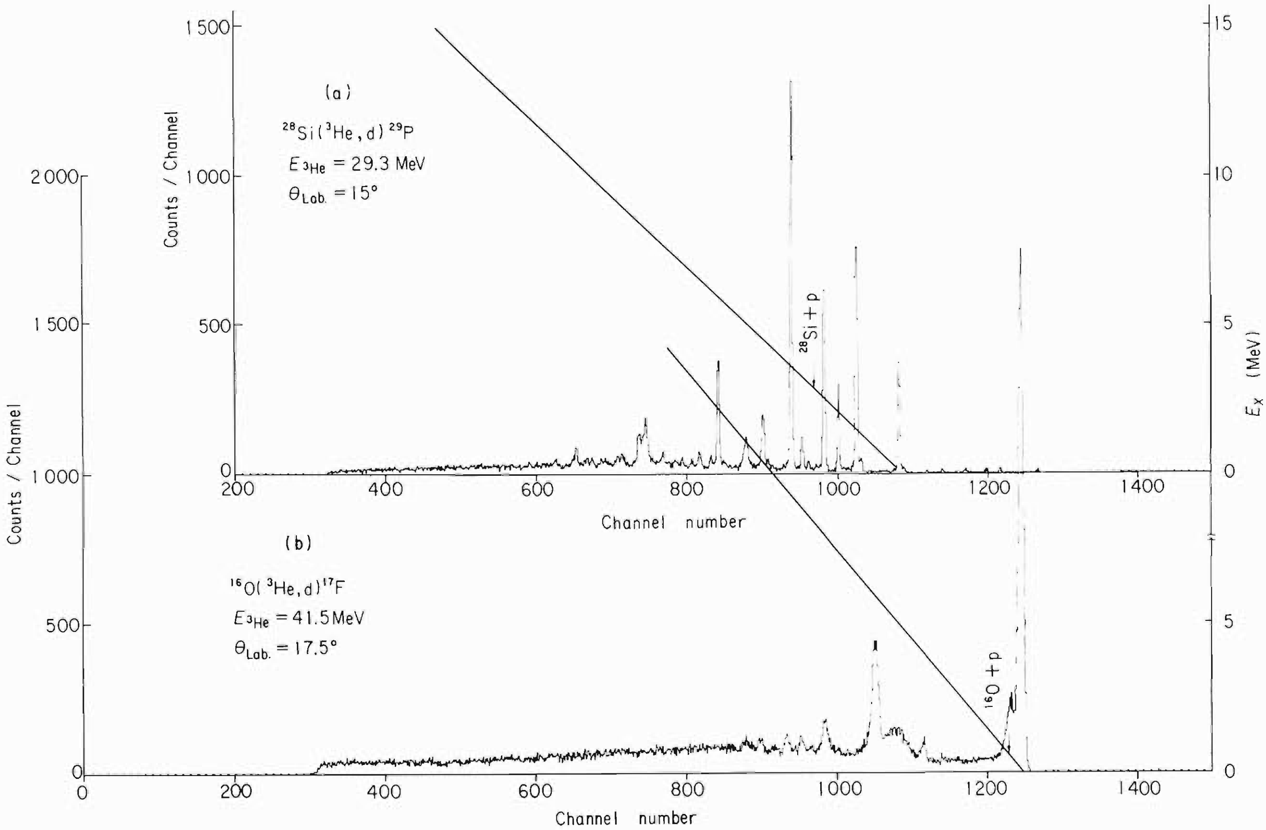

Fig. 1. Typical spectra of deuteron from the reactions $^{28}Si(^{3}He, d)^{29}P$ and $^{16}O(^{3}He, d)^{17}F$.

Table 1. The optical potential parameters for ^{3}He and deuteron. The notations are the same as used in Ref. 1.

	v	r	a	W	r_W	a_W	W_D	r_D	a_D
^{3}He + ^{28}Si	151	1.11	0.73	24.8	1.60	0.756			
^{3}He + ^{16}O	185	1.18	0.56	8.17	1.67	1.46	2.1	1.0	0.86
d + ^{29}P	80	1.15	0.81				20	1.34	0.68
d + ^{17}F	79.3	1.15	0.81				20	1.34	0.68

	V_{SO}	r_{SO}	a_{SO}	r_C
^{3}He + ^{28}Si	6.4	1.28	0.41	1.25
^{3}He + ^{16}O	4.5	1.3	0.6	1.3
d + ^{29}P				1.4
d + ^{17}F				1.4

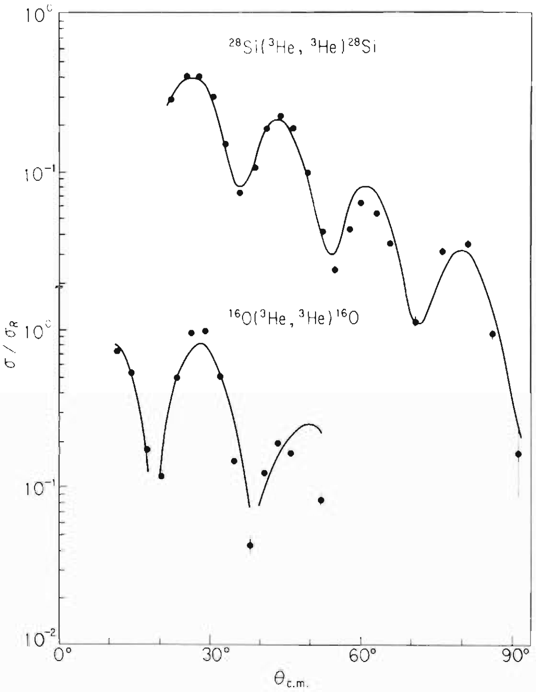

Fig. 2. The angular distributions of ^{3}He elastically scattered from ^{28}Si and ^{16}O. The curves are obtained by an optical model calculation.

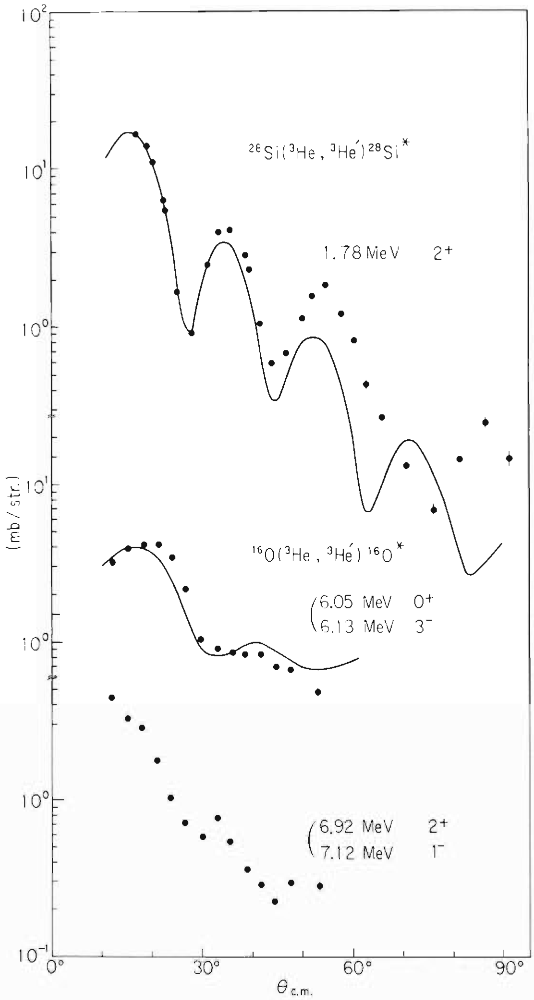

Fig. 3. The angular distributions of ^{3}He inelastically scattered from ^{28}Si and ^{16}O. The curves are obtained by a DWBA calculation using macroscopic form factors.

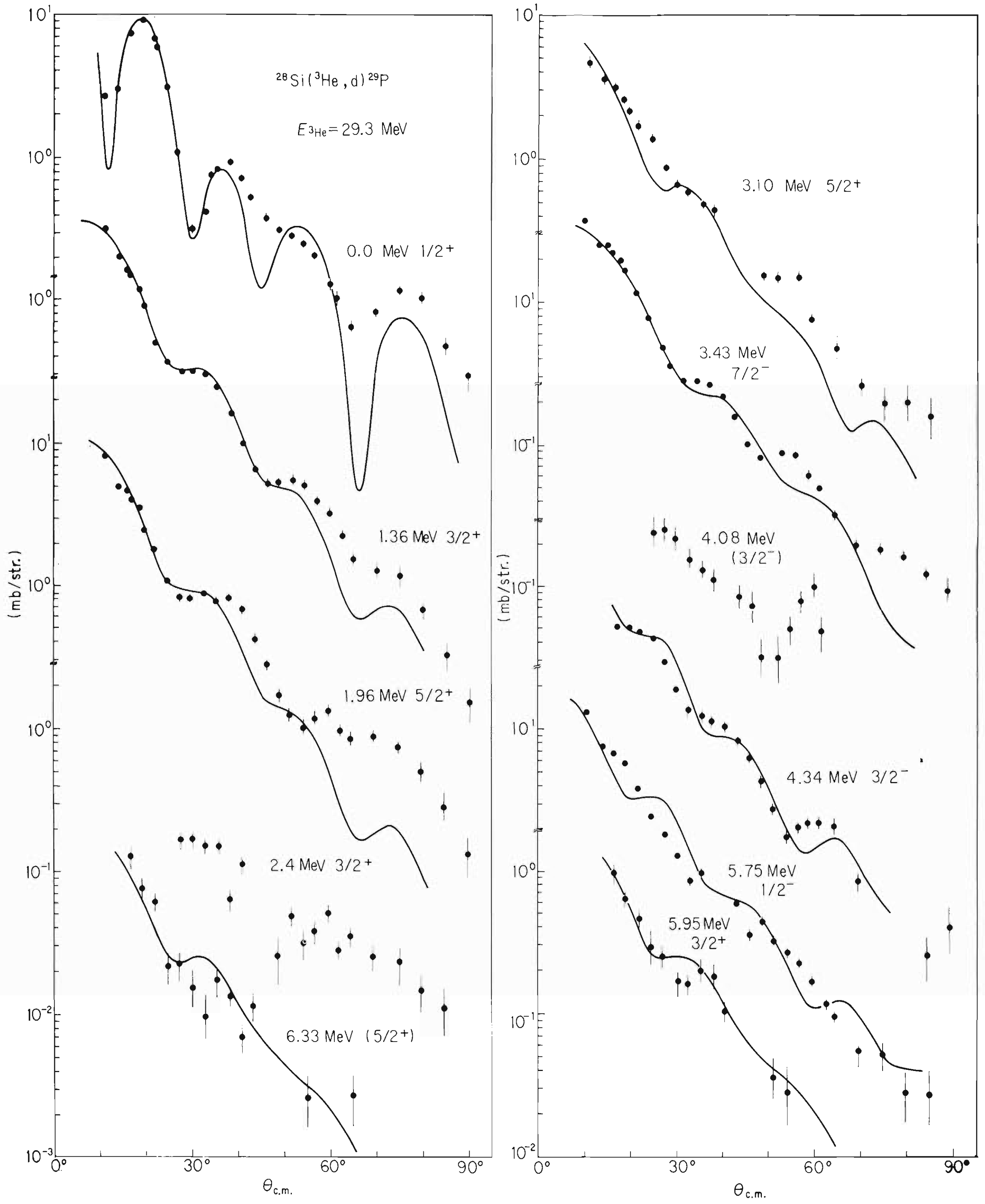

Fig. 4. The differential cross sections of the reaction ^{28}Si(^{3}He, d)^{29}P. The curves are obtained by a DWBA calculation. For the resonance states (higher energy states than 2.745 MeV), we used loosely bound form factors.

The energy spectra of deuteron, helium-3 and α-particles were measured by using an ORTEC particle identification system. Typical energy spectra of deuterons are shown in Fig. 1. Figure 2 gives the angular distributions of ^{3}He elastically scattered from ^{28}Si and ^{16}O, and the curves are obtained by an optical model calculation using the code "SEARCH",$^{1)}$ the parameters being given in Table 1. Figure 3 shows the angular distributions of ^{3}He inelastically scattered from ^{28}Si and ^{16}O.

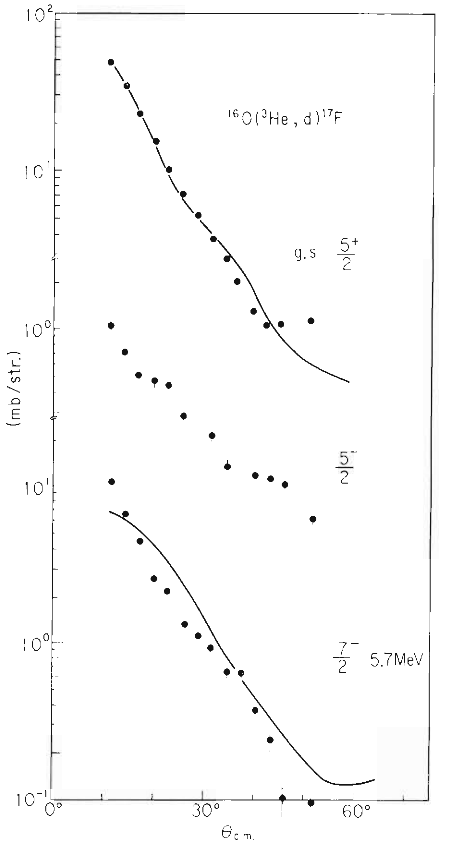

Fig. 5. The differential cross sections of the reaction ^{16}O (^{3}He, d)^{17}P. The curves are similar to those of Fig. 4. The resonance states are higher energy states than 0.601 MeV.

Figures 4 and 5 show the differential cross sections of the reactions ^{28}Si(^{3}He, d)^{29}P and ^{16}O (^{3}He, d) ^{17}F, respectively. The solid curves of Figs. 3, 4 and 5 give preliminary predictions obtained by a DWBA calculation using the code DWUCK with a computer TOSBAC-3400.

For the resonance states, we used loosely bound form factors. The optical potentials of deuteron were deduced from C. M. Perey and F. G. Perey's formula,$^{2)}$ and they are given in Table 1. Calculations using resonance form factors are now in progress.

References

1) T. Wada: IPCR Cyclotron Progr. Rep., 2, 87 (1968).
2) C. M. Perey and F. G. Perey: Nuclear Data Table, 13, No. 4, 293 (1974).

4-11. $^{58, 60, 62, 64}Ni(^3He, d)^{59, 61, 63, 65}Cu$ Reactions and the Correlation between Unbound States and Resonance States

H. Sakaguchi, M. Nakamura, S. Takeuchi,*
N. Nakanishi, and S. Takeda**

Particular interest in stripping reactions to unbound states was recently initiated by papers[1)-3)] reporting anomalies in (^{3}He, d) and (d, n) reactions. In spite of remarkable progress thereafter in the theoretical treatment[4)-6)] on one-nucleon transfer reactions to unbound states, it has not been established to use this reaction as a spectroscopical tool, because of the uncertainty in treating the continuum background, which is observed at the enhanced unbound state peak in the energy spectrum of emitted particles. The final state selectivity due to the direct reaction mechanism is, however, effective in these reactions if we choose the incident beam energy high enough, and this selectivity gives us useful information about the structure of resonance states found in (p, p_0) and (p, p') reactions on the same target.

^{3}He-beams of various energies between 22 and 47 MeV from the Cyclotron were bombarded on the Ni-isotope targets and emitted deuterons were measured with a $\Delta E - E$ counter telescope and a Goulding type particle identifier. Figure 1 shows typical deuteron spectra in (^{3}He, d)

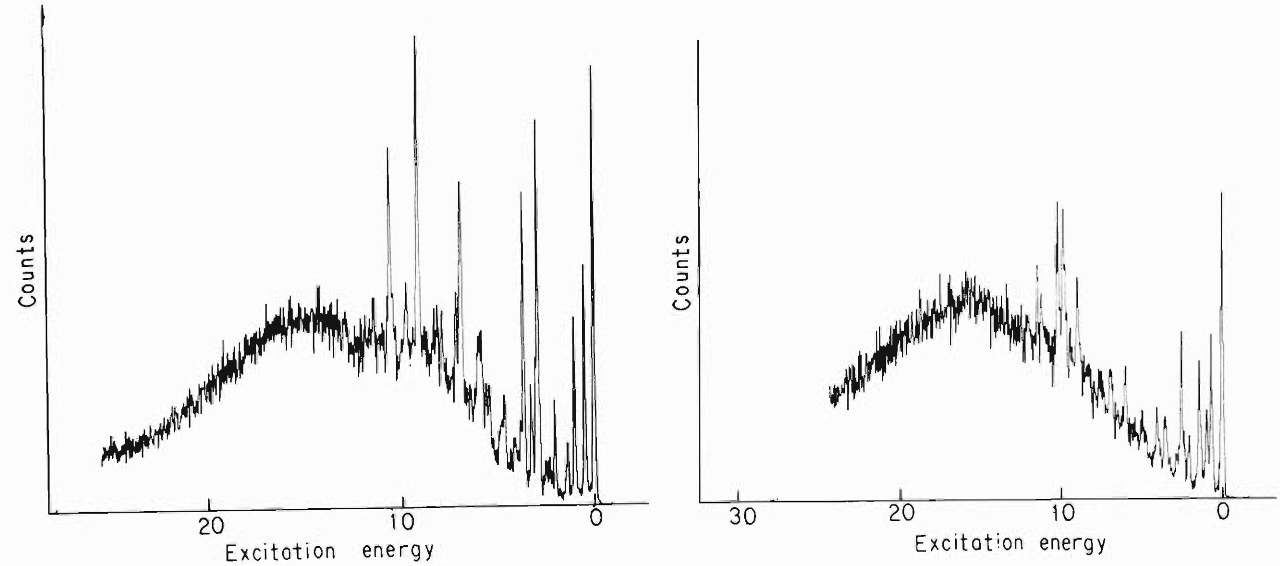

a) $^{60}Ni(^3He, d)^{61}Cu$, $\theta_{Lab} = 25°$, $E_{^3He}$ = 35.5 MeV

b) $^{62}Ni(^3He, d)^{63}Cu$, $\theta_{Lab} = 30°$, $E_{^3He}$ = 35.5 MeV

Fig. 1. Typical deuteron energy spectra obtained in (^{3}He, d) reactions.

---

* Department of Physics, Kyoto University

** National Laboratory for High Energy Physics

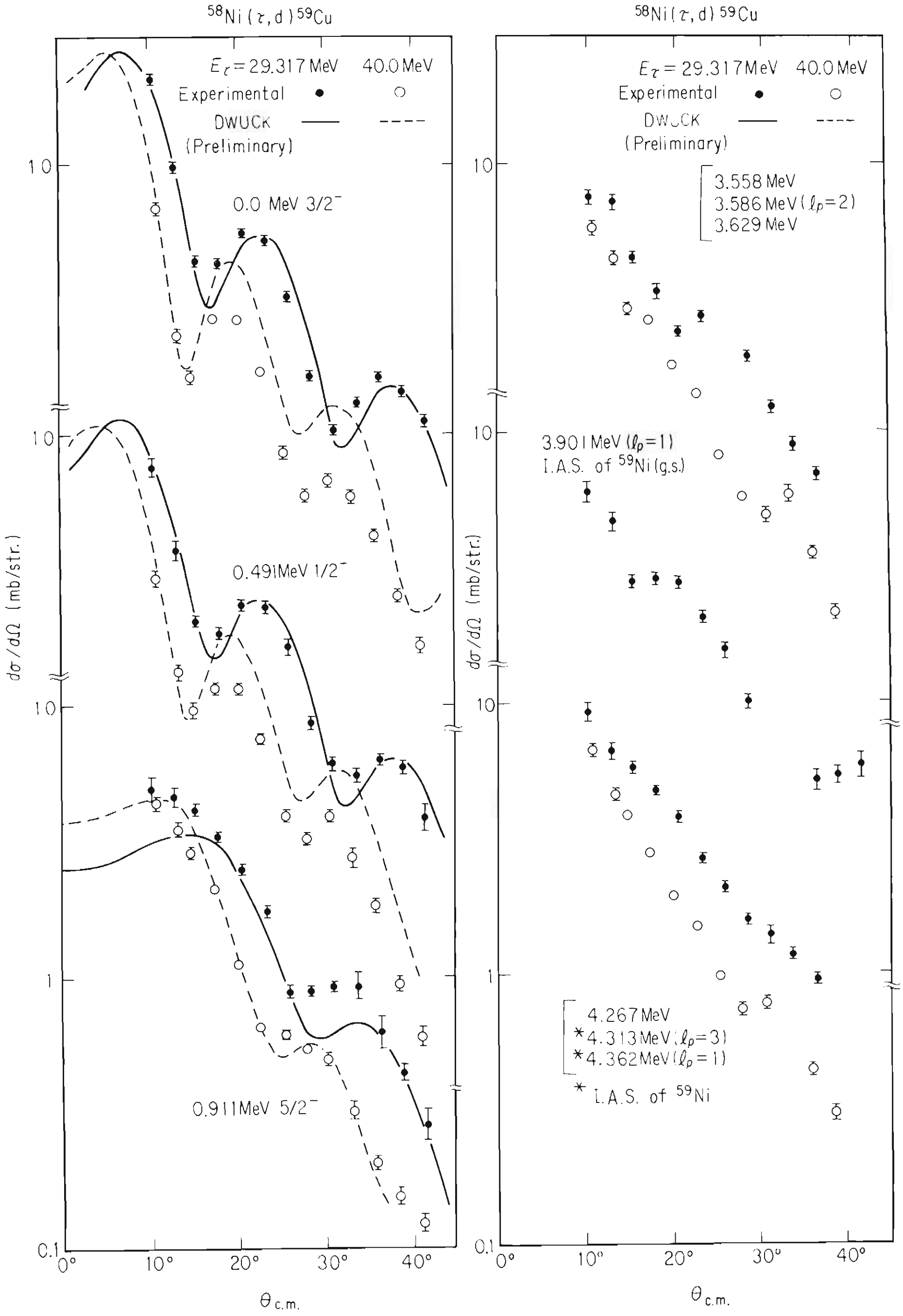

Fig. 2. Measured angular distributions in the ^{58}Ni(^{3}He, d)^{65}Cu reaction. Optical potential parameters used to calculate the DWUCK are V_R = 89.0 MeV, r_R = 1.15 fm, a_R = 0.81 fm, W_S = 19.6 MeV, r_I = 1.34 fm, a_I = 0.68 fm, for deuterons and V_R = 179.5 MeV, r_R = 1.11 fm, a_R = 0.77 fm, W_r = 20.6 MeV, r_I = 1.615 fm, a_I = 0.74 fm for ^{3}He.

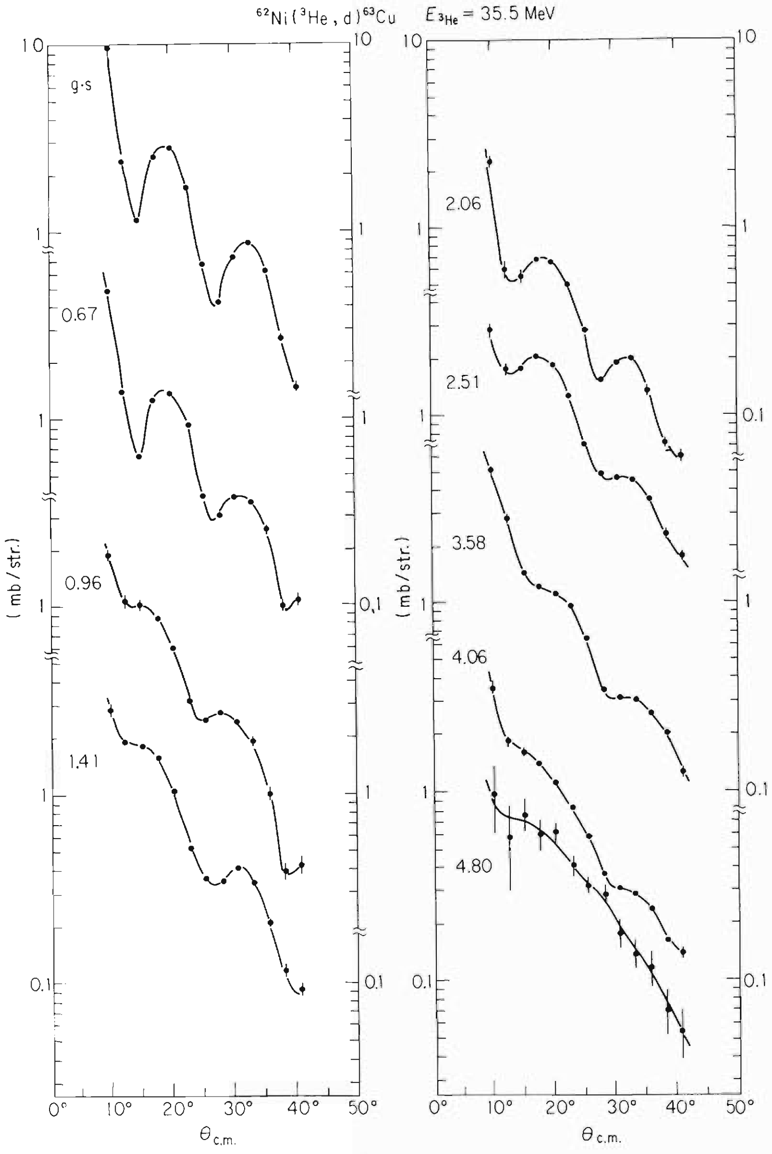

Fig. 3. ^{62}Ni(^{3}He, d)^{63}Cu angular distributions. Solid lines are used only to connect the measured values.

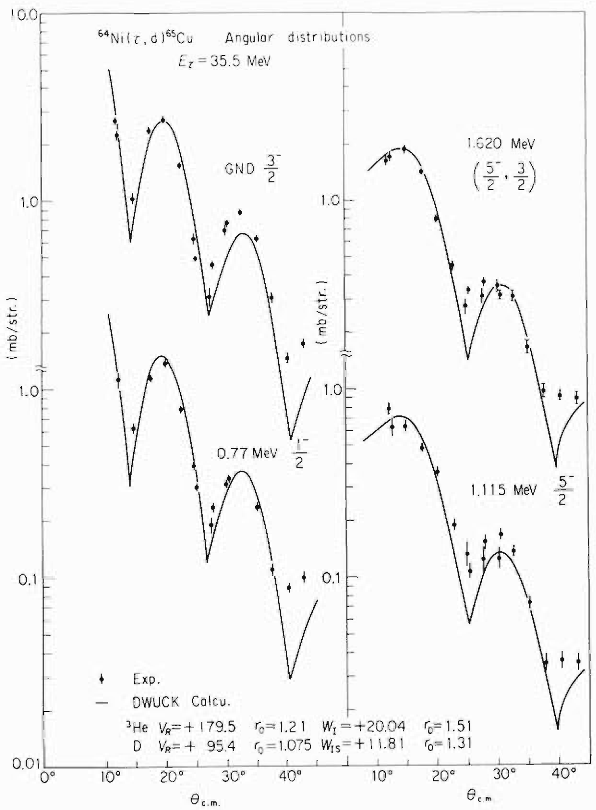

Fig. 4. ^{64}Ni(^{3}He, d)^{65}Cu angular distributions. Solid lines show the calculations with DWUCK. Used optical parameters are V_R = 179.5 MeV, r_R = 1.21 fm, W_V = 20.04 MeV, r_I = 1.51 fm for ^{3}He and V_R = 95.4 MeV, r_R = 1.0075 fm, W_S = 11.81 MeV, r_I = 1.31 fm for deuterons.

reactions. There we notice a remarkable gross structure of the background bump in the proton unbound energy region, over which enhanced peaks of unbound analog states are observed. Calculations using the Vincent-Fortune type DWBA analysis coded by Igarashi and Kawai,⁷⁾ where the radial integral to $r = \infty$ is replaced with the integral in the complex r-plane by use of the analytical continuation, enabled to explain only the 1/30 of the proton width Γ_p of the enhanced unbound peak. Angular distributions of ^{58,62,64}Ni(^{3}He,d)^{59,63,65}Cu are shown in Figs. 2, 3, and 4, respectively. For well-separated bound states, measured angular distributions were fitted using the code of DWUCK (see Figs. 2 and 4). In order to investigate the origin of the bump structure, energy spectra of deuterons were measured at various incident ^{3}He-beam energies, by changing the target mass. Remarkable features of the bump are as follows:

1) The yield of the background bump is strongly dependent on the incident beam energy. Bump cross sections grow up as the beam energy increases.

2) The position of the maximum in the bump energy spectrum relative to the proton separation energy does not change remarkably with increase of the target mass number.

Analysis on the bump structure using various form factors and models is in progress.

References

1) U. Strohbusch, H. J. Körner, G. C. Morrison, and J. P. Schiffer: Phys. Rev. Lett., 28, 47 (1972).

2) R. L. McGrath, N. Cue, W. R. Hering, L. L. Lee, Jr., B. L. Liebler, and Z. Vager: ibid., 25, 682 (1970).

3) S. A. A. Zaiai, C. L. Hollas, J. L. Horton, P. J. Riley, J. L. C. Ford, Jr., and C. M. Jones: ibid., p. 1503 (1970).

4) B. J. Cole, R. Huby, and J. R. Mines: ibid., 26, 204 (1971).

5) C. M. Vincent and H. T. Fortune: Phys. Rev., C4, 236 (1971).

6) C. M. Vincent and H. T. Fortune: ibid., C8, 1084 (1973).

7) Private communications and M. Kawai and M. Igarashi: Research Center for Nuclear Physics Report RCNP-P-1, p.40 (1974).

4-12. Analyses of Cr (^{3}He, d) Mn Reactions at 29.29 MeV

N. Nakanishi, S. Takeda,* H. Ohnuma, S. Yamada,
H. Sakaguchi, M. Nakamura, S. Takeuchi,** and K. Koyama

Differential cross sections were measured on the ^{50,52,54}Cr(^{3}He, d)^{51,53,55}Mn reactions at a ^{3}He-energy of 29.29 MeV[1] and analyses of them have been carried out.

As optical model parameters were employed a deep potential family ($V \approx 180$ MeV) for ^{3}He particles and a Perey-Perey's set for deuteron particles.

For proton-bound states, conventional DWBA analyses were carried out to obtain theoretical angular distributions and spectroscopic factors. As an example, the calculated results on ^{50}Cr(^{3}He, d)^{51}Mn reactions are shown in Fig. 1 and Table 1. In Fig. 1, $\ell_p = 2$ and $\ell_p = 1$ were assigned to the 2.99 MeV level transfer in Refs. 2 and 3 respectively. However, it can be seen that $\ell_p = 3$ gives better fits. Angular momentum $\ell_p = 3$ may be assigned to the 4.93 MeV level.

Table 1. Transition strength of the ^{50}Cr(^{3}He, d)^{51}Mn (bound states).

E_x	E_h = 29.29 MeV (Present)			E_h = 12 MeV[2]			E_h = 9.5 MeV[3]		
	ℓ_p	J^π	$C^2(2J+1)S$	ℓ_p	J^π	$C^2(2J+1)S$	ℓ_p	J^π	$C^2(2J+1)S$
0.24	3	$7/2^-$	2.26	3	$7/5^-$	2.33	3	$7/2^-$	2.62
1.83	1		0.56	1		0.63	1	$3/2^-$	0.75
1.95	1		0.23	1		0.21	1	$3/2^-$ $1/2^-$	0.33
2.13	1		0.39	1		0.35	1	$3/2^-$ $1/2^-$	0.54
2.84	1		0.25	1		0.20	1	$3/2^-$ $1/2^-$	0.39
2.99	(3)		0.90	2	$(3/2)^+$	0.15 (1d) 0.06 (2d)	1	$3/2^-$ $1/2^-$	0.04
3.28	3	$(5/2)^-$	1.89	3		0.84	3	$5/2^-$	2.69
4.44	3	$7/2^-$ IAS	0.85 (s=0.32)	3	$7/2^-$ IAS	0.55			
4.71	(0.2)		0.04	(2)		0.02			
4.93	3		0.08	1		0.04			
5.10 5.074	1	IAS	0.77	1	$1/2^-$ IAS	0.23			
5.128				1	$3/2^-$ IAS	0.37			

---

* National Laboratory for High Energy Physics.

** Kyoto University.

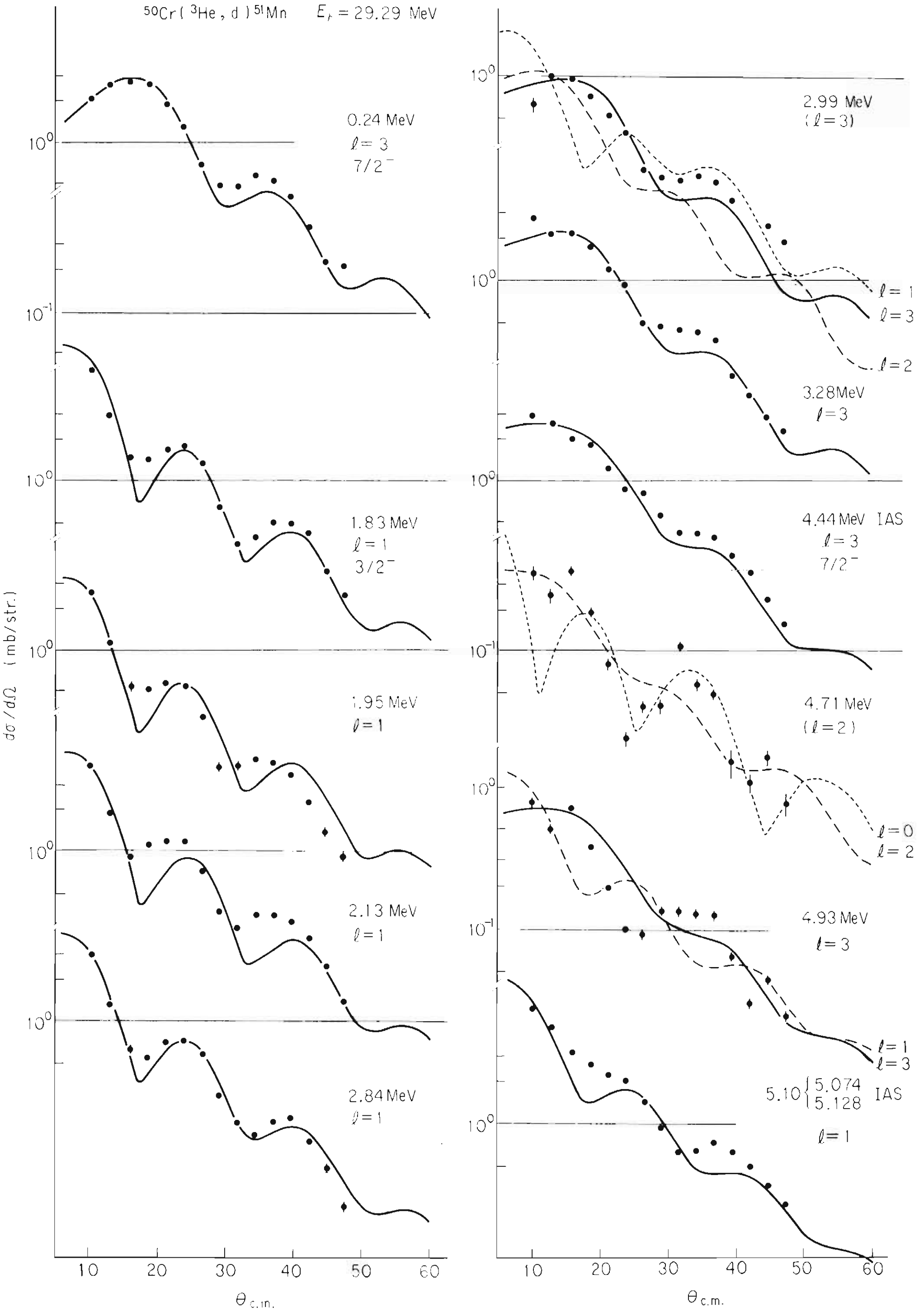

Fig. 1. Angular distributions for transitions to bound states of ^{50}Cr(^{3}He, d)^{51}Mn reaction at an incident energy of 29.29 MeV.

The 5.10 level is composed of IAS 5.074 and 5.128 MeV levels. It was unable to observe these levels separately.

For proton-unbound states we have carried out some trial calculations to reproduce these angular distributions. Some of them are shown in Figs. 2 and 3 for the E_x = 12.35 MeV $9/2^+$ state of ^{55}Mn (the isobaric analogue state of ^{55}Cr 2.09 MeV $9/2^+$ state). Figure 2 shows form factors for the parent nucleus, a loosely bound state and a single particle resonant state[4]

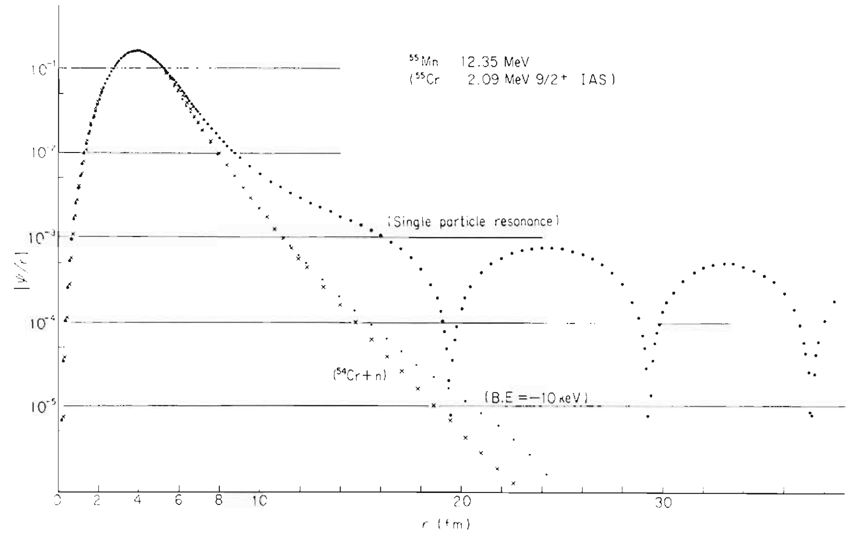

Fig. 2. Form factors for a 12.35 MeV $9/2^+$ state of ^{55}Mn. Cross sign, small dots and large ones show form factors of a neutron of a parent nucleus, of a proton loosely bound and of a proton on the assumption of a single particle resonance, respectively.

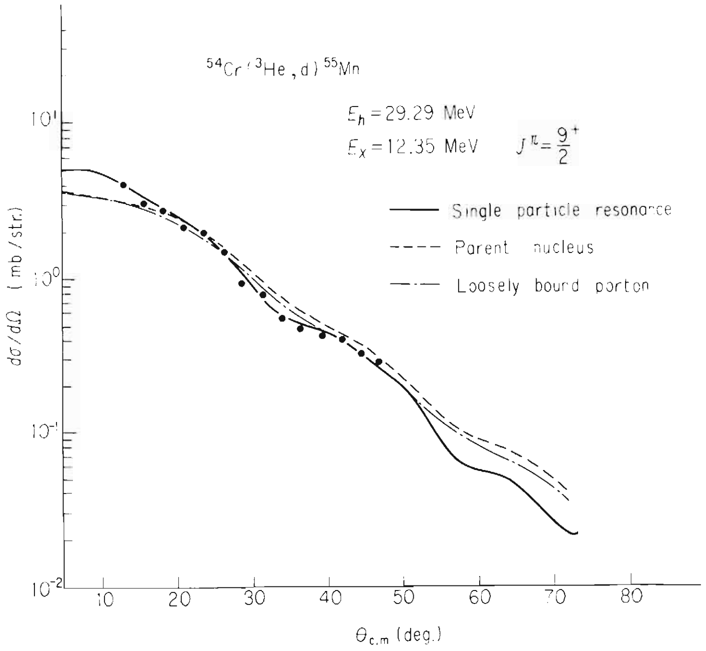

Fig. 3. A typical angular distribution for a ^{55}Mn 12.35 MeV $9/2^+$ proton-unbound state. Calculated curves are normalized arbitrarily to experimental points.

by cross signs, smaller and larger dots, respectively. Figure 3 shows the calculated angular distributions and the experimental values. In this case, proton form factors were employed as seen in Fig. 2. Overlap integrals were performed using a code “INS-DWBA2”,5) which adopts the Vincent-Fortune method6) in case of integration of a scattering state.

References

1) N. Nakanishi, S. Takeda, H. Ohnuma, S. Yamada, H. Sakaguchi, M. Nakamura, S. Takeuchi, and K. Koyama: IPCR Cyclotron Progr. Rep., 7, 42 (1973).

2) J. Rapaport, T. Belote, and W. E. Dorenbuch: Nucl. Phys., A100, 280 (1967).

3) B. Cǔjec and I. M. Szöghy: Phys. Rev., 179, 1060 (1969).

4) W. R. Coker and G. W. Hoffmann: Z. Physik, 263, 179 (1973).

5) The code “INS-DWBA2” was newly improved by M. Igarashi.

6) C. M. Vincent and H. T. Fortune: Phys. Rev., C2, 782 (1970).

4-13. Full Finite-Range DWBA Calculations for Heavy-Ion Induced Two-Nucleon Transfer Reactions

T. Takemasa

Recently heavy-ion induced two-nucleon transfer reactions have been of much interest. Several authors1)−3) have attempted to calculate differential cross sections of such reactions. However, all the calculations except the work of Bayman4) are based on a no-recoil approximation. Apparently it may be misleading to ignore the recoil effects for these reactions and the spectroscopic information can be only achieved through an exact finite-range calculation including a microscopic form factor.

We have recently completed a finite-range full-recoil DWBA code which also includes the microscopic form factor.5) The methodology given there used the multipole expansion of the two nucleon overlap in terms of the relative angular momentum $\tilde{\ell}$ of a transferred nucleon pair.

Here we report a finite-range full-recoil DWBA calculation for the reaction ^{12}C (^{18}O, ^{16}O) $^{14}C_{g.s.}$. The optical potential parameters are the same as those used in Ref.3; $V_0 = 200$ MeV, $W_{vol} = 10$ MeV, $R = 1.25\ (A_1^{1/3} + A_2^{1/3})$ fm, and $a_0 = 0.5$ fm. The overlap $<^{14}C\,|\,^{12}C>$ is assumed to be a pure $(0p_{1/2})^2$ configuration and $<^{18}O\,|\,^{16}O>$ to be the admixed configuration given by Federman and Talmi.6)

We first investigated the convergence of the $\tilde{\ell}$ series. The differential cross sections were calculated as a function of the quantum number $\tilde{\ell}$ (Fig. 1). As can be seen, the convergence is fairly rapid. We found that taking account up to $\tilde{\ell} = 3$ term is enough to ensure an accuracy of better than 1 – 2 % in the differential cross section. This fact points out that it is quite practical to use this method for the systematic analysis of experimental data.

In Fig. 2, the finite-range full-recoil DWBA calculations are compared with the finite-range no-recoil ones3) and also with the experimental data.7) The normalization factors $N = \sigma(\theta)_{exp.} / \sigma(\theta)_{theor.}$ for the full-recoil (no-recoil) curves are 250 (500), 111 (72), and 140 (138) for $E_{lab} = 16$, 20, and 24 MeV, respectively. The full-recoil curve at $E_{lab} = 16$ MeV is greatly different from the no-recoil curve. However, the recoil effects do not affect the shape of the angular distributions at $E_{lab} = 20$ and 24 MeV.

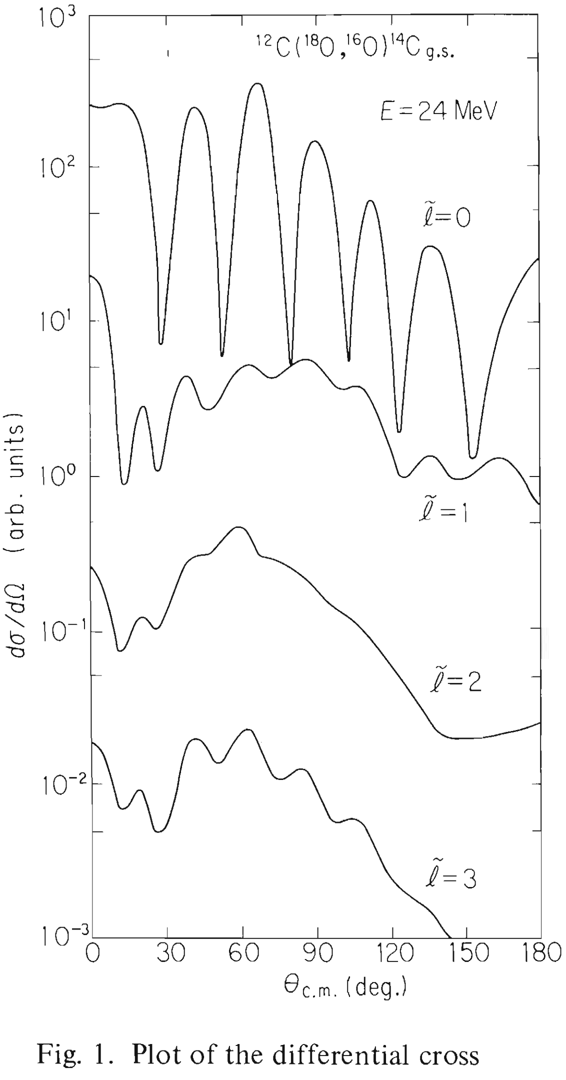

Fig. 1. Plot of the differential cross sections for the $\tilde{\ell} = 0 - 3$ for the reaction $^{12}C(^{18}O, ^{16}O)^{14}C_{g.s.}$ at E_{lab} = 24 MeV.

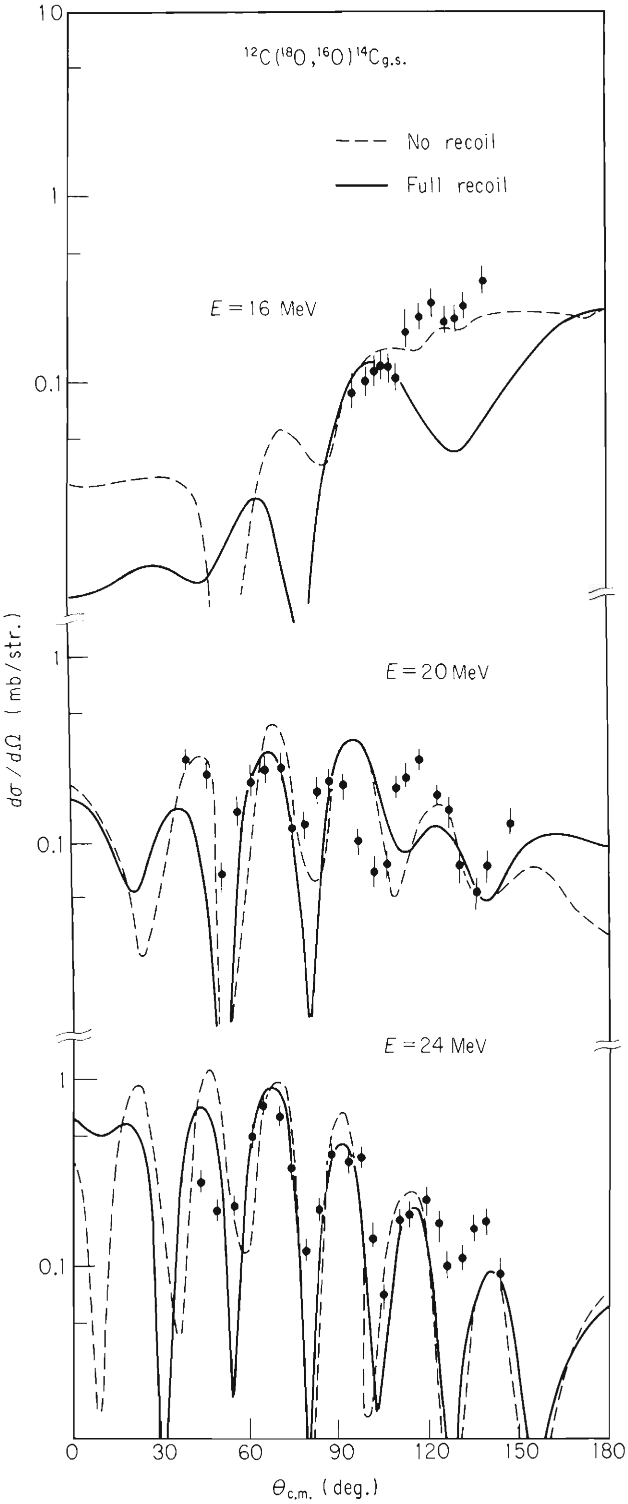

Fig. 2. Comparison of the finite-range full-recoil and finite-range no-recoil[3)] DWBA calculations with the experimental differential cross section.[7)]

References

1) A. J. Baltz and S. Kahana: Phys. Rev. Lett., 29, 1267 (1972).
2) A. Roberts: Nucl. Phys., A196, 465 (1972).
3) R. A. Broglia et al.: Kernforschungsanlage Jülich Internal Report, 1973, (unpublished).
4) B. F. Bayman: Phys. Rev. Lett., 32, 71 (1974).
5) T. Takemasa: Phys. Lett., (1975), (in press).
6) P. Federman and I. Talmi: Phys. Lett., 19, 590 (1965).
7) P. H. Barker et al.: Proc. Int. Conf. on Nuclear Reactions Induced by Heavy Ions, Heidelberg, 1969, North-Holland, Amsterdam, p. 152 (1970).

4-14. Two-Nucleon Transfer Reactions between Heavy Ions

T. Takemasa

A method[1] was developed for exact evaluation of the DWBA transition amplitude in two-nucleon transfer reactions between heavy ions. It is based on an expansion of a two-nucleon overlap fuction $\langle \Psi(b) | V | \Psi(b+2) \rangle$ in multipole series of the relative angular momentum $\tilde{\ell}$ of a transferred nucleon pair. The perturbation interaction acting between the core and each transferred nucleon is taken into account, and it is therefore possible to extract the proper spectroscopic information by comparing the calculated results with the experimental data.

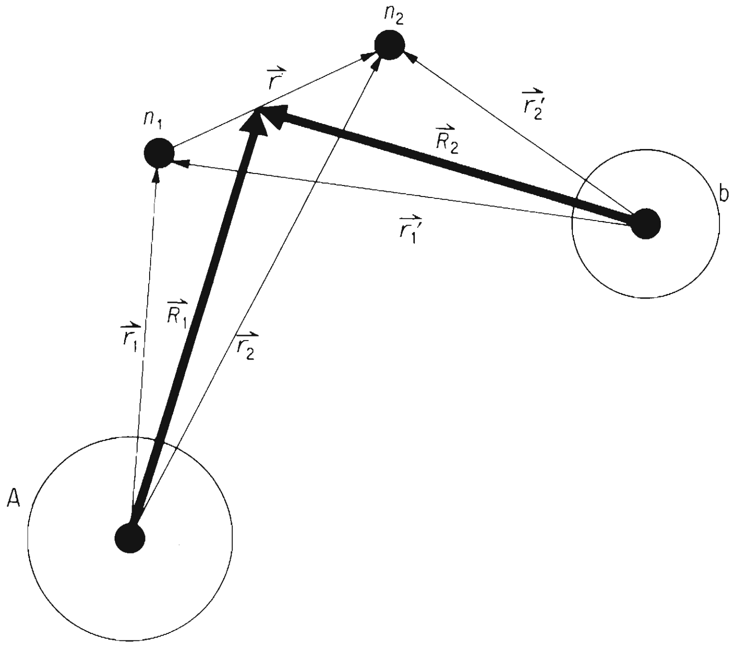

Fig. 1. Coordinate system for the reaction A(a, b)B where
B = A + 2n, a = b + 2n.

Figure 1 shows a relevant vector diagram for the two-nucleon transfer A(a, b) B (B = A + 2n, a = b + 2n). The form factor $< \Psi_B \ \Psi_b | \{V(r_1') + V(r_2')\} | \Psi_A \ \Psi_a \rangle$ (post representation) can be factorized as follows :

$$< \Psi_B \ \Psi_b | \{ V(r_1') + V(r_2') \} | \Psi_A \ \Psi_a >$$
$$= < \Psi_B | \Psi_A > < \Psi_b | \{ V(r_1') + V(r_2') \} | \Psi_a > . \qquad (1)$$

we consider a multipole expansion of the radial part of the overlap

$$< \Psi_b | \{ V(r_1') + V(r_2') \} | \Psi_a > :$$

$$\{ V(r_1') + V(r_2') \} \, \Phi^{L'}_{M'} (\vec{r}_1', \vec{r}_2')$$
$$= \sum_{\tilde{\ell}' \tilde{L}'} g^{L'}_{\tilde{\ell}' \tilde{L}'} (r, R_2) \, [Y_{\tilde{\ell}'} (\hat{r}) \times Y_{\tilde{L}'} (R_2)]^{L'}_{M'} , \qquad (2)$$

and a similar multipole expansion is carried out for the overlap $<\Psi_B|\Psi_A>$.[2] Inserting these expansions into Eqn. (1) and integrating over $\vec{r}$, we can obtain the following expression for the form factor :

$$F_{L,\mu}(\vec{R}_1, \vec{R}_2) \sum_{\tilde{\ell}\tilde{L}\tilde{L}'} \sum_{LL'S} S^*_{AB} S_{ab} \times C(LL'S\tilde{\ell}\tilde{L}\tilde{L}')$$

$$\times F^{LL'}_{\tilde{\ell}\tilde{L}\tilde{L}'}(R_1, R_2)\left[Y_{\tilde{L}}(\hat{R}_1)\times Y_{\tilde{L}'}(\hat{R}_2)\right]^L_\mu , \qquad (3)$$

where $S_{AB}(S_{ab})$ is the two-nucleon parentage coefficient for the target (projectile) nucleus, $C(LL'S\tilde{\ell}\tilde{L}\tilde{L}')$ is the angular momentum coupling coefficient and S is the total spin angular momentum of the two transferred nucleons. The radial part of the form factor $F^{LL'}_{\tilde{\ell}\tilde{L}\tilde{L}'}(R_1, R_2)$ can be expressed by

$$F^{LL'}_{\tilde{\ell}\tilde{L}\tilde{L}'}(R_1, R_2) = \int_0^\infty dr\ r^2\ f^{L}_{\tilde{\ell}\tilde{L}}(r, R_1)\times g^{L'}_{\tilde{\ell}\tilde{L}'}(r, R_2), \qquad (4)$$

where the function $f^{LL}_{\tilde{\ell}\tilde{L}}$ is the radial part of the multipole expansion of the overlap $<\Psi_B|\Psi_A>$.

The angular momentum coupling diagram is exhibited in Fig. 2. It is to be observed that the quantum number $\mathcal{L}$ is the total transferred angular momentum. The resultant formalism which can exactly treat the DWBA amplitude for the two-nucleon transfer between heavy ions has been coded by suitably extending the existing single-particle DWBA code DWBA-4.[3] The coding has been checked by comparing results with those given by Bayman.[4]

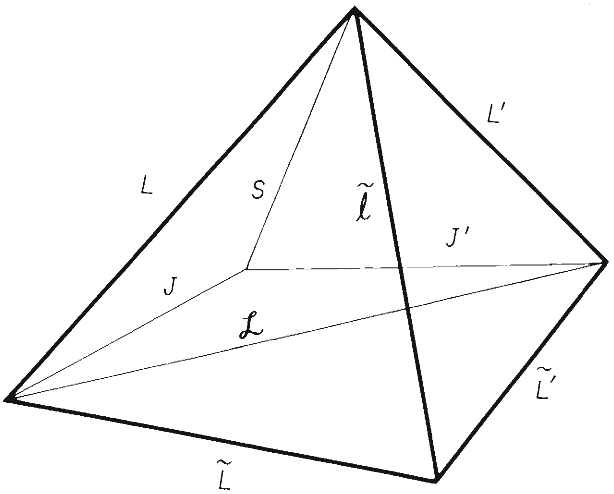

Fig. 2. Angular momentum coupling diagram in a transfer reaction. The total angular momentum of a transferred pair in the projectile nucleus is J' = L' + S and it is transferred to J = L + S in the residual nucleus. The total transferred angular momentum is $\mathcal{L}$ which is the sum of the center of mass angular momentums in the projectile and residual nuclei.

References

1) T. Takemasa: Phys. Lett., (in press).
2) C. W. Wong and D. M. Clement: Nucl. Phys., A183, 210 (1972).
3) H. Yoshida: DWBA code DWBA-4 (unpublished).
4) B. F. Bayman: Phys. Rev. Lett., 32, 71 (1974).

4-15. One-and Two-step Processes in the Heavy-Ion Induced Two-nucleon Transfer Reaction

T. Kammuri

Two-nucleon transfer reactions induced by light particles have been analyzed by means of the first-order DWBA method, in which the nucleon pair is assumed to be transferred through a single interaction with the core. In the collision between two nuclei in the independent-particle model limit, two nucleons can be transferred one by one, with one interaction in each transfer. Usually two nucleons have some degrees of correlation. At least they belong to the same nuclear system and can have a correlation distance of the order of nuclear diameter. Thus it is interesting to study competition between simultaneous and successive transfer processes in the heavy-ion induced reactions.[1), 2)]

The transition amplitude can be written as

$$T_{fi} = \langle f | V_f + V_f \frac{1}{E-H+i\varepsilon} V_i | i \rangle . \qquad (1)$$

We expand this to the second order of the interaction and take the same restricted class of intermediate states m :

$$T_{fi}^{(2)} = \langle f | V_f | i \rangle + \sum_m \langle f | V_f | m \rangle \frac{1}{E-H_m+i\varepsilon} \langle m | V_i | i \rangle , \qquad (2)$$

where H_m is the unperturbed Hamiltonian in the intermediate channel and V_α is the residual interaction in the α-channel. We refer each term of Eqn. (2) as the amplitude of the post or prior-post form. Due to the equality of the post and prior forms of the first order amplitude, Eqn. (2) is equivalent to

$$T_{fi}^{(2)} = \langle f | V_i | i \rangle + \sum_m \langle f | V_f | m \rangle \frac{1}{E-H_m+i\varepsilon} \langle m | V_i | i \rangle . \qquad (3)$$

Eqn. (2) can be rewritten so as to involve $\langle m | V_m | i \rangle$ instead of $\langle m | V_i | i \rangle$,

$$T_{fi}^{(2)} = \langle f | V_f | i \rangle - \sum_m \langle f | V_f | m \rangle \langle m | i \rangle + \sum_m \langle f | V_f | i \rangle \frac{1}{E-H_m+i\varepsilon} \langle m | V_m | i \rangle . \qquad (4)$$

If both the projectile and target systems can be described by the shell model within the given space of m, the first term is cancelled with the second term[1)] and we get the post-post form

$$T_{fi}^{(2)} = \sum_m \langle f | V_f | i \rangle \frac{1}{E-H_m+i\varepsilon} \langle m | V_m | i \rangle . \qquad (5)$$

Starting from Eqn. (3) we get the prior-prior form :

$$T_{fi}^{(2)} = \sum_m \langle f | V_m | i \rangle \frac{1}{E-H_m+i\varepsilon} \langle m | V_i | i \rangle . \qquad (6)$$

The reaction ^{48}Ca (^{16}O, ^{14}C) ^{50}Ti to the lowest 0^+, 2^+, 4^+, and 6^+ states of ^{50}Ti at 58 MeV incident energy[3)] has been analyzed in the no-recoil approximation. We have used the code TWOST.[4)] The optical parameters are taken from Ref. 3 : V = 37 MeV, r_{OR} = 1.35 fm, a_R = 0.42 fm, W = 78 MeV, r_{OI} = 1.27 fm, and a_I = 0.28 fm. Simple configurations are assumed for ^{50}Ti and ^{16}O :

$$<{}^{14}\mathrm{C}|{}^{16}\mathrm{O}>=(0p_{1/2})^2,\ <{}^{48}\mathrm{Ca}|{}^{50}\mathrm{Ti}>=(0f_{7/2})^2$$

The successive transfer is assumed to proceed via a channel m consisting of the ground states of ^{15}N and ^{49}Sc. The cross sections in various representations differ from each other by about 30 %. In Figs. 1 and 2 we have compared the experimental data with the results of calculation. The normalization constants defined by $N = \delta_{\exp} / \delta_{\mathrm{calc}}$ are listed in Table 1. It can be seen that the successive transfer dominates over the simultaneous transfer for all the transitions. It should be noted that, although the two-step angular distributions for 4^+ and 6^+ transitions shown in Fig. 2 do not have oscillatory behavior, we can change them so as to fit the experimental shape by varying the Q value for the first or second step while fixing the overall Q value.

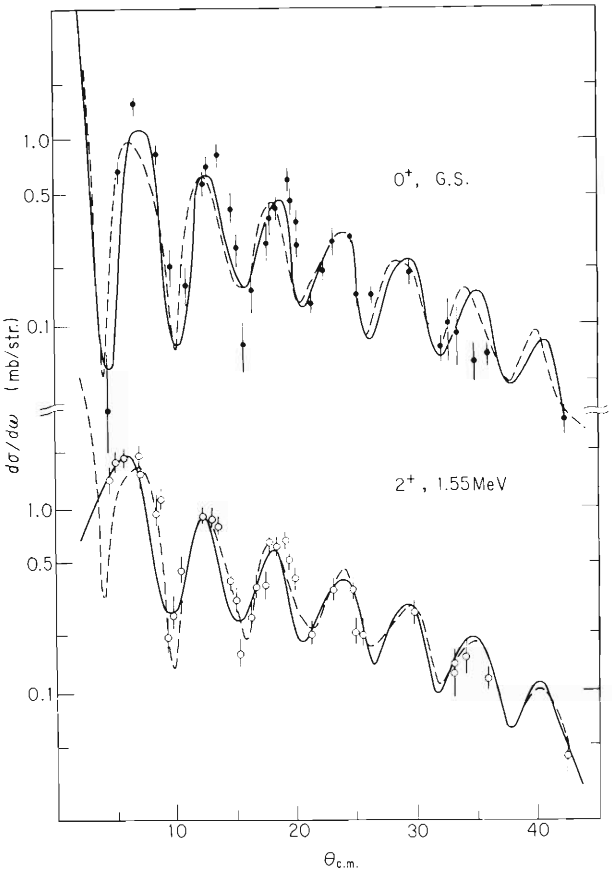

Fig. 1. Angular distributions for the reaction ^{48}Ca(^{16}O, ^{14}C)^{50}Ti leading to the lowest 0^+ and 2^+ states at incident energy of 58 MeV. The solid and dashed lines are the theoretical curves predicted by the one- and two-step DWBA, respectively.

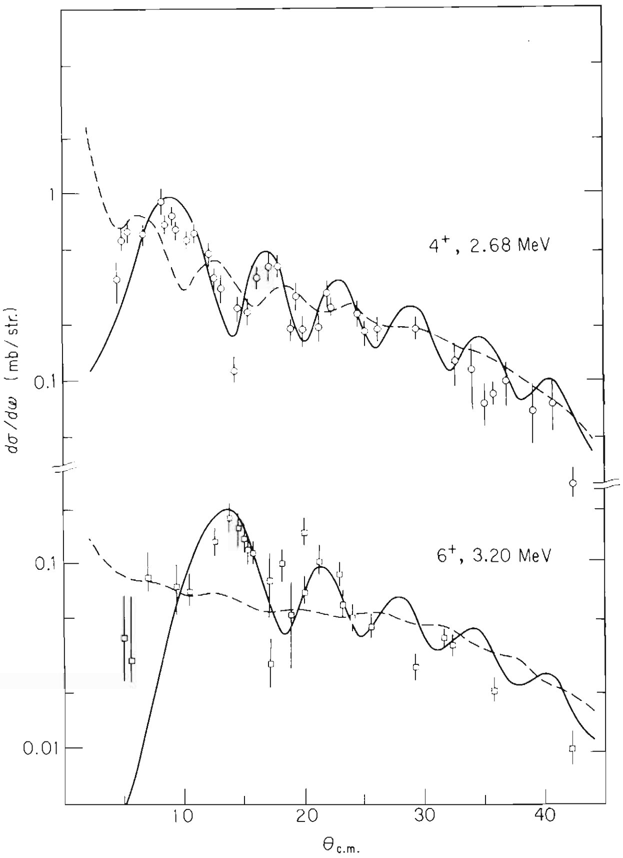

Fig. 2. Same as in Fig. 1 except for the transitions to the lowest 4^+ and 6^+ states.

Table 1. Normalization constant($N = \delta_{exp} / \delta_{calc}$) peak.

J^{π}	E*(MeV)	$N_{one\text{-}step}$	$N_{two\text{-}step}$
0^+	0.0	250	12.5
2^+	1.55	300	13.6
4^+	2.68	330	22.8
6^+	3.20	224	10

References

1) R. A. Broglia, U. Götz, M. Ichimura, T. Kammuri, and A. Winther: Phys. Lett., 45B, 23 (1973).

2) T. Kammuri: ibid., 51B, 442 (1974).

3) W. Henning, D. G. Kovar, B. Zeidman, and J. R. Erskine: Phys. Rev. Lett., 32, 1015 (1974).

4) M. Toyama and M. Igarashi: DWBA code "TWOST" (unpublished).

4-16. CCBA Analysis of (p, t) Reactions on Rare-Earth Nuclei

M. Wakai,* M. Sano,* T. Takemasa, and S. Yamaji

Nuclear reactions are usually analyzed by using a zero-range DWBA method and it is a very effective tool for study of the nuclear spectroscopy. Some of the present authors (M.S. and T.T.) and M. Sakagami$^{1)}$ analyzed (p, t) reactions on rare-earth nuclei by using the zero-range DWBA method. They explicitly took into account of the difference between the deformation of a target nucleus and that of a residual nucleus and obtained the following results: (1) the angular distribution and the neutron number dependence of the ground state cross section are in good agreement with the experimental results, (2) neither the magnitude of the cross section nor the angular distributions for the 2^+ and 4^+ state transitions are well reproduced. The finite range calculations$^{2)}$ were performed by one of the present authors (T.T.) and H. Yoshida to dissolve the discrepancy between the experimental and the theoretical results based on the zero-range DWBA. However the situation was not improved by introducing the effect of finite range of nucleon-nucleon interaction.

Recently, the importance of the channel-coupling was emphasized and the CCBA method was applied for analysis of (p, t) reactions.$^{3)}$ The CCBA calculations showed that the contribution of indirect processes is much larger than was expected and has an important effect on both the cross sections and the angular distributions to make the agreement between the experimental and theoretical results better. It has led us to reanalyze the (p, t) reactions on rare-earth nuclei by using the CCBA method. The transition amplitude of CCBA for a transfer reaction A(a, b)B is written as$^{4)}$

$$T = \langle \Psi_b^{(-)}(X_B, X_b, \gamma_b) | V(X, X_b) | \Psi_a^{(+)}(X_A, X_a, \gamma_a) \rangle .$$

Here $\Psi_a^{(+)}$ and $\Psi_b^{(-)}$ are solutions of a coupled-channel equation and a = b + x. We used the source-term method developed by Glendenning$^{5)}$ to get the transition amplitudes. In this analysis, the coupling of 0^+, 2^+, and 4^+ states of a ground band were considered. The angular momentum projection method is applied to obtain the nuclear wave functions of rotational states.$^{1)}$ The optical parameters used in the analysis are tabulated in Table 1. Figures 1 and 2 show the experimental$^{6)}$ and theoretical angular distributions for 0^+, 2^+, and 4^+ transitions of ^{172}Yb(p, t) ^{170}Yb. It can be seen that the CCBA method reproduces well the forward peak behavior of 2^+ transition which the DWBA cannot expalin at all. According to our calculations, an indirect process $0^+ \xrightarrow{\text{inel}} 2^+ \xrightarrow{\text{transfer}} 2^+$ gives a large contribution and makes the value of the cross section to 2^+ state much larger. The forward peak behavior of the 2^+ transition is reproduced by the interference between the direct $0^+ \rightarrow 2^+$ process and the indirect process mentioned

---

* Osaka University

Table 1. Optical parameters used in the CCBA calculations.

	Proton	Triton
V(MeV)	51.4	150.0
r'_0(F)	1.17	1.24
a(F)	0.73	0.67
W(MeV)	2.59	20.0
W_D (MeV)	7.50	0.0
r'_0(F)	1.31	1.46
a′(F)	0.65	0.79
r_c(F)	1.20	1.40

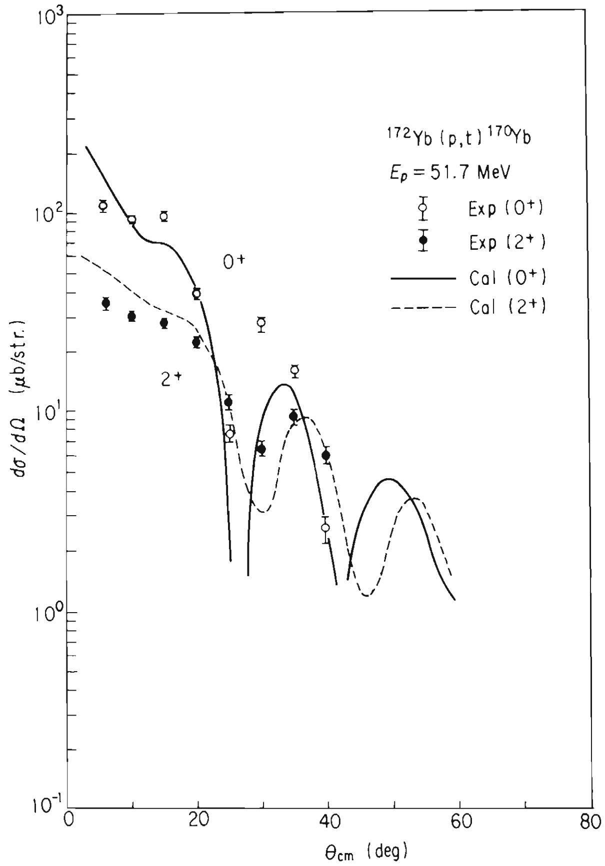

Fig. 1. Angular distributions for the g.s. and 2^+ transitions.

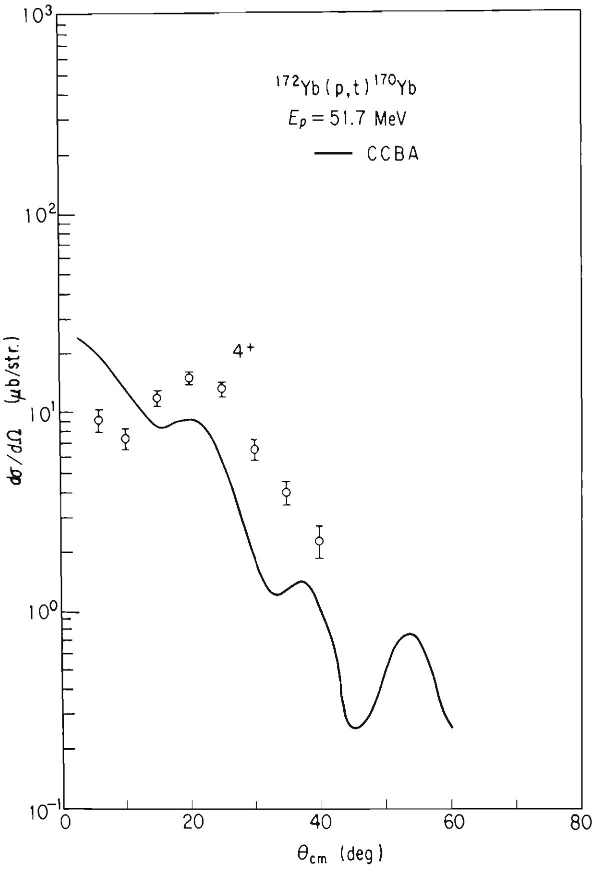

Fig. 2. Angular distributions for the 4^+ transition.

above. The summed cross sections $\sigma(I^+)$ are defined by the sum of differential cross sections taken for 5° steps in the range 5° – 45°, and the ratios $\sigma(I^+)/\sigma(0^+)$ are plotted in Fig. 3. The DWBA calculations[1)] give the ratios $\sigma(2^+)/\sigma(0^+) = 5 \sim 10\%$ and $\sigma(4^+)/\sigma(0^+) = 1 \sim 5\%$. They are too small compared with the experimental values: 20 ~ 40 % and ~ 5 % for 2^+ and 4^+ transitions, respectively. As is seen from Fig. 3, the CCBA calculations explain the experimental

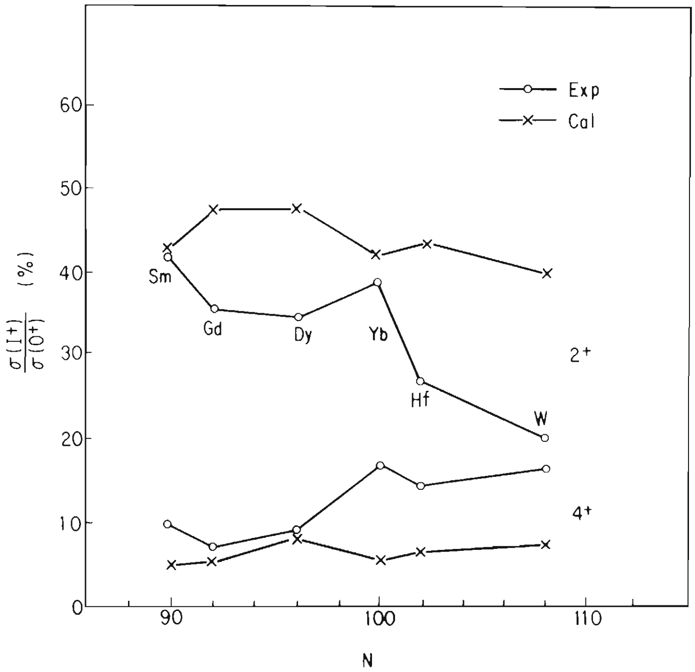

Fig. 3. The ratios $\sigma(2^+)/\sigma(0^+)$ and $\sigma(4^+)/\sigma(0^+)$ as a function of neutron number N.

values fairly well. It is due to increase of $\sigma(2^+)$ and $\sigma(4^+)$ which comes from the large contributions of indirect processes.

The optical parameters used in these calculations are preliminary ones and may not be most suitable. A parameter search is now in progress to get optimum values.

References

1) T. Takemasa, M. Sakagami, and M. Sano: Phys. Rev. Lett., 29 133 (1972).
2) T. Takemasa and H. Yoshida: Phys. Lett., 46B, 313 (1973); T. Takemasa: Nucl. Phys., A220, 31 (1974).
3) T. Tamura, D. R. Bes, R. A. Broglia, and S. Landsdowne: Phys. Rev. Lett., 25, 1507 (1970); ibid., 26, 156 (1971); R. J. Ascuitto, N. K. Glendenning, and B. Sϕrensen: Phys. Lett., 34B, 17 (1971); Nucl. Phys., A183, 60 (1972).
4) S. K. Penny and G. R. Satchler: Nucl. Phys., 53, 145 (1964).
5) R. J. Ascuitto and N. K. Glendenning: Phys. Rev., 181, 1396 (1969); ibid., C2, 415 (1970).
6) Y. Ishizaki: Proc. Phys. Soc. Japan, 26, 147 (1971); Y. Sugiyama, J. Kotame, T. Suehiro, Y. Saji, H. Ogata, A. Stricker, I. Nomaka, and Y. Ishizaki: J. Phys. Soc. Japan, 30, 602 (1973).

4-17. Folding Model for Nucleus-Nucleus Optical Potential

K. Kammuri and T. Wada

A nucleon-nucleus or alpha-nucleus elastic scattering has been described successfully by a folding model, in which an optical potential is approximated by a convolution of the target density with nucleon-nucleon or alpha-nucleon interaction.[1)-3)] Heavy-ion elastic scattering is usually treated by a simple optical potential with Woods-Saxon shape. The optical parameters show Igo's ambiguities.[4)] With the aim of dissolving such ambiguities, we applied the folding model to the heavy-ion scattering.

The real nuclear part of the optical potential is taken to be

$$V(r) = \int dr_1 \int dr_2 \rho_a(\vec{r}_1)\, v(\vec{r}_1\ \vec{r}_2')\, \rho_A(\vec{r}_2), \tag{1}$$

where ρ_a and ρ_A are the projectile and target total densities, respectively, and $v(r_1 - r_2')$ is an effective nucleon-nucleon interaction. Similarly the Coulomb part is given by

$$V_c(r) = \int dr_1 \int dr_2\ \rho_a^c(\vec{r}_1) \frac{1}{|\vec{r}_1 - \vec{r}_2'|} \rho_A(\vec{r}_2), \tag{2}$$

where ρ_c means a charge density. We assume that the imaginary part was proportional to the density overlap of two systems,

$$W(r) \equiv -\frac{2\pi\hbar^2}{M} W \int dr_1 \int dr_2\, \rho_a(r_1)\, \rho_A(r_1 - r). \tag{3}$$

The coordinate vectors are shown in Fig. 1.

The form factor for the collective inelastic excitation can be derived from the folding model. Assuming that only the even mass target system is excited vibrationally, its surface is expressed by

$$R = R_A\,(1 + \sum_{\lambda\mu} \alpha_{\lambda\mu} Y_{\lambda\mu}(\theta, \phi)). \tag{4}$$

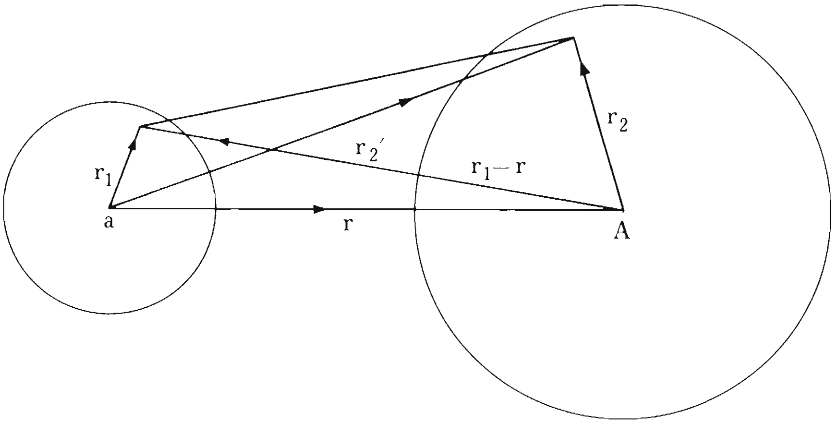

Fig. 1. Coordinate vectors.

By substituting Eqn. (4) into the density ρ_A (r, R), we obtain the coupling potential;

$$V_{coupl}(r) = \sum_{\lambda\mu} (\quad 1)^{\lambda \quad \mu} \alpha_{\lambda \quad \mu} Y^{*}_{\lambda\mu}(\theta,\phi) \, . \, v^{1)}_{cp,\lambda}(r) \tag{5}$$

where the complex form factor $v^{(1)}_{cp,\lambda}$ (r) is given by

$$v^{1)}_{cp,\lambda}(r) = 4\pi R_A \int r_2^2 dr_2 \left\{ \left[V^{(\lambda)}_{eff}(r_1 \, r_2) - i \frac{2\pi\hbar^2}{M} W \rho_a^{(\lambda)}(r_1 \, r_2) \right] \frac{d\rho_A(r_2, \ R_A)}{d R_A} + C^{(\lambda)}_{eff}(r_1 \, r_2) \frac{d\rho_A^{(}(r_2 + R_A)}{d R_A} \right\} \tag{6}$$

Here $V^{(\lambda)}_{eff}$ (r_1, r_2) is the λ-th multipole term of the effective projectile-target nucleon interaction;

$$V^{(\lambda)}_{eff}(r_1 \, r_2) = \frac{1}{2} \int_{-1}^{1} v_{eff}(r_2') \, P_\lambda \, (\cos \, \omega) \, d \, (\cos \, \omega), \tag{7}$$

where

$$v_{eff}(r_2') = \int \rho_a(\vec{r_1}) \, v(\vec{r_1} \quad \vec{r_2'}) d\vec{r_1}. \tag{8}$$

The Coulomb part $C^{(\lambda)}_{eff}$ (r_1, r_2) was defined in the same way, and $\rho^{(\lambda)}_a$ is given by Eqn. (7) by replacing $v_{eff}(r_2')$ by $\rho_a(r_2')$.

Here we report some results of analyses of the elastic scattering of high energy ^{14}N. An

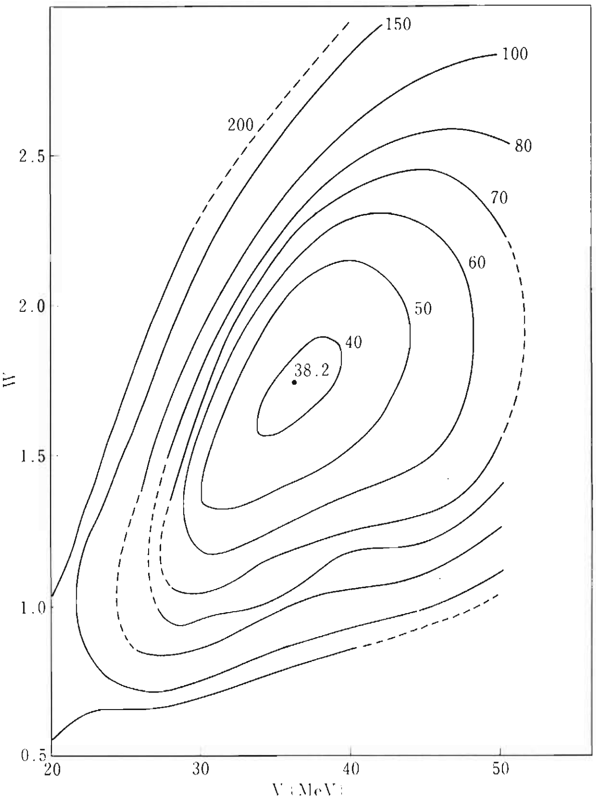

Fig. 2. Contour map of χ^2 for the elastic scattering of 84 MeV ^{14}N on ^{27}Al. Gaussian force with 1.22 fm range was used.

ordinary optical model analysis was reported by Kohno et al.$^{5)}$ The contour map of χ^2 defined by

$$\chi^2 = \frac{1}{N}\sum_{i=1}^{N} \left[(\sigma_{calc}(\theta_i) - \sigma_{exp}(\theta_i))/\Delta\sigma_{exp}(\theta)\right]^2, \tag{9}$$

is shown in Fig. 2 for the scattering of 84 MeV ^{14}N on ^{27}Al. The two-body interaction was taken to be a Gaussian shape with the range μ = 1.22 fm. We can see that there is only one minimum point in this map. By taking the shape to be Gaussian (μ = 1.5 fm), Yukawa (μ = 1.0 fm), or delta function, we have searched optimum values of two parameters, the strength V of the two-body force and the imaginary strength W by use of "SEARCH" code written by one of us.$^{6)}$ Shapes and parameters of the density distributions were taken from the results of electron scattering,$^{7)}$

$$\sigma(r) = \rho_0\left(1+\frac{wr^2}{R^2}\right)\begin{cases}\left[1+\exp\left(\frac{r-R}{a}\right)\right]^{-1} & (10\text{a})\\ \exp\left(-\frac{wr^2}{\alpha R^2}\right), & (10\text{b})\end{cases}$$

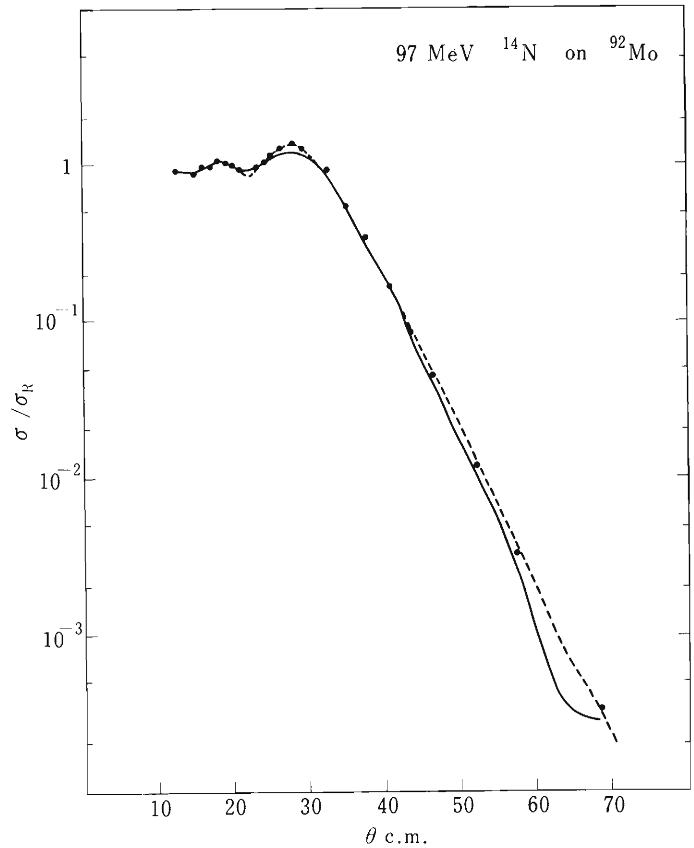

Fig. 3. Optical model analysis of the elastic scattering of 97 MeV ^{14}N on ^{92}Mo. Solid line is the folding model prediction. Dotted line is a curve calculated by use of the ordinary optical potential with parameters; V = 100 MeV, W = 25 MeV, r_0 = 1.13 fm, r_C = 1.2 fm, and a = 0.5 fm.

Table 1. Folding model parameters for the elastic scattering of ^{14}N.
(Projectile density is given by [1.03, 1.67])

	E	Target	Gaussisn (1.5 fm)		Yukawa (1.0 fm)		δ-force	
	(MeV)	density	V	W	V	W	V	W
			(MeV)	(MeV)	(MeV)	(MeV)	(MeV)	(MeV)
$^{14}N + ^{12}C$	65	[1.057, 1.33]	18.28	4.73	15.92	5.00	4.93	1.00
$^{14}N + ^{27}Al$	65	[1.02, 0.52, 0.0]	10.81	1.39	7.87	0.87	3.39	1.66
$^{14}N + ^{27}Al$	84	[1.02, 0.52, 0.0]	14.35	1.86	14.27	2.08	3.03	1.51
$^{14}N + ^{28}Si$	84	[1.02, 0.52, 0.0]	14.59	2.09	13.67	2.00	4.58	2.67
$^{14}N + ^{58}Ni$	84	[1.124, 0.5, −0.185]	8.94	0.62	7.78	0.58	2.47	0.41
$^{14}N + ^{92}Mo$	97	[1.073, 0.52, 0.0]	10.50	1.44	8.62	1.10	2.49	1.04

where $W = 3\alpha(2 + 5\alpha) / 2(2 + 3\alpha)$. In Table 1, the density parameters are denoted by $[r_0, a, w]$ for Eqn. (10a), or by $[r_0, \alpha]$ for Eqn. (10b). It should be noted that the strengths V given by other sources such as (p, p') are around 20 MeV for the Gaussian force ($\mu = 1.5$ fm) and 30 MeV for the Yukawa force ($\mu = 1.0$ fm).[8] Finally in Fig. 3, experimental angular distribution for the case of the elastic scattering of 97 MeV ^{14}N on ^{92}Mo is compared with the predictions of the folding model and ordinary optical model.[9]

References

1) G. W. Greenless, G. J. Pyle, and Y. C. Tang: Phys. Rev., 171, 1115 (1968).
2) P. Mailandt, J. S. Lilley, and G. W. Greenless: ibid., C8, 2189 (1973).
3) B. Tatischeff and I. Brissaud: Nucl. Phys., A155, 89 (1970).
4) G. Igo: Phys. Rev. Lett., 1, 72 (1958).
5) I. Kohno, S. Nakajima, T. Tonuma, and M. Odera: J. Phys. Soc. Japan, 30, 910 (1971).
6) T. Wada: Reports I.P.C.R.(in Japanese), 46, 21 (1970).
7) J. P. Vary and C. B. Dover: Phys. Rev. Lett., 31, 1510 (1973).
8) S. M. Austin: "The Two-Body Force in Nuclei", Plenum Press, N. Y. London, p. 285 (1972).
9) I. Kohno: Private communication.

4-18. Role of the ^{12}C-Core Exchange in the ^{16}O-^{12}C Elastic Scattering

H. Yoshida

The elastic scattering of two heavy ions which have identical cores with few nucleons outside of one of the cores generally shows the backward rise in the angular distribution. This backward rise of the angular distribution can be understood reasonably well as the transfer process of the outer nucleons superposed on the shape elastic process.$^{1)-8)}$ The reactions considered here are the following processes:

$$\underset{a}{(B+X)} + A \rightarrow \begin{cases} A + \underset{a}{(B+X)} \cdots\cdots\cdots\cdots\cdots\cdots\cdots\cdots \text{(D)} \\ B + \underset{b}{(A+X)} \cdots\cdots\cdots\cdots\cdots\cdots\cdots\cdots \text{(E)} \end{cases}$$

Reaction (D) is a direct shape elastic process and reaction (E), where the identical cores A and B are exchanged, is a transfer process of the cluster X. To take account of the both processes simultaneously, the total wave function Ψ properly antisymmetrized with respect to the interchange of the identical cores A and B was used:

$$\Psi = \chi(r_a)|aA\rangle + (-)^A \chi(r_b)|bB\rangle \ . \tag{1}$$

Here the function $\chi(r_a)$ describes the relative motion of the colliding particles a and A, and $|aA\rangle$ describes the intrinsic states of the two particles. The equation for the L-th partial wave of χ (r_b) is obtained from the total Hamiltonian as follows:

$$\left[\frac{\hbar^2}{2\mu}\left(\frac{d^2}{dr_b^2} - \frac{L(L+1)}{r_b^2}\right) + E_b - U_b(r_b)\right] \chi_L(r_b) \\ = (-)^A JN \int_0^\infty dr_a \, \chi_L(r_a) K_L(r_b, r_a) \ . \tag{2}$$

Here

$$K_L(r_b, r_a) = \left\{-\frac{\hbar^2}{2\mu}\left(\frac{d^2}{dr_b^2} - \frac{L(L+1)}{r_b^2}\right) + U_b(r_b) - E_b\right\} K_L^{(1)}(r_b, r_a) \\ + K_L^{(2)}(r_b, r_a), \tag{3a}$$

$$\begin{pmatrix} K_L^{(1)}(r_b, r_a) \\ K_L^{(2)}(r_b, r_a) \end{pmatrix} = r_a r_b \sum_{\tilde{N}\tilde{L}} \frac{S_{\tilde{N}\tilde{L}}(a \rightarrow B+X)}{2\tilde{L}+1} \int d\hat{r}_a \; Y_{LM}(\hat{r}_a) \int d\hat{r}_b \; Y^*_{LM}(\hat{r}_b) \\ \times \sum_M \Psi^*_{\tilde{N}\tilde{L}M}(r_{XA}) \; \Psi_{\tilde{N}\tilde{L}M}(r_{XB}) \begin{pmatrix} 1 \\ V_{XB}(r_{XB}) + V_{AB}(r_{AB}) - U_b(r_b) \end{pmatrix}. \tag{3b}$$

Table 1. Dependence of the calculated cross sections on the normalization constant N which can be regarded as the coupling strength of the transfer channel.

$\theta_{c.m.}$ \ N	1.0	1.5	2.0	2.5	
166°	0.58	0.56	0.56	0.55	E_L = 65 MeV
146°	0.25	0.22	0.20	0.20	
172°	2.21	2.34	2.25	2.06	E_L = 24 MeV
156°	2.01	1.67	1.45	1.29	

$\sigma_{cal}(\theta)/N^2$ (mb/str.)

are not large for incident energies above the Coulomb barrier, showing that the effect is not very important.$^{4)-5)}$ In fact, we can see from Table 1 that the calculated cross sections at E_L=65 MeV increase roughly with N^2 near the shell model limit (N=1.0) in consistence with the DWBA prediction. But the cross section at the second peak $\theta_{c.m.}$=156° of E_L=24 MeV shows a deviation from the N^2-dependence. The multistep transfer process plays a role in this case.

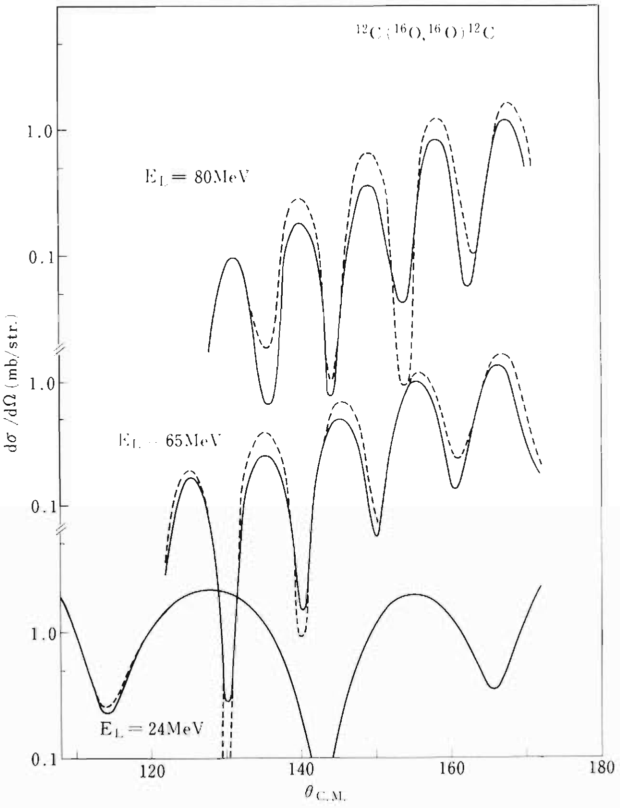

Fig. 2. Comparison of the results calculated by the local approximation (dashed lines) with those of exact calculations (solid line).

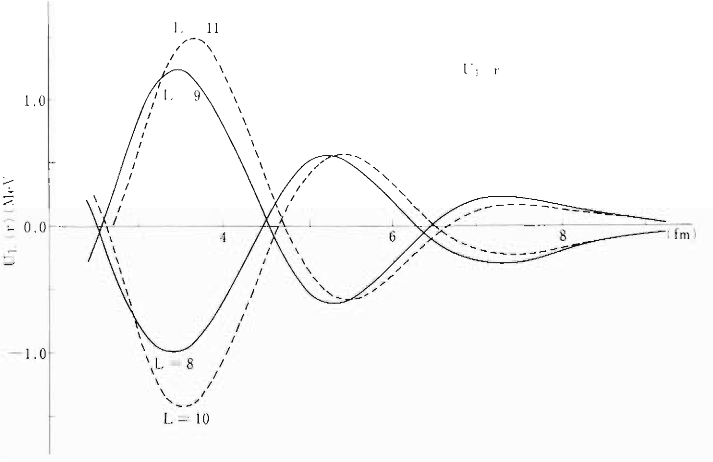

Fig. 3. The local approximation potential $U_L(r_b)$ for several L-values. The non-orthogonality term $K_L^{(1)}(r_b, r_a)$ is not included here.

The normalization constant N is introduced to the r.h.s. of Eqn. (2) so that the calculated values of the cross section may reproduce the experimental values at backward angles and J is the Jacobian of the transformation to the coordinate r_a. The spectroscopic factor $S_{\tilde{N}\tilde{L}}$ in Eqn. (3b) is calculated by assuming the configurations $p^{12}[444]\,{}^{11}S$ and $p^8[44]\,{}^{11}S$ for ^{16}O and ^{12}C states respectively. Eqn. (2) is solved numerically obtaining the angular distributions. The solution includes the multistep transfer process. The results are compared with those of DWBA to see the multistep transfer effect. As shown in Fig. 1, the differences from the DWBA results

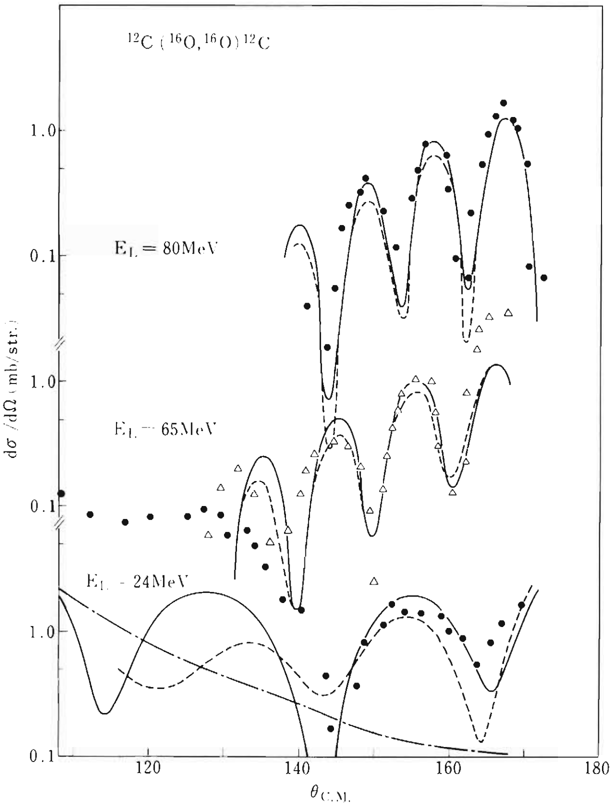

Fig. 1. Comparison of the present calculations (solid lines) with those of DWBA (dashed lines). The angular distribution obtained by use of the optical potential $U_b(r_b)$ only is drawn by a solid and dotted line at E_L = 24 MeV in order to show the importance of the interference with the DWBA amplitude. Parameter values of the optical potential are V = 30 MeV, W = 10 MeV, a_R = 0.8 fm, a_I = 0.45 fm, r_R = 1.2 (E_L = 24 MeV), 1.13 fm (E_L = 65 and 80 MeV) and r_I = 1.15 fm. The normalization constant is N = 1.0 for E_L = 24 MeV and N = 1.5 for E_L = 65 and 80 MeV.

At low energies, the r.h.s. of Eqn.(2) can be approximated by $U_L(r_b)\chi_L(r_b)$ where the local approximation potential $U_L(r_b)$ is given by

$$U_L(r_b) = (-)^A JN \int_0^\infty dr_a \, K_L(r_b, r_a), \tag{4}$$

since the partial wave $\chi_L(r_a)$ changes more slowly than the kernel $K_L(r_b, r_a)$. In fact, angular distributions calculated using the above approximation are similar to those obtained by the exact calculations at low energies (Fig. 2). The potential $U_L(r_b)$ shows the parity dependence$^{2)}$ as shown in Fig. 3. The potential is very much affected by the presence of the non-orthogonality term $K_L^{(1)}(r_b, r_a)$ in Eqn. (3) especially for lower partial waves and in nuclear interior regions. But the calculated angular distributions remain unchanged whether the non-orthogonality term is included or not (Fig. 4).

All the calculations have been performed so far by assuming the α-cluster transfer with a spectroscopic factor of S_{20} ($^{16}O \rightarrow {}^{12}C + \alpha$) = 0.296 obtained from configurations p^{12} [444] and p^8 [44] for ^{16}O and ^{12}C states respectively. The above choice of the configurations, however, predicts the existence of the α*-clusters in nuclei. Preliminary calculations show that the α*-clusters does not affect the angular distributions at low energies but at high energies the angular distributions are shifted to the backward angles. A further study on the effect of the

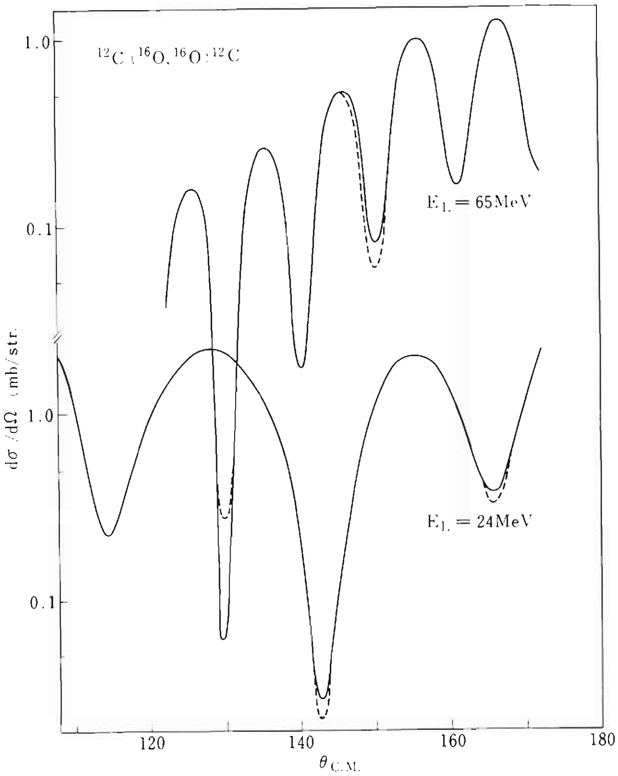

Fig. 4. The effect of the non-orthogonality term on the angular distributions. The results calculated with and without the non-orthogonality term are shown by the solid and dashed lines respectively.

α^*-clusters is now in progress.

References

1) A Gobbi, U. Matter, J,-L. Perrenoud, and P. Marmier: Nucl. Phys., A112, 537 (1968).

2) W. von Oertzen: ibid., A148, 529 (1970); W. von Oertzen and W. Nörenberg: ibid., A207, 113 (1973); H. G. Bohlen and W. von Oertzen: Phys. Lett., 37B, 451 (1971).

3) C. K. Gelbke, R. Bock, P. Braun-Munzinger, D. Fick, K. D. Hildenbrand, A. Richter, and W. Weiss: Phys. Rev. Lett., 29, 1683 (1972); K. D. Hildenbrand, R. Bock. H. G. Bohlen, P. Braun-Munzinger, D. Fick, C. K. Gelbke, W. von Oertzen, and W. Weise: Phys. Lett., 42B, 425 (1972); C.K. Gelbke, R. Bock, P. Braun-Munzinger, D. Fick, K. D. Hildenbrand, W. Weiss, and S. Wenneis: ibid., 43B, 284 (1973).

4) C. A. Mcmahan and W. Tobocman: Nucl. Phys., A202, 561 (1973).

5) G. Baur and C. K. Gelbke; ibid., A204, 138 (1973).

6) B. Imanishi: Preprint and private communications.

7) C. K. Gelbke, G. Baur, R. Bock, P. Braun-Munzinger, W. Grochulski, H. L. Harney, and R. Stock: Nucl. Phys., A219, 253 (1974).

8) G. Baur and H. H. Wolter: Phys. Lett., 51B, 205 (1974).

5. NUCLEAR PHYSICS

Nuclear Spectroscopy

5-1. Lifetime Measurement of the 6^+ (2976 keV) State in ^{46}Ca and E2 Effective Charges in $(1f_{7/2})^{\pm 2}$ Nuclei

W. Kutschera, G. D. Sprouse, H. Ikezoe,
Y. Yamazaki, and T. Nomura

The mean lifetime of the first excited 6^+ state in ^{46}Ca has been measured with the pulsed beam method to be $\tau_m = 15.2 \pm 0.8$ ns. The state was populated via the reaction $^{48}\mathrm{Ca}(\alpha, \alpha 2n)^{46}\mathrm{Ca}$ with 50 MeV α particles from the cyclotron. Electronic timing was performed between the natural beam bursts of the cyclotron and γ-rays observed with a Ge(Li) detector. Experimental details are described in Ref. 1.

Table 1 summarizes the present experimental information[1] on E2-decay properties of the 2^+, 4^+, and 6^+ states in $(1f_{7/2})^{\pm 2}$ nuclei. The last column gives the additional charges $\delta e = e_{\mathrm{eff}} - 1$ for protons and $\delta e = e_{\mathrm{eff}}$ for neutrons. The effective charges have been extracted from the relation:

$$e_{\mathrm{eff}} = \left(B(E2)_{\mathrm{exp}}/B(E2)_{\mathrm{theo}}\right)^{1/2}$$

Here, the theoretical B(E2) values have been calculated with pure $(1f_{7/2})^{\pm 2}$ configurations and harmonic oscillator wave functions.

The strong state dependence of the effective charges for ^{42}Ca and ^{42}Ti indicates large admixtures of other configurations in the 2^+ and 4^+ states of these nuclei. On the other hand, the $6^+ \rightarrow 4^+$ transitions in ^{42}Ca and ^{46}Ca are rather close to each other. Using the more refined wave functions of Ogawa,[2] who considers $(p_{3/2}f_{7/2})^2$ and $(p_{3/2}f_{7/2})^6$ configurations, one obtains a remarkable constant value of the neutron effective charge for the $6^+ \rightarrow 4^+$ transitions in ^{42}Ca and ^{46}Ca: $e_{\mathrm{eff}}(6^+ \rightarrow 4^+, {}^{42}\mathrm{Ca}) = 0.69 \pm 0.01$ e and $e_{\mathrm{eff}}(6^+ \rightarrow 4^+, {}^{46}\mathrm{Ca}) = 0.68 \pm 0.02$ e. These values should be close to the neutron core polarization charge in this mass region. It is interesting to note that this value is close to the macroscopic estimate of Bohr and Mottelson:[3]

$$e_{\mathrm{pol}}(\mathrm{neutron}) = (Z/A + 0.29)\ e = 0.72\ e.$$

The three proton nuclei ^{42}Ti, ^{50}Ti, and ^{54}Fe are difficult to compare with each other, since i) ^{42}Ti shows an exceptionally low effective charge for the $6^+ \rightarrow 4^+$ transition, and ii) the extraction of a reliable proton charge for the N = 28 isotones involves the more complex excitation of both protons and neutrons to other f-p orbitals in order to obtain wave functions of good isospin.

Table 1. E2-decay properties of 2^+, 4^+, and 6^+ states in $(1f_{7/2})^{\pm 2}$ Nuclei.

Nucleus	Main configuration	Transition	E_γ (keV)	τ_m [a] (ps)	B (E2) (e^2 fm^4)	δe [b] (e)
${}^{42}_{20}Ca_{22}$	$(\nu f_{7/2})^2$	$2^+ \rightarrow 0^+$	1524	1.19 ± 0.04	83.4 ± 2.8	2.09 ± 0.02
		$4^+ \rightarrow 2^+$	1227	4.5 ± 0.5	65 ± 7	1.85 ± 0.10
		$6^+ \rightarrow 4^+$	439	7.79 ± 0.13 ns	6.42 ± 0.11	0.86 ± 0.01
${}^{46}_{20}Ca_{26}$	$(\nu f_{7/2})^{-2}$	$2^+ \rightarrow 0^+$	1346	5.24 ± 0.54	35.1 ± 3.6	1.32 ± 0.07
				>8	<23	<1.1
		$4^+ \rightarrow 2^+$	1231	not measured		
		$6^+ \rightarrow 4^+$	399	15.2 ± 0.8 ns	5.31 ± 0.28	0.76 ± 0.02
${}^{42}_{22}Ti_{20}$	$(\pi f_{7/2})^2$	$2^+ \rightarrow 0^+$	1555	0.60 ± 0.10	150 ± 25	1.8 ± 0.3
		$(4^+) \rightarrow 2^+$	1121	>1.8	<230	<2.5
		$(6^+) \rightarrow (4^+)$	366	26 ± 5 ns	4.7 ± 0.9	−0.26 ± 0.07
${}^{50}_{22}Ti_{28}$	$(\pi f_{7/2})^2$	$2^+ \rightarrow 0^+$	1554	1.4 ± 0.2	66 ± 8	0.76 ± 0.11
		$4^+ \rightarrow 2^+$	1121	7.7 ± 1.5	60 ± 12	0.68 ± 0.17
		$6^+ \rightarrow 4^+$	524	0.61 ± 0.02 ns	33.8 ± 1.2	0.87 ± 0.04
${}^{54}_{26}Fe_{28}$	$(\pi f_{7/2})^{-2}$	$2^+ \rightarrow 0^+$	1408	1.38 ± 0.10	107 ± 8	1.18 ± 0.08
		$4^+ \rightarrow 2^+$	1131	5.7 ± 1.2	77 ± 16	0.85 ± 0.19
		$6^+ \rightarrow 4^+$	409	1.75 ± 0.03 ns	40.7 ± 0.7	1.00 ± 0.02

a) Averages of the values taken from various experiments.

b) $\delta e = e_{eff} - 1$ for protons and $\delta e = e_{eff}$ for neutrons.

References

1) W. Kutschera, G. D. Sprouse, H. Ikezoe, Y. Yamazaki, and T. Nomura: Phys. Rev. Lett. (in press).

2) K. Ogawa: Private communication.

3) A. Bohr and B. Mottelson: Nuclear Structure, Benjamin, New York, Vol. II Chapt. 6

5-2. High-Spin State Yields in ^{88}Y Relative to 1^+ State in ^{90}Nb Excited via ^{89}Y + α Reaction

A. Hashizume, Y. Tendow, T. Katou, and H. Kumagai

A natural yttrium target was bombarded with α-particles and the 382 keV (1^+) state in ^{90}Nb was excited via the ^{89}Y(α, 3n) reaction. In these experiments, the beam from Cyclotron was passed through a mechanical beam chopper and, using a pulsed beam technique, the half-life of the 382 keV state was determined to be 6.19 ± 0.08 ms.[1)]

During the course of the study, in the delayed γ-ray spectra, there were observed two 232 and 443 keV γ-rays, both decaying with a half-life of 14 ms (Fig. 1). These γ-rays were attributed to the cascade transitions from the 687 keV state to the ground state through the 231 keV (5^-) state in ^{88}Y.[2)] Figure 2 shows the relative excitation functions of those γ-rays together with the 258 keV γ-ray emitted from the above mentioned ^{90m}Nb. Because the Q value of ^{89}Y(α, αn)^{88}Y is lower than that of ^{89}Y(α, 3n)^{90}Nb, the isomer ^{88m}Y was conjectured to be

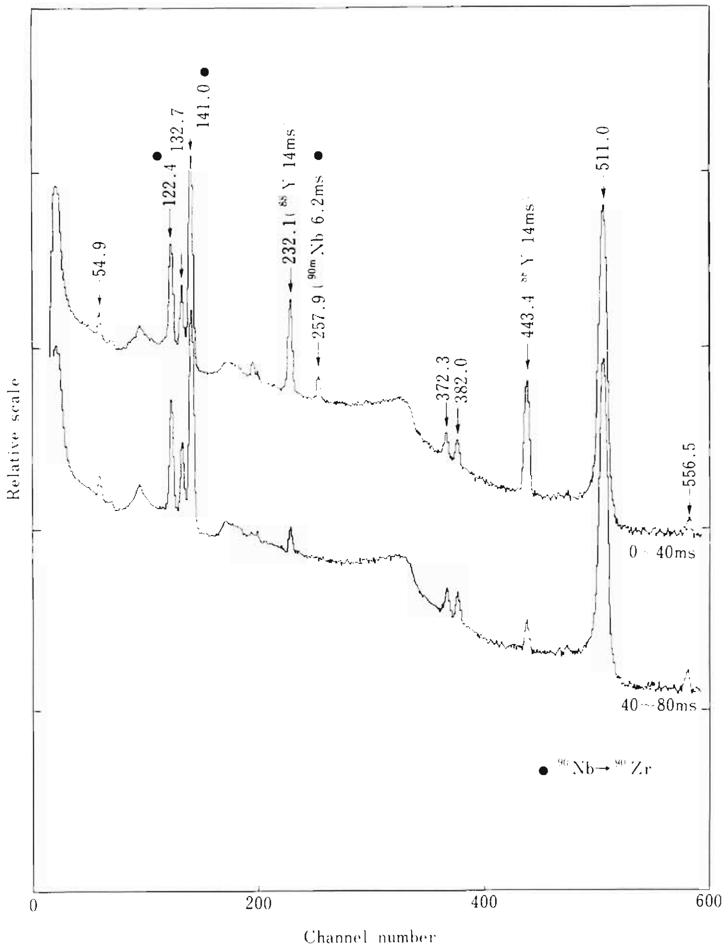

Fig. 1. Delayed γ-ray spectra observed by bombarding α-particles on ^{89}Y.

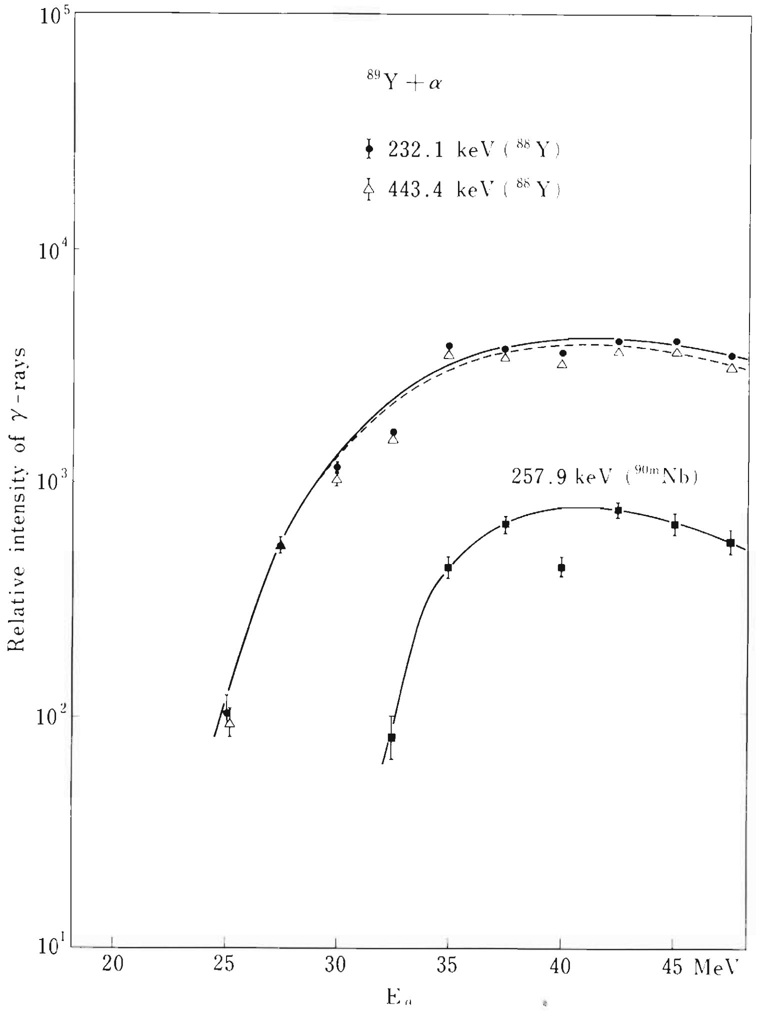

Fig. 2. Relative excitation functions taken by 257.4 keV γ-rays in ^{90}Nb, and by 232.1 and 443.0 keV in ^{88}Y.

produced by the former. The yield ratios Y(α, αn: 687 keV)/Y(α, 3n: 382 keV) were found as shown in Table 1. Corrections were made for half-lives and for conversion coefficients of γ-rays assuming 257.9 keV and 443 keV as E3 and 231 keV as M1. Because the spin and parity of the 382.1 keV state is 1+ and the 687 keV state is considered to be 8+, such a large yield of the metastable state in ^{88m}Y will be partly explained by its high spin, as the change of angular momentum from the compound nucleus is smaller than the transition to the state in ^{90m}Nb and this small change of angular momentum facilitates to feed the state in ^{88m}Y.

Table 1. Yield ratios of the 687 keV (8^+) state in ^{88}Y to the 382 keV (1^+) state in ^{90}Nb.

Energy (MeV)	32.5	35.0	37.5	40.0	42.5	45.0	47.5
Y(^{88m}Y)/Y(^{90m}Nb)	11	5.1	3.3	(4.6)	3.0	3.5	3.5

References

1) A. Hashizume, H. Kumagai, Y. Tendow, and T. Katou: Nucl. Instr. and Meth., 119, 209 (1974).

2) A. M. Morozov and V. V. Ramaev: Soviet Phys. JETP, 16, 314 (1963).

5-3. Short Life Radioisotopes and Isomers Observed via Ir + C Reactions

A. Hashizume, Y. Tendow, T. Katou, and H. Kumagai

In the region of nuclei whose mass numbers lie between about 190 and 210, many isomeric states have been found because high spin orbitals such as $h_{11/2}$ and $i_{13/2}$ are concerned with those states. With the aid of a beam bunching technique reported previously,[1),2)] the radioisotopes and/or isomers of the half-lives in the ms region produced by the reaction ^{191}Ir + C and ^{193}Ir + C were studied.

Powders of natural Ir and isotopically enriched ^{191}Ir were used as targets. A 50 cm^3 Ge(Li) and a pure Ge detectors with high resolution (600 eV at 122 keV) were employed for the detection of γ-rays. These detectors were placed at 90° to the direction of incident beams. Gamma-ray spectra in the delay-time range from about 1 ms to 1000 ms after the irradiation were studied as well as long lived residual activities. The excitation functions for γ-rays from Ir + C reactions with incident beam energies from 65 to 95 MeV were also examined.

Figure 1 shows the γ-ray spectra produced by the bombardment with C (95 MeV) on Ir and ^{191}Ir. In the case presented in this figure, the targets were bombarded for about 60 ms, and after 50 ms from the end of irradiation γ-ray spectra were taken by 4 (times) × 1024 (energies) channels for 800 ms. The irradiation was restarted after 100 ms delay from the end of the γ-ray measurements, and the same procedures were repeated. At a bombarding energy of 95 MeV, the (C, 5n) reaction was predominant and intense γ-rays emitted in the ground state decay of ^{200}Bi to ^{200}Pb together with de-exciting 428.2 keV γ-ray from the isomeric state in ^{200}Bi ($T_{1/2}$ = 0.4 s)[3)] were observed. Owing to the ^{191}Ir (C, 5n) reaction, a 248.5 keV isomeric transition ($T_{1/2}$ = 7.7 s) in ^{198}Bi was also confirmed. The peaks corresponding to 197.6 and 317.9 keV are due to the ground state decay of ^{198}Bi to ^{198}Pb. According to the preliminary measurements, the half-lives of 222.6 and 385.8 keV γ-rays were about 1 s. As the isomer at 609.3 keV in ^{197}Tl emits 222.5 and 386.7 keV γ-rays, these delayed γ-rays would be attributed to these transitions and the relative excitation curves for the (C, 5n) reaction shown in Fig. 2 are not qualitatively contradictory to the (C, α 2n) reaction. However, there are some discrepancies on the value of γ-ray energy and the half-life. Further, if the metastable state is excited through the ^{191}Ir (C, α 2n) ^{197}Tl reaction, there should be comparable feeds to the 748.5 keV ($T_{1/2}$ = 28.7 ms) state in ^{199}Tl through the ^{193}Ir (C, α 2n) ^{199}Tl reaction. We could not find any γ-rays corresponding to the de-exciting transitions from the isomer decaying with such a half-life. Further investigations is in progress comparing the Ir + C with Re + N and Ir + B reaction to reveal the true origin of the two γ-rays and to establish the quantitative relations between isomers and isotopes produced in the ^{191,193}Ir + C reactions.

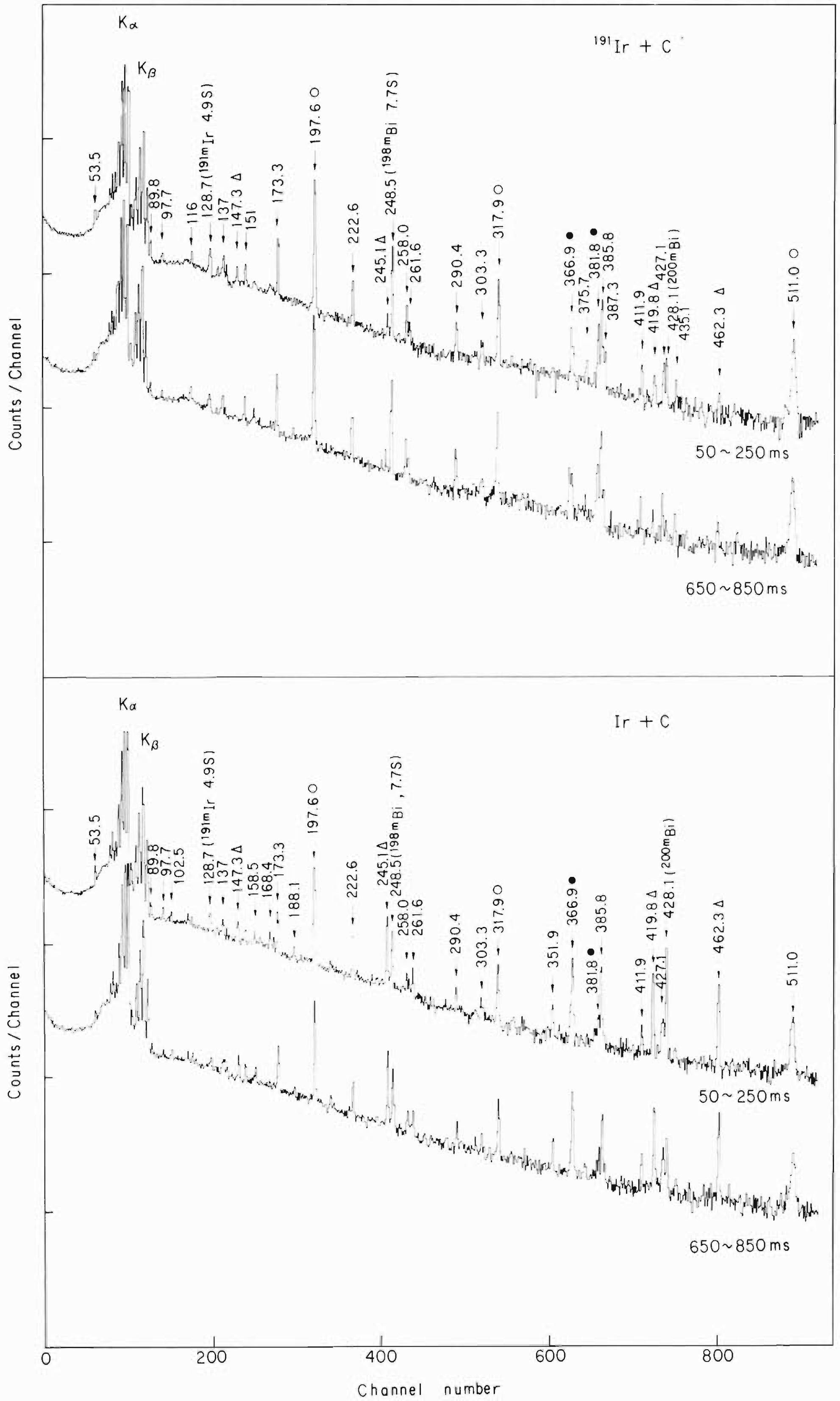

Fig. 1. The γ-ray spectra from RI and isomers produced by ^{191}Ir + C and ^{nat}Ir + C reactions measured with a pure germanium detector. Energy values and assignment for γ-rays are given above the spectra with ^{198}Bi → ^{198}Pb (○), ^{199}Pb → ^{199}Tl (●), ^{200}Bi → ^{200}Pb (△). The ordinate is arbitrary scale.

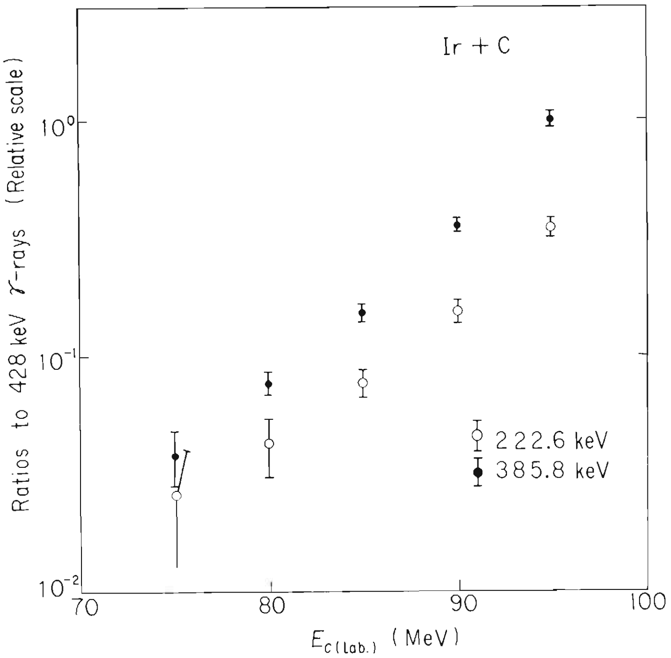

Fig. 2. Excitation curves for 222.6 and 385.8 keV γ-rays relative to 428.1 keV (^{200m}Bi) γ-ray.

References

1) A. Hashizume, Y. Tendow, T. Katou, and H. Kumagai: IPCR Cyclotron Prog. Rep., 7, 79 (1973).

2) A. Hashizume, H. Kumagai, Y. Tendow, and T. Katou: Nucl. Instr. and Methods, 119, 209 (1974).

3) U. Hagemann, K. H. Kaun, W. Neubert, W. Schulz, and F. Stary: Nucl. Phys., A197, 111 (1972).

5-4. Monopole Effective Charges

T. Suzuki

Much has been written on the importance of electric and magnetic core-polarization phenomena in nucleus.[1] In particular, the effects of electric quadrupole and magnetic dipole polarizations are extensively studied. The former is illustrated by the electric quadrupole moments and transition probabilities associated with the single-neutron configuration,[1,2] while the latter is recognized from the deviation of the observed magnetic moments from the Schmidt values.[1,3] Their effects are usually expressed in terms of a renormalization of the charge or spin g-factor of the valence-nucleons, that is, a quadrupole "effective charge" or an "effective g_S-factor".[1]

On the other hand, the change in the charge radius of a nucleus induced by the addition of another neutron is systematically observed throughout the periodic table, as is well known as isotope shift.[1,4] This phenomenon is interpreted to be due to a monopole core-polarization effect, which may be expressed in terms of a monopole effective charge.[5]

The core-polarization charges can be estimated in terms of the coupling of an extra particle with the collective vibrations of the core. A large part of the electric quadrupole polarization charge (the polarization g_S-factor) is considered as coming from the virtual excitation of the electric quadrupole state (the magnetic dipole state) of the core whose excitation strength exhausts a large fraction of the classical energy-weighted sum rule value.[1-3,6] Indeed, recently, such collective states have been observed in the continuum region through electron and hadron scatterings.[7] The existence of a collective monopole state, which carries most of the classical energy-weighted sum rule value, is also expected in a nucleus as pointed out by many authors.[5,8]

We have studied monopole effective charges, which are interpreted as resulting from the virtual excitation of such a collective state in the core. The eigenfrequency of the monopole vibration and the interaction Hamiltonian between a particle and the vibration are obtained by making use of various sum rules.[9] The isoscalar and isovector monopole polarization charges are estimated to be 0.125e and $0.0645e\tau_3$, respectively. Isotope and isotone shifts calculated by employing these effective charges are in good agreement with experimental results. A large part of the Nolen-Schiffer anomaly can be also explained in terms of the isovector monopole polarization charge.

References

1) A. Bohr and B. R. Mottelson: "Nuclear Structure", Benjamin, New York, 1 (1969).

2) H. Horie and A. Arima: Phys. Rev., 99, 778 (1955); S. Fallieros and R. A. Ferrell: ibid.,

116, 660 (1959).

3) R. J. Blin-Stoyle: Proc. Phys. Soc., A66, 1158 (1953); A. Arima and H. Horie: Progr. Theor. Phys., 11, 509 (1954).

4) L. R. B. Elton: "Nuclear Sizes", Oxford University Press, Oxford, (1961); Y. N. Kim: "Mesic Atoms and Nuclear Structure", North-Holland, Amsterdam (1971).

5) R. W. Sharp and L. Zamick: Nucl. Phys., A208, 130 (1973); T. Suzuki: Preprint.

6) T. Suzuki: Phys. Rev., C8, 2111 (1973).

7) R. Pitthan and Th. Walcher: Phys. Lett., 36B, 563 (1971); S. Fukuda and Y. Torizuka: Phys. Rev. Lett., 29, 1109 (1972); M. Nagao and Y. Torizuka: ibid., 30, 1068 (1973); M. B. Lewis and F. E. Bertrand: Nucl. Phys., A196, 337 (1972); Y. Torizuka: Proc. Intern. Conf. Nucl. Structure Studies Using Electron Scattering and Photoreaction, Sendai (1972); E. Spamer: ibid.; L. W. Fagg: Proc. Intern. Conf. Photonuclear Reaction and Application, Asilomar (1973); Y. Torizuka: ibid.; M. B. Lewis: ibid.; Th. Walcher: Proc. Intern. Conf. Nucl. Phys., Munich (1973).

8) J. Blomqvist: Nucl. Phys., A103, 644 (1967); J. Damgaard, V. V. Gortchakov, G. M. Vagradov, and A. Molinari: Nucl. Phys., A121, 625 (1968); L. Zamick: Phys. Lett., 31B, 160 (1970); N. Auerbach: Nucl. Phys., A182, 247 (1972); R. W. Sharp and L. Zamick: ibid., A223 331 (1974).

9) T. Suzuki and C. Hinohara: Phys. Rev., C9, 1186 (1974); T. Suzuki: Nucl. Phys., A220, 569 (1974).

6. NUCLEAR INSTRUMENTATION

6-1. Performance of the IPCR Polarized Ion-Source

S. Motonaga, T. Fujisawa, M. Hemmi, H. Takebe
K. Ikegami, and Y. Yamazaki

A polarized ion-source was successfully operated on the test bench and is now being installed in a cyclotron. The performance of the polarized ion-source was described.

(1) General description

The general design and overall components of the IPCR polarized ion source were described in previous reports.$^{1)}$ The source is based on the atomic beam principle. Radio frequency transitions followed by strong field ionization are used to produce a maximum obtainable nuclear polarization. General arrangement of the source is shown in Fig. 1 schematically. The hydrogen or deuterium molecules are dissociated in a pylex bottle by an rf discharge at a frequency of 20 MHz. The power dissipated in the discharge is 250 W. The pylex bottle is cooled by air blast. Dissociated atoms diffuse through a single nozzle of inside-diameter of 3.5 mm and length of 10 mm into a sextupole magnet. The electron spin states of the atoms are separated in the field of sextupole magnet having a tapered aperture from 6.5 to 13.0 mm along its axis of 35 cm and producing a maximum field strength of 7.2 k gauss at pole tip radius. The atomic beam polarized with respect to the electron spin is subjected to a high-frequency electromagnetic field which induces transition by adiabatic passage$^{2)}$ and then ionized by electron impact in the strong magnetic field.

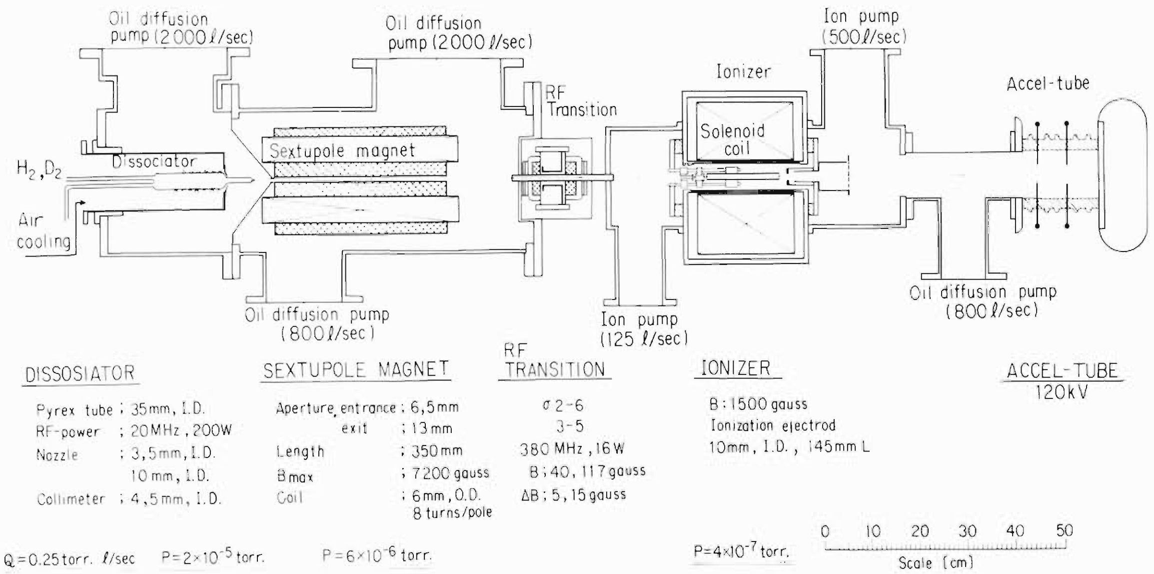

Fig. 1. General arrangement of the polarized ion source.

Two medium field transitions are used enabling different nuclear polarization states to be selected in a simple manner. For deuterium both transitions of 3 to 5 and 2 to 6 are available at a frequency of 380 MHz, with static fields at 40 and 120 gauss, respectively. These transitions are done separately to obtain tensor polarization of $P_{ZZ} = -1$ (3 to 5) and $P_{ZZ} = +1$ (2 to 6). Best measured neutron anisotropies N (0°)/N (90°) from the T (d, n) ^{4}He reaction are 0.657 and 1.418 corresponding to $P_{ZZ} = +0.516$ and -0.562.

(2) Measurement

The intensity of the atomic beam at the entrance to the ionizer was 3×10^{15} atoms/cm$^2\cdot$ sec measured by means of the compression tube method using an ionization gauge. Pictures on MoO_3 targets placed at about 35 cm apart from the exit of the sextupole magnet showed focusing and separating effects for the electron spin states.

The efficiency of ionization of the ionizer was observed by adding hydrogen gas into the ionizing chamber and measurering the increase in the extracted ion beam current. The efficiency was 4×10^{-3}. Although this is not equal to the efficiency of ionizing an atomic beam because the mean velocity of the atoms is higher than in the present measurement, it can be used for comparative measurement.

The emittance of beam extracted from the ionizer was not measured. However, divergence of ion beam seems to be not so large. The beam spot at a distance of 60 cm from the extraction electrode in the ionizer was found less than 40 mm in diameter.

The ion beam intensity of 1 μA was observed on optimum operation as the difference of the currents at the end of the accelerating tube when the sextupole magnet was turned off and on. For several hours of operation the beam intensity of 0.6 μA was maintained stably. Therefore, the intensity of 5 nA should be obtained at the target when the source is installed in a cyclotron whose overall efficiency of injection, acceleration, extraction and transportation of beam is about 1 %.

The tensor polarization of the deuteron beam was measured by the neutron anisotropic factor on the T(d, n) ^{4}He reaction as described above. The differential cross section is independent of the vector polarization of the beam and for a deuteron having the tensor component $P_{ZZ}$$^{3)}$ it is given by

$$\sigma_{\mathrm{pol}}(\theta) = \sigma_{\mathrm{unpol}}\left[1 - \frac{1}{4} P_{zz}(3\cos^2\theta - 1)\right],$$

where θ is the angle between the spin quantization axis and the emitted neutron in the system of the center of mass. Two plastic scintillators where placed at 0° and 90° with respect to the beam direction and were 50 cm apart from a Tritium-Titanium target to detect emitted neutrons. The asymmetry is of the form:

$$R = [\sigma(0^\circ)/\sigma(90^\circ)]_{\mathrm{pol}} = [N(0^\circ)/N(90^\circ)]_{\mathrm{pol}} \times [N(90^\circ)/N(0^\circ)]_{\mathrm{unpol}},$$

where σ is the cross section and N is counts of the emitted neutrons. The asymmetry was measured as a function of the static field B_e at a fixed frequency. For a frequency of 380 MHz

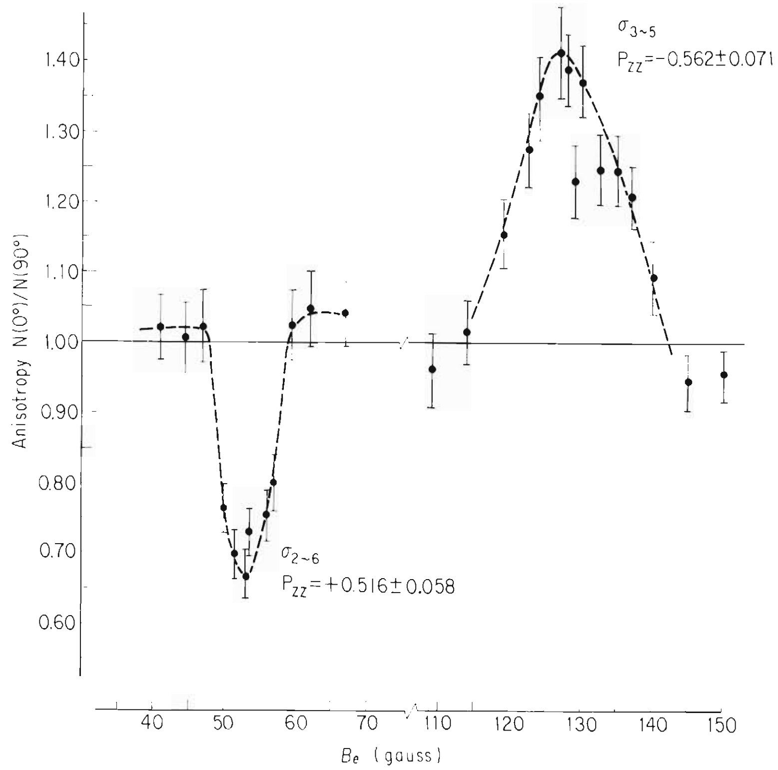

Fig. 2. Neutron anisotropy in the $T(d, n)^4He$ reaction with polarized deuterons.

the static field was varied in the regions from 40 to 150 gauss in order to investigate the behavior of the 2 to 6 and the 3 to 5 transitions. The results are shown in Fig. 2. The maximum values of the asymmetry measured were

$$R = 0.657 \pm 0.034 \qquad \text{for 2 to 6}$$
$$R = 1.418 \pm 0.69 \qquad \text{for 3 to 5,}$$

corresponding to

$$P_{zz} = 0.516 \pm 0.058 \text{ for 2 to 6}$$
$$P_{zz} = -0.562 \pm 0.071 \text{ for 3 to 5.}$$

These values include only a correction for detector background with no beam on the target. It is wellknown that an unanalyzed beam contains unpolarized D_2^+ components which dilutes the measured polarization of the atom. The maximum peak of the polarization is relatively sharp for the 2 to 6 transition. The 3 to 5 transition, however, shows a broad top in which the static field can be varied without losing the polarization. In both cases the slopes were quite steep. Since the values of the asymmetry of the 3 to 5 transition are not critically affected by the drift of the field, this transition should be chosen in connection with the weak field rf transition in order to change the sign of the polarization in case of operation in the accelerator. Table 1 shows parameters of rf transition and polarization.

To investigate the efficiency of transition probability for various strengths of the rf rotating field B_1, the neutron anisotropy was measured as a function of the rf rotating field

Table 1. RF-transition parameters.

Particle	# 1 Transition	Frequency (MHz)	Staticfield (gauss)	Gradient ΔH	# 2 Transition	Frequency (MHz)	Staticfield (gauss)	Gradient ΔH	Polarization P_{zz} P_{zz}
Hydrogen	$\pi 1, 2, 3$	10	8	2					-1
					$\sigma 2, 4$	1480	150	5	$+1$
Deuterium	$\pi 1, 2, 3, 4$	10	11	3					$-\frac{2}{3}$, 0
					$\sigma 3, 5$	378	117	5	$+\frac{1}{3}$. -1
	$\pi 1, 2, 3, 4$	10	11	3	$\sigma 3, 5$	378	117	5	$-\frac{1}{3}$, -1

π: static field is perpendicular to rf fields.

σ: static field is parallel to rf fields.

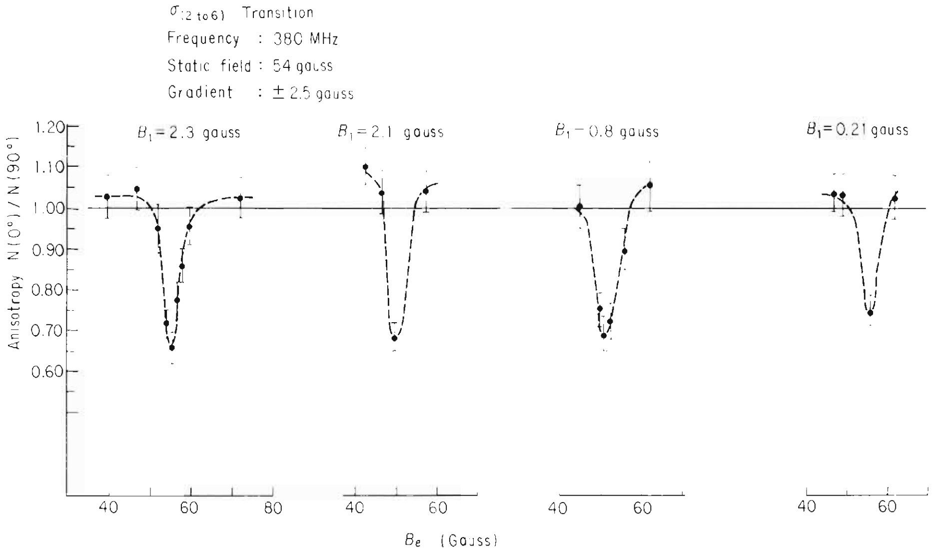

Fig. 3. Neutron anisotropy for different strengths of rf rotating field.

which was varied from 0.21 to 2.3 gauss at 380 MHz. As shown in Fig. 3, remarkable increase in the asymmetry was not observed.

The polarization values are smaller than the theoretically expected maximum values. This suggests that there is a possibility of improving our apparatus. Perhaps the simplest way is to decrease the partial pressure of the deuterium gas in the ionizing region.

Also the most important problem is to increase the ion beam intensity. For the present ionizer of the source,$^{1)}$ a gridded electrode used to focus and accelerate the ion beam is a mesh made of stainless steel wire of 0.15 mm in diameter and 0.55 mm in pitch. Although the present transparency of the ion beam through the gridded electrode is 47 %, the increase of the transparency can easily be achieved. Another improvement is to put the ionizer as near to the exit of sextupole magnet as possible. By making these improvements, the ion beam of 2 μA or more could be expected.

References

1) S. Motonaga, M. Hemmi, T. Fujisawa, and Y. Yamazaki: IPCR Cyclotron Progr. Rep., 4, 100 (1970); S. Motonaga, T. Fujisawa, K. Ikegami, H. Takebe, and M. Hemmi: ibid, 6, 12 (1972).

2) A. Abragam and J. M. Winter: Phys. Rev. Lett., 1, 374 (1958).

3) A. Galonski, H. B. Willard, and T. A. Welton: ibid., 2, 349 (1959).

6-2. Investigation of Residual Gases in the Ionizer of Polarized Ion Source

K. Ikegami and H. Takebe

Polarized atoms are ionized by electron bombardment in the ionizer of a polarized ion source which is being assembled.1) The ionization process of atomic hydrogen (or deuterium) by electron bombardment is

$$H + e^- \rightarrow H^+ + 2e^- .$$

Possible processes in which unpolarized background ions are produced from molecular hydrogen remaining in the ionizer are

$$H_2 + e^- \rightarrow {H_2}^+ + 2e^- ,$$
$$H_2 + e^- \rightarrow H^+ + H + 2e^- .$$

The first process producing a molecular ion beam is important only in a case that acceleration of ion is made without analyzing the atomic mass. The unpolarized ions which are produced in the second process cannot be removed in the accelerator.

One of the other constituents of the residual gas is water vapor. Keller2) has shown that the effective cross section for producing protons from water vapor by 80 eV electrons is 40 times as large as that from molecular hydrogen. However, the vapor pressure of water at $-100°C$ is about 10^{-5} Torr and decreases by a factor of about ten per 10°C decrease of temperature.3) Therefore use of the liquid nitrogen traps will be very effective to suppress this source of the background.

(1) Analysis of the residual gases

The amount of the residual gases such as the molecular hydrogen (H_2) and water vapor

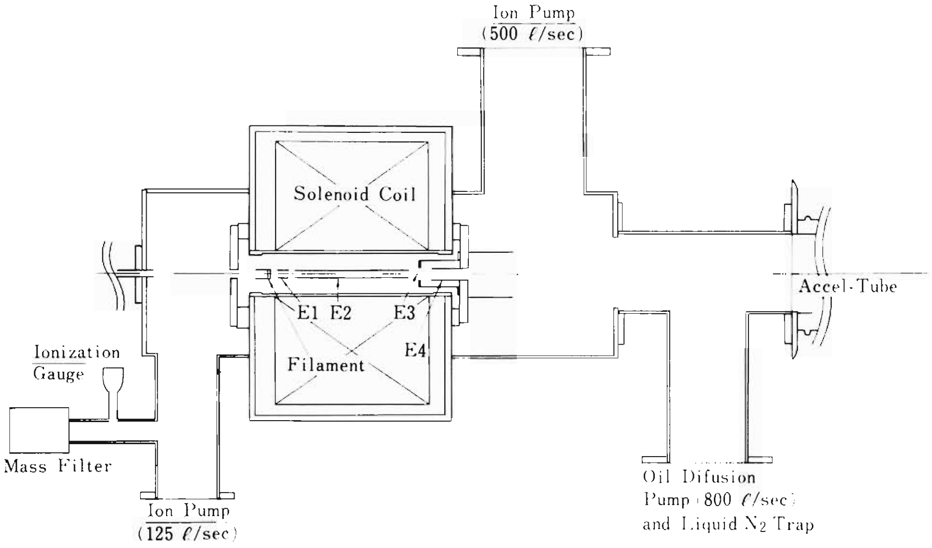

Fig. 1. Block diagram of experimental arrangement.

(H_2O) in the ionizer was measured using a quadrupole mass filter. A block diagram of the arrangement for measurement is shown in Fig. 1. Evacuation of the vacuum chamber was made by two diode sputter ion pumps of 125 and 500 ℓ/s for N_2. An oil diffusion pump with liquid N_2 trap was also used to evacuate inert gases in the ionizer. The amount of outgassing and leakage rate of the vacuum chamber was measured to be less than 2×10^{-6} Torr. ℓ/s.

(2) Structure of the ionizer

A tantalum filament was placed at one end of the ionizer and heated to about 2300°C by direct current. Electrons were drawn off the filament by the electrode E_1. Electrons travel guided by the magnetic field produced by a solenoid coil along E_1, E_2, and are reflected at the other end by negative potentials of E_3 and E_4. All of these electrodes were washed with acetone and deionized water in an ultrasonic bath several times and dried in an oven at 80 − 150°C to clean their surface. A typical set of operating parameters of the ionizer were as follows: Magnetic field of solenoid coil: 1200 gauss, Filament current: 30 A, Extractor (E_1): 0.88 kV, 87 mA, Ionization column (E_2): 0.62 kV, 61 mA.

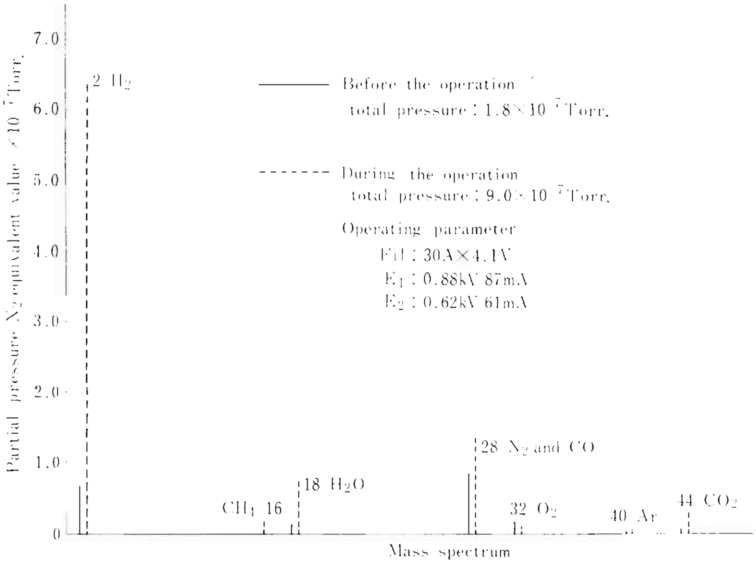

Fig. 2. Mass spectrum of residual gases.

(3) Results of observation of the residual gases during operation of the ionizer

Figure 2 shows the variation of mass spectrum of the residual gases in the ionizer before and during operation. The total pressure increased suddenly to 9×10^{-7} Torr from 1.7×10^{-7} Torr when we started the operation of the ionizer. Each peaks of the residual gases was identified with the cracking pattern coefficient[4)] and the partial pressure was given with relative sensitivity to that of the nitrogen gas.[5)] The observed residual gases were hydrogen, water vapor, nitrogen, carbon monoxide, oxygen, carbon dioxide, and argon before the operation of the ionizer. Under these conditions, each partial pressure was less than 10^{-8} Torr.

On the other hand, the partial pressure for H_2 was greatly enhanced when the ionizer was operated. The partial pressure of H_2 was 7×10^{-7} Torr. 76 % of the total pressure.

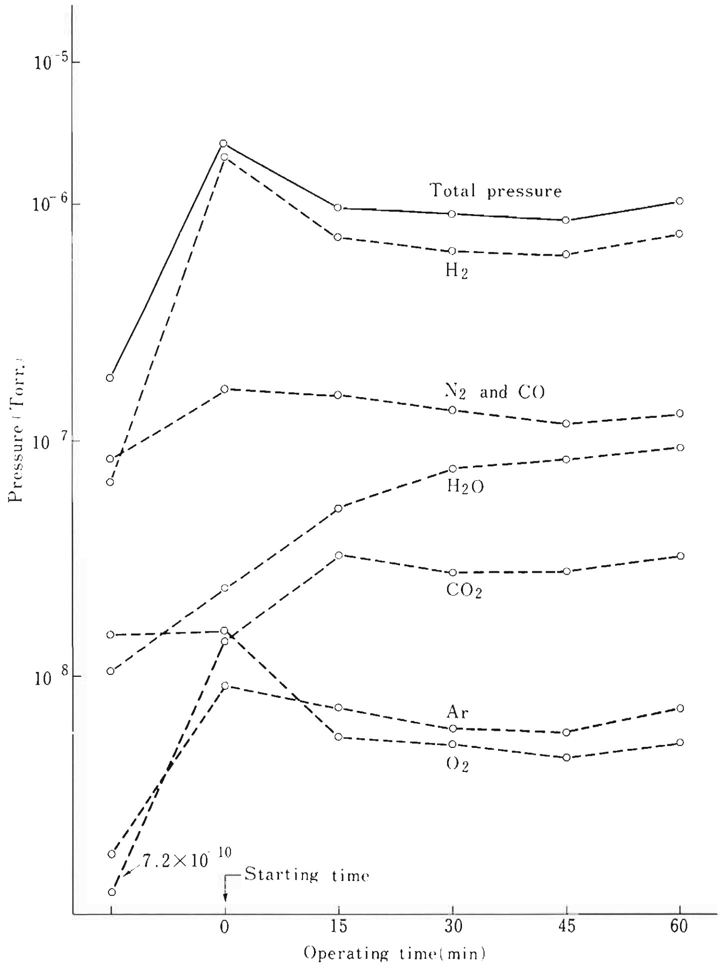

Fig. 3. Change of the partial pressure with operating time of ionizer.

Figure 3 shows the change of the partial pressure of residual gases with the operation time of the ionizer. The partial pressures of H_2 and N_2 decreased slightly during the operation. It seems that the partial pressure of H_2O increases slowly during the operation because of the gradual rise of temperature of wall of the ionization region and the electrodes.

(4) Future improvement

If an atomic beam with an intensity of the order of 10^{15} atoms/cm^{2}s at a velocity of 2.5×10^5 cm/s (at T = 400 K) enters the ionizer, the equivalent beam pressure is about 10^{-7} Torr. Therefore it is desirable to reduce the partial pressure of residual gas to less than σ_r (cross section for residual gas) $/\sigma_a$ (cross section for atoms) times the equivalent atomic beam pressure. The required improvements are given below

a) A liquid nitrogen trap has to be placed near the ionization region.

b) The wall of vacuum envelope adjacent to the ionization region must be cooled by a suitable coolant.

c) The inner wall of the steel vacuum envelope of the ionizer should be polished and electroplated with tin.

After making these improvements one can expect that the partial pressures of hydrogen molecule and water vapor in the ionization vacuum chamber are suppressed considerably.

References

1) S. Motonaga, T. Fujisawa, M. Hemmi, H. Takebe, K. Ikegami, and Y. Yamazaki: IPCR Cyclotron Progr. Rep., 8, 84 (1974).
2) R. Keller, L. Dick, and M. Fiedecaro: Report CERN 60 – 2 (1960).
3) H. Kumagai, G. Tominaga, Y. Tsuji, and G. Honkoshi: "Vacuum Science and Engineering", Shokabo, Tokyo, p. 299 (1970).
4) T. Hayashi and S. Komiya: "Ultrahigh Vacuum", Vol. 6, Vacuum Technology, Nikkankogyo, Tokyo, p. 92 (1964).
5) G. Tominaga: J. Vacuum Soc. Japan, 2, 19 (1955); 1, 27 (1955).

6-3. Mechanical Design of a Polarized Ion Source for the INS Cyclotron

I. Takeshita

Details of the mechanical design of a polarized ion source, which is to be installed in the cyclotron, are described in the present article. The fabrication of the source is now under way. A simplified layout of the source is shown in Fig. 1. The height of the source was limited to be less than 2 m, because of the available vertical space.

Figure 2 shows a schematic drawing of the IPCR polarized ion source. Basic design of the source followed that of TEXAS A & M University, which is characterized in the dissociation at high pressure of 2 Torr. The source consists of four vacuum chambers of stainless steel, three of

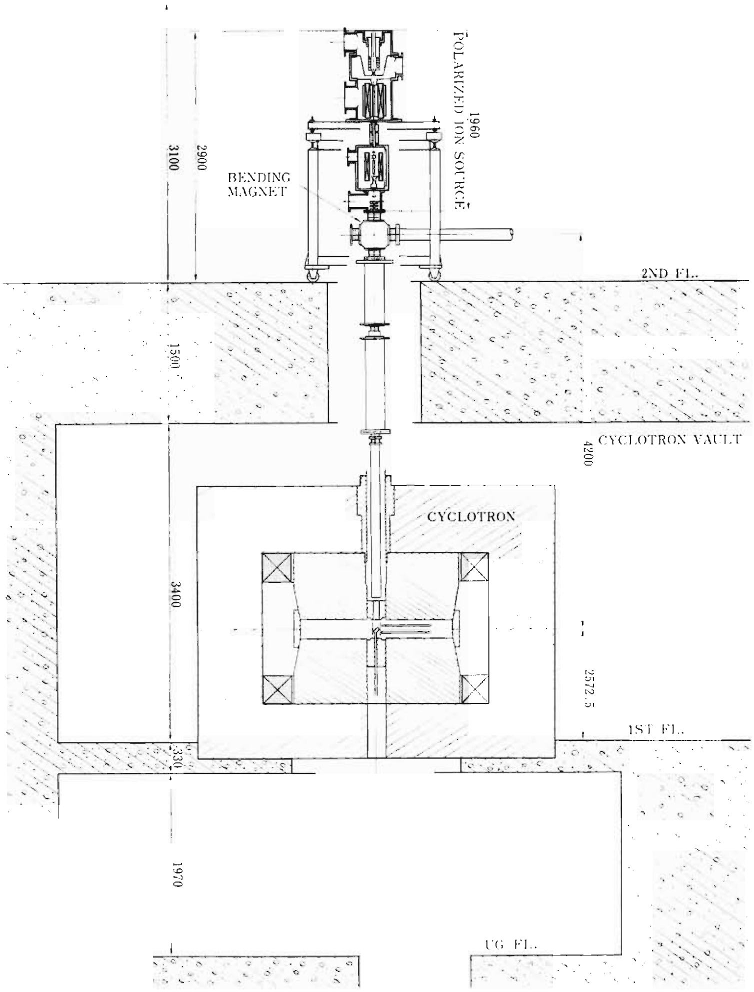

Fig. 1. Simplified layout of the ion source.

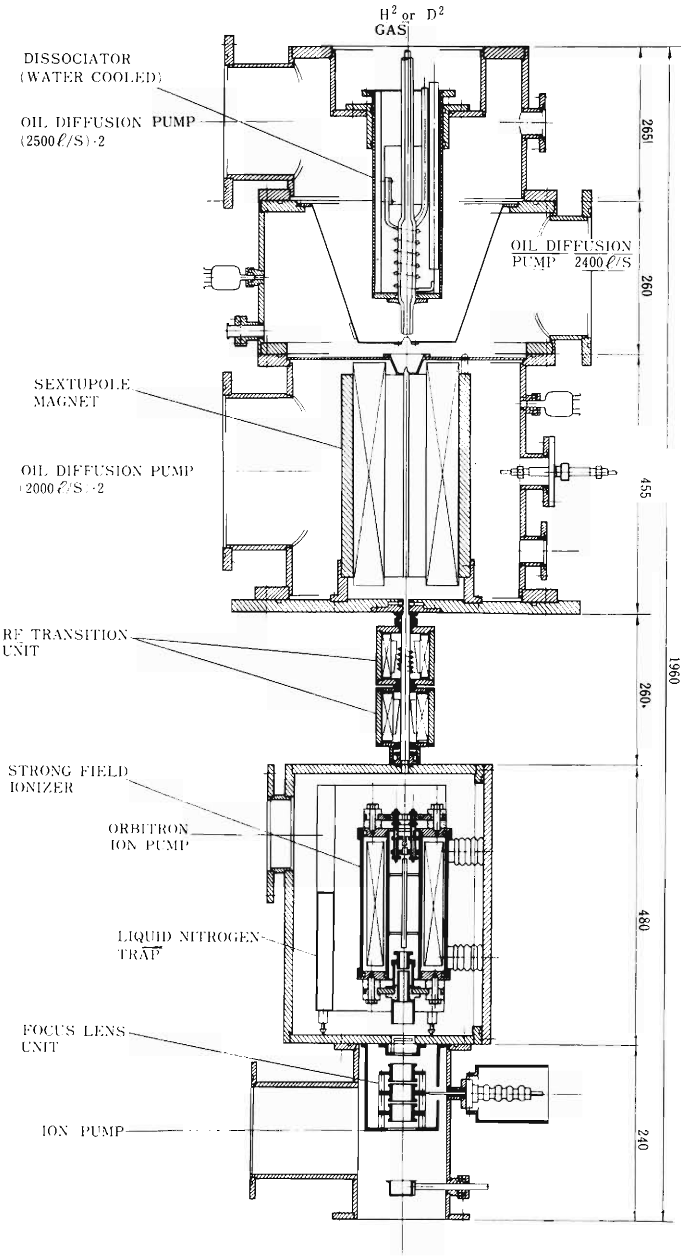

Fig. 2. Schematic drawing of the IPCR polarized ion source.

which are evacuated with five 2400 ℓ/s oil diffusion pumps and the other is pumped with a orbitron ion pump of 1000 ℓ/s. In the vacuum system, the pressure varies from 2 Torr in the dissociation chamber to 3×10^{-7} Torr in the ionization vacuum chamber.

Some notable designs were done in the mechanical design of the ionizer in order to fulfill the following specifications. A sectional view of the strong field ionizer is shown in Fig. 3. The strong field ionizer is placed in the ionization vacuum chamber, which is a cubiform of 36 cm in width, 40 cm in length and 48 cm in height. A solenoid produces a magnetic field parallel to the atomic beam. An electron gun is placed at one end of the ionization area and extraction electrodes which have negative potential are placed at the other end. The electrons make circulating motion in the ionization area before collision.

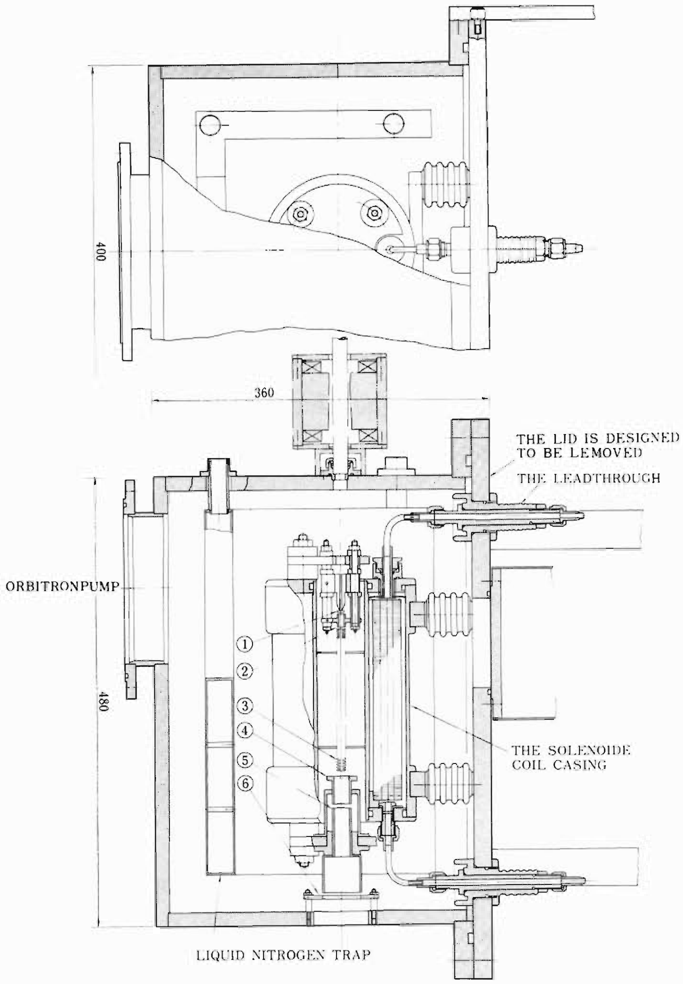

1. Filament (Ta);
2. Grid, E_1 (Ta);
3. Ionization column, E_2 (Ta),

4.
5. } Extraction electrodes, E_3, E_4 (Cu);

6. Grided electrode, E_5 (stainless steel wire).

Fig. 3. A sectional view of the strong field ionizer.

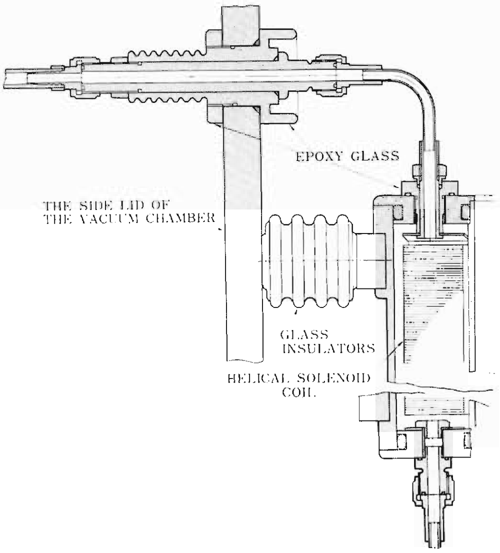

Fig. 4. A drawing of one of the electric leadthroughs.

The solenoid casing and all of the leadthroughs are mounted on the side lid of the vacuum chamber. The lid was designed to be removed easily for exchange of the filament or for re-alignment of the electrodes and magnetic field.

In order to inject an ion beam to the injection system with maximum energy of 20 keV, the solenoid coil, the filament, and all of the electrodes are biased at a positive potential of 20 keV to the ground. The ionizer vacuum chamber is at the ground potential. Therefore, the solenoid coil casing and all of the electric and cooling leadthroughs must be insulated electrically from the vacuum chamber. The solenoid casing is mounted on the side lid of the vacuum chamber with four glass insulators. A drawing of one of the electric leadthroughs is shown in Fig. 4. This leadthrough is used to supply an electric current of 150 A to the solenoid and feed Freon coolant simultaneously under 20 keV electric potential to the ground. An epoxy glass insulator is used because it can be manufactured easily. Before attaching the lead through to the vacuum chamber the insulation of the lead through was tested under vacuum up to 20 keV without any trouble.

As shown in Fig. 3 or 4 a compact helical solenoid coil was made by stacking annular plates of copper of 1 mm in thickness, 130 mm in outer diameter, and 66 mm in inner diameter. Electric current density is 4.7 A/mm^2 at 150 A maximum current and the maximum heat dissipation of 1.2 kW is removed with Freon coolant.

A particular attention was paid for keeping high vacuum in the ionization chamber. Thus the surface of the solenoid coil casing, which is exposed in the vacuum, was polished by electrolysis, and the inner surface of the vacuum chamber was polished by using high pressure blast of glass beads.

7. ATOMIC AND SOLID-STATE PHYSICS

7-1. Inner-Shell Excitation by Nitrogen Ions and Alpha Particles (3)

Y. Awaya, K. Izumo, T. Hamada, M. Okano,
A. Hashizume, T. Takahashi, Y. Tendow, and T. Katou

Recently, some experimental studies have shown the deviation from the Z_1^2- dependence in the K-shell ionization cross section[1)-5)] where Z_1 is the atomic number of the incident particle. The plane wave Born approximation predicts that $R_{2K} \equiv [\sigma_{2K}(Z_1')/Z_1'^2]/[\sigma_{2K}(Z_1)/Z_1^2]$ equals unity, where the $\sigma_{2K}(Z_1)$ is the K-shell ionization cross section of the target atom of atomic number Z_2. The cause of this deviation would be twofold, i.e. increased binding energy of target electrons (prevailing for $v_1 < v_{2K}$) and the polarization of them (prevailing for $v_1 \gtrsim v_{2K}$), where, v_1 and v_{2K} ($\equiv Z_2e^2/\hbar$) are the velocity of projectile and that of K-electron of target atom, respectively. These two processes have Z_1^3-dependence and their contributions to the cross section are in the opposite direction. They cancel each other at $v_1/v_{2K} = \theta_K/2$, that is, $R_{2K} = 1$, where $\theta_K \equiv 2I_{2K}/Z_2^2$, and I_{2K} (in a.u.) is the ionization energy of K-shell.[1)]

We measured the X-rays from the target atoms induced by 5 MeV/amu N-ions and α-particles. The target atoms ranged from Cr to Bi and the preliminary results of the work were reported previously.[6),7)] We reanalyzed the ratio of the K X-ray yields of N-ion and α-particle bombardment to study the deviation from the Z_1^2-dependence.

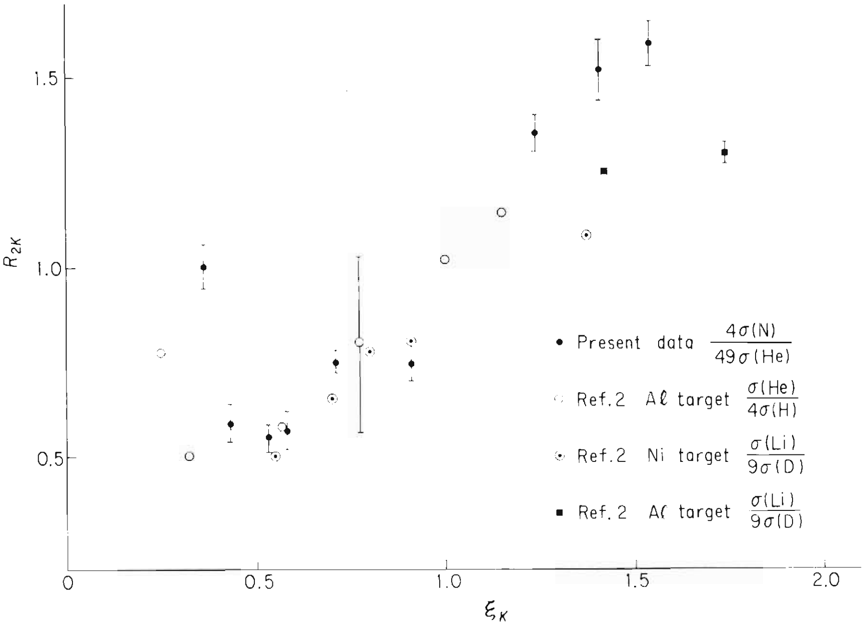

Fig. 1. Ratios R_{2K} of K-shell ionization cross sections as a function of ξ_K.

In order to obtain a universal curve, values of R_{2K} were plotted as a function of ξ_K, where $\xi_K \equiv v_1/(\theta_K v_{2K}/2)$, since R_{2K} becomes unity at $\xi_K = 1$ as described above. In our experiment v_1 is constant whereas Z_2's take values of 24 to 83; on the other hand, single element was bombarded with projectiles of different velocities in the literature cited.$^{1)\sim 4)}$ The result is shown in Fig. 1 together with the data obtained by Basbas et al.$^{2)}$; the tendency of the deviation from the Z_1^2 dependence is similar. The amount of the deviation depends on the projectile and target combination. It seems that some universality holds between R_{2K} and ξ_K and this result shows that the main mechanism for K-shell ionization under the present experimental conditions is the direct Coulomb excitation.

References

1) G. Basbas, W. Brandt, and R. Laubert: Phys. Lett., 34A, 277 (1971).
2) G. Basbas, W. Brandt, R. Laubert A. Ratkowski, and A. Schwarzschild: Phys. Rev. Lett. 27, 171 (1971).
3) C. W. Lewis, J. B. Natowitz, and R. L. Watson: ibid., 26, 481 (1971); Phys. Rev., A, 5, 1773 (1972).
4) G. Basbas, W. Brandt, and R. Laubert: ibid., 7, 983 (1973).
5) N. Cue, V. Dutkeiwicz, P. Sen, and H. Bakhu: Phys. Rev. Lett., 32, 1155 (1974).
6) Y. Awaya, T. Hamada, M. Okano, A. Hashizume, T. Takahashi, K. Izumo, Y. Tendow, and K. Katou: IPCR Cyclotron Progr. Rep., 7, 87 (1973).
7) K. Izumo, Y. Tendow, Y. Awaya, T. Katou, M. Okano, A. Hashizume, T. Takahashi, and T. Hamada: ibid., p. 93.

7-2. Positron Annihilation in V and Nb

N. Shiotani, T. Okada, and H. Sekizawa

Systematic studies of the electronic structures of transition metals by measuring the angular distribution of the positron annihilation radiation are in progress.

After completion of the experimental studies on V and Nb, a detailed theoretical calculation employing APW method has been made by Wakoh et al.[1] The (100) experimental angular distribution curve for Nb is shown in Fig. 1 together with the theoretical curve as an example. The agreement is fairly good and the fine structures in the experimental curve are identified as the corresponding ones on the theoretical curve. Anisotropies of the experimental angular distribution curves, i.e., the differences between the curves along three major crystallographic directions, are shown in Fig. 2 together with the theoretical ones calculated by Wakoh et al.

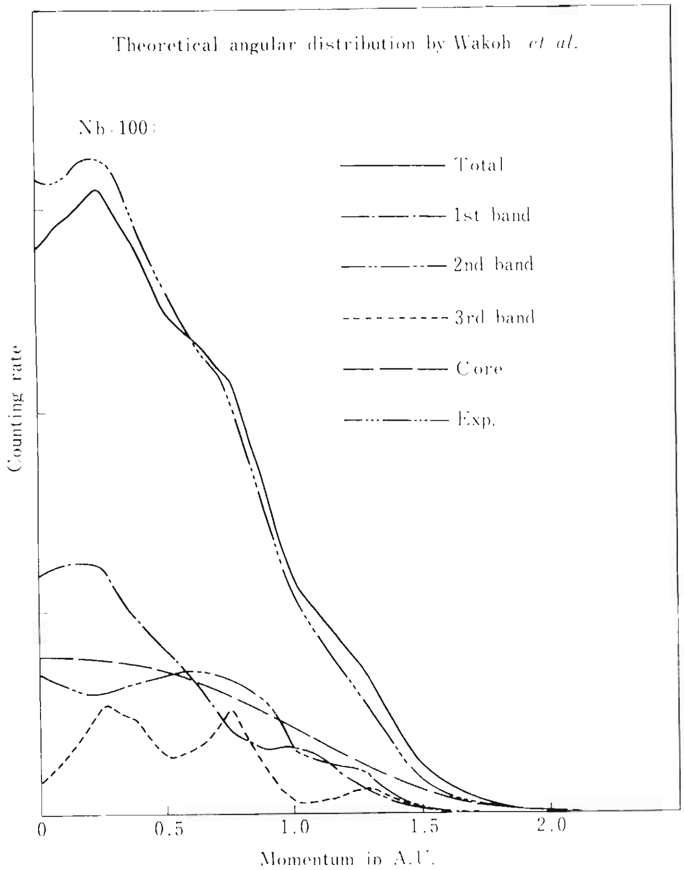

Fig. 1. Experimental angular distribution in Nb together with the theoretical ones with individual contributions from the core states, the first, second, and the third bands taken from Ref. 1.

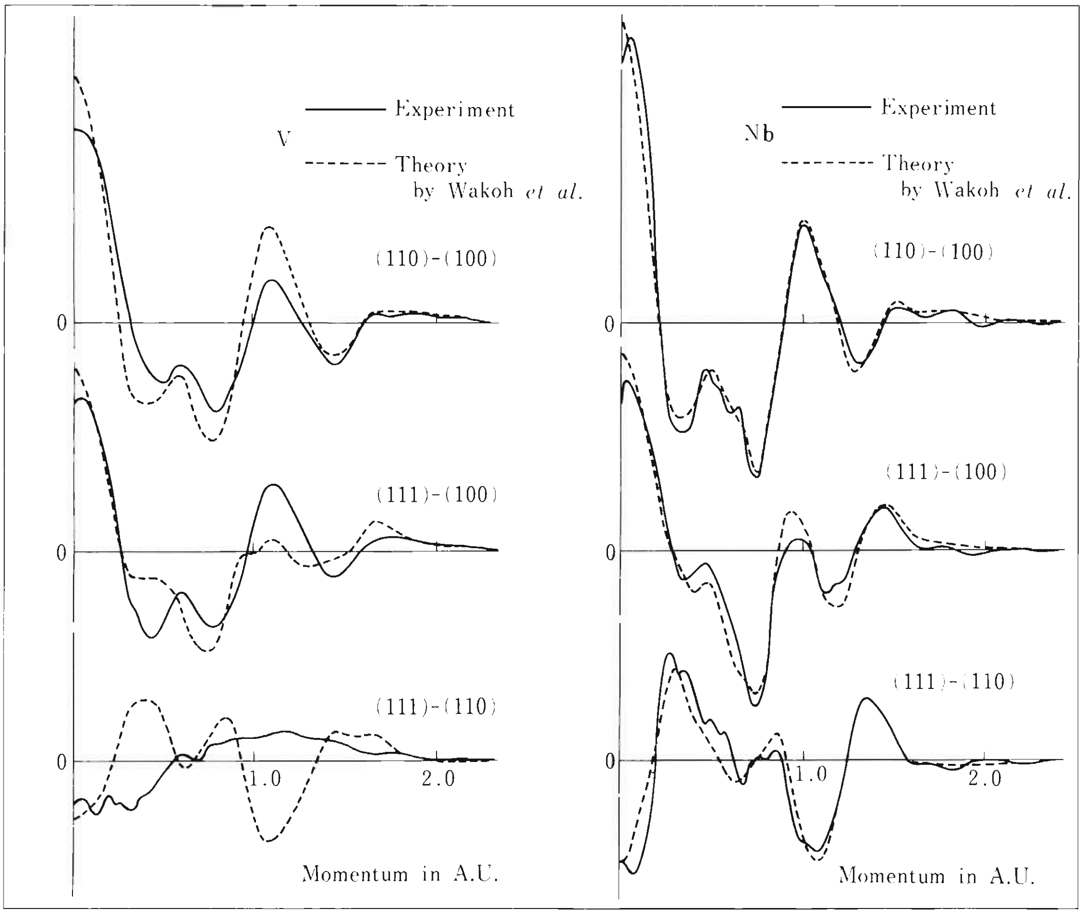

Fig. 2. Experimental anisotropy curves and theoretical ones calculated by Wakoh et al. for V and Nb.

The agreement is fairly good for V and excellent for Nb.

These comparisons between experiments and theory have established the validity of the one-electron approximation of the band electrons in transition metals on the one hand, and revealed the limitation of the applicability of the independent particle model to this problem on the other hand.

A detailed report will be published elsewhere.[2)]

References

1) S. Wakoh, Y. Kubo, and J. Yamashita: J. Phys. Soc. Japan, 38, 416 (1975).
2) N. Shiotani, T. Okada, T. Mizoguchi, and H. Sekizawa: ibid., p. 423.

7-3. A Damage Function Based on the Focused Replacement Collision Model

H. Sakairi, E. Yagi, A. Koyama, and R. R. Hasiguti

A damage function $\nu(E_p)$ represents the average number of displaced atoms created by a collision cascade initiated by a primary knocked-on atom with an energy E_p. A simple expression of it was given by Kinchin and Pease[1] and the refined one by Snyder and Neufeld.[2] Results of calculation with these expressions, however, give a larger number of displaced atoms than the experimental values by a factor of 4 – 5.[3],[4] The discrepancy is probably due to the focused replacement collision sequences being neglected in the basic assumption. It is an effect of the periodicity of crystal structure, which was predicted theoretically[5] and revealed by a computer simulation.[6]

As reported previously,[7] the defect production rate in Cu and ordered alloy Cu_3Au irradiated below 10 K with charged particles from the cyclotron shows that the number of atomic replacements is in proportion to the number of atomic displacements, suggesting that almost all displacements occur as a result of replacements. Therefore the damage function was reconsidered according to the focused replacement model as follows.

The basic equation is the same as used by Snyder and Neufeld, that is,

$$\nu(E_p) = \int_0^{E_p} \nu(E_2)\frac{dE_2}{E_p} + \int_0^{E_p-E_d} \nu(E_p-E_2-E_p)\frac{dE_2}{E_p} \tag{1}$$

The first integral in the right-hand side is the average number of displaced atoms in the collision cascade initiated by the primary knocked-on atom whose energy was reduced from E_p to E_2 by the first scattering. The second integral is that created by the secondary knocked-on atom produced by that scattering. Here E_d is the threshold energy for displacements and dE_2/E_p is the probability of finding the scattered atom with energy in dE_2 at E_2, given by the hard sphere approximation.

Boundary conditions were taken as

$$\nu(E_p) = 0 \qquad \text{for} \quad E_p < E_d, \tag{2a}$$

$$= 1 \qquad E_d \leq E_p \leq E_F, \tag{2b}$$

where E_F is the focusing energy.

Equation 1 was integrated analytically to $\nu(E_p) = \ln(E_p/E_F)$ for E_p between E_F and $E_F + E_d$, and numerically above $E_F + E_d$. An example of the results of calculation is given in Fig. 1. The tangent of the asymptotic linear line is given by $\alpha E_F^{-\beta}$, where α and β are functions of E_d as shown in Fig. 2. This expression holds in the energy region where elastic collisions dominate electronic excitations, above which the expression must be given in such a modification as proposed by Kinchin and Pease.

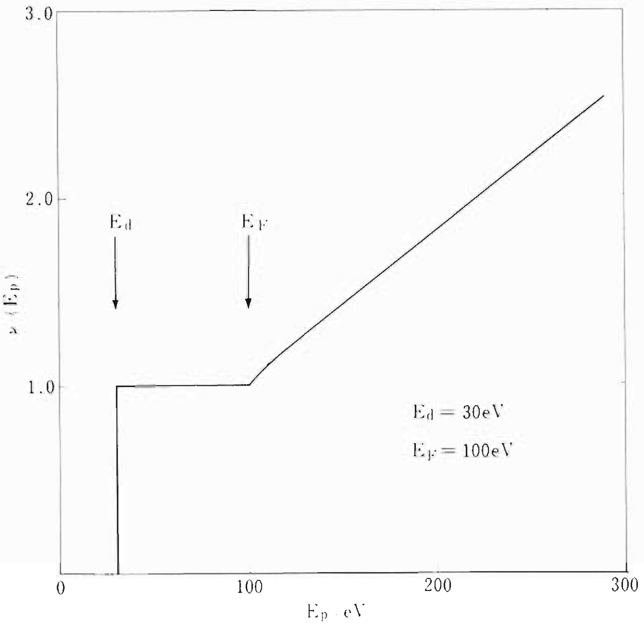

Fig. 1. An example of $\nu(E_p)$ curve calculated for E_F = 100 eV and E_d = 30 eV.

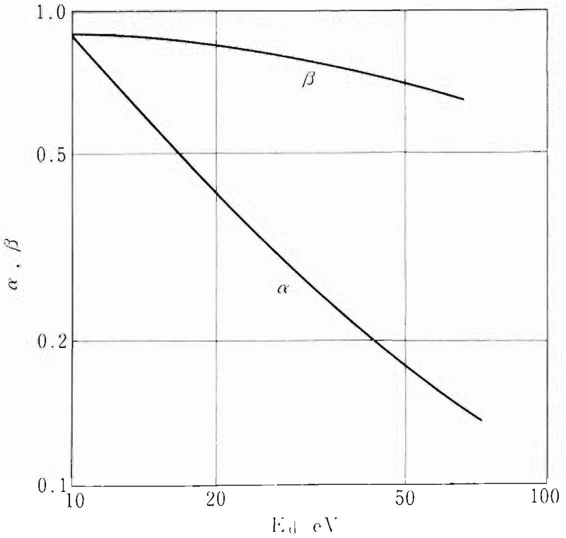

Fig. 2. α and β as functions of E_d.

Snyder and Neufeld took a boundary condition,

$$\nu(E_p) = 1 \qquad \text{for} \quad E_d \leq E_p \leq 2E_d,$$

instead of (2b) and obtained 0.56 E_d^{-1} as the tangent of the asymptotic line. Thompson intuitively proposed to replace E_d simply by E_F for including the focused replacement sequences into the model.[8] This is shown, however, to be incorrect by the present calculation.

For E_d = 22 eV, which is accepted as the average threshold energy for displacement in Cu,[9] α is 0.37 and β is 0.83. Then E_F must be taken 135 eV to make up the difference between the theory and experiments on the damage function by the contribution from focused replacement chains only. If the contribution from electronic excitations, which was neglected in the present consideration, is assumed to be about 20 %,[10] it decreases to about 100 eV. These values are large compared with the theoretical values of E_F for Cu obtained by the computer simulation (~ 40 eV).[6] Another experiment to estimate the E_F values is now in progress. It is also hoped that theoretical models for the calculation on focused replacement collision sequences are reexamined.

References

1) G. H. Kinchin and R. S. Pease: Rep. Prog. Phys., 18, 1 (1955).
2) W. S. Snyder and J. Neufeld: Phys. Rev., 97, 1636 (1955).
3) H. G. Cooper, J. S. Koehler, and J. W. Marx: ibid., p. 599.

4) D. K. Holmes: "Interaction of Radiation with Solids", ed. R. Strumane et al., (North Holland Publishing, 1964) p. 147.

5) R. H. Silsbee: J. Appl. Phys., 28, 1246 (1957).

6) J. B. Gibson, A. N. Goland, M. Milgram, and G. H. Vineyard: Phys. Rev., 120, 1229 (1960).

7) H. Sakairi, E. Yagi, A. Koyama, T. Karasawa, and R. R. Hasiguti: IPCR Cyclotron Progr. Rep., 5, 101 (1971).

8) M. W. Thompson: "Defects and Radiation Damage in Metals", (Cambridge Univ. Press, 1969) p. 241.

9) J. W. Corbett: "Electron Radiation Damage in Semiconductors and Metals", Solid State Physics, ed. F. Seitz and D. Turnbull, Suppl. 7, (Academic Press, 1966) p. 240.

10) G. Dearnaley, J. H. Freeman, R. S. Nelson, and J. Stephen: "Ion Implantation", (North Holland Publishing, 1973) p. 161.

7-4. Secondary Electron Emission from Al and Ni by Fast-proton Bombardment

A. Koyama, E. Yagi, and H. Sakairi

Secondary electron emission ratios γ were measured on Al and Ni for fast-protons (2 ~ 10 MeV) from the cyclotron. The specimens were mirror-polished and cleaned in an etanol-acetone mixture with an ultrasonic cleaner.

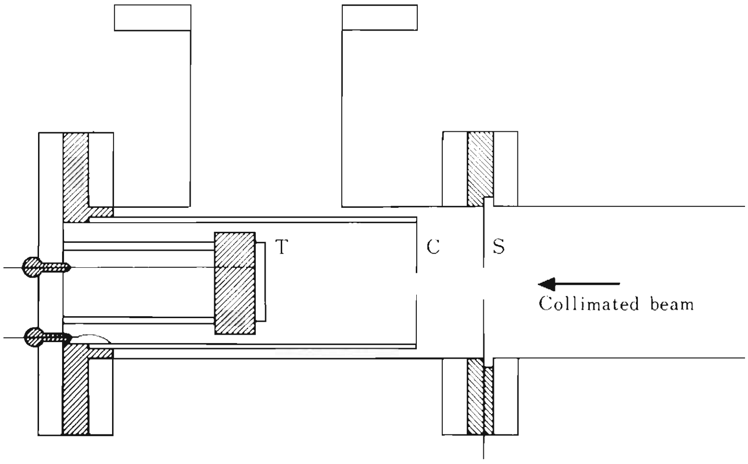

Fig. 1. Target-collector system. T: target, C: collector, S: secondary electron suppressor.

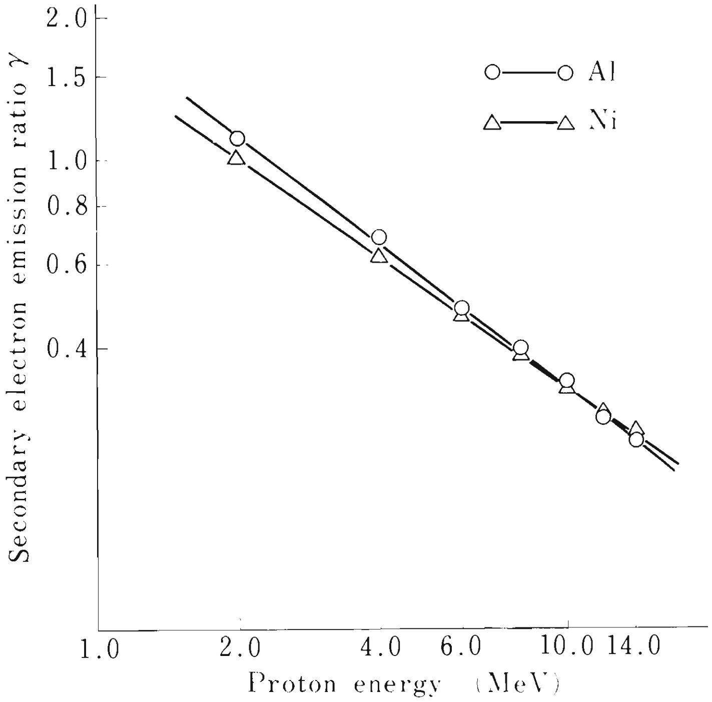

Fig. 2. Dependence of secondary-electron emission ratio on the incident proton energy.

Figure 1 shows the target-collector system used for the experiments. Figure 2 shows the experimental results on γ which fit the following formulas:

$$\gamma_{Al} = 1.85E_I^{-0.75}, \text{ and}$$

$$\gamma_{Ni} = 1.62E_I^{-0.70},$$

where E_I (MeV) is the energy of incident protons.

Aarset et al. measured γ_{Al} at the lower energies, below 2 MeV,$^{1)}$ and the results can be expressed by the next equation,

$$\gamma_{Al} = 1.08E_I^{-0.67}.$$

A theoretical expression for γ is generally given as

$$\gamma = \alpha E_I^{-\beta},$$

in which α is mainly related to the transport of the inner secondary electrons and the emission from the metal surface, while β is to the mechanism of the direct excitation of metal electrons by incident particles. Therefore α is influenced by the surface conditions while β is not for the high incident energy and the thin surface contaminant layer in these experiments.

According to the theoretical calculation by Ghosh et al., who improved the one by Sternglass,$^{2)}$ the energy dependence of γ was expressed as follows:$^{3)}$

$$\gamma_{Al} \sim E_I^{-0.90}, \text{ and}$$

$$\gamma_{Ni} \sim E_I^{-0.80}.$$

There is an apparent discrepancy between the experimental and theoretical energy dependence. Improved calculations are now in progress.

References

1) B. Aarset, R. W. Cloud, and J. G. Trump: J. Appl. Phys., 25, 1365 (1954).
2) E. J. Sternglass: ibid., 108, 1 (1957).
3) S. N. Ghosh and S. P. Khare: Phys. Rev., 125, 1254 (1962).

8. RADIOCHEMISTRY AND NUCLER CHEMISTRY

8-1. Charged-Particle Activation Analysis

T. Nozaki, M. Iwamoto, Y. Yatsurugi, and N. Akiyama

After our previous report,$^{1)}$ we have applied charged-particle activation analysis to the following four studies: (1) examination of reliability and accuracy in the calibration curve for the infrared spectrophotometry of oxygen in semiconductor silicon, (2) search for effects of impurity carbon on electronic properties of semiconductor silicon, (3) investigation of the relationship between ambient carbon monoxide concentration and carbon and oxygen contents of molten silicon in the single-crystal formation of semiconductor silicon, and (4) development of convenient procedures for the determination of oxygen in various high-purity matrices by activation with the $^{16}O(^{3}He, p)^{18}F$ reaction. In addition, the determination of surface impurities by charged-particle activation analysis is under planning. Some results for studies (1) and (2) have already been published.$^{2),3)}$

The equilibrium constant for the carbon monoxide concentration ([CO] in atm) and the carbon and oxygen contents ([C] and [O] in wt ppm) can be calculated from the solubility of carbon and oxygen$^{1),2)}$ and the free energy for the reaction of $SiC + SiO = 2Si + CO$. It is obtained as:

$$K = \frac{[CO]}{[C]\,[O]} = 1.9 \times 10^{-7}$$

Preparing silicon crystals under various conditions and analyzing them, we examine the validity of this equation for the equilibrium condition and also deviations from it in non-equilibrium states which are usually encountered in the practical single-crystal formation.

For reliable and sensitive determination of oxygen by the $^{16}O(^{3}He, p)^{18}F$ reaction, a convenient technique for the chemical separation of the ^{18}F involving sample decomposition should be developed for each matrix. We tested the usefulness of the following decomposition methods: (1) dissolution in alkaline solutions, (2) oxidative dissolution in acids in a closed system, and (3) electrochemical dissolution. The ^{18}F in the resultant solution has proved to be made radiochemically pure by the following steps: (1) precipitation of PbFCl or coprecipitation of CaF_2 with $CaCO_3$, (2) steam distillation of fluorine in the precipitate as H_2SiF_6, and (3) precipitation of benzidine fluorosilicate or LiF from the distillate. Our final aim is to make a convenient manual for routine determination of oxygen in a variety of matrices.

References

1) T. Nozaki, Y. Yatsurugi, and N. Akiyama: IPCR Cyclotron Progr. Rep., 6, 106 (1972).
2) Y. Yatsurugi, N. Akiyama, Y. Endo, and T. Nozaki: J. Electrochem. Soc., 120, 975 (1973).
3) N. Akiyama, Y. Yatsurugi, Y. Endo, Z. Imayoshi, and T. Nozaki: Appl. Phys. Lett., 22, 630 (1973).

8-2. Mössbauer Emission Spectroscopy of ^{119}Sn after the EC Decay of ^{119}Sb

F. Ambe and S. Ambe

Mössbauer emission studies of the electronic state in ^{119}Sn after the EC decay of ^{119}Sb[1)–8)] have been extended further to various antimony and tellurium compounds labeled with ^{119}Sb or ^{119m}Te (parent of ^{119}Sb). A new series of experiments has also been started, in which tin compounds irradiated with charged particles were analyzed as the Mössbauer source.

The data accumulated so far on ^{119}Sn in the Sn-Sb-Te system have led to a systematics of the isomer shift. As is seen in Table 1, the isomer shift of the ^{119}Sn atoms increases with an increase in the electronegativity of the nearest neighboring atoms independently of the structure of the matrix. This is also true even if they are tin atoms in a defect state. In case of the sources labeled with ^{119m}Te, one cannot be certain a priori whether or not the ^{119}Sn atoms produced by successive EC decays of ^{119m}Te via ^{119}Sb occupy the original site of ^{119m}Te, since the recoil energy accompanying the EC decay of ^{119m}Te to ^{119}Sb is estimated to be of the same order of magnitude as the displacement energy in solid. However, if the dominant emission lines observed for $Sn^{119m}Te$ and $Sb_2{}^{119m}Te_3$ are assumed to represent the ^{119}Sn atoms in the original site of ^{119m}Te, their isomer shifts fit very well the systematics as shown in Table 1.

The systematics derived above was utilized in its turn to determine the lattice position of the ^{119}Sb atoms produced by proton reactions on tin in SnSb and SnTe. Powder samples of

Table 1. The isomer shifts of defect and normal ^{119}Sn in Sn-Sb-Te system.

Matrix	Method	Nearest Neighbor of ^{119}Sn	Isomer Shift[a)]
$Sn^{119m}Te$	emission	Sn	2.26[b)]
$Sn^{119}Sb$	emission	Sn	2.43
$Sb_2{}^{119m}Te_3$	emission	Sb	2.30[b)]
^{119}Sb metal	emission	Sb	2.66
SnSb	absorption	Sb	2.79
^{119m}Te metal	emission	Te	3.00
$^{119}Sb_2Te_3$	emission	Te	3.37
SnTe	absorption	Te	3.54

a) mm/s v s , $BaSnO_3$ at 78 K.

b) The value refers to the dominant line.

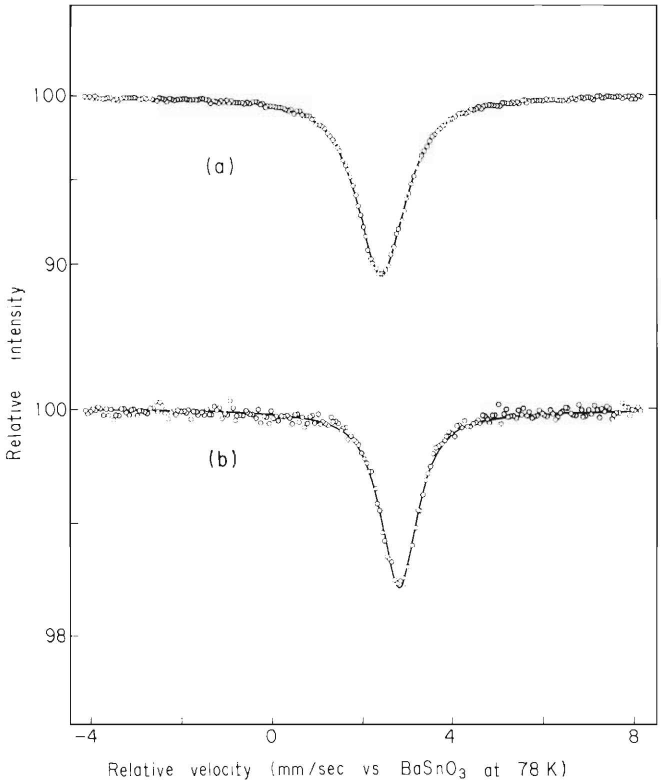

Fig. 1. Mössbauer (a) emission and (b) absorption spectra of p-irradiated SnSb at liquid nitrogen temperature.

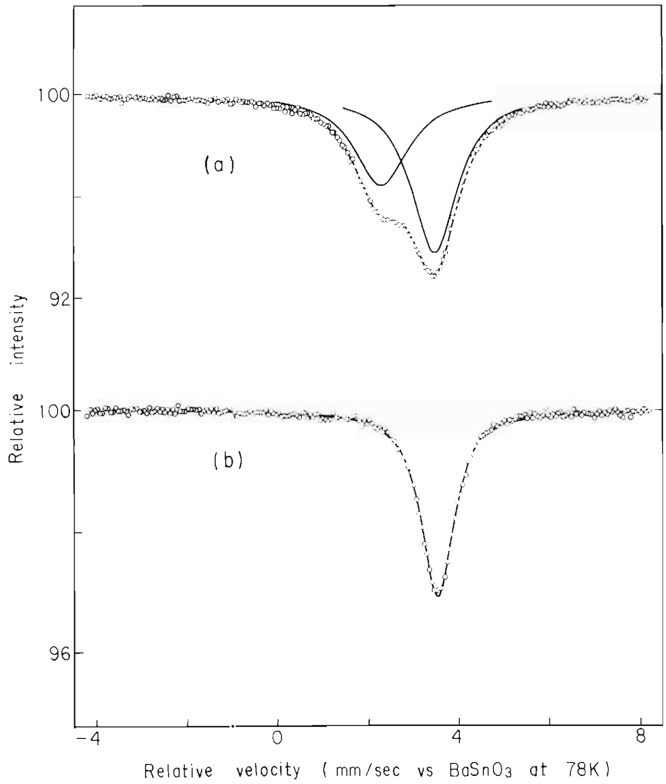

Fig. 2. Mössbauer (a) emission and (b) absorption spectra of p-irradiated SnTe at liquid nitrogen temperature.

SnSb and SnTe were irradiated with 16-MeV protons in a helium atmosphere. Since tin metal enriched in ^{120}Sn (^{120}Sn 98.39 %, ^{119}Sn 0.39 %) was used for preparation of the samples in order to minimize the resonant self-absorption of the 23.8 keV Mössbauer γ-rays in the sources, the main nuclear reaction leading to ^{119}Sb must have been the ^{120}Sn (p, 2n) ^{119}Sb reaction. The Mössbauer emission and absorption spectra of the irradiated samples were measured at liquid nitrogen temperature. The standard absorber and source used in each measurement were $BaSnO_3$ and $Ba^{119m}SnO_3$ respectively.

Typical spectra obtained are shown in Figs. 1 and 2. The emission spectra (1 (a) and 2 (a)) represent the electronic state of ^{119}Sn in the Mössbauer level after the EC decay of ^{119}Sb produced by the proton reactions, while the absorption spectra (1 (b) and 2 (b)) show the radiation effect of the protons on the matrices.

As is seen in Fig. 1 (a), the SnSb irradiated with protons gave an emission line with an isomer shift of 2.4 mm/s. From the systematics shown in Table 1, this line is attributed to the ^{119}Sn atoms replacing the Sb-site of SnSb. The emission spectra of p-irradiated SnTe were composed of two lines with isomer shifts of 2.3 and 3.5 mm/s, which can be assigned similarly to the ^{119}Sn in the Te- and Sn-sites respectively (Fig. 2 (a)). As the recoil energy associated with the EC decay of ^{119}Sb to ^{119}Sn is not large enough to displace an atom in solid, the lattice positions of ^{119}Sn determined from the emission spectra are considered to represent simultaneously those of the preceding ^{119}Sb recoiled by the proton reactions. Therefore, the following conclusion can be drawn from the assignment described above: In case of SnSb all the recoil ^{119}Sb atoms produced by the proton reactions were stabilized in the Sb-site, while in SnTe the ^{119}Sb atoms were distributed among the Sn- and Te-sites. These observations show that the final lattice positions of the recoil ^{119}Sb atoms in the matrices are determined in the repairing process of the disordered lattice near the end of the recoil track. The absorption spectra of the irradiated SnSb and SnTe (Figs. 1 (b) and 2 (b)) revealed no significant difference from those of the unirradiated samples. This means that the radiation effect of protons on the matrices was less than the detection limit of the measurement.

References

1) F. Ambe, H. Shoji, S. Ambe, M. Takeda, and N. Saito: Chem. Phys. Lett., 14, 522 (1972).
2) S. Ambe, F. Ambe, and N. Saito: Radiochim. Acta, 19, 121 (1973).
3) F. Ambe and S. Ambe: Phys. Lett., 43A, 399 (1973).
4) F. Ambe, S. Ambe, and H. Shoji: Radiochem. Radioanal. Lett., 15, 349 (1973).
5) F. Ambe, S. Ambe, H. Shoji, and N. Saito: J. Chem. Phys., 60, 3773 (1974).
6) F. Ambe and S. Ambe: Bull. Chem. Soc. Japan, 47, 2875 (1974).
7) S. Ambe and F. Ambe: Radiochim. Acta, (in press).
8) S. Ambe and F. Ambe: Inorg. Nucl. Chem. Lett., 11, 139 (1975).

8-3. Behavior of Tritium and Hydrogen Atoms on Metal Surface

M. Aratani

The behavior of tritium and hydrogen atoms mainly on titanium surface has been studied by means of a charge spectrometer, the details of which being previously reported[1),2)]. Tritium atoms were fixed on the surface of a titanium plate (10 mm × 15 mm) in the form of titanium hydride. This was used as a beta-ray source and as an ion source of the spectrometer. The effective radioactivity was 96 mCi. Counting rates of various ions were measured at pressures from 6×10^{-5} to 2×10^{-7} Torr for $^{1}H_2$ and ^{4}He gases. In the present experiment, $^{1}H_2$ and ^{4}He were used instead of $^{3}H_2$ and ^{3}He, decay product of tritium, for the reason that use of tritium-containing gases in a metal chamber resulted in a "sticky" adsorption on the inside wall of the chamber,[3),4)] and an isotope effect did not affect adsorption and ionization.

As a result of measurement, it was revealed that there appear i) ground-state ions of helium at above 3×10^{-6} Torr, ii) metastable ions of helium at above 6×10^{-6} Torr, iii) ground-state ions of hydrogen molecules at above 1.8×10^{-6} Torr, iv) metastable ions of atomic hydrogen at above 3.6×10^{-6} Torr, and v) ground-state ions of atomic hydrogen in every run in the pressure range examined. Pressure dependence of the counting rates of the ions from i) to iv) is given by a linear expression, which is reasonably interpreted in terms of Henry-type adsorption and ionization of the adsorbed neutral species on the surface. The discussion will be published elsewhere.[5)]

On the other hand, the ions described in v) show entirely different behavior from the others. Pressure dependence of the ion counting rate is given by a cubic root expression. Threshold pressure does not appear in the pressure range examined. Extrapolation by the cubic root expression gives a threshold value of 10^{-9} Torr. This small value suggests that the ions are derived from the very "sticky" species on the surface. The cubic root expression implies that the species contains three atoms of hydrogen, for example, H_3, H_3C, H_3O, and so on. Helium, the decay product of tritium, is not "sticky" at any pressure below 3×10^{-6} Torr as decribed in i) and ii).

One of the most practical conclusions to be emphasized here is that hydrogen as well as tritium should be used in the pressure range below 10^{-9} Torr or in a solid form in order to avoid the "sticky" adsorption.

References

1) M. Aratani, M. Inarida, and N. Saito: IPCR Cyclotron Progr. Rep., 4, 117 (1970).
2) Y. Kawana and M. Aratani: Int. J. Mass Spectrometry Ion Phys., 10, 493 (1972/73).
3) A. Shimamura, M. Tonuma, I. Sakamoto, and I. Kohno: Reports I.P.C.R., (in Japanese)

48, 69 (1972).

4) T. Shiokawa: Private communication.

5) M. Suehiro, M. Aratani, and N. Saito: Mass Spectroscopy (in press).

8-4. Mass Asymmetry in the Fission of Actinide Nuclei

S. Yamaji, A. Iwamoto,* S. Suekane,** and K. Harada*

For the five isotopes of Th, Pu, Cm, Fm, and No and eight isotopes of U, the contour maps of the constant total potential energy were plotted as a function of the center separation Z_0 and the fragment deformations δ. The calculation was performed based on Strutinsky's prescription,$^{1)}$ in which the liquid-drop model of von Groote and Hilf$^{2)}$ and the modified two-center harmonic oscillator shell model were used for the macroscopic and microscopic parts, respectively.

The results of these systematic calculations of the actinide nuclei are collected in Table 1, in which the positions of the ground state, first saddle, second minimum, and the second saddle are shown.

Also are shown the ground state energy (E_{GS}) relative to the spherical liquid-drop model energy and heights of the first saddle (E_{BI}), the second minimum (E_{II}) and the second saddle (E_{BII}) relative to the ground state.

The discussion about these results by comparing with those of Möller and Nix$^{4)}$ will be given elsewhere and the present discussion is restricted to the mass asymmetry.

(1) Mass asymmetry and importance of some level pairs

In order to investigate the origin of mass asymmetry, in Fig. 1 the single particle level diagram at the second saddle is shown as a function of the fragment mass ratio. These are the neutron levels of ^{236}U because the neutrons are more responsible for the asymmetry than protons.

From Fig. 1 some pairs of levels with quantum numbers of (N O Λ) and (N + 1 1 Λ), for instance, pairs of ([615] $11/2^+$, [505] $11/2^-$), ([512] $3/2^-$, [402] $3/2^+$), ([512] $5/2^-$, [402] $5/2^+$), etc, can be found near the Fermi level. As was already pointed out in Refs. 5 and 6, these level pairs play an important role in directing the fission to an asymmetric path. The spacings of these levels are small at the symmetric deformation. The reason is that they begin to degenerate as Z_0 becomes large in the case of symmetric deformation and that the degeneracy occurs at an early stage of fission as they have small n_z. The level pairs are connected with the relation,

$$\Delta N = 1, \quad \Delta n_z = 1, \quad \Delta\Lambda = 0,$$

---

* Japan Atomic Energy Research Institute.

** Osaka City University.

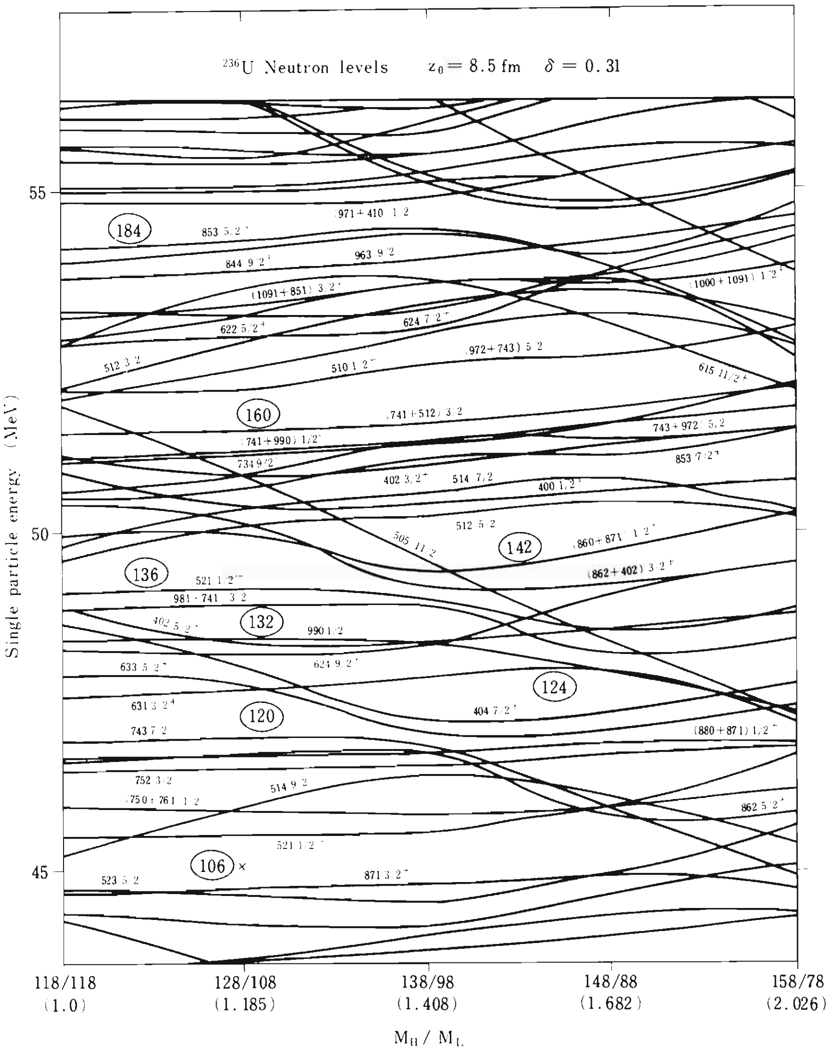

Fig. 1. The neutron single-particle level diagram of ^{236}U calculated at the second saddle point ($Z_0 = 8.5$ fm and $\delta = 0.31$) for symmetric fragmentation as a function of the mass ratio of the fragments. Each energy level is labelled by the asymptotic quantum number of Nilsson $(Nn_Z\Lambda)\Omega^\pi$ which is defined here as that of the main component of the wave function at the second saddle point for the symmetric fragmentation.

so that they have a large matrix element for the octupole deformation. Therefore they repel each other when the potential deforms asymmetrically and then level spacings between them become large.

The most apparent example of this phenomenon can be seen in the pair ([615] $11/2^+$, [505] $11/2^-$). As a result, there occurs a rather large energy gap between neutron number 142 and 144 at $M_H/M_L \approx 144/92$. This energy gap causes the asymmetric fragmentation.

It should be noted that the single particle levels as a function of mass ratio based on the

Table 1. The calculated locations and energies of the ground state, first saddle, second minimum, and second saddle. All energies are in unit of MeV and Z_0 are in unit of fm. At the second saddle, the most favorable masses of heavy fragments, M_H, and those of light fragments, M_L, are also shown. For the nuclei with asterisk, the contour maps of the collective potential energies are very irregular and in particular the locations of the second saddle are very ambiguous. So the mass ratios of these nuclei have little reliance. The locations were determined by the visual interpolation from the contour maps. The errors due to the procedure are about ± 0.2 fm for center separation Z_0 and ± 0.02 for deformation δ.

	Ground state			First saddle			Second minimum			Second saddle					
	Z_0	δ	E_{GS}	Z_0	δ	E_{BI}	Z_0	δ	E_{II}	Z_0	δ	E_{BII}	M_H	M_L	M_H/M_L
$^{232}_{90}\mathrm{Th}_{142}$	0.0	0.18	1.3	2.7	0.20	2.3	4.5	0.30	1.0	9.0	0.35	7.3	147	85	1.729
$^{236}\mathrm{Th}_{146}$	0.0	0.20	0.3	2.7	0.25	4.2	4.5	0.30	1.8	9.0	0.32	7.1	148	88	1.681
$^{240}\mathrm{Th}_{150}$	0.0	0.20	−0.5	2.5	0.27	5.0	5.0	0.30	3.0	9.0	0.30	8.4	147	93	1.580
$^{244}\mathrm{Th}_{154}$	0.0	0.20	−0.5	2.5	0.28	5.5	5.6	0.23	3.6	9.8	0.21	9.1	146	98	1.489
$^{248}\mathrm{Th}_{158}$	0.0	0.19	0.1	2.5	0.29	5.4	5.5	0.56	3.4	13.0	0.11	11.1	129	119*	1.084
$^{232}_{92}\mathrm{U}_{140}$	0.0	0.19	1.2	3.5	0.23	1.8	4.7	0.29	0.3	8.2	0.35	4.3	147	85	1.729
$^{234}\mathrm{U}_{142}$	0.0	0.20	0.8	3.5	0.20	2.7	4.5	0.30	0.7	8.5	0.35	5.1	148	86	1.720
$^{236}\mathrm{U}_{144}$	0.0	0.20	0.2	3.2	0.23	3.2	4.5	0.30	1.3	8.5	0.31	5.3	146	90	1.622
$^{238}\mathrm{U}_{146}$	0.0	0.20	−0.3	3.5	0.20	4.8	4.5	0.30	1.8	8.8	0.32	6.2	148	90	1.644
$^{240}\mathrm{U}_{148}$	0.0	0.20	−0.7	2.8	0.25	5.2	4.5	0.30	2.2	8.9	0.30	6.7	147	93	1.580
$^{242}\mathrm{U}_{150}$	0.0	0.20	−1.0	2.5	0.26	5.8	5.7	0.21	2.7	8.8	0.30	7.3	147	95	1.547
$^{246}\mathrm{U}_{154}$	0.0	0.20	−1.0	2.4	0.27	6.0	5.9	0.21	3.3	9.0	0.31	7.2	149	97	1.536
$^{250}\mathrm{U}_{158}$	0.0	0.20	−0.3	2.5	0.28	5.4	5.8	0.26	3.4	11.1	0.08	8.7	130	120*	1.083
$^{236}_{94}\mathrm{Pu}_{142}$	0.0	0.21	0.1	3.1	0.23	3.4	4.8	0.30	0.5	8.0	0.35	3.4	146	90	1.622
$^{240}\mathrm{Pu}_{146}$	0.0	0.20	−0.9	2.9	0.24	5.4	4.7	0.30	1.5	8.5	0.30	4.8	145	95	1.526
$^{244}\mathrm{Pu}_{150}$	0.0	0.20	−1.7	2.5	0.26	6.2	6.0	0.20	2.3	9.0	0.25	6.6	145	99	1.464
$^{248}\mathrm{Pu}_{154}$	0.0	0.21	−1.6	2.5	0.27	6.1	6.2	0.21	3.0	10.0	0.15	7.8	136	112*	1.214
$^{252}\mathrm{Pu}_{158}$	0.0	0.21	−0.9	2.5	0.28	5.7	6.0	0.26	3.0	12.0	0.00	6.2	129	123*	1.048
$^{238}_{96}\mathrm{Cm}_{142}$	0.0	0.20	−0.6	3.0	0.24	3.7	4.8	0.36	0.5	7.6	0.36	2.0	145	93	1.559
$^{242}\mathrm{Cm}_{146}$	0.0	0.20	−1.7	2.8	0.24	5.6	4.8	0.30	1.4	8.3	0.29	3.8	144	98	1.469
$^{246}\mathrm{Cm}_{150}$	0.0	0.20	−2.3	2.5	0.26	6.6	6.1	0.21	2.0	8.6	0.28	5.0	145	101	1.435
$^{250}\mathrm{Cm}_{154}$	0.0	0.20	−2.3	2.4	0.27	6.9	6.3	0.22	2.7	9.6	0.16	6.7	138	112*	1.232
$^{254}\mathrm{Cm}_{158}$	0.0	0.20	−1.7	2.5	0.27	6.4	6.9	0.19	2.6	9.2	0.04	3.4	127	127*	1.000
$^{240}_{98}\mathrm{Cf}_{142}$	0.0	0.21	−1.3	3.0	0.24	3.8	5.0	0.30	0.1	7.5	0.35	0.8	144	96	1.500
$^{244}\mathrm{Cf}_{146}$	0.0	0.21	−2.2	2.7	0.25	5.7	5.0	0.31	0.9	8.3	0.31	2.0	145	99	1.464
$^{248}\mathrm{Cf}_{150}$	0.0	0.21	−2.9	2.5	0.26	6.7	6.4	0.20	1.6	10.0	0.10	4.3	130	118*	1.101
$^{250}\mathrm{Cf}_{152}$	0.0	0.20	−2.9	2.5	0.27	6.6	8.2	0.12	1.5	9.4	0.05	3.9	132	118*	1.118
$^{252}\mathrm{Cf}_{154}$	0.0	0.21	−2.9	2.4	0.27	7.0	9.1	0.00	1.6	10.8	0.00	3.4	130	122*	1.065
$^{256}\mathrm{Cf}_{158}$	0.0	0.21	−2.9	2.5	0.30	6.8	9.3	0.00	0.6						
$^{242}_{100}\mathrm{Fm}_{142}$	0.0	0.21	−1.9	2.8	0.25	4.2	5.3	0.31	−0.4	6.6	0.41	−0.3	141	101	1.396
$^{246}\mathrm{Fm}_{146}$	0.0	0.21	−2.8	2.6	0.25	5.8	5.1	0.31	0.3	6.5	0.43	1.9	146	100	1.460
$^{250}\mathrm{Fm}_{150}$	0.0	0.20	−3.4	2.5	0.26	6.8	6.5	0.21	1.1	9.5	0.03	2.6	128	122*	1.049
$^{254}\mathrm{Fm}_{154}$	0.0	0.20	−3.4	2.5	0.27	7.1	8.1	0.12	1.3	9.5	0.05	1.4	128	126*	1.015
$^{258}\mathrm{Fm}_{158}$	0.0	0.19	−2.8	2.4	0.27	6.6									
$^{244}_{102}\mathrm{No}_{142}$	0.0	0.21	−2.2	2.8	0.25	3.7	5.7	0.33	−1.6	6.4	0.40	−2.2	139	105	1.323
$^{248}\mathrm{No}_{146}$	0.0	0.20	−3.1	2.7	0.25	5.6	5.4	0.33	−0.4	6.6	0.42	−0.4	144	104	1.384
$^{252}\mathrm{No}_{150}$	0.0	0.20	−3.7	2.5	0.27	6.6	6.7	0.22	0.2	8.7	0.25	1.0	143	109	1.311
$^{256}\mathrm{No}_{154}$	0.0	0.20	−3.7	0.5	0.37	6.6	7.3	0.20	0.2	9.8	0.09	0.8	131	125*	1.048
$^{260}\mathrm{No}_{158}$	0.0	0.20	−3.5	2.5	0.27	7.0									

asymmetric two-center shell model can give results very similar to those of Ref. 5 based on the one-center deformed shell model in which the strength of the Y_3 and Y_5 deformations must be carefully adjusted to reproduce the mass asymmetry.

(2) Constancy of the mass of the heavy fragments

We tried to understand a very interesting result that the masses of the heavy fragments are fairly constant (see Table 1). In Fig. 2 is shown the dependence of the shell correction energies of the neutron and the proton on the nucleon number and the mass ratio at the second saddle point (Z_0 = 8.5 fm, δ = 0.31), respectively.

From Fig.2(a), the energy gain in the shell correction energy of the neutron is about 5 MeV in the region of the neutron number 140 — 150, as the mass ratio increases from 1.0 to 2.0 and is most responsible for the mass asymmetry. The large energy gain comes from the rapid fall of the level [505] $11/2^-$, as was pointed out in Fig. 1.

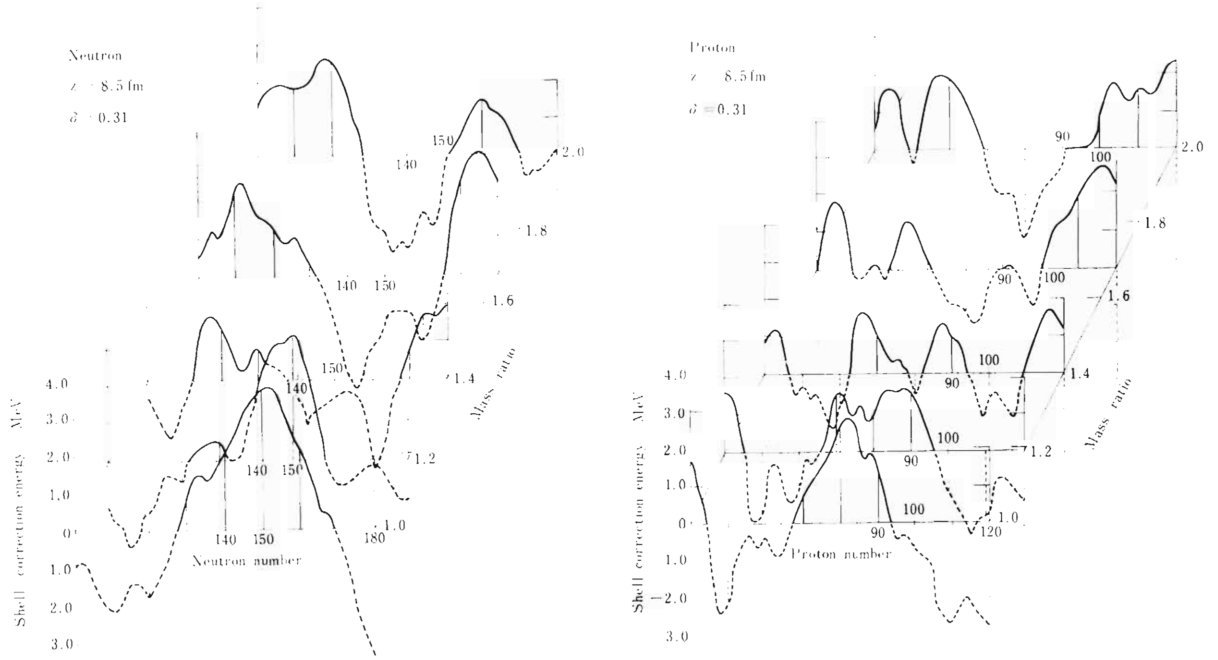

(a) (b)

Fig. 2. The shell correction energy at the second saddle point (Z_0 = 8.5 fm, δ = 0.31) as a function of the mass ratio and the nucleon number. The single particle level of ^{236}U are used for the calculation of the shell correction energy.

The neutron number at which the shell correction energy is minimum decreases from 160 to 140 as the mass ratio increases from 1.4 to 1.6 in Fig. 2(a).

This tendency of the shell correction energy of the neutron is consistent with the constancy of the mass of the heavy fragments through the isotopes.

In Fig.2(b), it can be seen that the energy gain in the shell correction energy of the proton with the proton number 90 is about 2 MeV as the mass ratio increases from 1.0 to 2.0.

However, the energy gain decreases as the proton number increases from 90 to 100. The energy gain is negative by about 1.5 MeV for the proton number 100, as the mass ratio increases from 1.0 to 2.0. The shell correction energy of the proton in Th and U region enhances the ratio of the mass asymmetry, while in No and Fm region it reduces the ratio of the mass asymmetry due to the shell correction energy of the neutron. Therefore, the constancy of the masses of the heavy fragments can qualitatively be understood for both isotopes and isotones in the actinide region.

The small discrepancy between the results shown in Table 1 and those of the above discussion comes from the facts that the position of the second saddle point is different for each nucleus, as can be seen in Table 1, and that the loss of the liquid-drop model energy due to the increase of the mass ratio reduces the most favorable mass ratio predicted by the shell correction energy only.

References

1) V. M. Strutinsky: Nucl. Phys., A95, 420 (1967); A122, 1 (1968).
2) H. V. Groote and F. Hilf: Nucl. Phys., A129, 513 (1969).
3) J. Maruhn and W. Gireiner: Zeit. Phys., 251, 431 (1972).
4) P. Möller and J. R. Nix: 3rd IAEA Symp. Physics and Chemistry of Fission, Rochester 1973 (IAEA, Vienna, 1974), Paper IAEA-SM-174/202.
5) C. Gustafsson, P. Möller, and S. G. Nilsson: Phys. Letters, 34B, 349 (1971).
6) B. L. Andersen: Phys. Letters, 42B, 307 (1972).

9. RADIATION CHEMISTRY AND RADIATION BIOLOGY

9-1. Heavy-Ion Radiolysis of Liquid Aldehydes

M. Matsui and M. Imamura

We have reported the significant LET effects observed for liquid aliphatic ketones over a wide LET range up to 90 eV/Å.$^{1), 2)}$ In these studies, the radiolytic yields of the main gaseous products, H_2 and CO, showed peaks in the range of LET = 50 – 70 eV/Å, and the ratios of the two yields, $G(H_2)/G(CO)$, increased steadily with an increase in LET. These results suggest the thermal decomposition of free radicals and/or the formation of highly excited states in a confined volume of the track cores of heavy-ion radiations.

An extensive study has been carried out also for some liquid aliphatic aldehydes; the preliminary results obtained for propionaldehyde will be described in this report. Emphasis is put on the radiolysis results in the relatively high LET region using N ions of 43 – 45 MeV (LET≈65 eV/Å).

The main gaseous products from aldehyde were H_2 and CO, the yields of which were determined by gaschromatography. Their yields increased steadily with an increase in LET; $G(H_2)$ and G(CO) at LET of 60 eV/Å were approximately 5 and 2, respectively. This result is in contrast with the case of pure ketones and indicates that an excessive energies deposited in the track core of high-LET particles may easily be transferred to the outside of the core, as in the case of ketones containing a small amount of H_2O. However, in view of the increase of the ratio, $G(H_2)/G(CO)$, with an increase in LET, thermal decomposition of free radicals produced from excited molecules must be important within high-LET tracks.

Major products other than H_2 and CO were C_2-hydrocarbons: C_2H_2, C_2H_4, and C_2H_6, which were not detected by gaschromatography from samples irradiated at low doses, however. They were observed to form and increase at a dose above 2 x 10^{19} eV. The yields of H_2 and CO showed no dose dependency.

It has been demonstrated$^{3), 4)}$ that liquid aldehydes containing olefin hydrocarbons produce telomers, $RCO(CH_2-CH_2)_nR$ (R=alkyl radicals), by γ-ray irradiation, and that the degree of telomerization increases with temperature. In the present study, a considerable amount of liquid with high boiling point was produced at a dose of around 1 x 10^{19} eV, where no C_2-hydrocarbons were detected. This product did not contain diethylketone (n=0), and presumably comprises several kinds of telomers. The production of C_2-hydrocarbons above 2 x 10^{19} eV is considered to be due to the secondary radiolytic decomposition of these telomers. Further studies are in progress.

References

1) M. Matsui, M. Imamura, and T. Karasawa: IPCR Cyclotron Progr. Rep., 5, 90 (1971); 7, 112 (1973).
2) M. Matsui and M. Imamura: Bull. Chem. Soc. Japan, 47, 1113 (1974).
3) K. Hirota and M. Hatada: ibid., 33, 1682 (1960); K. Hirota, S. Iizuka, H. Ochi, and M. Hatada: ibid., 36, 115 (1963).
4) C. E. Stoops and C. L. Furrow: J. Org. Chem., 26, 3264 (1961).

9-2. Optical and ESR Studies on Single Crystals of KBr and CdS Irradiated with Heavy Ions

K. Kimura, M. Matsui, and M. Imamura

Interaction of ionizing radiations with condensed matter produces highly excited states along their paths. Several short-lived species (excited states, excitons, ions, electrons, and neutral free radicals) are formed in the next physico-chemical stage. These species are localized in the vicinity of the radiation paths for a short time, forming spurs or tracks; the spatial distribution of these species is dependent upon the LET of the radiation.

Several studies have been made on the spatial distribution of these intermediates species in X- or γ-ray irradiated glasses and solids, but quite few in heavy ion-irradiated systems. Heavy ions having LET much higher than that of X- or γ-rays may give higher local concentrations of the species with different spatial distribution.

We have already reported ESR studies on some organic crystals irradiated with heavy ions.[1), 2)] It was found that these studies could provide valuable information on the spatial distribution of intermediate species, and therefore on the primary processes of radiation chemistry.

This report presents the results of color-center formation in KBr and emission from CdS by C-ion irradiation.

(1) Color centers produced in KBr single crystals

KBr single crystals were subjected to 85-MeV C-ion irradiation at 77 K, and their optical absorption and ESR spectra were recorded. ^{60}Co-γ irradiation was also carried out for comparison.

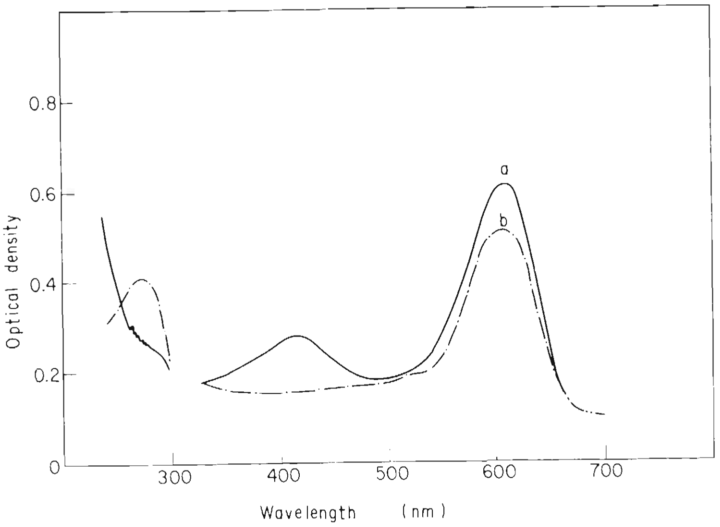

Fig. 1. Absorption spectra of the C ion-irradiated (a) and the γ-irradiated (b) KBr single crystals recorded at 77 K.

Figure 1 shows the electronic spectra. The species having a peak at 600 nm may be assigned to the F-center. The V_k-center (λ_{max} = 410 nm) was not observed for the C ion-irradiated sample. In contrast, the V_4-center, which was not observed for the γ-irradiated sample, appeared at 275 nm. The significant difference in the electronic spectra may be due to the thermal effect in heavy-ion tracks or an essentially different process between the two systems.

ESR spectra of the F-center are shown in Figs. 2 and 3. These spectra were recorded at

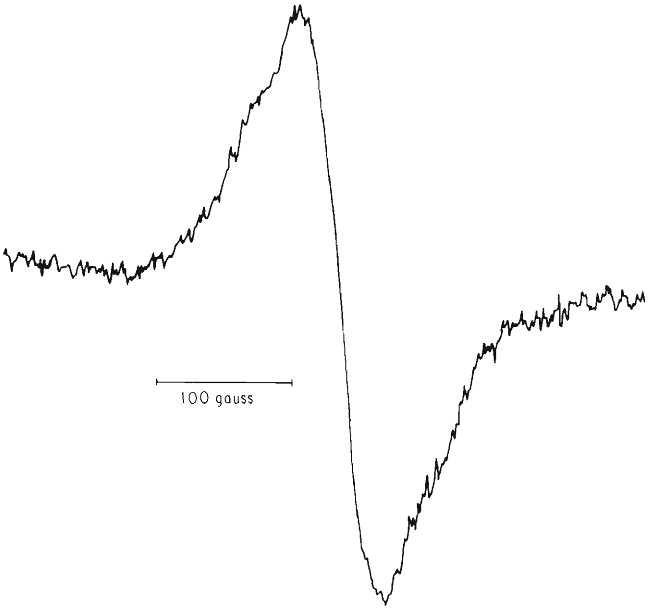

Fig. 2. ESR spectrum of the C ion-irradiated KBr single crystal recorded at 77 K after annealing at 130 K.

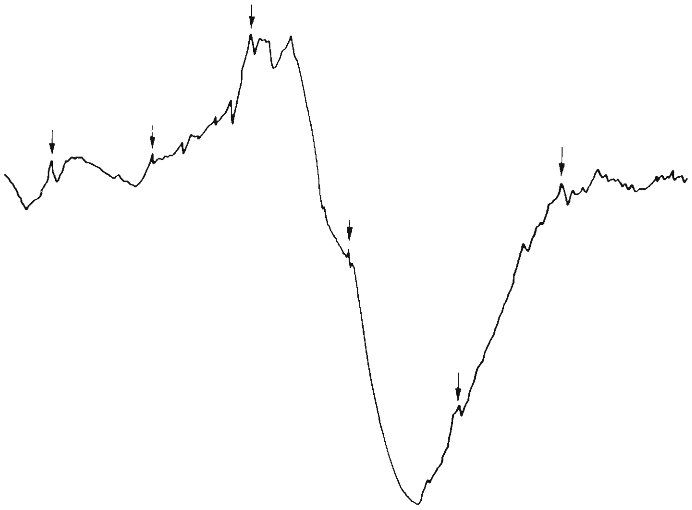

Fig. 3. ESR spectrum of the γ-irradiated KBr single crystal recorded at 77 K after annealing at 130K. Arrows indicate Mn^{2+} standard signals.

77 K after annealing the samples at 130 K; the annealing eliminated the spectra due to species other than F-centers. The linewidth of the spectrum for the C ion-irradiated sample is only a quarter of that for the γ-irradiated one.

The linewidth sharpening may be accounted for in terms of the exchange narrowing between F-centers trapped closely in the C ion-irradiated sample. In fact, on increasing the temperature of the C ion-irradiated sample to about 200 K, at which the F-centers become mobile, its linewidth showed broadening to the same extent as that for the γ-irradiated one. This argument is also supported by the experimental results on power saturation. A mean separation between F-centers in the C ion-irradiated sample was estimated to be 4 – 5 lattice units.

(2) Emission from CdS single crystals.

Determination of emission spectra during heavy-ion irradiation is one of the important experiment which may provide information on the nature of excited states produced by heavy-ion irradiation. No similar studies have been reported so far.

Preliminary experiments have been carried out to detect emission spectra from CdS single crystals under 85-MeV C-ion irradiation. Emission could be detected successfully and its spectrum was recorded by use of a monochromator and a photomultiplier; the spectrum gives peaks between 480 and 500 nm. However, owing to the weakness of the emission, no detailed results are available at this time. Improvement of the apparatus is now going on.

References

1) K. Kimura, M. Kikuchi, M. Matsui, T. Karasawa, M. Imamura, Y. Tabata, and K. Oshima: IPCR Cyclotron Progr. Rep., 6, 110 (1972).

2) K. Kimura, M. Matsui, T. Karasawa, and M. Imamura: ibid., 7, 114 (1973).

9-3. LET Effect on the Radiation-Induced Polymerization of Styrene

T. Yasukawa, T. Takahashi, M. Matsui, and M. Imamura

Radiation-induced polymerization in bulk and solutions is not a homogeneous reaction, because primary radicals or ions produced by irradiation are distributed inhomogeneously in spurs or tracks. Fair portions of active species are deactivated by neutralization or recombination in spurs without participation in polymerization, and only those active species which escape spurs initiate polymerization reactions. Under ordinary conditions, radiation-induced polymerization of styrene proceeds following the radical mechanism and polystyryl radicals are mostly deactivated by the recombination between them. The coupling between polymeric radicals is diffusion-controlled and consequently considered sensitive to the degree of polymerization of polymeric radicals. For the time being, however, the chain-length effects on the coupling process of polymeric radicals have not been elucidated sufficiently.

The chain-length distribution of polymer reflects accordingly the initial distribution of primary active species and the coupling processes of polymeric radicals. Hence, it would afford valuable information to investigate the LET effects on the molecular weight distribution of polystyrene obtained by various kinds of radiation.

Table 1. The G-values of gaseous products and polystyrene in the C ion-induced polymerization reaction of styrene. At room temperature and the total dose of 4.1 x 10^{18} eV in vacuo.

Product	H_2	C_2H_2	C_2H_4	C_2H_6	Polymer
G-value	1.34	0.21	0.03	0.87	0.04

Purified styrene sealed in vacuo in an irradiation vessel equipped with a thin Al window was irradiated with 83 MeV C ions to a dose of 4.1×10^{18} eV. Irradiated solutions were degassed by freeze-thaw cycles, and gaseous products were analyzed by gaschromatography. Polymer was separated from styrene monomer by vacuum distillation. Table 1 shows the G-values of gaseous products and polymer. The composition and the G-values of gaseous products are similar to those of ordinary compounds whereas the G-value of polymer chains is considerably small. The molecular weight distribution of polystyrene is shown in Fig. 1. Fair portions of polymer have a molecular weight larger than 1 x 10^6; this fact shows that some polymeric radicals have lifetimes as long as 10 s. Different from ordinary polystyrenes obtained by radical initiators or

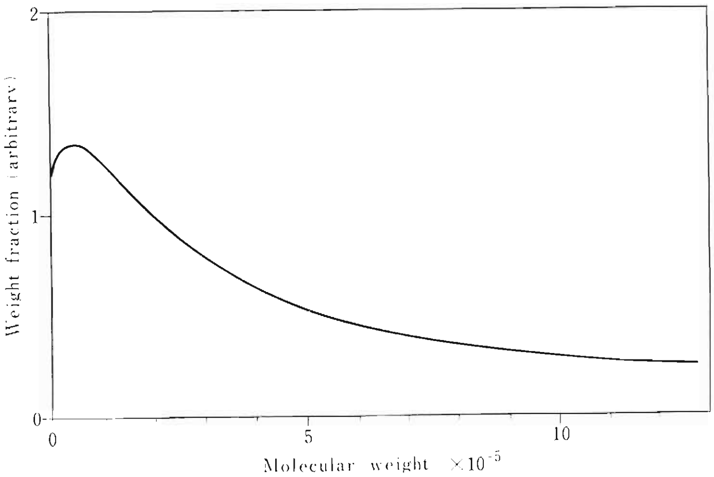

Fig. 1. Molecular weight distribution of polystyrene obtained by C-ion irradiation at room temperature. Energy of incident C-ions was 17.0 MeV and a total dose was 4.1 x 10^{18} eV.

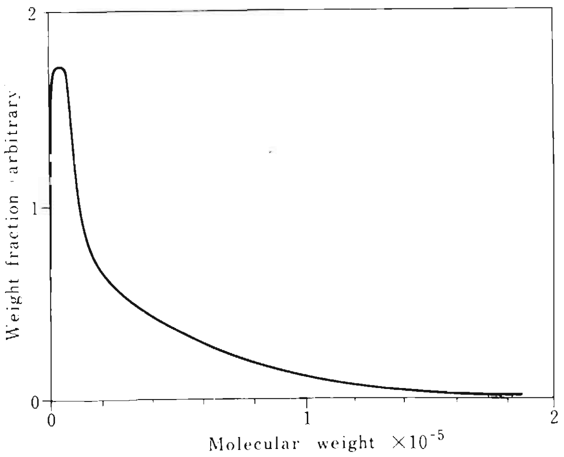

Fig. 2. Molecular weight distribution of polystyrene obtained by electron irradiation at 30°C. Total dose was 6 x 10^{18} eV/g.

photo-polymerization, the polystyrene obtained by C-ion irradiation has a considerably large value of $M_w/M_n = 4.48$. (M_w and M_n stand for the weight-average and number-average molecular weights, respectively.) These results suggest that growing radicals are not distributed homogeneously in solution. After all, we may well consider that in the C ion-induced polymerization of styrene, only a small portion of primary radicals (< 1 %) escapes the tracks to initiate polymerization reaction effectively, and that spatial distribution of growing radicals is considerably inhomogeneous.

In order to avoid secondary reactions, electron irradiation of styrene was carried out by means of a flow method. Styrene flowing in a stainless-steel pipe of 4 mm ϕ was irradiated with 1.5 MeV electrons through a slit 5 mm wide. Styrene monomer was circulated by using a gear pump at a rate of 10 mℓ/s at 30°C; the dose rate was ca. 3×10^{18} eV/g. s.

Figure 2 shows the molecular weight distribution of polymer obtained under these conditions. Different from Fig. 1, the distribution is fairly sharp and M_n is small. Although experimental conditions were considerably different from those for the C-ion irradiation, these results suggest that growing radicals are distributed homogeneously in respective volume elements of styrene flowing in the pipe.

Details of the experiments and discussion will be published elsewhere.

9-4. Inactivation of a Radioresistant Vegetative Bacterium Micrococcus radiodurans by Charged Particles

A. Matsuyama, T. Takahashi, and F. Yatagai

Since the repair capacity for radiation damages in DNA is expected to affect the LET effect upon bacterial inactivation, it is interesting to investigate the inactivation of repair-proficient bacteria by charged particles of different LET's. Micrococcus radiodurans has been found to have an efficient DNA repair capacity which may be responsible for its extraordinary resistance to γ- and X-rays.[1)-4)] Thus, in a series of our studies on bacterial inactivation by cyclotron beams, the LET dependence of the cellular radiosensitivity of M. radiodurans was determined under the same experimental condition as E. coli, and the results obtained were compared with those reported by Dewey.[5)]

Since the parameters of the survival curve of M. radiodurans considerably varied according to conditions, care was taken for the preparation of cell suspensions to be irradiated. M. radiodurans was grown overnight in a TGY broth (0.5 % Difco tryptone, 0.1 % glucose, and 0.3 % yeast extract; pH 7.0) at 37°C in a shaker culture under an aerobic condition. A 0.5 mℓ portion of the first culture was transferred into a 10 mℓ fresh TGY broth, and after 4 h of the second incubation at the same temperature, log-phase cells were centrifuged and washed twice with a 0.067 M phosphate buffer. The cell pellet obtained was maintained in an ice bath until use. Immediately before irradiation, cells were suspended in the 0.067 M phosphate buffer at a concentration of about 1×10^{-8} cells/mℓ. Preparation of the monolayer of bacterial cells on membrane filters and irradiation were performed as previously described.[6)] Survivors were determined by plating appropriate dilutions on a TGY agar.

Some examples of survival curves determined for α-particles, carbon, and nitrogen ions as well as ^{60}Co γ-rays are shown in Fig. 1. M. radiodurans gave the non-exponential survival curve consisting of a shoulder, followed by an exponential slope not only for ^{60}Co γ-rays but also for all charged particles used in this study. This observation is compatible with the results obtained by Dewey (the same bacterium)[5)] and by Mortimer et al. (yeasts).[7)] However, Todd[8)] reported that the survival curve of cultured mammalian cells becomes exponential in the LET region higher than about 220 keV/μm and the shoulder disappears from the curve. LET dependence of the length of the shoulder and the inactivation constant (k) calculated from the exponential slope are shown in Figs. 2 and 3, respectively. The results can be tentatively summarized as follows: (1) the length of the shoulder on the survival curve increases with increasing LET, especially in the LET region for heavy ions, (2) the inactivation constant k appears to decrease without any distinct peak as LET increases, and (3) the effective inactivation cross section (S_{eff}) for the exponential slope, which represents the relative effectiveness per particle, is remarkably dependent upon LET in the region for α-particles, but little dependence is observed for heavy ions (Fig. 4).

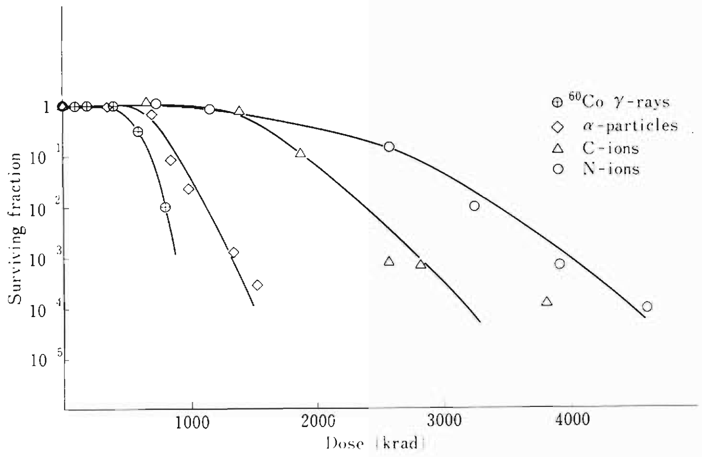

Fig. 1. Survival curves of M. radiodurans.

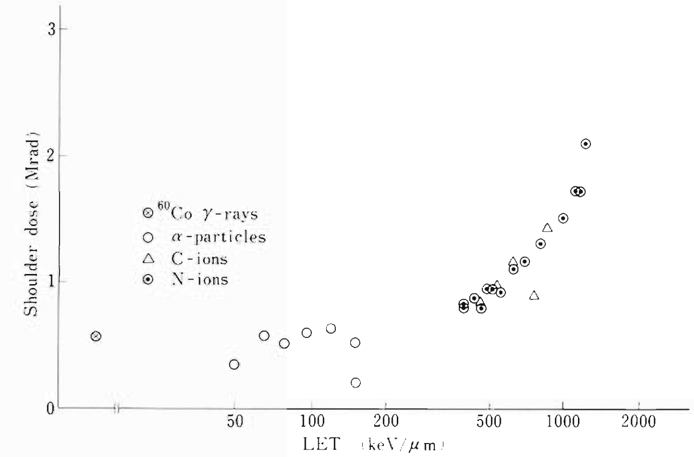

Fig. 2. LET dependence of the length of the shoulder on survival curves of M. radiodurans.

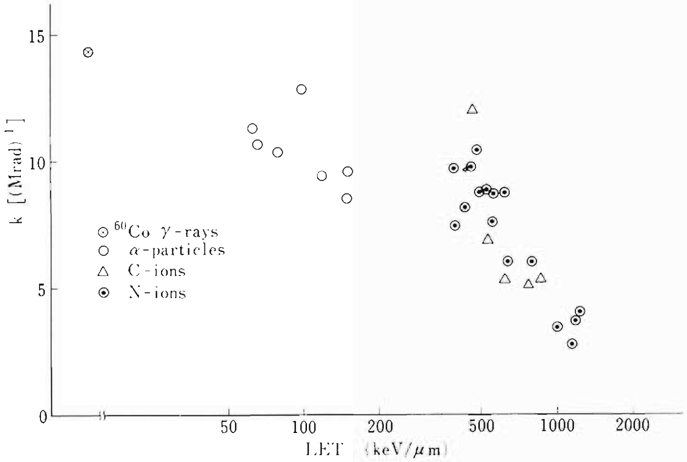

Fig. 3. LET dependence of inactivation constant (k) for the exponential slope of survival curves of M. radiodurans. (The inactivation constant k is the reciprocal of D_{37} for the exponential slope.)

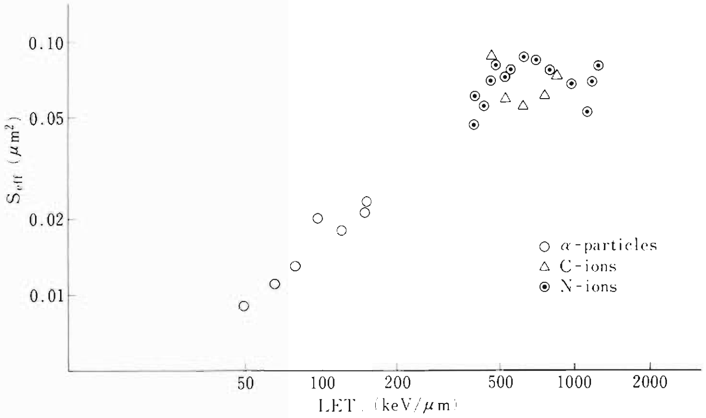

Fig. 4. LET dependence of effective inactivation cross section (S_{eff}) for M. radiodurans.

The result concerning LET dependence of the shoulder length is consistent with that obtained by Dewey^5) as mentioned above, whereas changes in the inactivation constant appear somewhat different. Further determination and analysis of the data are now under way. (The results described here are also slightly different from those reported in previous notes^6),9) of this series. The difference might be partly due to different experimental conditions, which will be discussed in the future study.)

References

1) B. E. B. Mosely and H. Laser: Nature, 206, 373 (1965).
2) C. J. Dean, P. Feldschreiber, and J. T. Lett: ibid., 209, 49 (1966).
3) S. Kitayama and A. Matsuyama: Biochem. Biophys. Res. Commun., 33, 418 (1968).
4) A. D. Burrell, P. Feldschreiber, and C. J. Dean: Biochim. Biophys. Acta, 247, 38 (1971).
5) D. L. Dewey: Int. J. Radiat. Biol., 16, 583 (1969).
6) A. Matsuyama, T. Karasawa, S. Kitayama, and R. Takeshita: IPCR Cyclotron Progr. Rep., 3, 101 (1969).
7) R. Mortimer, T. Brustad, and D. V. Cormack: Radiat. Res., 26, 465 (1965).
8) P. Todd: Radiat. Res. Suppl.,7, 196 (1967).
9) A. Matsuyama, T. Karasawa, T. Takahashi, Y. Asano, K. Igarashi, H. Kano, E. Fukuda, and Y. Ando: IPCR Cyclotron Progr. Rep., 4, 132 (1970).

9-5. LET Effects on Production of DNA Single-Strand Breaks and Their Repair in E. coli B/r

K. Igarashi, F. Yatagai, T. Takahashi, and A. Matsuyama

In a previous paper,[1] it was reported that the efficiency of production of DNA single-strand breaks in E. coli B_{s-1} decreases proportionally with increasing LET_∞ above 90 keV/μm. Since there are pieces of evidence that DNA is a target molecule for bacterial inactivation, the LET effect on DNA-strand breakage in bacterial cells endowed with different DNA-repair capacities has been investigated. In this report, the production and repair of DNA single-strand breaks in E. coli B/r cells irradiated with α-particles and nitrogen ions accelerated in the cyclotron are described. For comparison, irradiation with ^{60}Co γ-rays was also carried out. Procedures of irradiation and determination of DNA single-strand breaks in log-phase cells of E. coli B/r labeled with ^{3}H-thymidine were the same as previously reported.[1)-3)]

Survival curves of E. coli B/r determined for ^{60}Co γ-rays, α-particles, and nitrogen ions were all exponential. Figure 1 shows the sedimentation profiles in alkaline sucrose gradients of ^{3}H-DNA from E. coli B/r cells irradiated with these three kinds of radiation. For all types of radiation used here, irradiation was performed with three different doses giving surviving fractions of 1×10^{-2}, 1×10^{-4}, and 1×10^{-6} in order to confirm the linear relationship between the number of DNA-strand breaks and dose. Using values of the number-average molecular weight of DNA calculated from the sedimentation profiles, one can obtain the dose-response curves for DNA-strand breakage produced by radiations and then values of the efficiency of DNA single-strand break production, E_{sb} (eV/break). As can be seen in Fig. 2, E_{sb} increases with increasing LET_∞. Although the number of data obtained with E. coli B/r is still insufficient, it appears that E_{sb} can be regarded as a linear function of LET_∞ and the LET_∞-E_{sb} curve for nitrogen ions shifts to the higher LET side as compared with that for α-particles. These results obtained with strain B/r are consistent with those reported with strain B_{s-1}. However, E_{sb} values of strain B/r were larger than those of strain B_{s-1} at the same LET. This difference in E_{sb} values between these two strains will be examined in further determinations.

In order to compare the rates of DNA repair after exposure to ^{60}Co γ-rays and nitrogen ions, cells were reincubated at 37°C for 40 min after irradiation. Figure 3 shows examples of sedimentation profiles of ^{3}H-DNA during the course of post-irradiation incubation. Both doses indicated in Fig. 3 gave a surviving fraction of 1×10^{-4}. Relationships between the time of post-irradiation incubation and the number of DNA single-strand breaks calculated from sedimentation profiles during post-irradiation incubation are illustrated in Fig. 4. The results indicate that DNA single-strand breaks are hardly repaired after the exposure to nitrogen ions, while they are appreciably rejoined after γ-ray irradiation, and that nitrogen ions produce a smaller number of single breaks than γ-rays at the same cell survival lebel (Fig. 4).

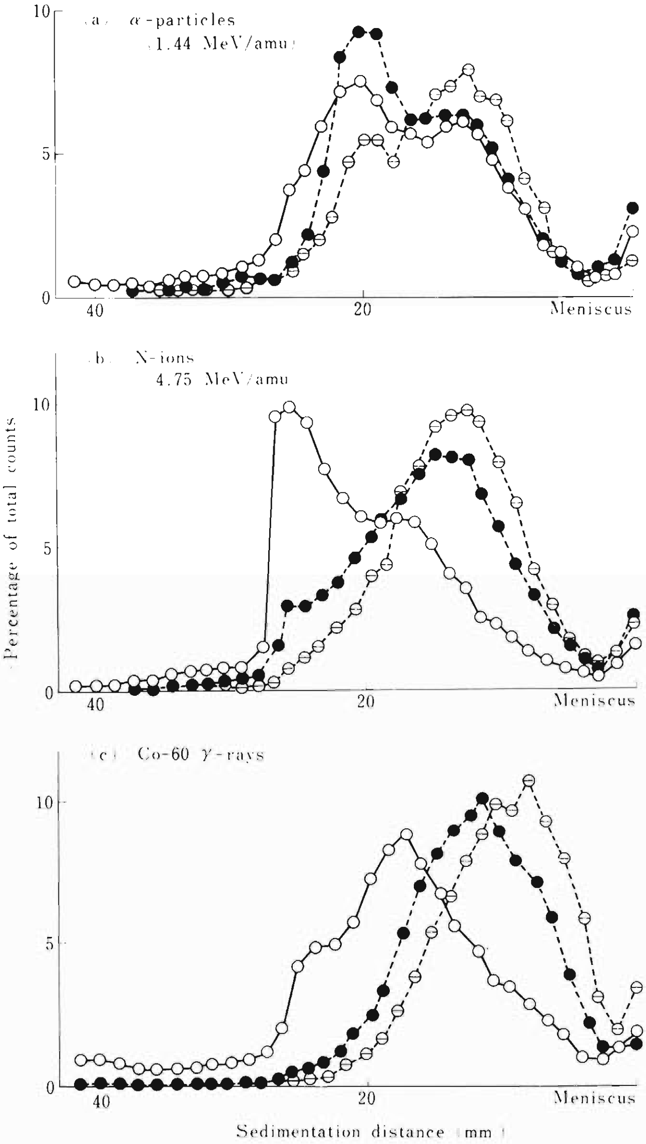

Dose:

(a) ○, 38.6 krad; ●, 57.4 krad; ⊖, 77.6 krad
(b) ○, 42.8 krad; ●, 80.2 krad; ⊖, 140 krad
(c) ○, 28.0 krad; ●, 56.0 krad; ⊖, 112 krad

Surviving fraction:
(a) and (b) ○, 1×10^{-2}; ●, 1×10^{-4}; ⊖, 1×10^{-6}
(c) ○, 1×10^{-1}; ●, 1×10^{-2}; ○, 1×10^{-4}

Fig. 1. Sedimentation profiles of ^{3}H-DNA from E. coli B/r immediately after irradiation.

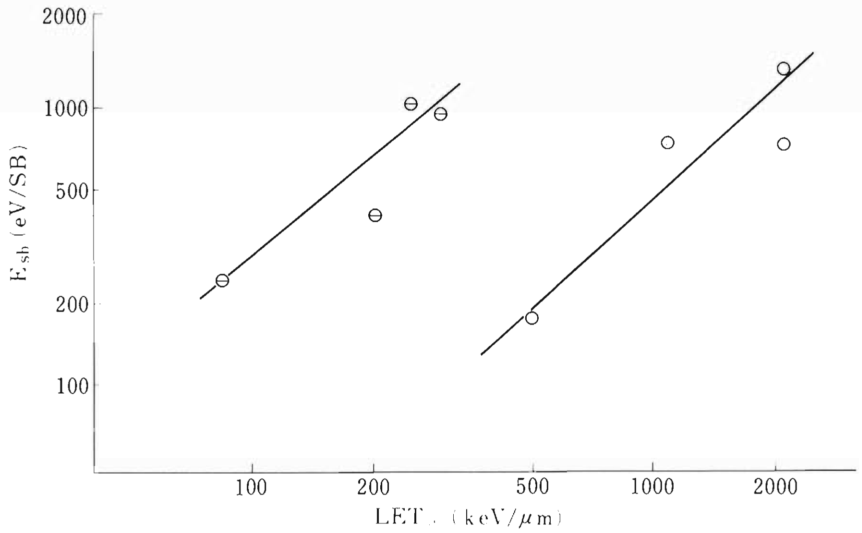

Fig. 2. LET dependence of the efficiency of DNA single-strand break production (E_{sb}) in E. coli B/r. ⊖, α-particles; ○, nitrogen ions.

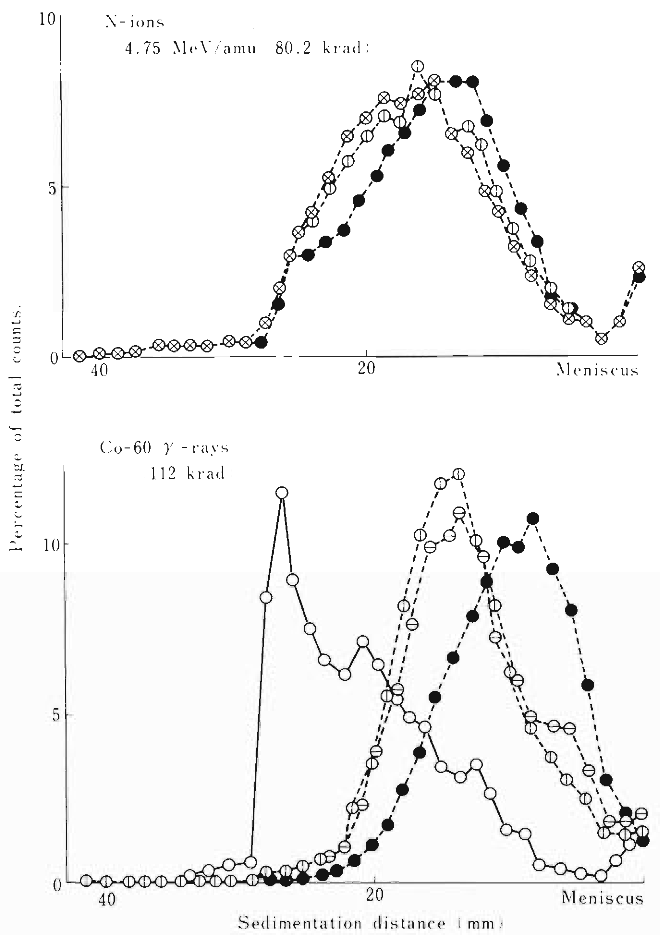

○, Unirradiated; ●, Irradiated, no reincubation; ⊖, ⦶, and ⊗, Irradiated, reincubated for 5, 15, and 40 min, respectively.

Fig. 3. Sedimentation profiles of ^{3}H-DNA from E. coli B/r after post-irradiation incubation.

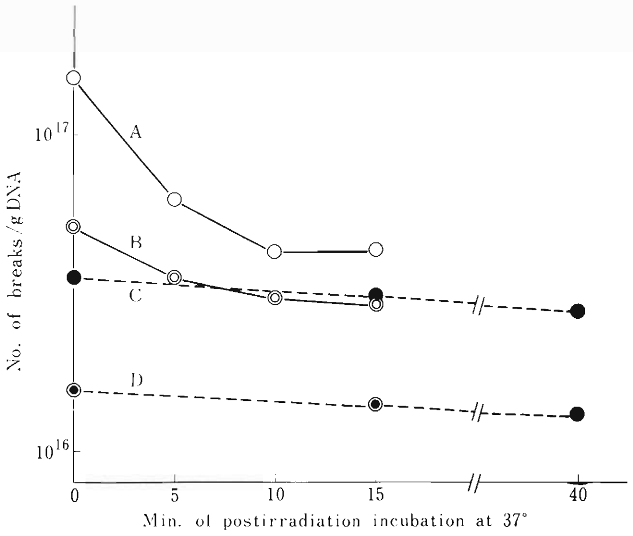

Fig. 4. Changes in number of radiation-produced DNA single-strand breaks in E. coli B/r during post-irradiation incubation. A and B: 112 krad and 56 krad of ^{60}Co γ-rays, respectively; C and D: 80.2 krad and 42.4 krad of nitrogen ions, respectively. Surviving fraction: A and C, 1 x 10^{-4}; B and D, 1 x 10^{-2}.

References

1) K. Igarashi, F. Yatagai, T. Takahashi, and A. Matsuyama: J. Radiat. Res., 15, 148 (1974).
2) A. Matsuyama, T. Karasawa, S. Kitayama, and R. Takeshita: IPCR Cyclotron Progr. Rep., 3, 101 (1969).
3) K. Igarashi, F. Yatagai, T. Takahashi, and A. Matsuyama: ibid., 7, 122 (1973).

10. PREPARATION OF RADIOISOTOPES AND LABELED COMPOUNDS

10-1. Production of Radioisotopes and Preparation of Labeled Compounds for Medical Use

T. Nozaki, S. Ambe, M. Iwamoto, A. Tahara, T. Ohsawa,
T. Karasawa, M. Okano, T. Ido, K. Fukushi, K. Suzuki,
L. Iwata, T. Hara, and K. Taki

We have continued our work on the preparation of ^{18}F-organic compounds and the measurement of their in vivo distributions. The production of ^{28}Mg and $^{13}NH_3$ and the preparation of seleno-methionine labeled with ^{72}Se and ^{73}Se have also been studied. Further, our production techniques for ^{43}K and ^{123}I recently have been notably improved.

By the reaction of Ag ^{18}F with 6-chloro-9-benzylpurine in toluene, 6-fluoro-9-benzylpurine-^{18}F was prepared. This compound was found to have a marked tendency of being concentrated in brain. The ^{18}F-labeling of some physiologically active steroids has aroused our interests for medical use. Introduction of ^{18}F-atom into the steroid molecule was completed by cleavage of epoxide ring with $B^{18}F_3\cdot Et_2O$. The utilization of other fluorinating reagents (e.g., $CF_3O^{18}F$) is now under study.

The yields of ^{28}Mg for triton-induced reactions were already reported.$^{1)}$ Possible α-particle reactions for the production of ^{28}Mg were also examined, and a convenient process for the carrier-free separation of ^{28}Mg from an aluminum target was devised. A paper describing details of these studies is in press.$^{2)}$

The proton bombardment of water has been used for the production of ^{13}N. The excitation curve for the reaction of $^{16}O(p, \alpha)^{13}N$ was measured; a ^{13}N activity sufficient for diagnostic use is shown to be obtained by this bombardment even for an incident energy of 9 MeV. A major portion of the ^{13}N thus produced in water was found to be usually in anionic states. The ^{13}N was converted into carrier- and salt-free $^{13}NH_3$ by a reductive distillation, and its distribution in mice was measured. The $^{13}NH_3$ has proved to be useful in heart scanning.

Now in Japan, two medical-use cyclotrons are under trial operation and a so-called Baby Cyclotron capable of producing only ^{11}C, ^{13}N, ^{15}O,and ^{18}F is under construction. Most of our present experiments are so designed as to give good empirical bases for satisfactory uses of each of the new machines.

References

1) T. Nozaki, M. Furukawa, S. Kume, and R. Seki: IPCR Cyclotron Progr. Rep., 5, 83 (1971).
2) T. Nozaki, M. Furukawa, S. Kume, and R. Seki: Int. J. Appl. Radiat. Isotopes, (in press.)

11. RADIATION MONITORING

11-1. Routine Monitoring

K. Koda, I. Sakamoto, and I. Usuba

Results of routine monitoring on the cyclotron obtained from January to December 1973 are described.

No remarkable change in leakage radiation and residual activities was observed during this period.

(1) Surface contamination

The surface contamination of the floor of the cyclotron room, where the highest level of contamination had usually been detected in the cyclotron building, has been kept to be about $10^{-6} - 10^{-7}$ μCi/cm^2 as a result of wiping-off of the floor twice a year.

(2) Drainage

The concentrations of radioactive nuclides in drain water and sediments in the drainage tank of the cyclotron building were measured and found to be of the order of 10^{-7} μCi/cm^3 and 10^{-4} μCi/cm^3, respectively. This difference would have been caused by the absorption of radioactive nuclides dissolved in drain water by the sediment.

(3) Personnel monitoring

Owing to the revision of the regulation of the work in the cyclotron vault as described in a previous report,¹⁾ the exposure of workers decreased remarkably as shown in Table 1.

It was shown that no one received a dose above 1000 mrem and the average value of dose per person in this period was cut down to less than one-half of that in the previous year.

Table 1. Annual exposure dose distribution of the workers and average dose from 1969 to 1973.
(Dose accumulated from April to next March.)

Year	Total number of workers	Dose distribution (mrem)					Average dose per person (mrem)
		Undetectable	10 ~ 100	101 ~ 300	301 ~ 1000	>1000	
1969	46	–	11	17	16	2	318
1970	49	–	19	12	15	3	299
1971	50	7	15	15	12	1	261
1972	47	10	17	12	7	1	199
1973	48	14	22	11	1	0	79

Reference

1) K. Koda, I. Sakamoto, and I. Usuba: IPCR Cyclotron Progr. Rep., 7, 134 (1973).

12. A NEW MACHINE

12-1. The Variable-Frequency Linac Project Status at Autumn 1974

M. Odera

It was admitted by the Government to start the construction of a linac cavity in the 1974 fiscal year. A team for detailed engineering design was organized and investigations including experimentation with cavity models and manufacturing of prototype drift tubes and modulated light signal transmitting, receiving, and decoding circuits to be used in an injector system are in progress. Discussions on fabrication techniques are being made with several firms.

Owing to inflation at a rocketing rate from the fall of the last year, we have met difficulties to procure things with the expenses estimated in the budget proposed at the beginning of 1973. Some alterations in specifications of several components were inevitable. Fortunately, for the vacuum system, a development of new type pumps seems to warrant the spesifications without much degrading its performance. To change the design of the radiofrequency resonator is more difficult and its possibility is still being investigated.

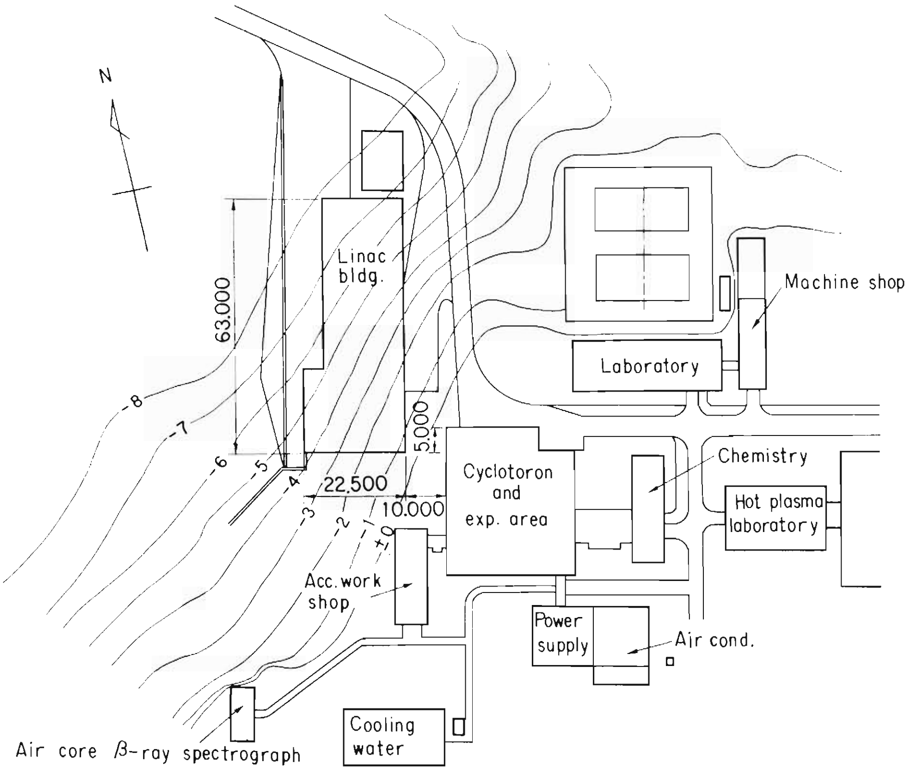

Fig. 1. Site of the planned linac building near the cyclotron facilities.

Our building schedule is lengthened by one year because of delay of installation of air conditioning equipment and pushing up of the cost.

A design study of cavity using models has almost completed. A continuous operation for the range of frequency from 18 to 43 MHz seems to be assured and on a reduced duty factor a much wider range is usable if an obround shape for the cavity cross section is chosen. The cavity models will be discussed in the following reports. The site of construction under plan is indicated in Fig. 1. It is on a slope slanting down westward from just outside of the shielding wall of the cyclotron experimental area. Excavation of the ground will begin next summer.

12-2. Design Study Using Cavity Models

M. Odera, Y. Chiba, Y. Miyazawa, and M. Hemmi

We studied following subjects using cavity models at atmospheric pressure.

(1) Determination of details of cavity parameters: Since field patterns around the drift tubes are difficult to estimate accurately by calculation owing to smallness of symmetry of the structure of the cavity, the pattern and the highest frequency have to be determined by experiment.

(2) Estimation of power loss: For the same reason stated above, the power loss at higher frequencies has to be estimated by the models.

(3) Field distribution along the acceleration axis: This is necessary for the determination of drift tube length.

(4) Search of parasitic resonances. Though the fundamental resonant frequency is determined by the length of center stem and the capacity of drift tube and so only a simple spectrum for higher resonant frequencies is expected, particular construction of the cavity might induce odd resonances unexpected. It is desirable to know whether or not those unwanted resonances exist and interfere with the fundamental mode.

Table 1. Summary of results obtained by studying models.

Type of cavity	II	III	IV
Resonant frequency (MHz)	18 – 50	15 – 40	17.5 – 56
Frequency range for uniform voltage distribution (MHz)	18 – 49	15 – 38	17.5 – 45
Frequency range within power limit (MHz)	18 – 45	15 – 40	17.5 – 43

Four models were tested and the results were used for the design of real cavities. Table 1 shows a brief summary of the test. Model I is omitted there since its role was mainly exploratory. In Table 1, the range of frequency is given for 2,000 mm stroke for the shorting plane, the criterion of uniformity for voltage is ±10 % and the power loss limit means an electrical shunt impedance larger than 200 kΩ. The last value gives a power dissipation within 230 kW for peak voltage 300 kV across the tube gap.

12-3. Summary of Measurements on Electrical Characteristics of Model Cavities I and II

M. Odera and Y. Chiba

Since a new configuration of a resonator is planned as an accelerating structure of the linac, detailed investigation of the characteristics of the resonator has been made for these years.

Figures 1 and 2 show dimensions of two real scale models of cavities I1) and II. They differ in the method of frequency change and in the material of fabrication. The model II has a single shorting plane movable along the center stem and is made of plywoods lined with thin copper plates, whereas the model I has two moving panels and two large capacity compensators and is fully made of aluminum.

Model I, which is the first model constructed, was used to survey the working principle of the quarter wave resonator having a large width compared with the length and loaded heavily with drift tubes at the voltage loop.1) It was made to be able to change volume of various parts separately and freely to find out any odd resonances and the effect of asymmetry of the structure. No significant odd mode was found, but degradation of quality factors was clearly observed when a right-left asymmetry was introduced about a plane including the acceleration axis and the center stem. In studying the performance of this model by use of a perturbation technique we proved the validity of the principle of the cavity; namely, the voltage distribution along the acceleration axis is fairly uniform for a wide frequency range,2) which permits acceleration of ions with different mass to charge ratios at different frequencies, and the frequency spectra of higher modes

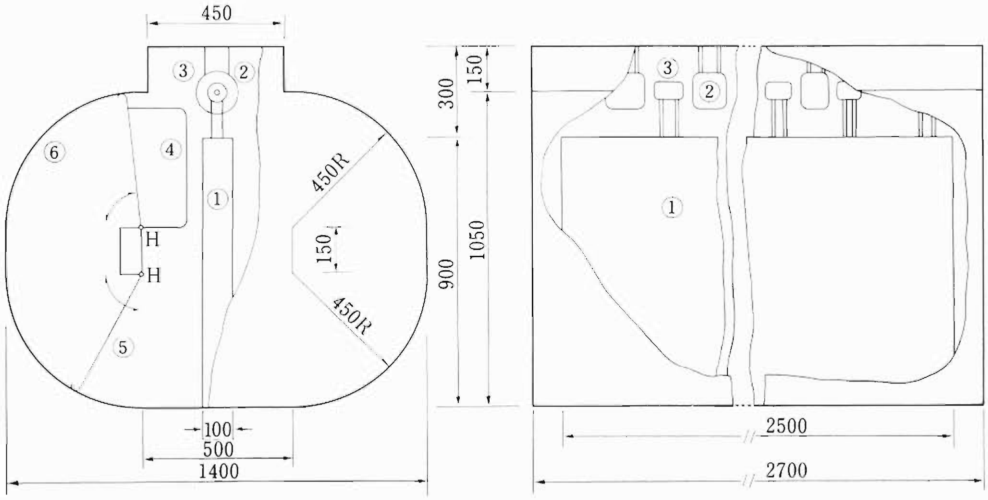

Fig. 1. Model I: ① center stem; ② drift tubes at ground potential, the outer diameter being 130 mm; ③ drift tubes at radiofrequency high voltage, the outer diameter being 60 mm; ④ capacity compensators; ⑤ movable panels; and ⑥ outer conductors.

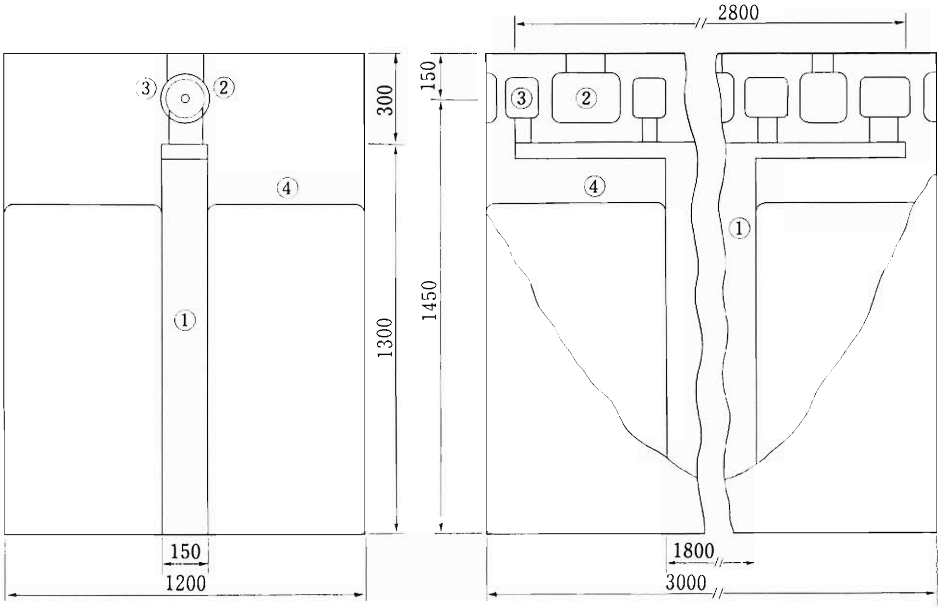

Fig. 2. Model II; ① center stem; ② drift tubes at ground potential, the outer diameter being 160 mm; ③ drift tubes at radiofrequency high voltage, the outer diameter being 130 mm; and ④ movable shorting plane.

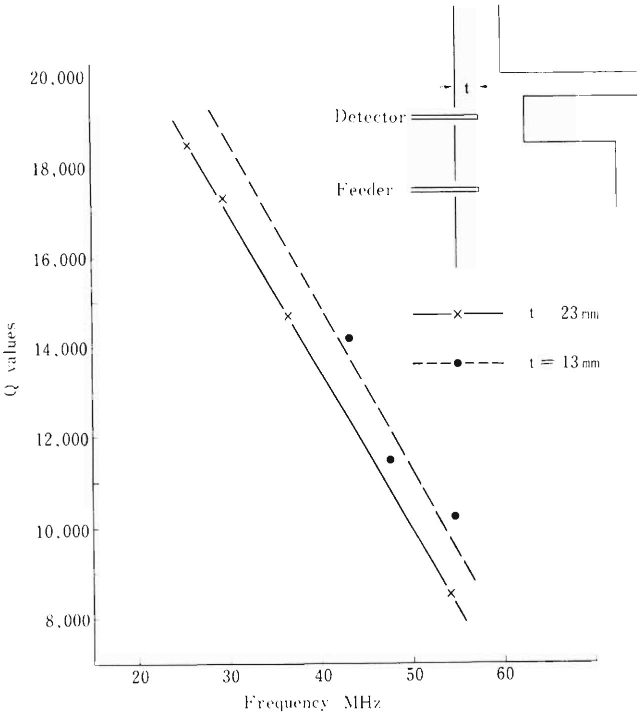

Fig. 3. An example of the effect of coupling strength of a detector or a feeder with a cavity on measured quality factors. The values are for the model II with drift tubes removed.

are simple[2] and discrimination of them presents no problem in operation.

Model II was constructed as a full-sized model in which a shorting plane was used as a device for frequency change. It was mainly used to estimate power dissipation especially at higher frequencies. The method of measurements is shown in Fig. 1 in an article 12-12 in this Progress Report,[3] and is the same as that used in the design work of the cyclotron,[4] except a PIN diode bridge was used instead of a vacuum tube as a switching element. Power feeding and signal pick-up were made by capacitive probes attached to one side of the cavity.

Figure 3 shows the effect of coupling strength on the measured Q values suggesting larger true values for a cavity when loading by a generator or a detector was able to be eliminated. Figure 4 shows the Q values and electrical shunt impedances obtained by this method. The latter is defined here as (peak voltage across drift tube gaps)^2/(2X power loss). This curve is of service to estimate the radiofrequency power required for this type of cavity.

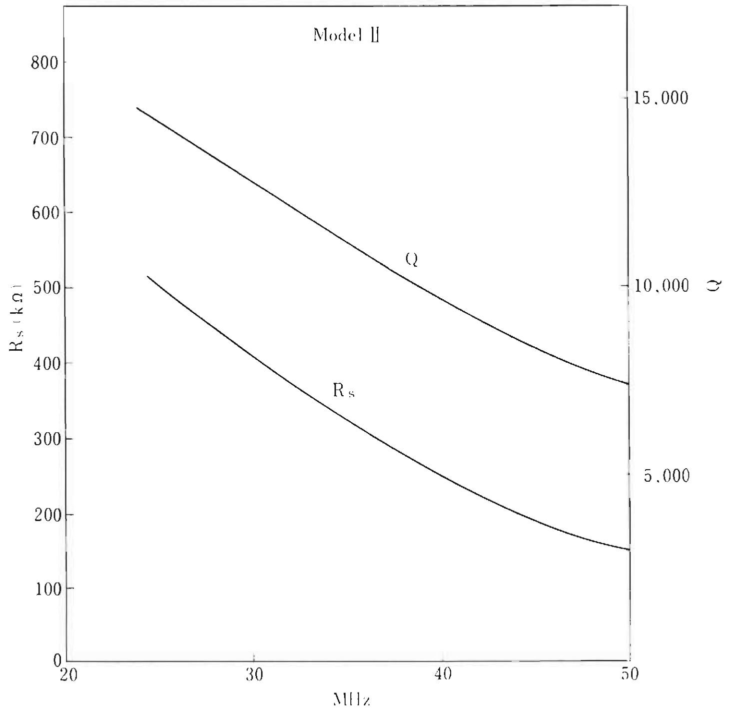

Fig. 4. Quality factors Q and electrical shunt impedance Rs as a function of resonant frequency.

References

1) M. Odera: IPCR Cyclotron Progr. Rep., 6, 16 (1972).
2) M. Odera, T. Tonuma, M. Hemmi, and Y. Chiba: ibid., 7, 143 (1973).
3) S. Takeda: ibid., 8, 157 (1974).
4) M. Odera, Y. Chiba, T. Fujisawa, Y. Miyazawa, and O. Terajima: Sci. Papers I.P.C.R., 67, 99 (1973).

12-4. Voltage Distribution at the Gap of Model II with the Drift Tubes Removed

Y. Chiba and M. Odera

Voltage distributions along the axis of acceleration of various models show several characteristic features in common: distinct change of distribution according to harmonic numbers; voltage drop at both extreme gaps which becomes more distinct at higher frequencies; and variation of voltage more remarkable than the corresponding error of gap length.

In order to study the nature of these characteristics, the drift tubes were removed and spacers made of copper plates were inserted to give a capacity equivalent to that of drift tubes. Figure 1 shows one of the settings and Fig. 2 an example of corresponding field distributions. The curves show high sensitivity for small undulation on the surface of copper plates and the distinct change of voltage distribution according to the harmonic number is also clearly observed here. These patterns can be easily explained and the corresponding frequencies be estimated approximately by postulating resonances in the parallelepiped volume which is formed by cutting half the cavity through the center symmetry plane including the acceleration axis. There are other resonances at very high frequencies which resemble an H-type mode of cylindrical cavities.

Next, a part of the gap was made narrow to see the effect of local deviation of capacity distribution. Figure 3 shows its geometry and voltage distribution thereof. A gradual elevation of field strength towards the part having high capacity was seen. This effect of nonuniform distribution of capacity or other parameters upon field deviation also present in the Alvarez and

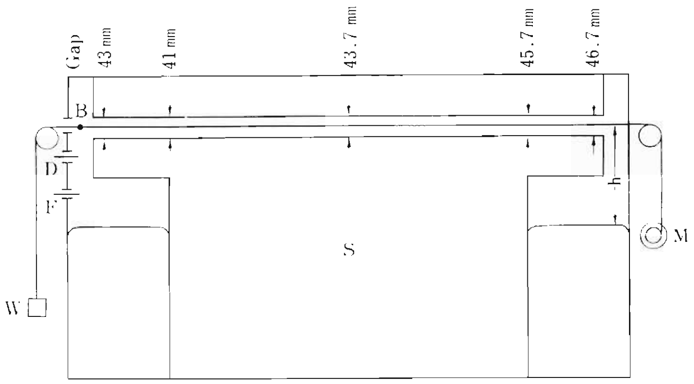

Fig. 1. Model II with drift tubes replaced with spacers. S, center stem; D, detector probe; F, power feeder; B, metal bead; M, motor to drive a string for translation of bead through gap; W, weight to give tension to the string; h, distance of shorting plane from the acceleration axis.

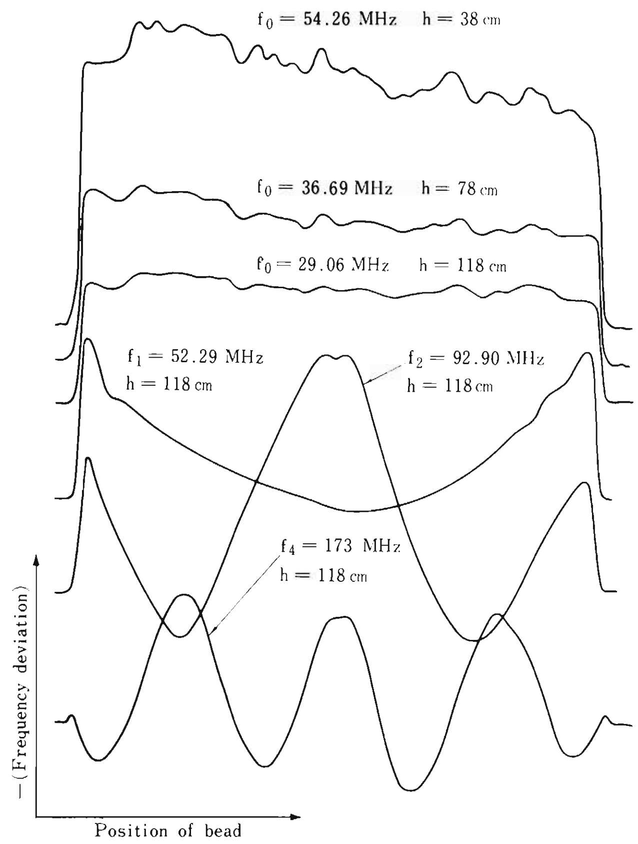

Fig. 2. Field patterns expressed by frequency distribution. Numbers following a letter f denote order of harmonics.

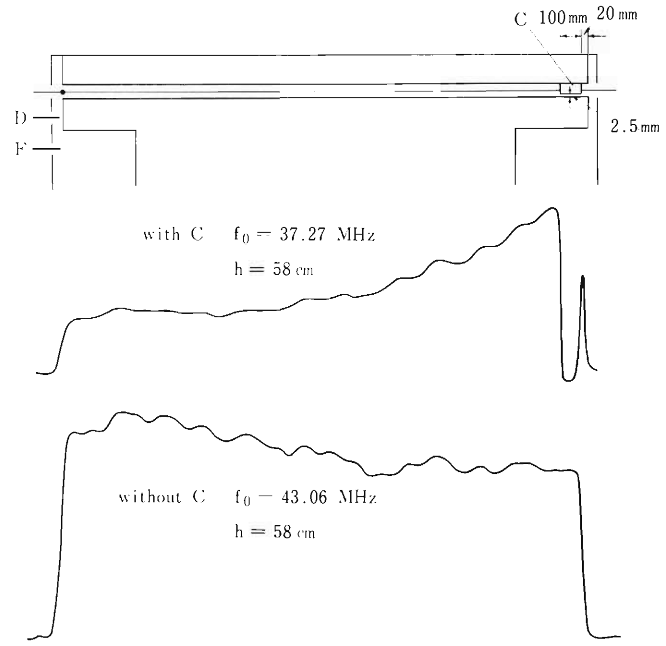

Fig. 3. Effect of local deviation of capacity along the acceleration axis. Reversal of slope of distribution shall be noted.

Inter-digital H-type resonators. The sloping of field strength may be expressed in another way that the field strength is larger around the part where local resonant frequency is lower than in other parts of the cavity. Such an effect explains the phenomenon mentioned in the first part, namely, the field strength in the narrow gap is elevated more than the value given by the value of gap length. It would be possible to describe this phenomenon quantitatively by considering local deviation of high frequency current. However we were satisfied using the knowledge for improvement of the characteristics of the cavity which proved to be very useful.

The lowering of field strength at the extreme gaps when the open end of the cavity is loaded with drift tubes may be accounted for by adding the tank-end effect similar to that of H-type resonator to the above effect of local parameters deviation which is inevitable for the extreme gaps.

12-5. Results of Measurements on Model III of Linac Cavity having a Stem of Circular-Shape

M. Odera

Model II, which has a stem of a rectangular shape, has excellent electrical characteristics[1] such as a wide frequency range, ease of discrimination of higher modes, good Q factors, and uniformity of voltage distribution along the acceleration axis. However, its mechanical construction is not very advantageous for actual fabrication, especially when a single shell structure is adopted,[2] and the outer conductor has to support the atmospheric pressure as well as high frequency currents.

If a circular shape can be used, most of the mechanical difficulties of a single shell structure would be eliminated. Model III was manufactured to investigate this possibility. It was made of plywoods and lined with copper plates. It has a polygonal cross section instead of circular on account of prompt fabrication. Figure 1 shows the structure of model III.

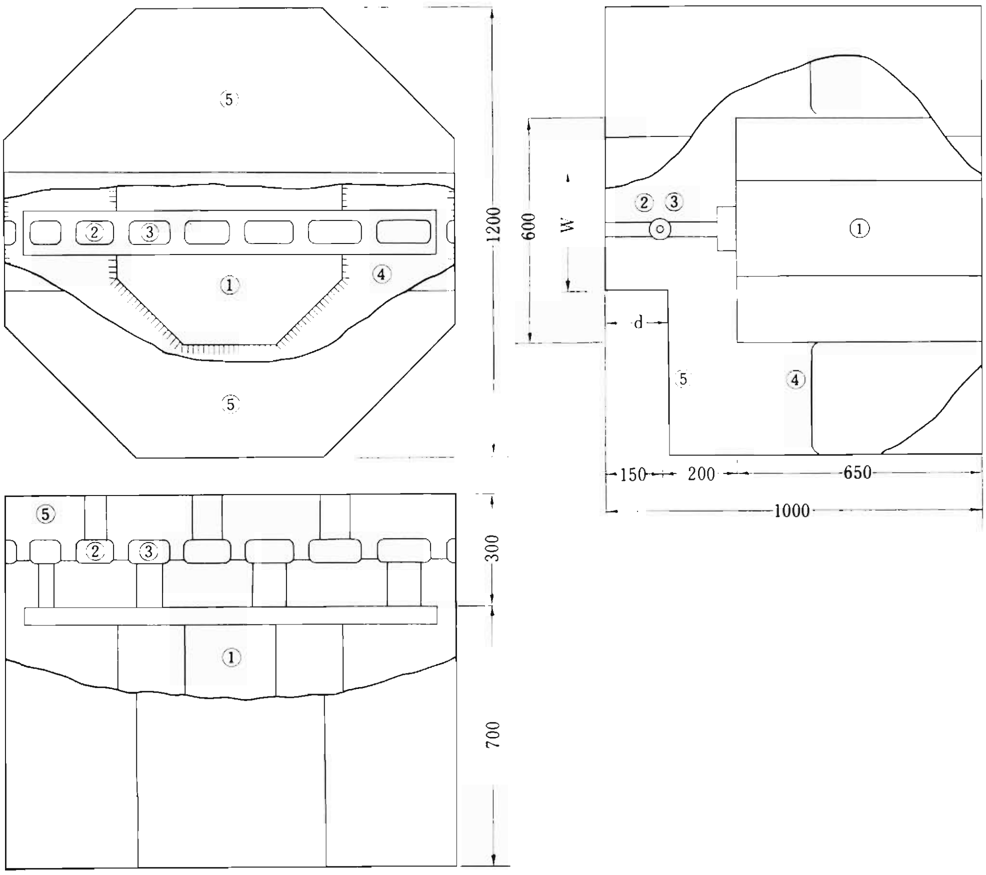

Fig. 1. Model III: 1, center stem; 2, drift tubes at ground potential; 3, drift tubes at radiofrequency high voltage; 4, shorting plane; 5, liners which bound a volume around each drift tube.

As expected, voltage distribution is not very favorable and various improvements were tried by shaping volume around drift tubes. Figure 2 gives an example showing the effect of shaping. Although the method was very effective, the distribution comparable to those obtained for the rectangular one at 50 MHz was unable to be realized above 40 MHz. On the other hand, the quality factors were superior to model II reflecting more uniform current density around the stem of model III.

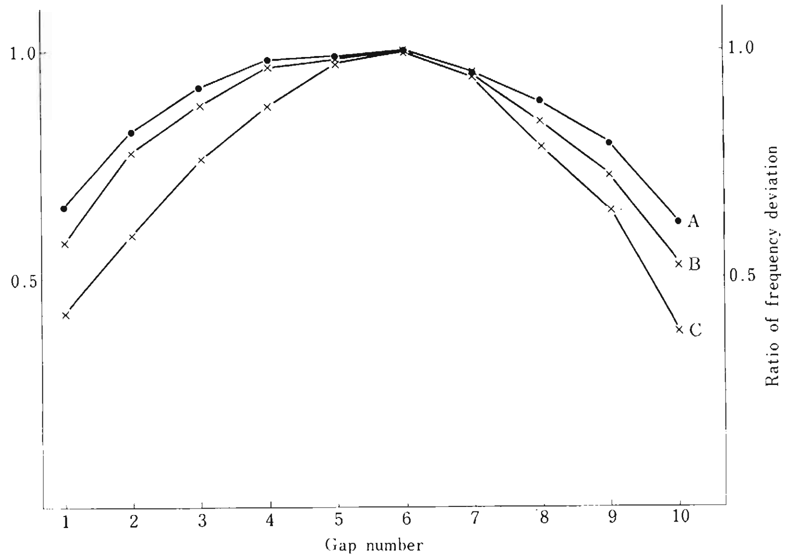

Fig. 2. Variation of field pattern along the acceleration axis by change of the shape of volume around the drift tube.

Curve A: d = 170 w = 330

Curve B: d = 170 w = 490

Curve C: d = 0 w = 1220

Voltage distribution is given by square-root of the ratio of frequency deviation.

References

1) M. Odera and Y. Chiba: IPCR Cyclotron Progr. Rep., 8, 139 (1974).
2) Linac Design group: ibid., p. 148.

12-6. Results of Measurements on the Model IV of the Linac Cavity

Y. Miyazawa, M. Hemmi, and M. Odera

The model IV is a scaled model by 1/2.5 of a configuration chosen as a structure of the first cavity. Figure 1 shows its construction. It is made of plywoods lined with copper plates as was done in the model III. The characteristic impedance of transmission line is 32 ohm. Figure 2 gives its resonant frequencies as a function of position of the shorting plane. Overall property of this model is similar to that of the model II but by shaping the volume around the drift tubes as was done in the model III, a wider frequency change was found possible. As is seen in Fig. 2, it can resonate from 17.5 to 55 MHz and the frequency range is more than enough for the present project.

Quality factor of 11,900 for 42 MHz is also satisfactory and is a little better than that of model II.[1]

The voltage distributions along the axis of acceleration show somewhat less quality than in model II and this cavity can be used up to 45 MHz with ±10 % uniformity criterion. Further improvement in this respect is planned.

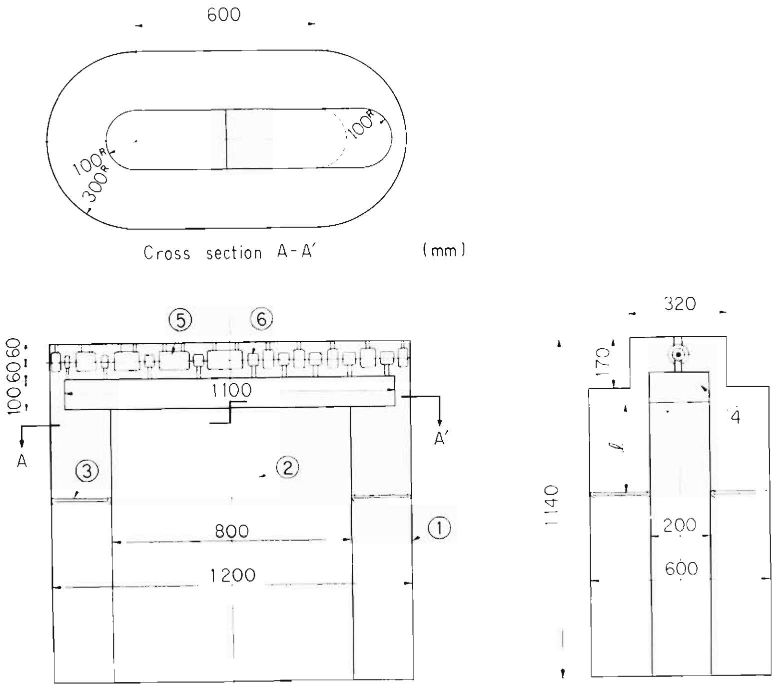

Fig. 1. Model IV; 1, outer conductor; 2, center stem; 3, shorting plane; 4, drift tube supporting arm; 5, drift tubes at ground potential, quadrupoles will be installed; 6, drift tubes at radiofrequency high voltage and no quadrupoles.

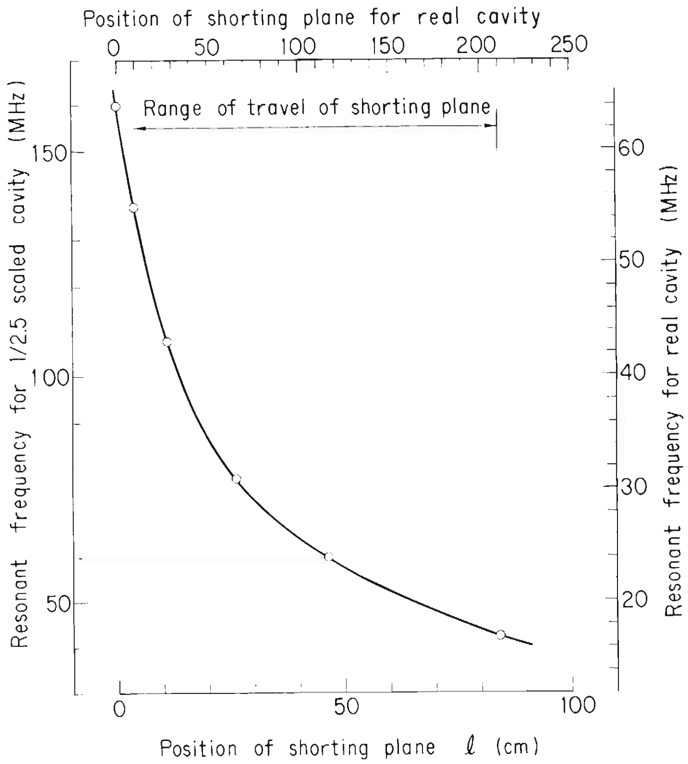

Fig. 2. Resonant frequencies of model IV. Right and upper scales indicate values coresponding to those for a real cavity.

Reference

1) M. Odera and Y. Chiba: IPCR Cyclotron Progr. Rep., 8, 139 (1974).

12-7. Design of the Linac Cavity

General

M. Odera, Y. Chiba, M. Hemmi, T. Inoue,
Y. Miyazawa, T. Tonuma, and F. Yoshida

The cavity is the most crucial element for success of the present project, and also is the most expensive part. As described in other reports,[1)-4)] several choices in designing the cavity are possible. Weighing ease of operation, maintainance, future improvement, cost of fabrication etc., we have to decide a final design.

At present, because of a vacuum problem, we have abandoned a double-shell structure which consists of a vacuum vessel and a radiofrequency resonator. If a single shell scheme is to be used, mechanical strength necessary for supporting atmospheric pressure is unpractically large for a rectangular shape as in the model II, so other structures must be adopted. A circular shape is most favorable in this respect but its electrical characteristics measured with the model III[3)] are not very attractive. However, it might be the best one when acceleration of ions was limited to those having mass-to-charge ratios larger than 6. Then, the highest frequency needed would be below 35 MHz, and at such a low frequency there is no problem of non-uniform field distribution. Moreover, mechanical construction is simple and fabrication is not difficult.

On the other hand, the shape of the model IV consisting of two semi-circular and straight parts has characteristics between those of oblong and circular cross sections. Electrically, it has a range enough for resonant frequency and good quality factors. Mechanically, though it is necessary in the designing against excessive deformation the precaution is not so much required as in the oblong case. Therefore, we have decided to go on with this type until some necessity for alteration is found. Figure 1 in Ref. 4 shows a sketch of the obround-shaped cavity.

Due attention to vacuum and radio-frequency requirements must be paid in the design. As for the vacuum, clean and high vacuum is most desirable. Exclusion of organic contamination and water from the surface of the vacuum vessel is necessary and efforts to keep the surface area as small as possible is imperative. The single-shell structure satisfies the last requirement better than the double-shell cavity.

Fine adjustment of frequency must be possible. One or two capacity compensators must be provided per cavity in addition to a movable shorting plane which can be positioned in steps of less than 1 mm. Such a small step of the plane permits setting of frequency within 100 kHz and finer tuning may be made by the compensators.

Close tolerances in mechanical fabrication are not required in this type of cavity except for those concerning the alignment of drift tube axes. Especially, misalignment of the quadrupole focusing elements induces directly loss of beam or broadening of beam profile. Therefore, the drift tubes which contain quadrupoles must be carefully manufactured so that the axis of tube aperture should rigorously coincide with that of quadrupole; this is necessary to make it possible to align the focussing quadrupoles by use of tube apertures.

Beam dynamics demands higher field gradients for shorter drift tubes where the velocity of particle is small. That means that larger ampere-turns are required for coils packed in narrower spaces. Methods for fabrication and cooling of the coils are being studied and tried at present.[5] A final design will be decided within several months.

References

1) M. Odera, Y. Chiba, Y. Miyazawa, and M. Hemmi: IPCR Cyclotron Progr. Rep., 8, p. 138 (1974).
2) M. Odera and Y. Chiba: ibid., p. 139
3) M. Odera: ibid., p. 144.
4) Y. Miyazawa, M. Hemmi, and M. Odera: ibid., p. 146.
5) T. Inoue: ibid., p. 159.

12-8. Design of the Linac Cavity

Mechanical Problems

Y. Miyazawa and M. Odera

The cavity must not deform and disturb the alignment of the drift tubes when the cavity is evacuated. Parts of the vacuum tank which have the largest effect on the drift tube alignment are the bottom and upper lids. The center stem is fixed on the bottom lid and a small warping of the latter will induce a large displacement of the drift tubes attached on the top of the long stem. It is not determined yet how to support the earth-side drift tubes, but if the upper lid is used for the support, a reinforcement of the lid must be made sufficiently, because the earth-side drift tubes contain focusing quadrupole magnets in them and an effect of misalignment of the axes of the magnets on the beam quality is much larger than that of drift tubes on the center stem which do not have quadrupoles installed.

The side wall of the vacuum tank of which the inner surface is an outer conductor of the co-axial resonator shall be well reinforced. Equations for calculation of the deformation which proved effective in the design of the cavity of the cyclotron having a similar shape to that of the present linac were applied to estimate a necessary reinforcement. A deformation of the outer shell is expected to be smaller than 0.5 mm and the displacement of the drift tubes should be within 0.2 mm.

The movable shorting plane has a traveling distance of 2000 mm in high vacuum. The position of the plane must be adjustable in steps of 1 mm or less from the control room. Shorting contacts should provide a resistanceless path for large high-frequency currents. It is planned to press contacts made of silver wire to the wall of the cavity with a force of around 4 kg/cm along the wire. Bellows pressurized by air and a lever mechanism can be used for this purpose. Shorting contacts of the cyclotron to which a pressure of 2 kg/cm is applied show no sign of excessive heating by high-frequency currents up to 50 A/cm^2 in the period of 7 years of operation. Of course, different frequencies are used for the cyclotron so that the difference in the skin depth must be taken into account. However, thin flexible copper tapes connecting those contacts with parts where cooling pipes are soldered can be made shorter for the linac, since there is no need to make the stem movable like the cyclotron where the position of the dee electrode has to be readjusted at times. Shortening a heat conducting path is effective to suppress the temperature rise of the contactor leads.

12-9. Design of the Linac Cavity

Cooling

Y. Miyazawa and M. Odera

The cavity walls must be well cooled, otherwise rising temperature might bring about some trouble. In particular non-uniform local heating must be avoided carefully.

Figure 1 shows current densities at shorting contacts as a function of drift tube voltage. The inset illustrates the parts of contact where the currents i_1, i_2, and i_3 flow. Figure 2 shows the maximum ohmic loss density at each part of the cavity made of copper. The cooling problem is most serious for the highest frequency, because it is at this frequency that the skin depth is smallest and the current density is largest. Therefore, cooling channels must be provided as many as possible to avoid heating at the highest frequency. The largest heat generation per unit area is expected at the rounded part of the center stem as can be seen from Fig. 2. The flow rate of cooling water or the number of cooling channels should be determined, corresponding to the distribution of radio-frequency loss.

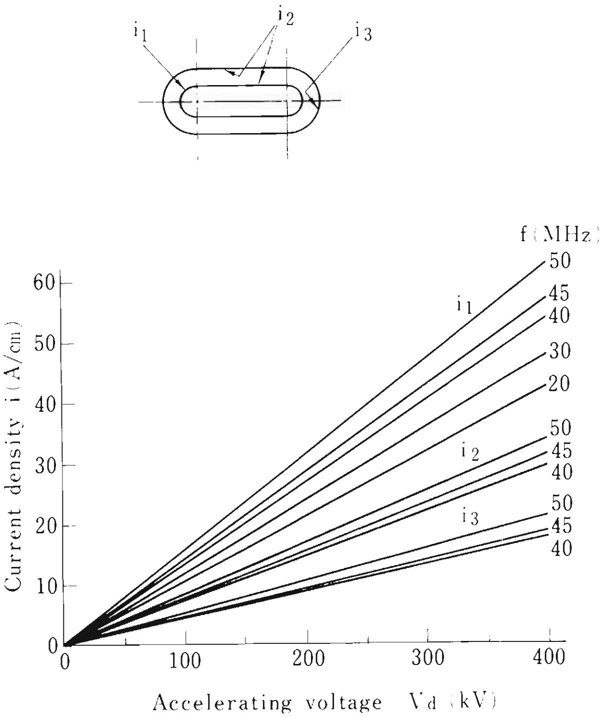

Fig. 1. Surface current density at shorting contacts as a function of voltage across drift tube gaps. i_1, i_2, and i_3 correspond to the currents at the places indicated in the inset above.

Frequency is a parameter.

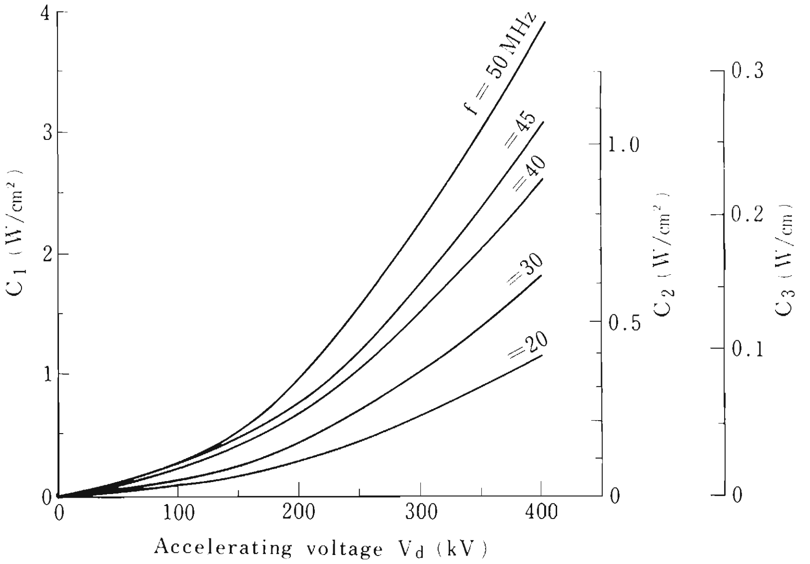

Fig. 2. Power dissipation per unit area of the cavity at shorting contacts. C_i represents the loss at the place i of Fig. 1.

12-10. Design of the Linac Cavity

Vacuum Consideration

Y. Miyazawa and M. Odera

The design of the vacuum system should be made according to the following requirements: firstly, to minimize beam intensity attenuation or beam quality degradation due to collision of heavy ions with residual gases in acceleration; secondly, to avoid as far as possible adsorption of organic substances and water vapor onto the surface of the vacuum vessel, since such a contamination is known to reduce the threshold value for sparking in vacuum by high-frequency voltage.

The first requirement is necessary for acceleration of very heavy ions with a mass of about 200. Charge exchange cross sections are in the neighborhood of 10^{-14}cm^2 for such ions and loss of the beam intensity by the process is by no means negligible even at a low pressure like 10^{-7} Torr.

The second is a general requirement every linac except for a case where the particle velocity has reached nearely the velocity of light already. Usually, a velocity profile is pre-determined for each geometry and a corresponding acceleration voltage must be exactly maintained. Although these conditions are somewhat relaxed in our linac by an adoption of a variable frequency scheme, the largest voltage sustainable determines the maximum energy obtainable by the linac. The higher voltage holding capacity is obviously desirable.

In order to attain a good vacuum the following precautions are necessary: exposuring of surfaces of organic materials such as O-ring seals must be minimized; the inner surface area of the vacuum vessel should be kept as small as possible; the material of the inner surface should be chosen to keep the out-gassing rate very low; the method of fabrication ought not to induce occlusion of organic substances such as oil and grease under the surface nor to leave voids with small openings to vacuum; only such a pump which has little possibility of introducing oil, water or other undesirable substances should be used.

We intend to use cryo-pumps and turbo-molecular pumps in parallel to reach a pressure as low as 10^{-7} Torr with least condensation of undesirable substances on the surface of the vessel. Roughing-pumps such as rotary or Roots blower pumps are to be operated only above 10^{-1} or 1 Torr to prevent backstreaming of oils. A cryo-pump having pumping speed of 5,000 ℓ/sec for N_2 gas (for example, Philips K-20) will be installed next spring and be evaluated whether it is suited for our purpose or not.

A major portion of the inner surface is covered with copper for conduction of radio-frequency current. Fortunately, the out-gassing rate of copper is not bad and is in the range of 10^{-10} Torr. ℓ/(sec.cm^2) after several tens of hour of pumping. For other parts, stainless steel is mainly used and, when use of iron is inevitable, electroplating with copper or nickel is planned to prevent rusting of iron. As noted in another place,$^{1)}$ a single-shell structure adopted has much smaller surface area than a double-shell structure and it makes attainment of high vacuum easier.

In introducing mechanical movements into the vacuum system, a predominant use of metal bellows is planned and a linear motion through an O-ring seal should be avoided as far as possible.

Reference

1) Linac design group: IPCR Cyclotron Progr. Rep., 8, 148 (1974).

12-11. Distribution of Magnetic Flux Density in the Poles of Drift Tube Quadrupole Lenses

M. Hemmi and M. Odera

Since the requirement of radial focusing cannot be satisfied under the condition of longitudinal or phase stability in acceleration, some means must be provided to compensate a radial defocusing force in a linac. In the present linac, magnetic quadrupole lenses are planned to be installed in the drift tubes which are at radiofrequency ground potential.

Because the required field gradient for focusing is much larger for heavy ions of small velocity than for protons injected at several hundred kV, we have to use a 3π length for the first few sections as stated previously.$^{1)}$ However, a use of 3π sections makes the cavity longer and the effective shunt impedance lower. Therefore generating as high field gradient as possible is desired to save radiofrequency power under a given condition of an aperture for beam, and limited outer diameter and length of the drift tube in which the quadrupole lens is to be contained.

To get a high field gradient between pole gaps, magnetic saturation of iron must not occur in the poles or yokes at too early stage of excitation. An uniform field distribution throughout iron is most favorable for the purpose, but it seems impossible to achieve the condition for a so complex field distribution in gaps of quadrupoles and we can at most hope to avoid extreme non-uniformity by suitably shaping poles. We chose several kinds of poles generally used and tried to find out some compromise between pole shape and coil space.

Figure 1 shows a testing magnet assembly and Fig. 2 gives dimensions of poles tested and the flux density distributions. As seen in Fig. 2, a straight pole will saturate at its base and others at other places. Of course, maximum of the flux density decreases with an increase in the pole tapering angle. However, an excessive taper makes the space for coils narrower and power

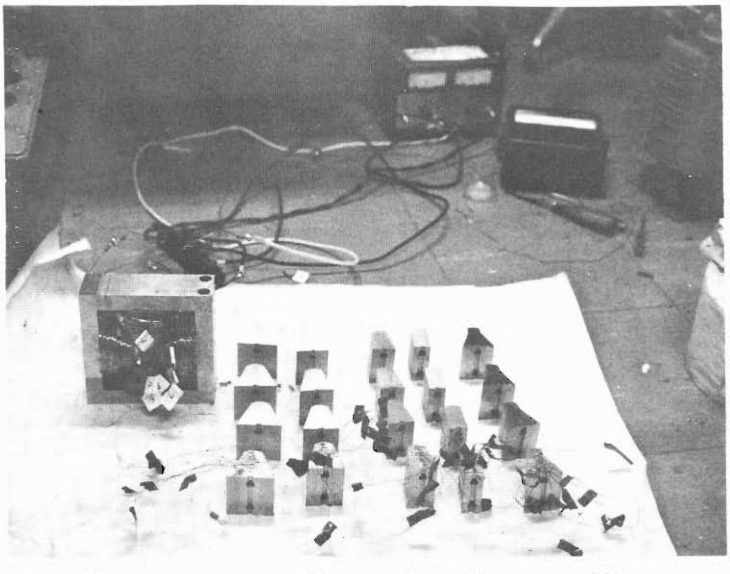

Fig. 1. Quadrupole magnet assembly and its pole pieces of various shapes.

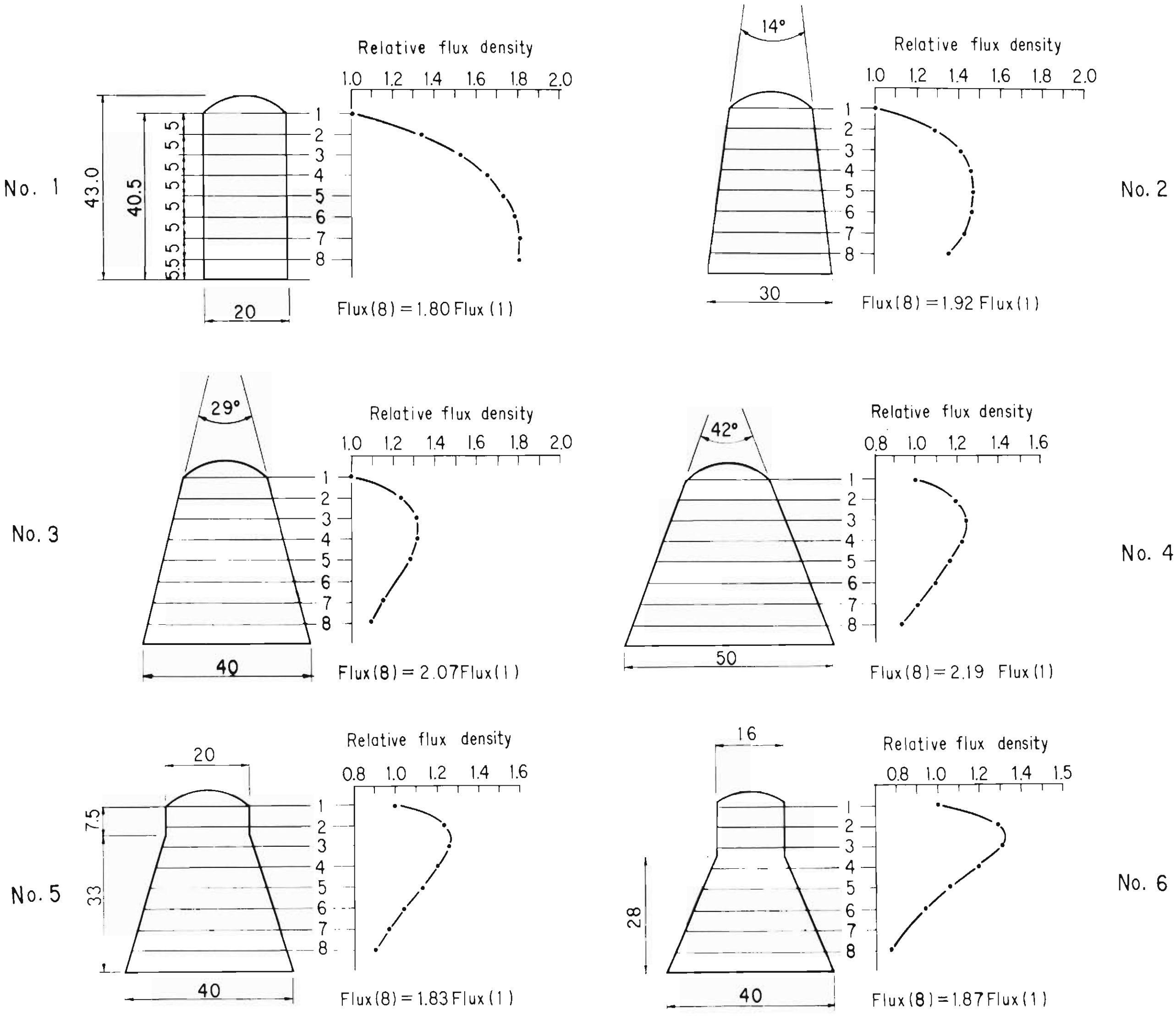

Fig. 2. Shapes of pole pieces and distribution of magnetic flux density. Below each figure, total flux at search coil No.8 is given by a ratio to those at No.1.

consumption for given ampere-turns would increase. Quantity of flux also increases as is written below each figure. However, a rapid growth of flux was seen only for the part above No.3 coil and flux leakage between poles was not large at the lower part. Decrease of flux bridging at the upper portion was tried by cutting the pole top as shown in Nos.5 and 6. Measurements showed that the maximum density in No.5 was nearly the same with that of No.4, whereas the quantity of flux at the base is smaller. The smaller flux allows use of thinner yokes, so that quadrupole diameter hence drift tube diameter can be made smaller. The smaller the tube diameter, the better is the cavity quality factor.

Reference

1) T. Tonuma, F. Yoshida, and M. Odera: IPCR Cyclotron Progr. Rep., 6, 18 (1972).

12-12. A Circuit Using a PIN Diode Switch for Measurements of the Q-values of a Cavity at High Resonant Frequencies

S. Takeda

A method which enables measurements of the large Q-values of a cavity was used for the design and conditioning work of the radiofrequency system of the cyclotron.[1] The same method can be applied to the design of the linac cavity by taking care of much higher frequency used.

Figure 1 shows a block diagram of measurement and Fig. 2 shows a new circuit using a PIN diode bridge as a switching element instead of a vacuum hard tube used previously. The latter cannot work at 50 MHz or higher frequencies necessary for study of the linac models.[2] The circuit contains a self-running multi-vibrator which determines the time cycle of switching, generating exponentially decaying curve, and triggering signal for other circuits. The length of the gate and the time constant of decay are adjustable by helical ohms. Large change of these can be made by replacement of resistors or capacitors.

The output impedance of the switching circuit is not very high and a due precaution is necessary to get correct Q-values of a cavity. An example of measurements was given in Ref.3.

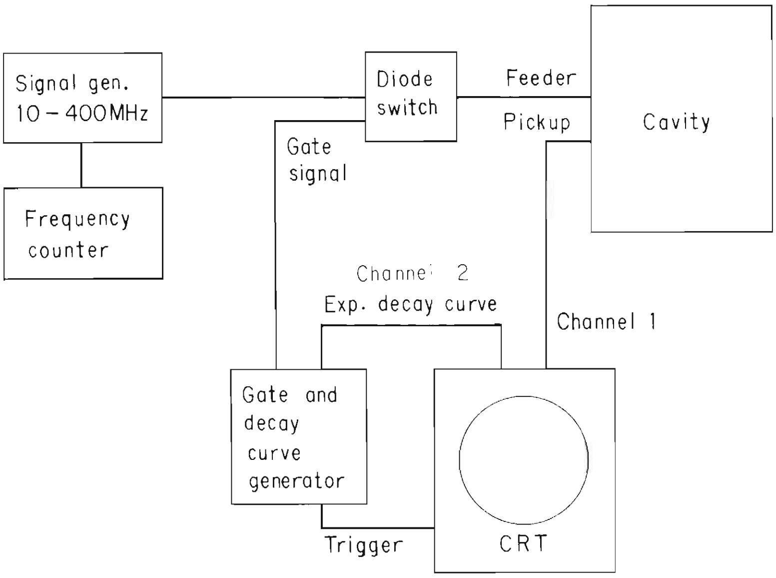

Fig. 1. A block diagram of measurement of quality factors. The diode switch can be attached directly to the power feeder.

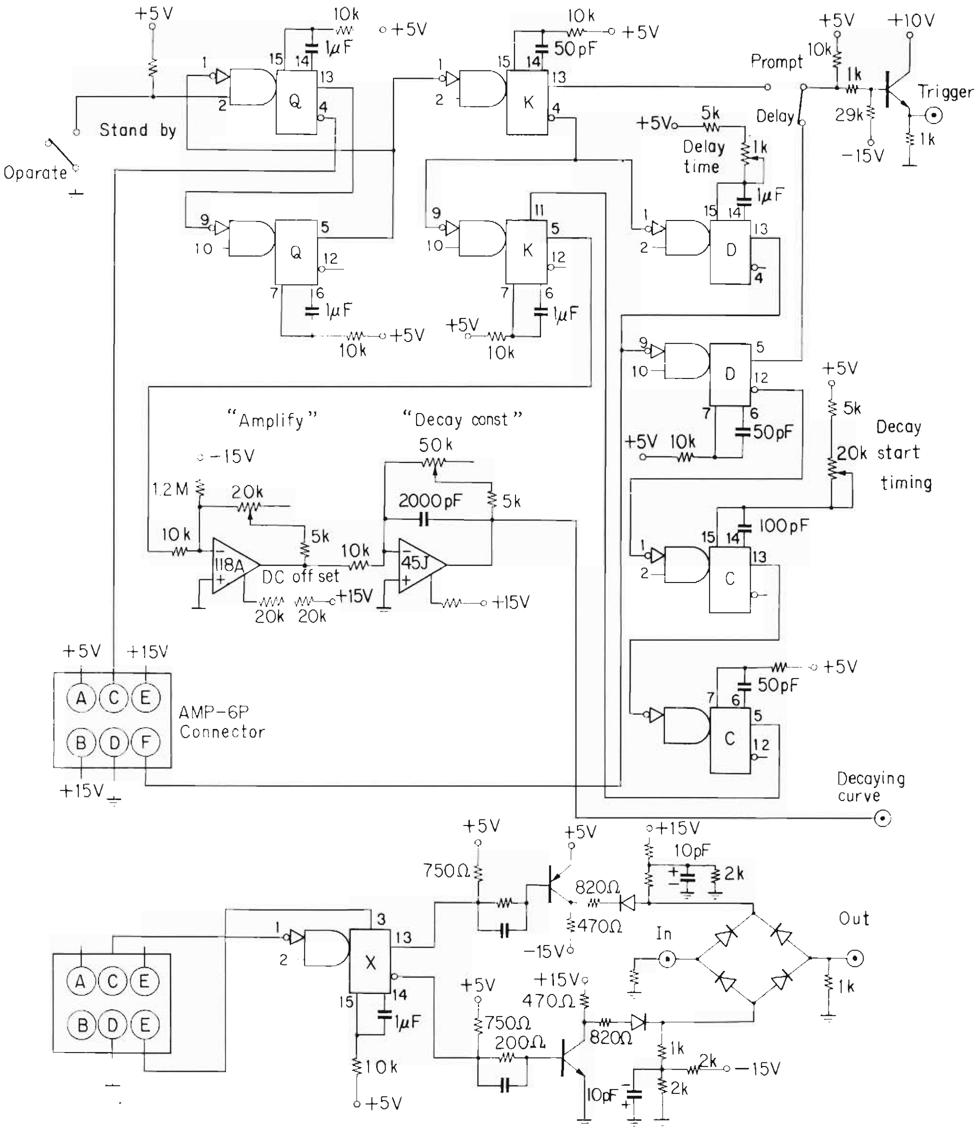

Fig. 2. Circuits for measurement. The upper one is a gate and an exponentially decaying curve generator and the lower is a diode switch. The integrated circuits Q,K,D,C and X are of type SN-74123-N and diodes are 5082-3081 of the Hewlett-Packard Co.

References

1) M. Odera, Y. Chiba, T. Fujisawa, Y. Miyazawa, and O. Terajima: Sci. Papers, I.P.C.R., 67, 99 (1973).

2) M. Odera: IPCR Cyclotron Progr. Rep., 8, 144 (1974); Y. Miyazawa, M. Hemmi, and M. Odera: ibid., p.146

3) M. Odera and Y. Chiba: ibid., p.139.

12-13. Trial Fabrication of Coils for Drift Tube Quadrupoles

T. Inoue and M. Odera

Strong field gradients are required for drift tube quadrupoles to focus low velocity heavy ions with a large mass-to-charge ratio. However, only a small volume is available for coils because of

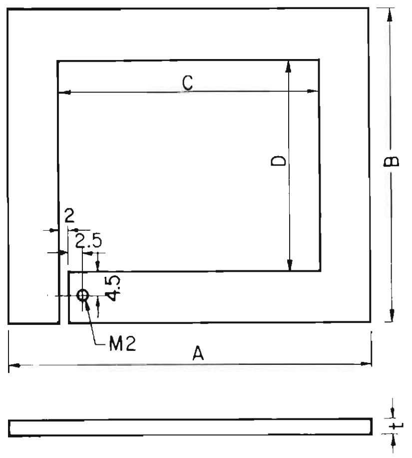

No.	A	B	C	D	t
	Dimensions				
1	72	62	52	42	3
2	72	60	52	40	3
3	72	58	52	38	3
4	72	56	52	36	3
5	72	54	52	34	3
6	72	52	52	32	3
7	72	50	52	30	3
8	72	48	52	28	3

Fig. 1. Dimensions of copper frames which form together a 7-turn coil of a pole of the shortest drift tube quadrupole magnet.

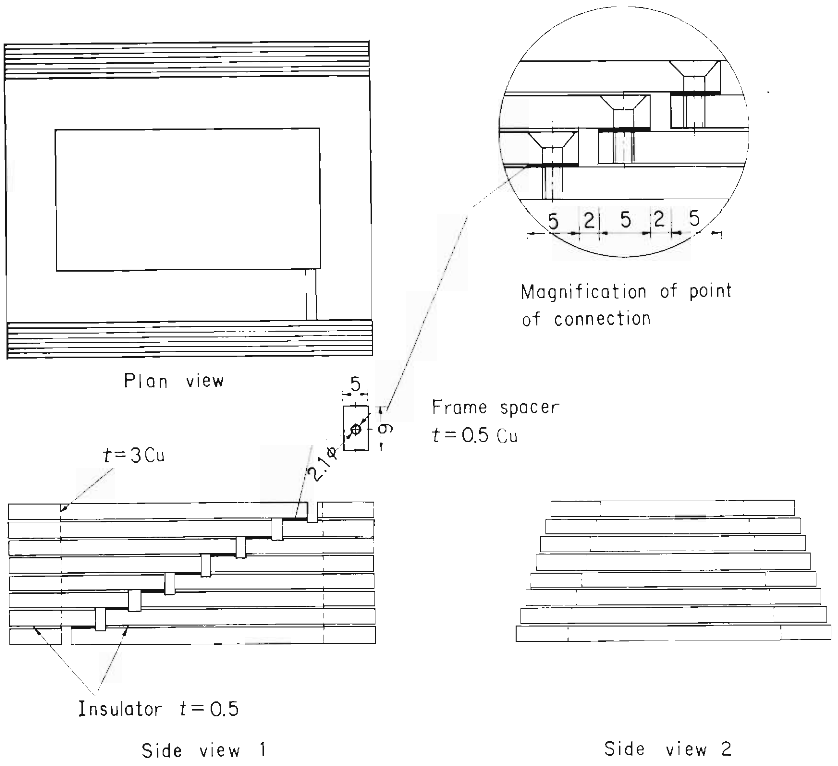

Fig. 2. A rectangular coil made from the frames. Details of construction can be seen in the upper right magnified figure in a circle.

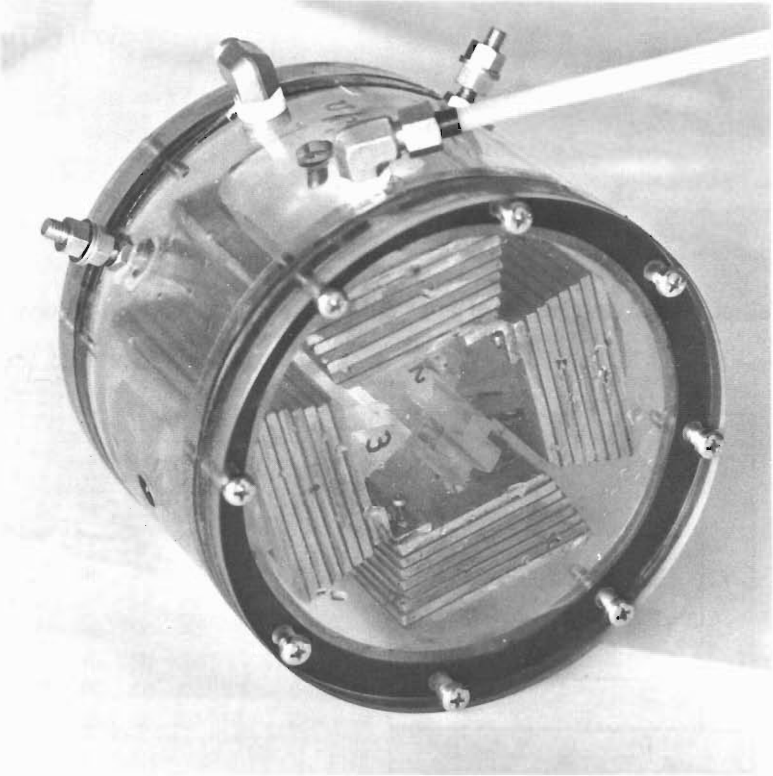

Fig. 3. A container made of acrylite to investigate coolant flow.

the short length of the low-energy drift tubes in which they are to be installed. In order to produce the ampere-turns required to get the strong field gradient without an excessive heat generation in the small space, coils having a good packing factor must be used. The structure of the coils should be designed so as to make removal of the heat generated feasible. The tape coil method devised at Super HILAC laboratory[1)] is an excellent example to do so.

We have manufactured coils by stacking thick rectangular copper frames cut as shown in Fig. 1. By suitably changing the position of cutting and hard-soldering them together, a seven-turn coil was formed as shown in Fig. 2. It is to be sealed in a drift tube and cooled with Freon-113 or deionized water flowing around it. Since a current as large as 500 A is estimated to be necessary to obtain a maximum field gradient of 7 kG/cm for the 24 mm-pole gap, efficient cooling of the coils is necessary. A current density in the conductor amounts to 17 A/mm^2. Figure 3 is a photograph of a container simulating a drift tube shell to investigate visually the coolant flow in a drift tube.

Reference

1) R. M. Main, K. Halbach, P. Kennedy, R. Yourd, A. Watanabe, and D. Kolody: UCRL-18240 (1968).

12-14. Effects of Non-uniformity of Voltage between Drift Tube Gaps

T. Tonuma, F. Yoshida, and M. Odera

Voltage between drift tube gaps in the linac cannot be constant over the whole range of frequency. At low frequencies it is almost constant but nonuniformity appears at higher frequencies. Therefore, the actual phase oscillation of an ion at high frequencies is expected to vary widely in comparison with that in the flat distribution, assumed for the determination of length and position of drift tubes. An example is presented here for the first cavity.

The length and the position of drift tubes were determined for a uniform 180 kV voltage

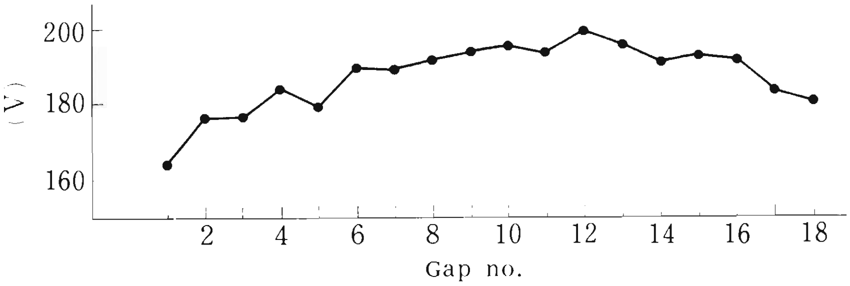

Fig. 1. Voltage distribution along the axis of acceleration in case of frequency 30.8 MHz.

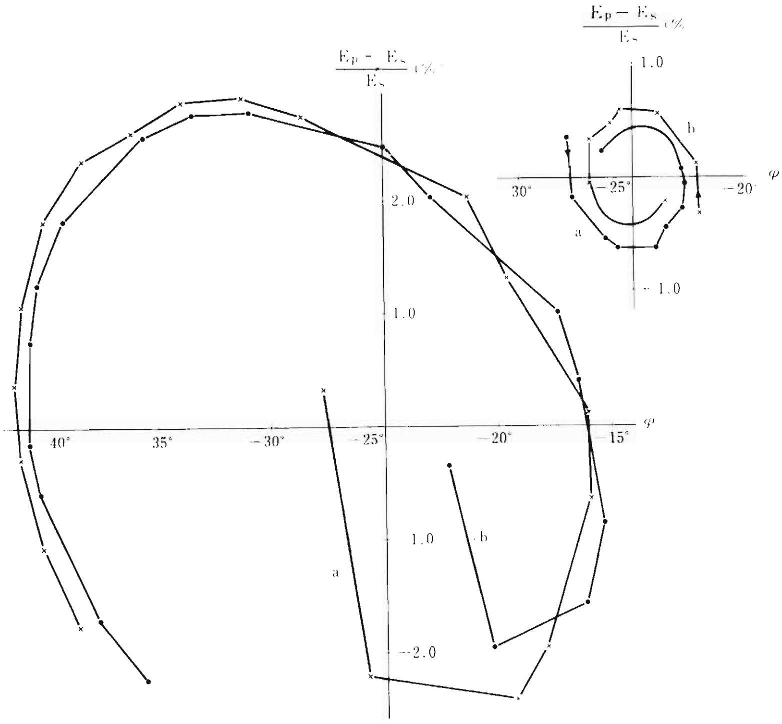

Fig. 2. Phase oscillation. Curve (a) is for 451.66 kV, −27.87° and (b) is for 448.34kV, −22.13° as starting conditions.

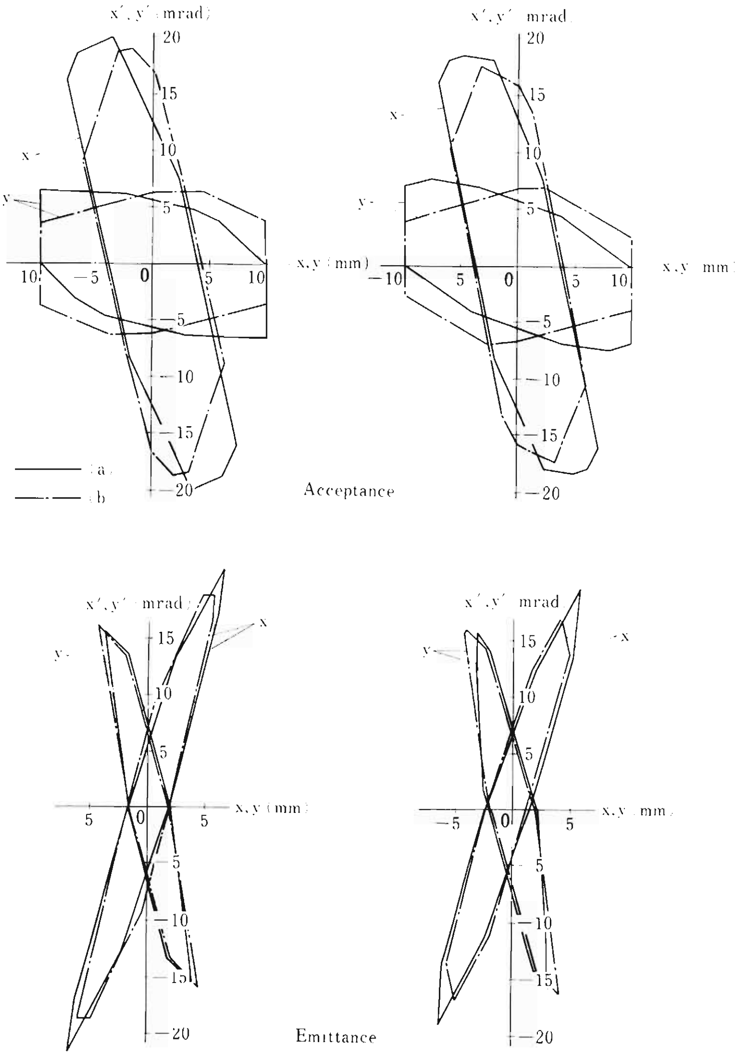

Fig. 3. Radial acceptance and emittance. Diagrams of x and y are for the vertical and horizontal directions, respectively. Lens sequence is vertically focusing and horizontally defocusing at the entrace.

distribution and with parameters as follows: m/q = 4, f = 40 MHz, injector voltage of 450 kV, synchronous phase of −25°, 4.0 cm gap length between drift tubes, and for the drift tubes of Nos. 1 − 9 and $3\pi/\pi$ mode, and of Nos. 10 − 19 and π/π mode.

Figure 1 shows the voltage distribution experimentally obtained in case of frequency 30.8 MHz given by the model IV (see 12 − 6 in this progress report).

Figure 2 shows phase shift φ vs. energy shift $(E_p - E_s)/E_s$ of an ion, where energy E_s is of synchronous particles in the standard distribution and E_p is of other particles. In the left of Fig. 2, phase oscillation of an ion is calculated using the distribution shown in Fig. 1, and the ideal phase oscillation having the standard distribution of 180 kV voltage is shown in the right. Curves (a) and (b) represent the phase oscillations of possible ions bunched at 451.66 kV, −27.87°, and 448.34 kV, −22.13° at injection, respectively.

Figure 3 shows radial acceptance and emittance diagrams of an ion passing through a 20 mmϕ aperture of drift tubes under the focusing condition $\cos\mu$ being equal to 0.7 and with phase oscillations given in Fig. 2. Diagrams on the left and right correspond to the phase oscillations shown on the left and right of Fig. 2, respectively.

It has been found that non-uniform voltage distribution in this degree gives large phase oscillations; nevertheless, results in little effects on the radial acceptance and emittance compared with that given by the standard distribution.

12-15. Computer Codes for Orbit Dynamics in the Heavy Ion Linac

F. Yoshida, T. Tonuma, and M. Odera

For the investigation on ion orbit dynamics of linac, programs consisting of three codes have been developed and prepared using the Honeywell DDP-124 computer in this laboratory.

The first code calculates the following parameters: the length of each drift tube in an accelerating tank; the magnetic field gradients of a quadrupole magnet contained in the drift tube which satisfy focusing conditions of ion trajectories; the necessary voltage of an injector; and the accelerating field between drift tubes needed for a given synchronous phase. These parameters are calculated under a given objective for the energy to be gained. Transit time factors are determined by an electric field distribution in a gap between two drift tubes measured using a perturbation technique. In addition, this code can print or plot phase oscillation vs. energy shift by giving numerically a voltage distribution which is non-uniform along the axis of acceleration and is different from a standard distribution used for determination of the length of drift tubes.

The second code describes an ion trajectory in a tank, which is calculated taking into account radial defocusing of an ion beam by the accelerating rf field, and motion in the focusing magnetic field gradients of quadrupole magnets and field-free regions. This code, also, gives radial acceptance and emittance of ion beam at one time by the inputs of apertures of drift tubes and the possible deviations of quadrupole magnets from the axis of acceleration caused by alignment errors.

As the emitted beam of the first tank has to be accepted by the next tank, matching of the emittance of the former with the acceptance of the latter is necessary. Therefore, the third code calculates an ion trajectory between two tanks by giving the distance of two tanks and the position and the field gradient of doublet or triplet quadrupole magnets.

13. LIST OF PUBLICATIONS

1) I. Kohno: "Elastic and Inelastic Scatterings of ^{14}N and ^{12}C Projectiles by ^{12}C, ^{27}Al, ^{28}Si, and ^{58}Ni", Sci. Papers I.P.C.R., 68, 38 (1974).
2) T. Wada and S. Yamaji: "Automatic Search Code for Coupled-Channel Calculation", Sci. Papers I.P.C.R., 68, 65 (1974).
3) F. Yatagai, T. Takahashi, Y. Kitajima, and A. Matsuyama: "Inactivation of Bacterial Spores by Charged Particles", J. Rad. Res., 15, 90 (1974).
4) K. Igarashi, F. Yatagai, T. Takahashi, and A. Matsuyama: "LET Dependence of DNA Single-Strand Scission in E. coli B_{s-1} by Charged Particles", J. Rad. Res., 15, 148 (1974).
5) A. Iwamoto, S. Suekane, S. Yamaji, and K. Harada: "Asymmetric Fission of ^{236}U", Progr. Theor. Phys., 51, 1617 (1974).
6) M. Matsui and M. Imamura: "Radiation Chemical Studies with Cyclotron Beams. III. The Heavy-Ion Radiolysis of Liquid Aliphatic Ketones", Bull. Chem. Soc. Japan, 47, 1113 (1974).
7) T. Nozaki, Y. Yatsurugi, N. Akiyama, Y. Endo, and Y. Makide: "Behaviour of Light Impurity Elements in the Production of Semiconductor Silicon", J. Radioanal. Chem., 19, 109 (1974).
8) K. Matsumoto, T. Kataoka, H. Kamei, M. Terasawa, T. Karasawa, J. Sakairi, and E. Yagi: "Embrittlement of Austenitic Stainless Steels Irradiated with α-Particles", Trans. Iron and Steel Inst. Japan, 14, 118 (1974).
9) A. Hashizume, H. Kumagai, Y. Tendow, and T. Katou: "A Mechanical Beam Chopper System for the Measurement of Half-Lives in the Millisecond Region" Nucl. Instr. Meth., 119, 209 (1974).
10) T. Inamura, F. Kearns, and J.C. Lisle: "Doppler Broadened γ-Ray Lineshape Analysis in Multiple Coulomb Excitation", Nucl. Instr. and Meth., 123, 529 (1973).
11) T. Suzuki: "New Giant Resonances", Nucl. Phys., A217, 182 (1973).
12) O. Hashimoto, A. Sumi, T. Nomura, S. Nagamiya, K. Nakai, T. Yamazaki, and K. Miyano: "Measurement of the g-Factor of the 0.57 ms 7^+ State in ^{202}Tl", Nucl. Phys., A218, 180 (1974).
13) T. Takemasa: "Finite-Range Calculation of Two-Neutron Transfer Reactions on Rate-Earth Nuclei", Nucl. Phys., A220, 31 (1974).
14) T. Suzuki: "Sum Rule Approach for Nuclear Vibrations and Effects of Core Polarization", Nucl. Phys., A220, 569 (1974).
15) T. Suzuki: "Momentum Transfer Dependence of the Effective Charge for Electroexcitation", Phys. Rev., C8, 2111 (1973).
16) T. Suzuki and C. Hinohara: "Sum Rules and Nonexchange Force", Phys. Rev., C9, 1186 (1974).
17) T. Nomura, K. Hiruta, M. Yoshie, and O. Hashimoto: "Alpha-Decay of ^{215}Fr", Phys. Rev.,

C9, 1168 (1974).

18) F. Kearns, G.D. Dracoulis, T. Inamura, J.C. Lisle, and J.C. Willmott: "Lifetimes of High Spin Rotational States", J. Phys. A: Math., Nucl. Gen., 7, L11 (1974).

19) S. Yamaji, T. Fujisawa, H. Kamitsubo, K. Matsuda, S. Motonaga, F. Yoshida, H. Sakaguchi, and K. Masui: "The Multi-Step Process in the ^{12}C(^{3}He, α)^{11}C Reaction". J, Phys. Soc. Japan, 37, 1191 (1974).

20) N. Shiotani, T. Okada, T. Mizoguchi, and H. Sekizawa: "Angular Distribution of Positron Annihilation Radiation in Vanadium and Niobium – Experiment", J. Phys. Soc. Japan, 38, 423 (1975).

21) I. Kohno: "Elastic and Inelastic Scattering of ^{14}N and ^{12}C Projectiles by ^{12}C and ^{28}Si", J. Phys. Soc. Japan, (in press).

22) M. Suehiro, M. Aratani, and N. Saito: "Ionization Caused by Beta Emitters", Mass Spectroscopy, 22, 183 (1974).

23) T. Takemasa: "Full Finite-Range Calculation for Heavy Ion Two Nucleon Transfer Reactions", Phys. Lett. (in press).

24) N. Nakanishi and H. Sakaguchi: "(^{3}He, d) Reactions on Cr and Ni Isotopes", Rep. of the Symp. on Nuclear Reaction, RCNP-P-1, p. 45 (1974).

25) T. Nozaki, M. Iwamoto, and T. Ido: "Yield of ^{18}F for Various Reactions from Oxygen and Neon", Int. J. Appl. Radiat. Isotopes, (in press).

26) T. Nozaki, M. Furukawa, S. Kume, and R. Seki: "Production of ^{28}Mg by Triton and α-Particle Induced Reactions", Int. J. Appl. Radiat. Isotopes, (in press).

27) F. Ambe and S. Ambe: "Chemical Effects of Neutron-Induced Nuclear Reactions in Halates and Related Compounds IV. The (n, γ) and (n, 2n) Reactions in Chlorates", Radiochim. Acta, 19, 42 (1973).

28) S. Ambe, F. Ambe, and N. Saito: "The Oxidation States of ^{119}Sb after the EC Decay of ^{119m}Te in TeO_2 and H_6TeO_6", Radiochim. Acta, p. 121.

29) F. Ambe, S. Ambe, H. Shoji, and N. Saito: "Mössbauer Emission Spectra of ^{119}Sn after the EC Decay of ^{119}Sb in Metals, Oxides and Chalcogenides of Antimony and Tellurium", J. Chem. Phys., 60, 3773 (1974).

30) S. Ambe and F. Ambe: "A Mössbauer Study of the Oxidation State of ^{119}Sn after the Successive EC Decays of ^{119m}Te in Telluric Acid", Radiochim. Acta (in press).

31) F. Ambe and S. Ambe: "A Mössbauer Study of the Valence States of ^{119}Sn after the EC Decay of ^{119}Sb in Antimony and Tellurium Iodides", Bull. Chem. Soc. Japan, 47, 2875 (1974).

32) S. Ambe and F. Ambe: "Mössbauer Emission Spectrum of ^{119}Sn in ^{119}Sb (OH) (C_2O_4)", Inorg. Nucl. Chem. Lett., 11, 139 (1975).

(Papers presented at international meetings)

1) T. Mikumo, I. Kohno, K. Katori, T. Motobayashi, S. Nakajima, M. Yoshie, and H. Kamitsubo: "Optimum Q-values in Multi-nucleon Transfer Reactions sufficiently high above the Coulomb Barrier", Intern. Conf. Reactions between Complex Nuclei, Held at Vanderbilt University, Nashville, Tennessee, June 10-14 (1974).
2) M. Yoshie, K. Katori, I. Kohno, T. Mikumo, T. Motobayashi, S. Nakajima, and H. Kamitsubo: "Single-nucleon Transfer on ^{92}Mo Induced by ^{14}N and ^{12}C ions", Intern. Conf. Reactions between Complex Nuclei, Held at Vanderbilt University, Nashville, Tennessee, June 10-14 (1974).
3) M. Matsui and M. Imamura: "Heavy-Ion Radiolysis of Liquid Aliphatic Ketones", 5th Intern. Congr. Rad. Res., Seattle, Washington, U.S.A., July (1974).
4) A. Matsuyama, T. Takahashi, K. Igarashi, and F. Yatagai: "Studies on bacterial inactivation and DNA-strand break formation by the cyclotron beam", 5th Intern. Congr. Rad. Res., Seattle, Washington, U.S.A., July (1974).
5) T. Nozaki: "Cyclotron Production of Medical-use Radioisotopes in Japan ",The 1st World Congr. Nuclear Medicine, Tokyo, Oct. (1974).
6) T. Ido: "Synthesis and In Vivo Distribution Patterns of ^{18}F-Organic Compounds", The 1st World Congr. Nuclear Medicine, Tokyo, Oct. (1974).
7) T. Higasi, M. Kanno, K. Tomura, and T. Nozaki: "Accumulation of Europium in Tumor", The 1st World Congr. Nuclear Medicine, Tokyo, Oct. (1974).

14. LIST OF PERSONNEL

Members of the Board

HAGIHARA Hitosi 萩原仁 (Chairman)
KAMITSUBO Hiromichi 上坪宏道
NOZAKI Tadashi 野崎正
HAMADA Tatsuji 浜田達二
NAKANE Ryohei 中根良平
ODERA Masatoshi 小寺正俊

Users Committee

HAMADA Tatsuji 浜田達二 (Chairman)
KAMITSUBO Hiromichi 上坪宏道
MATSUYAMA Akira 松山晃
ODERA Masatoshi 小寺正俊
SEKIZAWA Hisashi 関沢尚
IMAMURA Masashi 今村昌
KOHNO Isao 河野功
NOZAKI Tadashi 野崎正
SAKAIRI Hideo 坂入英雄

Operation and Machine Maintenance Group

FUJITA Shin 藤田新
KAGEYAMA Tadashi 影山正
KOHNO Isao 河野功
OGIWARA Kiyoshi 荻原清
IKEGAMI Kumio 池上九三男
KOHARA Shigeo 小原重夫
NAKAJIMA Hisao 中嶋尚雄
TAKEBE Hideki 武部英樹

New Machine Group

CHIBA Yoshiaki 千葉好明
INOUE Toshihiko 井上敏彦
KOHNO Isao 河野功
ODERA Masatoshi 小寺正俊
TONUMA Tadao 戸沼正雄
HEMMI Masatake 逸見政武
KAMITSUBO Hiromichi 上坪宏道
MIYAZAWA Yoshitoshi 宮沢佳敏
SHIMAMURA Akira 島村晏
YOSHIDA Fusako 吉田房子

Scientific and Engineering Personnel

Cyclotron Laboratory

CHIBA Yoshiaki 千葉好明
FUJITA Jiro 藤田二郎
INAMURA Takashi 稲村卓
KAMITSUBO Hiromichi 上坪宏道
KOHNO Isao 河野功
MOTONAGA Shoshichi 元永昭七
NAKANISHI Noriyoshi 中西紀喜
ODERA Masatoshi 小寺正俊
SUZUKI Toshio 鈴木敏男
WADA Takeshi 和田雄
YOSHIDA Fusako 吉田房子
FUJISAWA Takashi 藤沢高志
HEMMI Masatake 逸見政武
INOUE Toshihiko 井上敏彦
KARASAWA Takashi 唐沢孝
MIYAZAWA Yoshitoshi 宮沢佳敏
NAKAJIMA Shunji 中島諄二
NOMURA Toru 野村亨
SHIMAMURA Akira 島村晏
TONUMA Tadao 戸沼正雄
YAMAJI Shuhei 山路修平

(Visitors)

ICHIMURA Munetake 市村宗武 (Univ. of Tokyo)
FUJINO Takeo 藤野武夫 (Inst. Nucl. Study, Univ. of Tokyo)
HANAZONO Sakae 花園 栄 (Inst. Nucl. Study, Univ. of Tokyo)
HIRUTA Kotaro 蛭田幸太郎 (Tokyo Inst. Tech.)
IMANISHI Bunryu 今西文竜 (Nihon Univ.)
KAMMURI Tetsuo 冠 哲夫 (Univ. of Osaka)
KATORI Kenji 鹿取謙二 (Tokyo Univ. of Educ.)
KAWAI Mitsuji 河合光路 (Tokyo Inst. Tech.)
KOIKE Masahiro 小池正宏 (Inst. Nucl. Study, Univ. of Tokyo)
KOYAMA Katsuji 小山勝二 (Inst. Nucl. Study, Univ. of Tokyo)
KUTCHERA Walter (Technische Universität Munchen)
MIKUMO Takashi 三雲 昴 (Tokyo Univ. of Educ.)
NAKAI Koji 中井浩二 (Dept. Phys., Univ. of Tokyo)
NAKAMURA Masanobu 中村正信 (Dept. Phys., Kyoto Univ.)
OHNUMA Hajime 大沼 甫 (Inst. Nucl. Study, Univ. of Tokyo)
SAKAGUCHI Harutaka 坂口治隆 (Dept. Phys., Kyoto Univ.)
SEKIGUCHI Masayuki 関口雅行 (Inst. Nucl. Study, Univ. of Tokyo)
SPROUSE, Gene (State Univ. of New York at Stony Brook)
TAKEDA Shigeru 竹田 繁 (Nat. Lab. High Energy Phys.)
TAKEMASA Tadashi 武政尹士 (Univ. of Osaka)
WAKAI Masamichi 若井正道 (Univ. of Osaka)
YAMADA Satoru 山田 聡 (Tokyo Inst. Tech.)
YOKOMIZO Hideaki 横溝英明 (Inst. Nucl. Study Univ. Tokyo)
YOSHIDA Hiroshi 吉田 弘 (Univ. of Osaka)

(Students)

FUKUDA Tomokazu 福田共和 (Univ. of Tokyo)
IKEZOE Hiroshi 池添 博 (Univ. of Tokyo)
KANAI Tatsuaki 金井達明 (Tokyo Univ. of Educ.)
MOTOBAYASHI Tohru 本林 透 (Univ. of Tokyo)
OOI Takao 大井孝雄 (Tokyo Univ. of Educ.)
YAMAZAKI Yoshishige 山崎良成 (Univ. of Tokyo)
YOSHIE Morio 吉江森男 (Tokyo Univ. of Educ.)

Radiation Laboratory

AWAYA Yohko 粟屋容子
HASHIZUME Akira 橋爪 朗
KATOU Takeo 加藤武雄
KUMAGAI Hidekazu 熊谷秀和
TAKAHASHI Tan 高橋 旦
HAMADA Tatsuji 浜田達二
IZUMO Koichi 出雲光一
KONNO Satoshi 金野 智
OKANO Masaharu 岡野真治
TENDOW Yoshihiko 天道芳彦

(Visitors)

DOKE Tadayoshi 道家忠義 (Waseda Univ.)
IIO Masahiro 飯尾正宏 (Tokyo Metropol. Jeriatric Hosp.)
NAGAHARA Teruaki 永原照明 (Rikkyo Univ.)
SUZUKI Kazuaki 鈴木一明 (Japan Anal. Chem. Res. Inst.)
HAYASHIBE Shogo 林部昭吾 (Tohoku Univ.)
FUJIOKA Manabu 藤岡 学 (Tohoku Univ.)

Nuclear Analytical Chemistry Laboratory

AMBE Fumitoshi 安部文敏
ARATANI Michi 荒谷美智
NOZAKI Tadashi 野崎 正
AMBE Shizuko 安部静子
IWAMOTO Masako 岩本正子
SAITO Nobufusa 斎藤信房

(Visitors)

AKIYAMA Nobuyuki 秋山信之 (Komatsu Electronic Metals Co., Ltd.)
FUKUSHI Kiyoshi 福士 清 (Nat. Inst. of Radiological Sciences)
HARA Toshihiko 原 敏彦 (Nat. Nakano Chest Hosp.)
TAKI Koh 滝 幸 (Kitazato Univ. Dept. of Hygiene)
IDO Tatsuo 井戸達雄 (Nat. Inst. of Radiological Sciences)
KASIDA Yoshihiko 樫田義彦 (Nat. Inst. of Radiological Sciences)
YATSURUGI Yoshifumi 八剣吉文 (Komatsu Electronic Metals Co., Ltd.)

Synthetic Organic Chemistry Laboratory

OHTSUKA Yasuo 大塚晏央
TAHARA Akira 田原 昭

Radiobiology Laboratory

IGARASHI Kazui 五十嵐一戉
MATSUYAMA Akira 松山 晃

(Student)

YATAGAI Fumio 谷田貝文夫 (Graduate Course of Sci. Engg., Waseda Univ.)

Radiation Chemistry Laboratory

IMAMURA Masashi 今村 昌
MATSUI Masao 松井正夫
KIMURA Kazuie 木村一宇

(Visitors)

YASUKAWA Tamio 安川民男 (Tohoku Univ.)
TAKAHASHI Tohru 高橋 太 (Tohoku Univ.)

Metal Physics Laboratory

HASIGUTI R. Ryukiti 橋口隆吉
SAKAIRI Hideo 坂入英雄
YAGI Eiichi 八木栄一
KOYAMA Akio 小山昭雄
SHIOTANI Nobuhiro 塩谷亘弘

(Visitors)

ISHINO Shiori 石野 栞 (Univ. of Tokyo)
MISHIMA Yoshitsugu 三島良績 (Univ. of Tokyo)
SHIRAISHI Haruki 白石春樹 (Nat. Res. Inst. for Metals)

Magnetic Materials Laboratory

OKADA Takuya 岡田卓也
SEKIZAWA Hisashi 関沢 尚

(Vistor)

MIZOGUCHI Tadashi 溝口 正 (Gakushuin Univ.)

Work Shop

TAKESHITA Isao 竹下勇夫

Radiation Monitoring and Safety Office

KODA Kugao 甲田陸男
USUBA Isao 薄葉 勲
SAKAMOTO Ichiro 坂本一郎

15. LIST OF OUTSIDE USERS AND THEIR THEMES

Description is in the order of themes, energies of particles used, and names of persons and institutions responsible for the themes are added. Numbers in parentheses are total beam times and frequency of irradiation between Jan. and Dec. 1974. The outside users' publications are listed at the end of this chapter.

1) “Production of ^{18}F for Bone Scanning”
   ^{3}He – 18,25 MeV
   H. Kakehi, Chiba Univ. Hospital
   A. Tsuya, National Cancer Res. Inst. (20 h, 5)
2) “Production of ^{43}K for Heart Scanning”
   α – 27 MeV
   M. Nakamura
   Med. Dept., Kyushu Univ. (23 h, 5)
3) “Study of the Production of ^{61}Co, ^{61}Cu, ^{135}La, and ^{123}I”
   ^{3}He – 40 MeV, α – 40 MeV
   Y. Homma
   Chem. Dept., Tokyo Metropolitan Univ. (18 h, 6)
4) “Production of ^{123}I for Diagnostic Use”
   ^{3}He – 38, 39 MeV
   N. Nakazawa
   First Radioisotopes Co. (11 h, 2)
5) “Studies on ^{53}Mn”
   d – 15 MeV, ^{3}He – 20 MeV
   S. Shibata
   Chem. Dept., Kyushu Univ. (22 h, 2)
6) “Measurement of the Cross Section of the ^{151,152}Eu (p, n) Reaction”
   p – 15 MeV
   K. Komura
   Inst. for Nucl. Study, Univ. of Tokyo (3 h, 1)
7) “Determination of the Half-life of ^{59}Ni”
   p – 17 MeV
   H. Mabuchi
   Inst. for Solid State Physics, Univ. of Tokyo. (5 h, 1)
8) “Simulation of Swelling of Stainless Steel with Cyclotron Irradiation”
   α – 30, 35.

M. Terasawa
Toshiba R. and D. Center (12 h, 3)

9) "Radiation Damage of Stainless Steel"
α – 36
K. Shiraishi
Japan Atomic Energy Research Inst. (12 h, 1)

10) "Study of Effect of Helium Bubbles on the Mechanical Behavior of Stainless Steel SUS 32 and 316 and Zircaloy Cladding"
α – 36 MeV
S. Kawasaki, T. Furuta, and T. Katou
Japan Atomic Energy Research Inst. (83 h, 7)

11) "Levels of ^{136}Ba from the Decay of ^{136}Cs"
d – 23 MeV
S. Hayashibe and M. Oshima
Faculty of Science, Tohoku Univ. (3 h, 1)

12) "Levels of ^{119}Sb from the Decay of ^{119m}Te"
α – 44 MeV
M. Fujioka, M. Yanbe, and M. Hirasawa
Faculty of Science, Tohoku Univ. (3 h, 1)

13) "The Electric Monopole Transition in ^{154}Gd Feeded by ^{154}Tb"
α – 38 MeV
H. Yamada
Nagoya Univ.
H. Kawakami, K. Komura, and M. Koike
Inst. for Nuclear Study (6 h, 1)

14) "Production of ^{130}I for Study of Angular Correlation of the Gamma-Rays of ^{130}Xe"
P – 15 MeV
S. Furusawa
Dept. Phys., Niigata Univ. (3 h, 2)

15) "Production of ^{206}Bi for Study of Angular Correlation of the Gamma-Ray of ^{206}Po"
p – 9, α – 40
S. Furusawa
Dept. Phys., Niigata Univ. (5 h, 1)

16) "Study of the Decay Chain of ^{156}Er"
C – 65 MeV
S. Iwata and T. Tamura
Research Reactor Institute, Kyoto Univ.
J. O. Rasmussen
Univ. of California (10 h, 2)

Publications

1. T. Furuta and S. Kawasaki: "The Influence of Helium Distribution and Grain Size on High-Temperature Embrittlement of Stainless Steel", J. Nucl. Mat., 50, 275 (1974).
2. T. Furuta and S. Kawasaki: "Stress-Rupture Properties of Helium-Injected Zircaloy-4", J. Nucl. Sci. Tech., 11, 268 (1974).
3. K. Matsumoto, T. Kataoka, H. Kamei, M. Terasawa, T. Karasawa, H. Sakairi, and E. Yagi: "Embrittlement of Austenitic Stainless Steels Irradiated with α - particles", Trans. Iron and Steel Inst. Japan, 14, 118 (1974).

AUTHOR INDEX

IPCR **Cyclotron Progress Report**

理化学研究所サイクロトロン年次報告 第8巻(1974)

印　刷　昭和50年（1975）3月25日
発　行　昭和50年（1975）3月30日
発行者　理化学研究所
代表者　星野敏雄
〒351　埼玉県和光市広沢2番1号
電話（0484）62－1111
編集者　理化学研究所サイクロトロン運営委員会
委員長　浜田達二
印刷所　丸星印刷株式会社
〒101　東京都千代田区神田神保町1丁目42番地

定価 3,000円

理化学研究所

埼玉県　和光市　広沢